High-Resolution Study of Selected Intraday Variable Sources

Dissertation

zur

Erlangung des Doktorgrades (Dr. rer. nat.)

der

Mathematisch-Naturwissenschaftlichen Fakultät

der

Rheinischen Friedrich-Wilhelms-Universität Bonn

vorgelegt von

Krisztina Éva Gabányi

aus

Budapest (Ungarn)

Bonn, 2006

Angefertigt mit Genehmigung der Mathematisch-Naturwissenschaftlichen Fakultät der Rheinischen Friedrich-Wilhelms-Universität Bonn

1. Referent: Prof. Dr. Uli Klein

2. Referent: Priv. Doz. Dr. Walter Huchtmeier

Tag der mündlichen Prüfung: 12.06.2006

Contents

Preamble

In the 1930's, a new window on the sky was opened. Karl Jansky's discovery of the radio emission of the Milky Way was the birth of a new field in astronomy, radio astronomy. Astonishing new objects were discovered during the coming decades: pulsars, quasars, the cosmic microwave background, etc.

Radio waves are affected by the ionized interstellar medium through which they pass. Wide ranges of scattering effects can occur and influence the observed characteristics of compact radio objects. Distinguishing between scattering-induced and source-intrinsic phenomena is very important, both in studying the interstellar matter of the Milky Way and in investigating the physical properties of the background source itself.

A large number of flat spectrum extragalactic radio sources exhibit Intraday Variability, which is thought to be at least partly due to interstellar scintillations. This phenomenon is still not understood completely. Can propagation effect alone account for all of the observed variability characteristics? How important is the contribution from the intrinsic structure of the source? What is the mixing ratio between extrinsic and intrinsic effects? In what extent are the radio observations of Active Galactic Nuclei influenced by the interstellar matter of the Milky Way?

In this thesis, these questions are investigated through different observational approaches:

- IDV observations of selected samples of flat spectrum radio sources are presented. The dependence of variability characteristics on the galactic latitude is discussed.
- The interplay between extrinsic and source intrinsic effects is studied in detail for a specially selected scatter broadened quasar using single dish and interferometric measurements.
- Investigating the milliarcsecond to sub-milliarcsecond structure of an IDV source at the highest angular resolution in closely-spaced epochs in time can reveal the possible changes in the source structure on IDV time-scales. Space-VLBI data of total and polarized intensity of an IDV blazar are analyzed and discussed.

Conventions and constants used in this thesis

Cosmology Throughout this thesis Cold Dark Matter (CDM) cosmology is used. The cosmological parameters are those derived from the Wilkinson Microwave Anisotropy Probe (WMAP) Observations (Spergel et al. 2003):

The Hubble constant is: $H_0 = 71\,\mathrm{km\,s^{-1}\,Mpc^{-1}}$
Dark energy density: $\Omega_\Lambda = 0.73$
Matter density: $\Omega_\mathrm{M} = 0.27$

Spectral index The spectral index (α) is defined as: $S \sim \nu^{+\alpha}$, where S is flux density and ν is the observing frequency.

Non standard units Measurement units used in this thesis:
Rayleigh: 1 Rayleigh is the flux of 10^6 photons emitted in all directions per square centimetre, per second.
Jansky: $1\,\mathrm{Jy} = 10^{-26}\,\mathrm{W\,Hz^{-1}\,m^{-2}}$
Parsec: $1\,\mathrm{pc} = 3.08568 \cdot 10^{16}\,\mathrm{m}$
Astronomical Unit: $1\,\mathrm{AU} = 1.5 \cdot 10^{11}\,\mathrm{m}$

1 Introduction

1.1 Active galactic nuclei

The term active galactic nuclei (AGN) refers to the central regions of those 7 % of all galaxies in which the energy output exceeds the amount that can be attributed to ordinary stellar processes. The luminosities of AGN range between 10^{42} erg s^{-1} and 10^{48} erg s^{-1}, 10^4 times larger than that of a typical galaxy. These enormous luminosities are produced within a small volume of a few pc and can be observed over broad range of frequencies, from radio bands to the extreme γ-rays at TeV energies.

1.1.1 Classification of AGN

Various types of AGN exist. The first AGN type objects were discovered in the 1940s in the optical waveband by Carl Seyfert (Seyfert 1943). This class of extremely bright, mostly spiral galaxies were then named *Seyfert galaxies*. (Although their unusual emission-lie spectra had been noticed earlier, see Mayall 1934, and references therein). They are characterized by a luminous core and very bright emission lines. Type 1 Seyfert galaxies exhibit both narrow and broad emission lines, whilst type 2 show only narrow emission lines. Recently, there are indications that the two types of Seyfert galaxies do not group in clearly separated classes, but they follow a continuous distribution between the types (Williams et al. 2002; Dewangan & Griffiths 2005).

Naturally, as the observing technique develops, the classification evolves as well. Another type of AGN, named *quasar* was originally the abbreviation of quasi stellar radio object, since the first ones were observed as the point-like optical counterpart of the radio sources 3C 48 by Matthews & Sandage (1963) and 3C 273 by Schmidt (1963). Nowadays though, quasars are divided into subgroups depending on their radio luminosities, and the ratio between radio-loud and radio-quiet quasars is roughly one to ten. Quasars outshine their host galaxies, their hosts appear usually just as faint emission in deep optical images.

Interestingly, the name of another class of AGN, the so called *BL Lac objects* or *BL Lacs*, is also a "living proof" of the history of identification of AGN. The designation BL Lacertae was originally meant to indicate a variable star in the Lacerta constellation, but later turned out to be an extragalactic object, an archetype of highly variable type of AGN. Other typical features are the high polarisation and the lack of emission lines.

Blazars unite the highly variable AGN, the BL Lacs, and the so called *optically violently variable* (OVV) quasars.

Radio galaxies, another type of active galaxies, show strong radio emission and extended structure (up to the order of 1 Mpc). Their radio emission usually comes from

regions far away from the corresponding optical objects. These regions, called lobes, are powered by highly collimated jets, originating from the galactic nucleus. A typical classification scheme of radio galaxies is based upon their morphology. Fanaroff & Riley (1974) distinguish between radio galaxies, depending upon whether their highest surface brightness region(s) is (are) close to the core (edge darkened, FR sources), or are at larger distances (edge brightened, FR sources). Fanaroff & Riley (1974) found that this taxonomy coincides with differences in radio luminosity: FR sources are more powerful than FRI. More precisely, most of the sources that have a luminosity at 178 MHz less than $2 \cdot 10^{25} \cdot h_{100}^{-2} \mathrm{W\,Hz^{-1}}$ are FR sources (where h_{100} is the Hubble constant in units of 100 $\mathrm{km\,s^{-1}\,Mpc^{-1}}$), whilst brighter sources are nearly all FR . It is not clear, what causes the dichotomy. Perhaps the central engines of the two types are intrinsically different and thus produce different kinds of jets, or the host galaxies have different environments. Even the distinction is not clear, some sources have been found with a "hybrid" structure: they reveal FR morphology on one side and an FR -like jet on the other side (Gopal-Krishna & Wiita 2000).

Similar to the Seyfert galaxies, radio galaxies can also be divided into subgroups of narrow line and broad line radio galaxies according to their line spectrum. As this distinction occurs in different AGN types, the designation of *type AGN* and *type AGN* is formed. Type AGN have both narrow and broad emission lines, type AGN have only narrow emission lines.

There are numerous other types and subclasses of AGN, such as *Low Luminosity AGN* (LLAGN), *Low Ionization Nuclear Emission Region Galaxies* (LINERs), *Ultra-Luminous Infra-Red Galaxies* (ULIRGS), *Gigahertz Peaked Sources* (GPS), *Compact Steep-Spectrum Source* (CSS), etc. Here, they are not presented in detail, since the focus of this thesis is different.

1.1.2 Unification model

Unification models have been proposed to explain the different types of AGN as different manifestations of the same type of object viewed under different aspect angle. The concept of the unification paradigm (see reviews by Urry & Padovani 1995; Urry 2004) is the following (see Figure 1.1):

- The central engine powering the AGN is a super-massive ($10^6\ M_\odot$ to $10^{10}\ M_\odot$) black hole accreting matter from its surrounding.
- The in-falling matter forms an accretion disk. The typical radius of the accretion disk is of the order of a few AUs. It is heated by viscous and magnetic processes, emits at optical through X-ray energies. The most important unsolved problems are the structure of the accretion disk (clumpy or smooth), the applicability of advection dominated accretion flow (ADAF) models to the innermost part of the disks, and the existence of a hot X-ray emitting corona above the disk.
- The fast-moving clouds producing the broad emission lines (from the broad line region, BLR) are located around and above the accretion disk.
- A dusty torus surrounds the central engine with an inner radius of order one parsec. The actual shape of this structure is still uncertain; it is not clear whether it is really

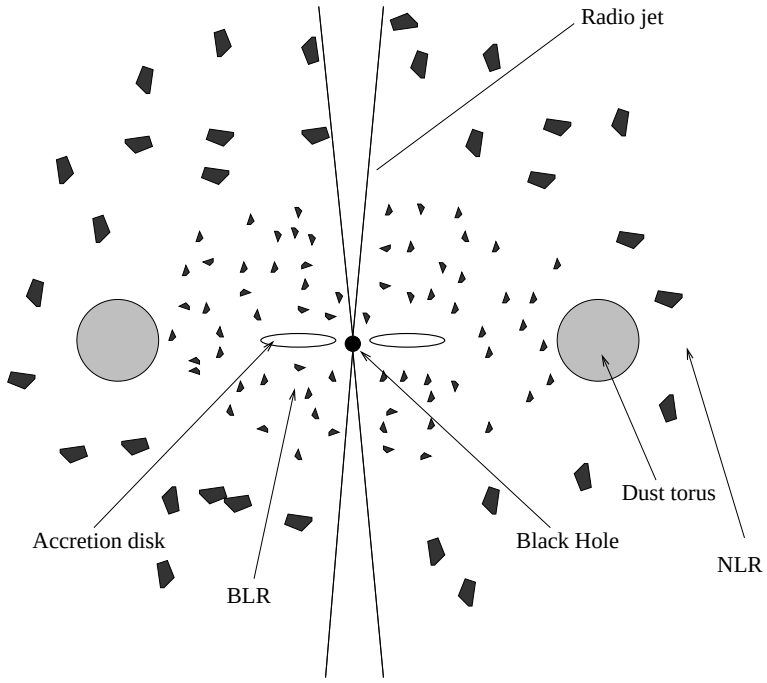

Figure 1.1: Schematic diagram of the unified model of AGN (following Urry & Padovani 1995).

torus-like. Recent findings of infrared observations suggest a clumpy structure of the obscuring torus (e.g. Beckert 2005, and references therein).

- Beyond the obscuring torus, slower moving clouds of gas compose the narrow line region (NLR), producing the emission lines with narrower widths.

- Perpendicular to the plane of the accretion disk, plasma is ejected in the form of highly collimated jets. The speed of the plasma is relativistic, and the opening angle of the jet is thought to be narrow, less than 10°. The jets are thought to be formed within a few tens to 100 Schwarzschild radii of the black hole. They extend outward to several kpc, in some cases as far as a Mpc, and the most powerful ones form huge radio lobes. How the jets are formed and how they maintain their shape is studied through more and more elaborate numerical simulations. In the last decades there has been growing evidence that magnetic fields play an important role in the process. Different magneto-hydrodynamical simulations can produce collimated relativistic jets. However, they are not able to maintain the outflows seen kiloparsecs or even parsecs away from the black hole (Camenzind 2005, and references therein). No code is available yet that follows the evolution of plasma outflows from the immediate vicinity of the black hole to the region where the collimation occurs. Observations of M 87 for example suggest that the opening angle of the jet at its base is large ($\geq 60°$) and collimation takes place after a few tens Schwarzschild radii (Junor et al. 1999; Krichbaum et al. 2004).

This paradigm seems to be valid for all radio loud AGN, and without the last ingredient (jets) it holds for radio quiet AGN as well.

According to this paradigm, when the observer looks at the same "beast", depending upon the viewing angle one can see objects with different characteristic features. Looking in the jet direction, we observe BL Lacs, or OVVs. Otherwise, at larger, but still small angles, we can observe both the narrow and broad emission lines (type AGN). As the angle between the jet and the line of sight increases further, we see quasars. At large enough angles the torus starts to obscure the inner broad line region and we see narrow line radio galaxies or Seyfert 2 (type) AGN.

This work is focused on radio loud quasars. When I use the word quasar or AGN I refer to radio loud objects.

Nowadays, it is generally assumed, that every massive galaxy (including our Milky Way) harbours super-massive black holes in their centres. Direct observational evidence (based upon detections of stellar dynamics) exist in at least three prominent galaxies: the Milky Way, NGC 4258 and in M 31 (Bender et al. 2005, and references therein). The question, how (and whether) "activeness" can be related to the evolutionary stage of galaxies is still unanswered. These theories are referred to as "Grand Unification".

1.2 Relativistic jets

1.2.1 Synchrotron radiation

Synchrotron radiation is named after a type of particle accelerators, where this kind of radiation was first produced. (It was also called magneto-bremsstrahlung in the past, although this term is not used nowadays). Synchrotron radiation is emitted when a relativistic charged particle is accelerated in a magnetic field. Let's consider a charged particle moving in a magnetic field **B** with a velocity of **v**. The Lorentz force (**v** × **B**) causes the particle to move along a helical path around the magnetic field line given by:

$$\nu_g = \frac{qB}{2\pi\gamma mc}, \tag{1.1}$$

where ν_g is the gyration frequency, q is the charge, m is the mass, $\gamma = 1/\sqrt{1 - v^2/c^2}$ is the Lorentz factor of the particle and c is the speed of light. In the case of a non-relativistic particle, the emitted radiation would be dipole radiation. For an observer at rest, relativistically moving particle emits radiation into a narrow cone with an opening angle of $1/\gamma$. Because the mass of the electron is much smaller (approximately 2000 times) than that of a proton, the acceleration of the electrons is larger than that of the protons for the same kinetic energy, and so astronomically observed radiation originates from mainly electrons (or positrons), the contribution of protons is mostly negligible.

The observed radio spectra of AGN can usually be described by a power law, $S \sim \nu^{\alpha}$, where S is the flux density, ν is the observing frequency and α is the spectral index. Such spectra can be produced by an ensemble of electrons with a power law energy distribution:

$$n(E)\,dE \sim E^{-p}dE, \tag{1.2}$$

where E is the particle kinetic energy and p is a constant related to the spectral index, α, as $\alpha = (1 - p)/2$. This spectrum is strictly valid if there is no absorption by electrons, that is in a plasma that is optically thin to its own radiation (i.e. extended regions of radio source).

Compact regions of AGN often have flat or inverted spectra, a result of synchrotron self-absorption. It can be shown (Rybicki & Lightman 1979) that in an optically thick medium, the form of the spectrum is: $S \sim \nu^{5/2}$. So far, the exponent 5/2 has never been observed. More compact sources have flatter spectra, whilst extended sources have more complex spectra. This can be explained by a superposition of different parts of the source having different turn-over frequencies (they become optically thick at different frequencies).

The intensity of the radiation can be expressed in terms of the brightness temperature. The brightness temperature is equivalent to the temperature of a black body which radiates the same flux density as the source. It is defined as:

$$T_{\mathrm{B}} = \frac{c^2}{2k_{\mathrm{B}}}\frac{I}{\nu^2}, \tag{1.3}$$

where k_{B} is the Boltzmann's constant, c is the speed of light and I is the intensity in MKS units ($\mathrm{J\,s^{-1}\,m^{-2}\,Hz^{-1}\,sr^{-1}}$). The flux density is the intensity integrated over the solid angle: $S = \int I \cos\theta d\Omega$.

Equating S with the synchrotron flux density at the self absorption frequency (S_{m}) and using the usual units, T_{B} can be written as (see e.g. Ghisellini et al. 1993):

$$T_{\mathrm{B}} = 1.77 \cdot 10^{12}\left(\frac{S_{\mathrm{m}}}{{\nu_{\mathrm{m}}}^2\theta^2}\right)(1+z)\,, \tag{1.4}$$

where z is the redshift of the source, S_m measured in Jy, θ in mas ν_m in GHz and θ is the source size. The multiplicative constant has a unit of $\mathrm{m^2\,J^{-1}\,s^{-2}}$, thus the T_{B} is obtained in K.

1.2.2 Inverse Compton radiation

In a compact source, the emitted synchrotron photons can be inverse Compton scattered by their own electrons (so called synchrotron self-Compton process, SSC). In the "normal" Compton scattering, photons scatter off electrons and lose some energy in the recoil. In the inverse Compton process, the photon gains energy from the moving electron. (In the rest frame of the electron, the kinematics are the same as in the "normal" Compton scattering.) The acquired energy is proportional to the square of the Lorentz factor of the scattering electron. This process can be responsible for the high energy photons of AGN. Depending on the value of γ, radio and infrared photons can be scattered up to X-ray and gamma-ray energies.

In the left side of Fig. 1.2 (taken from Camenzind 2002), the spectrum of a BL Lac object (Mrk 421) is displayed. It is dominated by synchrotron emission from the radio to the optical region and inverse Compton emission in the X-ray and gamma ray regimes. In contrast the spectral energy distribution (SED) of a typical quasar is displayed in the right plot in Fig. 1.2; it exhibits three distinct "bumps" in the IR, in the UV, and in the hard X-ray, corresponding to the dusty torus, to the accretion disk and to the reflection of the accretion disk.

The energy loss rates of the electron in the synchrotron process and in the inverse Compton scattering are similar:

$$-\left(\frac{dE}{dt}\right)_{\mathrm{synch}} = \frac{4}{3}\sigma_{\mathrm{T}} c u_{\mathrm{mag}} \beta^2 \gamma^2 \tag{1.5}$$

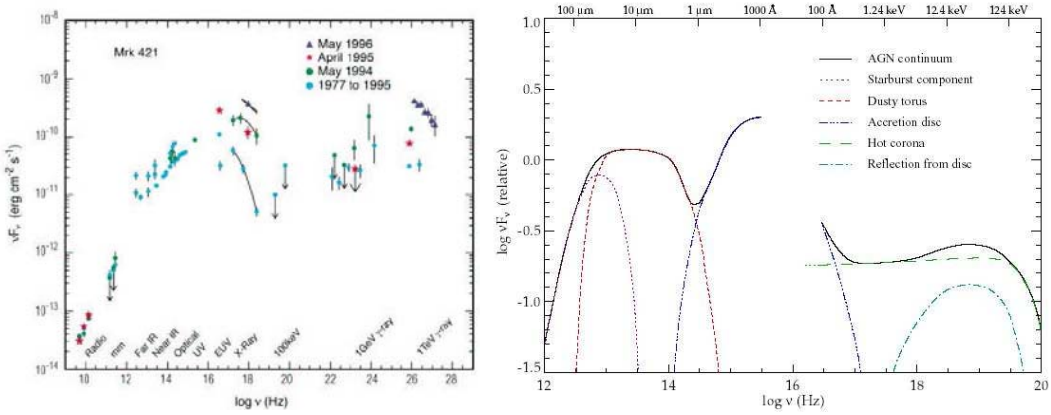

Figure 1.2: Spectral energy distribution of the BL Lac object Mrk 421 (left hand side) and a typical quasar (right hand side). The spectra of BL Lac objects are dominated by synchrotron emission between radio and optical regime and inverse Compton emission in the X-ray and gamma-ray regimes. In a typical quasar spectrum usually three distinct features can be identified. (Images taken from Camenzind 2002).

$$-\left(\frac{dE}{dt}\right)_{\mathrm{iC}} = \frac{4}{3}\sigma_{\mathrm{T}} c u_{\mathrm{rad}} \beta^2 \gamma^2, \tag{1.6}$$

where σ_{T} is the Thomson cross section, u_{mag} and u_{rad} are the energy density of the magnetic field and the electromagnetic radiation respectively. The ratio between the luminosity of the first scattered Compton photons and the luminosity of the synchrotron photons is the ratio between the radiation energy density and the magnetic field energy density:

$$\frac{L_{\mathrm{iC}}}{L_{\mathrm{synch}}} = \frac{u_{\mathrm{rad}}}{u_{\mathrm{mag}}} \tag{1.7}$$

Expressed in terms of the brightness temperature, T_{B} (Kellermann & Pauliny-Toth 1969):

$$\frac{L_{\mathrm{iC}}}{L_{\mathrm{synch}}} \sim \left(\frac{T_{\mathrm{B}}}{10^{12}\,\mathrm{K}}\right)^5 \frac{\nu_{\mathrm{a}}}{100\,\mathrm{GHz}} \left[1 + \left(\frac{T_{\mathrm{B}}}{10^{12}\,\mathrm{K}}\right)^5\right], \tag{1.8}$$

where ν_{a} is the turnover frequency. When the brightness temperature is below 10^{12} K, synchrotron emission dominates. Above this value, however, the luminosity of the Compton photons dominates of the luminosity of the synchrotron photons. Then the inverse Compton scattering of the already once-scattered photons (the second order inverse Compton scattering) becomes important. This leads to the so called “Compton catastrophe”: electrons lose their energy rapidly and the brightness temperature decreases back to 10^{12} K, where the energy losses from inverse Compton scattering and synchrotron radiation are of the same order. Kellermann & Pauliny-Toth (1969) conclude that the highest achievable brightness temperature in AGN is 10^{12} K.

However, Readhead (1994) gave a different value for the lower limit for the maximum intrinsic brightness temperature: $5 \cdot 10^{10}$ K to 10^{11} K. This is the so called equipartition brightness temperature limit. He assumed that the sources are near to equipartition of energy between the radiating particles and the magnetic field.

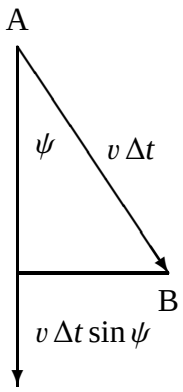

Figure 1.3: Illustration of how the illusion of superluminal motion is formed. The observer is in the direction of the vertical arrow. A jet component originates in point A, moves with an intrinsic velocity of v towards point B, during a time interval Δt. The apparent separation measured by the observer is $s_{\rm app} = v\,\Delta t\,\sin\psi$. The apparent time interval is $\Delta t_{\rm app} = \Delta t - v\,\Delta t\,\cos\psi$. Therefore the apparent speed can be calculated as $v_{\rm app} = \Delta s_{\rm app}/\Delta t_{\rm app}$.

In several radio loud AGN, however, brightness temperatures in excess of the Compton limit were deduced from variability time-scales via the light travel time argument (see Sect. 1.3). Additionally, in a couple of cases the observed X-ray flux was considerably lower than predicted by SSC models (Marscher et al. 1979; Ghisellini et al. 1993). The explanation for these phenomena is relativistic motion within the source which leads to relativistic Doppler boosting, see Sect. 1.2.3.

This thesis basically deals with apparent Compton-limit violations in various AGN and the possible explanations for this phenomenon.

1.2.3 Superluminal motion and relativistic beaming

Superluminal motion in AGN was predicted by Rees (1966) to explain the excess of brightness temperatures in rapidly varying synchrotron sources. Superluminal motion was first observed with interferometric technique by Whitney et al. (1971) and Cohen et al. (1971) in the quasar 3C 279.

Relativistic motion seen at a small viewing angle (see Figure 1.3) causes the illusion of an emitting region moving superluminally i.e. faster than the speed of light. Consider an emitting blob moving with an angle ψ to the line of sight, with a speed v. It emits radiation at point A and later, after a time Δt, at point B. However, from the observer's point of view the apparent distance is only $v\,\Delta t\,\sin\psi$. During the time Δt, the blob travelled $v\,\Delta t\,\cos\psi$ in the direction toward the observer, so the arrival time difference between the two signals is reduced by this factor. Therefore the apparent speed in the plane of the sky perceived by the observer in units of c (speed of light) is given by:

$$\beta_{\rm app} = \frac{\beta\sin\psi}{1-\beta\cos\psi}, \tag{1.9}$$

where $\beta = v/c$.

For a given value of β, $\beta_{\rm app}$ is the function of the angle ψ. The maximum occurs at $\cos\psi = \beta$, then $\beta_{\rm app}^{\rm max} = \beta/\sin\psi = \gamma\beta$, where γ is the Lorentz factor. In order to detect superluminal motion, $\beta_{\rm app}^{\rm max} > 1$ has to be fulfilled; that means $\beta > 1/\sqrt{2}$.

The minimum Lorentz factor required for a given $\beta_{\rm app}$ value is

$$\gamma_{\rm min} = \sqrt{1+\beta_{\rm app}^2} \tag{1.10}$$

which corresponds to an angle of

$$\psi_{\gamma_{\rm min}} = \cot^{-1}\beta_{\rm app}. \tag{1.11}$$

When a radiating source moves with relativistic speed toward the observer, the observed flux density is Doppler boosted:

$$S_{\rm o} = \left(\frac{\delta}{1+z}\right)^{3-\alpha} S_{\rm e}, \tag{1.12}$$

where δ is the Doppler boosting factor defined as $\delta = (\gamma(1-\beta\cos\psi))^{-1}$, and α denotes the spectral index of the source. Due to geometrical considerations, the exponent changes to $(2-\alpha)$ in the case of a more realistic jet-like feature (Scheuer & Readhead 1979). Even for a moderate Doppler boosting factor of five, the flux density of a source at redshift one, with a spectral index of $\alpha = -0.5$, will be beamed by a factor approximately ten.

Similarly, when the source moves away from the observer, the flux density is reduced by the same factor. The ratio of the observed flux density between an approaching jet and a receding counter-jet is:

$$\frac{S_{\rm j}}{S_{\rm cj}} = \left(\frac{1+\beta\cos\psi}{1-\beta\cos\psi}\right)^{2-\alpha}. \tag{1.13}$$

This effect naturally provides the explanation for the observed one sided jet sources.

1.2.4 VLBI characteristics of jets

In the Very Long Baseline Interferometry (VLBI) images of AGN jets, the observed optically thick cores (so called VLBI-cores) represent the self-absorbed part of the conical jet, the so called jet base. This is the point where the jet becomes visible. Usually, the VLBI core is assumed to be stationary (see Sect. 4.5.3).

The observed superluminal features moving along the jet (VLBI components), are regions of enhanced emission (Blandford & Königl 1979; Reynolds 1982). In some sources features moving toward the core or stationary features other than the core, can also be detected. According to shock-in-jet models (e.g. Marscher & Gear 1985; Marscher et al. 1992), the moving components are caused by relativistic shocks propagating down the jet. This model was successfully applied in a number of sources, in e.g. 4C 39.25 (Marcaide et al. 1994), or BL Lac (Mutel et al. 1990). However, it cannot explain all the observed properties, for example intrinsic accelerations or long-lived components. The proposed alternative models involve interaction with the ambient plasma (Rose et al. 1987), such as two-fluid models (e.g. Pelletier & Sol 1992).

In several sources, apparently bent jet trajectories and components moving in different ballistic trajectories are observed. Models using helical motions are proposed to explain

curved trajectories seen for example in 3C 345 (Ros et al. 2000), S5 B 1803+78 (Britzen et al. 2005). Lobanov & Zensus (2001) observed a double helical structure in 3C 273 and interpreted it within the framework of Kelvin-Helmholtz instabilities . Their model reproduced the jet structure on scales up to 30 mas consistent with the general morphology of the jet on scales of up to 1 kpc.

Bent jets can be explained by precession in the region of the nucleus, which can be due to binary black holes (Begelman et al. 1980; Sillanpaa et al. 1988), or gravitational interaction between galaxies. Binary black hole models are successfully used in the description of several sources, such as OJ 287 (Valtaoja et al. 2000), 3C 273 and M 87 (Kaastra & Roos 1992), 3C 345 (Lobanov & Roland 2005), and PKS 0420-014 (Britzen et al. 2001).

1.3 Variability of AGN

Short time-scale variability and the high luminosity observed in AGN led to the discovery that the power of AGN is produced by a process more efficient than ordinary stellar processes and to the hypothesis that massive black holes are the central engines of AGN (Fabian 1979; Rees 1978). Variability studies provide crucial information about the parts of AGN that cannot be resolved with the current observational techniques. The minimum time-scale of the flux density changes is related to the size of the emitting region. If the observed time-scale of the variability (in the source frame) is $\Delta t_{\rm var}$, then the emission has to be produced in a region with size:

$$R \lesssim 2 \cdot c\Delta t_{\rm var}. \tag{1.14}$$

This condition (so called light-travel time argument) means that all parts of the source of the variation are causally connected, otherwise they would not vary in phase with each other and consequently the amplitude of the variations would be reduced.

The luminosity of AGN is observed to vary practically at every wavelength, from gamma-ray to radio. The time-scales range from several minutes to many years. The fastest variations are detected in the gamma-ray and X-ray regime, with a time-scale of 100 s. The time-scales of variations, the correlations between variations at different wavelengths, or the time lags between variations at different wavelengths in continuum or in different line components help in understanding the physical processes governing the various components of the AGN. In the different parts of an AGN, different emission mechanisms dominate, and each has its own characteristic frequency range. The sketch in Fig. 1.4 (taken from Marscher 2005) displays the physical structure, the various emitting regions, and the wavebands of the emitted radiation. In Fig. 1.2, the spectral energy distribution (SED) of a typical quasar with its various components is shown. The relationship and interconnections of these different emission regions and emission processes are not understood completely (e.g. connection between the inner-jet and accretion disk, connection between the jet and the central engine, the partial covering of the broadened X-ray Fe Kα line, etc.). Since the different components emitting in different wavebands are connected to each other, the best observational approach involves multi-waveband investigations across the electromagnetic spectrum. Naturally, multi-waveband, multi-epoch observations require a large amount of observing time on a number of high-class instruments (often involving satellites as well as ground based telescopes) with very different

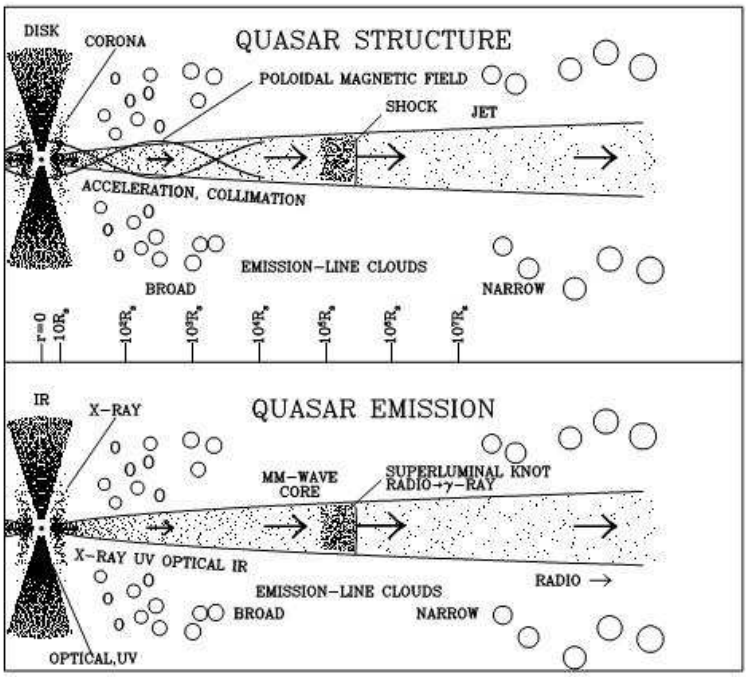

Figure 1.4: The structure and various emitting regions of an AGN without the radio lobes (Marscher 2005). The logarithmic length scale is in units of Schwarzschild radius. Only one superluminal knot is shown, usually many can be observed in the jet.

resolutions (and of course with very different weather conditions). Thus, organizing the observations and reducing the obtained datasets are rather complex and demanding tasks. However, these observations can provide answers to the most crucial questions concerning emission properties in AGN.

A combination of multi-waveband variability monitoring and multi-epoch Very Long Baseline Interferometry (VLBI) observations is one of the most effective tools. For exploring how the jet kinematics influence the spectral energy distribution or distinguishing effects of relativistic beaming from intrinsic jet parameter changes. With polarization information, one can pinpoint parcels of plasma emitting at different frequencies.

Another example for the efficiency of variability studies is the so called reverberation mapping technique (Peterson et al. 2004, and references therein). In this method, time delays between optical continuum and emission-line variations are used to deduce the size of the line-emitting region. Peterson et al. (2004) used this technique to determine the distance between the BLR and the central engine and hence estimate the masses of the central black holes in 35 AGN.

There is strong observational evidence that variability increases with decreasing (rest frame) wavelength, which holds over a wavelength range spanning at least the ultraviolet to near-infrared (Ulrich et al. 1997, and references therein). This fits well into a picture where relativistic electrons are injected or accelerated in the base of the jet giving rise first to a flare of emission of synchrotron radiation at UV, then at optical and millimetre wavebands. As the electrons propagate along the jet, through opacity effects and radiation losses, the flare shifts into longer radio wavelengths and hence the observed cm-radio

radio peaks follow their high frequency counterparts with a time lag.

1.3.1 Component ejection and variability

Time-scales of variations in the radio regime range from hours to years and are usually aperiodic. The major flux density variations in the radio regime can be modelled with exponentially growing and decaying flares (see Valtaoja et al. 1999). The first studies linking total flux density variations with moving VLBI components were carried out for BL Lac by Mutel et al. (1990). They found that the outbursts of BL Lac between 1980 and 1988 can be associated with the emergence of new superluminal components. Abraham et al. (1996) noticed that the estimated ejection times of seven VLBI components of 3C 273 were related to increases in the single-dish flux density. In the same source, Türler et al. (1999) also found a good correspondence between the ejection times of the VLBI components and the beginning times of total flux density flares. In PKS 0528+134, Krichbaum et al. (1996) reported a correlation between the ejections of mm-VLBI components and local minima in the 90 GHz light curve (see also Qian et al. 1998). Similarly, Valtaoja et al. (1999) were able to associate VLBI components with individual flares in the millimetre regime in 3C 345. Similar correlations were found in PKS 0420-014 (Britzen et al. 2000) and in 3C 279 (Wehrle et al. 2001).

Savolainen et al. (2002) compared VLBI and total flux density data of 27 γ-ray-bright blazars. They concluded that for most of the events, the beginning of the major total flux density flare can be used as an indicator of the ejection time of a new VLBI component. They reported that the most pronounced outbursts occurred in the innermost few tenths of mas of the core. Because of the limited resolution, these events could be detected in the VLBI images only as the brightening of the core (so called "core flares"). They were not able to determine how much of the flare is contained in the shock and how much is due to changes in the core itself. However, they suggest that it is possible to explain all the radio variations as shocks created and propagating down the jet.

From the variability time-scale, the size of the emitting region, and hence the brightness temperature can be calculated. Knowing the theoretical limit on T_{B} of a synchrotron source, the Doppler boosting factor can be obtained (e.g. Lähteenmäki et al. 1999). Usually, the logarithmic variability time-scale is used (e.g. Wagner et al. 1996):

$$t_{\mathrm{var}} = \left| \frac{d ln S}{dt} \right|^{-1} = \frac{\langle S \rangle}{\Delta S} \cdot \Delta t \tag{1.15}$$

where $\langle S \rangle$ is the mean flux density in Jy, ΔS is the standard deviation in Jy, and Δt is the duration of the variation in days. Then the source size can be written as:

$$\theta = 3.56 \cdot 10^{-4}\,\mathrm{day}^{-1}\,\mathrm{Gpc}^{-1} t_{\mathrm{var}} \left(\frac{1+z}{D_{\mathrm{L}}} \right) \mathrm{mas}, \tag{1.16}$$

where D_{L} is the luminosity distance in Gpc.[1] Substituting these values into equation 1.4, the apparent brightness temperature can be calculated. In the case of Doppler boosting,

[1] The luminosity distance is defined by the relationship between the bolometric flux S_{bol} and the bolometric luminosity (L_{bol}) as: $D_{\mathrm{L}} = \sqrt{L_{\mathrm{bol}}/4\pi S_{\mathrm{bol}}}$.

the observed brightness temperature is connected to the intrinsic brightness temperature as:

$$T_{\mathrm{B}}^{\mathrm{app}} = \delta^3 \cdot T_{\mathrm{B}}^{\mathrm{int}}. \tag{1.17}$$

For $T_{\mathrm{B}}^{\mathrm{int}}$ usually the Compton brightness temperature ($\sim 10^{12}$ K) or the equipartition brightness temperature ($\sim 10^{11}$ K) is assumed.

It is obvious, that the more rapid variations with time-scales of few days or less, in the radio bands imply the smaller emitting size and higher brightness temperatures. The most rapid observed variations infer brightness temperatures in the range of 10^{16} K to 10^{19} K which, in the framework of standard jet models, are hard to explain, since they would require excessive Doppler factors (30 to 200). In the next chapter, these fast variations and proposed explanations will be presented and discussed in detail.

2 Intraday Variability

Rapid flux density variations on time-scales of days or less than a day are observed in quasars and BL Lac objects through the entire spectrum from radio to gamma-ray. Short time-scale variations of quasars in the radio regime were discovered in the mid-eighties by Witzel et al. (1986) and Heeschen et al. (1987) and were named Intraday Variability (IDV, for a review see Wagner & Witzel 1995).

The IDV time-scales range from a few hours to several days. Originally, structure function (SF) analysis of the light curves led Heeschen et al. (1987) to distinguish between more rapid, type IDV sources – with time-scales of $\sim$ 0.5 days to 2 days – and slower type sources. The latter did not show clear maxima in their SF, but rather a monotonic increase within the observing time, suggesting a time-scale of $\geq$ 2 days. This classification mainly resulted from the limited observing time. (SF analysis is described in detail in Sect. 3.4.) Changes in the characteristic time-scales, such as a slow down or appearance of a sudden more pronounced state of variability are also common phenomena and have been observed in several sources, i.e. S5 0716+714 (Wagner & Witzel 1995; Qian et al. 1996b), PKS 0405-385 (Kedziora-Chudczer et al. 2001a), and S5 0917+624 (Kraus et al. 1999). Recently, extremely rapid IDV sources have been discovered: PKS 0405-385 (Kedziora-Chudczer et al. 1997), GB6 J 1819+3845[1] (Dennett-Thorpe & de Bruyn 2000), and PKS 1257-326 (Bignall et al. 2002). The time-scales of variations in those sources are as short as a few hours.

According to IDV surveys (such as Lovell et al. 2003; Kraus et al. 2003; Cimó 2003; Kedziora-Chudczer et al. 2001b), 20 % to 25 % of all compact flat spectrum extragalactic radio sources show IDV. Steep spectrum sources or more extended core-jet sources do not show IDV.

The variability is usually strongest at lower radio frequencies (2 GHz to 5 GHz), but IDV was also detected in the millimetre regime (Kraus et al. 2003; Cimó 2003). Correlation between the short time-scale variations in different wavebands (radio and optical) has been observed in S5 0716+714 (Wagner et al. 1996; Quirrenbach et al. 1991) see Fig. 2.1 and in S4 0954+658 (Wagner et al. 1993).

The peak-to-peak variations are in the order of a couple of percent in total intensity and usually much more in polarized intensity $\approx$ 20 % to 100 %. Polarization angle swings have been observed within a few hours for example in S5 0917+624 (Quirrenbach et al. 1989) and S5 1150+812 (Kochenov & Gabuzda 1999). Both correlation and anti-correlation between total and polarized intensity variations have been detected. Several times within the same sources both phenomena were detected and additionally transitions between these two stages have been observed as well.

[1] In the following, we refer to this source as J 1819+3845.

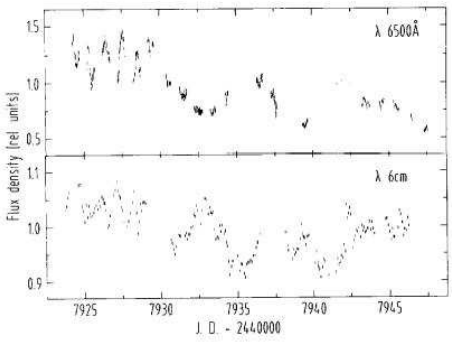

Figure 2.1: Normalized optical (top) and radio (bottom) light curves of S5 0716+714 by Quirrenbach et al. (1991).

To describe the strength of the variability, the modulation index and the variability amplitude are used. The modulation index is defined as the ratio of the standard deviation of flux density to the mean value of the flux density:

$$m = \frac{\sigma}{\langle S \rangle}. \tag{2.1}$$

It is useful to the compare the modulation index of a target source to that of an assumed non-variable, secondary calibrator. That appears in the definition of the variability amplitude:

$$Y = \sqrt{3\left(m^2 - m_0^2\right)}, \tag{2.2}$$

where m_0 denotes the modulation index of a source regarded to be stationary, during the observation. The variability amplitude of a secondary calibrator is by definition zero. (Both m and Y can be derived for variations of the total flux density as well as for variations in polarized flux density.)

Based upon the observed time-scales, causality arguments (as described in Sect 1.3) limit the size of the emitting region to a couple of light-days or light-hours, in the range of μas. Consequently, the inferred brightness temperatures are in the range of 10^{16} K to 10^{18} K; in the case of PKS 0403-385 the apparent brightness temperatures may reach $\sim 10^{21}$ K according to Kedziora-Chudczer et al. (1997). These are far in excess of the inverse Compton limit. Compton limit violations have already been observed in many cases and were explained by introducing relativistic beaming and Doppler boosting. However, in the case of IDV sources, the required Doppler factors are much larger than those so far observed with VLBI: in the range of 100 to 1000.

The theories for explaining IDV phenomenon can be divided into intrinsic and extrinsic explanations. These theories will be summarized in the following.

2.1 Intrinsic explanations

Source intrinsic theories try to explain the observed high brightness temperatures with different physical processes taking place in the varying sources. Most of these models

produce the required high Doppler boosting factors, for example with modified shock-in-jet models, or special geometrical considerations, etc. These theories deal with the standard synchrotron self-Compton processes, other explanations however propose alternative radiation processes. In the latter case, "Compton catastrophes" do not occur, thus the attainable brightness temperature is not limited.

Shocks in turbulent relativistic jets have successfully explained flares and outbursts seen in radio light curves (see Sect.1.3) and their propagation from higher to lower frequencies. In the shocks, magnetic fields are compressed and hence the variations also lead to variations in polarization and polarization angles (Hughes et al. 1985; Koenigl & Choudhuri 1985). Also, the simultaneous swings in radio and optical polarization can be explained via these models (Kikuchi et al. 1988). Different modifications of this model were invoked to explain the time-scales, quasi-periodicity, and frequency dependences observed in IDV sources.

Qian et al. (1991) propose a shock-in-jet-model, where the shock propagates through a jet, in which both the synchrotron-emitting electrons and the magnetic field are turbulent. The moving thin shock illuminates the inhomogeneous structure of the underlying jet. The size of the emitting region in this model is determined by the jet radius and the thickness of the shock. Hence, without invoking unreasonably high Doppler boosting factors, the brightness temperature problem can be avoided. In another model of Qian et al. (1996a) a shock moves along a magnetically confined jet with oscillating cross section.

A different type of theory to explain IDV is the so-called light-house effect (Camenzind & Krockenberger 1992). In that scenario, knots in the jet move on helical trajectories, thus the direction of beaming varies with time. The observer close to the axis of the jet detects flares as the beam sweeps across the line of sight (similar to pulsars). Several knots in the jet can produce quite complex light curves. Various VLBI observations indeed showed jet components moving on helical trajectories (e.g. Kellermann et al. 2004; Gómez et al. 1999). Quasi-periodic oscillations were interpreted in the framework of this model, for example in the case of 3C 345 (Ros et al. 2000, and references therein).

The swinging jet model of Gopal-Krishna & Wiita (1992) allows small variations in the direction of shocks occurring inside a relativistic jet. They were able to quantitatively explain the correlation (and anti-correlation) between the total and polarized flux density variations observed in several IDV sources.

Spada et al. (1999) propose a model, which can account for the observed IDV in cases where the apparent brightness temperature is lower than $3 \cdot 10^{17}$ K. Their model is a modified version of that by Salvati et al. (1998) which interprets the extremely fast variations in the TeV emission of Mrk 421. In their scheme, a slab of electrons travels along the steady jet with the same bulk Lorentz factor; these electrons radiate only when they pass through a conical shock, where they are accelerated to relativistic velocities in the comoving frame. Thus they radiate in succession rather than simultaneously.

Gopal-Krishna et al. (2004) argue that, if the jet opening angle is allowed to be $\sim 10^\circ$ on the parsec scale, then even the modest observed superluminal speeds ($v_{\rm app} \sim 3\,c$ to $5\,c$) would be enough to explain the required high Doppler and Lorentz factors. In that scenario, they associate the VLBI knots directly with shocks in the ultra-relativistic jet flow. Usually, these features are thought to be connected not to the fast "spine" but to a slower "surrounding" layer (e.g. Ghisellini et al. 2005, and references therein).

Begelman et al. (1994) examine the constraints on highly relativistic (with bulk Lorentz

factors up to 100) synchrotron emitting jets. They argue that the synchrotron radiative efficiency of such jets would be extremely small, implying that the jet would have to carry large fluxes of electromagnetic and kinetic energy to produce the observed radio emission. Thus, the radiative inefficiency places an upper limit on the attainable bulk Lorentz factor of the jet. Begelman et al. (1994) claim that this limit is just compatible with the observation (except for the three extreme fast IDVs, which exceed this limit); theoretically the required Doppler factors can be achieved. To obtain these speeds, they propose hydromagnetic acceleration processes instead of radiative or thermal acceleration processes.

Coherent radiation mechanisms avoid the problem of Compton catastrophes. For example, Benford (1992) reports on laboratory experiments of collective emission in turbulent plasma. Lesch & Pohl (1992) suggest a scenario, where coherent and incoherent processes together are responsible for the observed variability characteristics in AGN. Begelman et al. (2005) propose that high brightness temperature radiation could be a result from electron cyclotron maser instability in a thin layer along the wall of the jet.

2.1.1 Observational evidence in favour of extrinsic explanations

Shock-in-jet models with fine-tuning of their parameters can successfully explain the behaviour of several IDV sources:

- The model of Qian et al. (1991) can account for almost all of the observed features in S5 0917+624. Qian et al. (2002) showed that a two component shock model, where the polarization orientation of the shock component is approximately perpendicular to that of the underlying background component can explain the variations in polarized flux density, and the polarization angle as well.
- A slightly different shock-in-jet model (Qian et al. 1996a) was able to successfully interpret the correlated short time-scale optical and radio variations in S5 0716+714 and the quasi-periodicity in the radio spectral index between 5 and 8.3 GHz.
- Spada et al. (1999) demonstrate the effectiveness of their model on S5 0716+714.
- Begelman et al. (2005) claims that their cyclotron maser model can give account for the observed high brightness temperature of one of the most extreme IDV sources, J1819+3845.

2.2 Extrinsic explanation, scattering of radio waves in the ISM

While the intrinsic theories try to account for the inferred high Doppler boosting factors, the extrinsic explanation attack the problem from a different direction, claiming that the variations observed do not originate in the source itself, but are caused by a propagation effect, taking place in our Milky Way.

It has been known since the early 1970s that pulsars are subject to interstellar scintillation (ISS). Several effects of ISS have been observed on pulsars, such as angular broadening, intensity scintillations, broadening of the pulsar profiles due to the delayed

arrival of the scattered radiation, angular wandering of the scattered image and systematic drift slopes of the intensity ”“scintles”” in pulsar dynamic spectra.

Low frequency variations in extragalactic radio sources are confirmed to be connected to ISS as well. Low frequency variable extragalactic (LFV) sources (Fanti et al. 1981) experience variations of 3 % to 30 % over periods of months at frequencies below 1 GHz. First Shapirovskaya (1978) proposed ISS as an explanation for low frequency variability, later Rickett (1986) and Spangler et al. (1993) demonstrated that refractive interstellar scintillation (RISS) provides a satisfactory explanation for at least part of the observed LFV.

2.2.1 Parameterizations of electron density turbulence in the ISM

The electron density fluctuations in the interstellar medium are usually discussed in terms of a power spectrum: $P(\boldsymbol{q})$, where $\boldsymbol{q}$ is the three dimensional wavenumber. For wavenumbers between the inner scale ($1/q_{\text{inner}}$) and outer scale ($1/q_{\text{outer}}$), $P(\boldsymbol{q})$ can be described as a power law:

$$P(\boldsymbol{q}) = C_N^2(r)\,|\boldsymbol{q}|^{-\beta}, \tag{2.3}$$

where the factor $C_N^2(r)$ is assumed to vary slowly with position. For $|\boldsymbol{q}| > q_{\text{inner}}$ $P(\boldsymbol{q})$ falls rapidly to zero, for $|\boldsymbol{q}| < q_{\text{outer}}$, it saturates at a constant value.

Although observations have been made for more than 30 years now, none of the parameters (C_N^2, β, q_{inner}, q_{outer}) in equation 2.3 are fully characterized. To complicate the picture, these parameters can also depend upon the regions where the scattering material is located. The plot from Armstrong et al. (1995) in Fig. 2.2 shows the (logarithm of the) inferred three-dimensional electron density power spectrum versus the logarithm of the wavenumber. The figure illustrates the different observational techniques which are used to study the electron density power spectrum.

The inner and outer scales differ by at least seven orders of magnitude (e.g. Armstrong et al. 1995). Estimations of the inner scale range from 10^5 m to 10^9 m (e.g. Rickett et al. 1984; Gupta et al. 1993; Wilkinson et al. 1994; Molnar et al. 1995). Proposed estimates for the outer scale, range from a few AU to tens of parsecs (Desai et al. 1994; Gupta et al. 1993).

Usually the Kolmogorov value of $11/3$ is assumed for the power spectral index β, derived from most of the observations. However, there are particular lines of sight, where observations suggest values up to 4 (Bhat et al. 1999). A spectrum with $\beta = 4$ would mean that the interstellar plasma is entirely made of clouds with abrupt edges (for example shocks due to a supernova explosion). Armstrong et al. (1995) summarized the ISS observations of the nearby interstellar medium (up to 1 kpc) and concluded that the data are consistent with a Kolmogorov spectrum over the wavenumbers $10^{-13}\,\text{m}^{-1}$ to $10^{-6.3}\,\text{m}^{-1}$, and β equal to four is compatible with the data in this range, only if an outer scale of 10^{14} m to 10^{16} m is invoked.

The scattering measure (SM) is defined as the line of sight integral of the amplitude of the fluctuations:

$$\text{SM} = \int_0^D C_N^2\, ds, \tag{2.4}$$

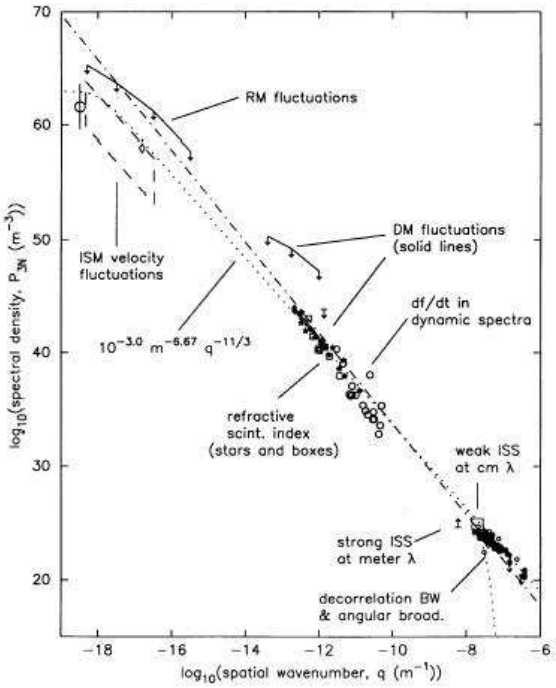

Figure 2.2: Logarithmic plot of the electron density power spectrum versus wavenumber from Armstrong et al. (1995). Different observational techniques are used in different part of the spectrum to reveal its characteristics. Dotted lines are Kolmogorov spectra with outer scale of 10^{18} m and inner scales of 10^5 m and 10^8 m. Dot-dashed line is a model spectrum having power law exponent of 4.

where D is the path length through the scattering medium. The strength parameter, C_N^2, and the SM can change by orders of magnitude over a few degrees. The model of Cordes et al. (1985) describes the electron density turbulence with two components: a thin one (scale height $\leq$ 100 pc) with $C_N^2 \approx \left(10^{-3} \text{ to } 1\right)\ \mathrm{m}^{-20/3}$, and a thick one (scale height $\geq$ 500 pc) with $C_N^2 \approx 10^{-3.5}\,\mathrm{m}^{-20/3}$. From the scintillation study of 20 pulsars, Bhat et al. (1998) modelled the local interstellar medium (LISM). Their best fit model requires a three-component scattering medium, where the solar neighbourhood is surrounded by a shell of much higher density fluctuations embedded in the normal, large-scale ISM. The line-of-sight-averaged value of C_N^2 for the inner cavity is $10^{-4.70}\,\mathrm{m}^{-20/3} < \overline{C_N^2} < 10^{-4.22}\,\mathrm{m}^{-20/3}$, for the outer ISM is $\overline{C_N^2} < 10^{-3.30}\,\mathrm{m}^{-20/3}$ and for the shell is $10^{-0.96}\,\mathrm{pc\,m}^{-20/3} < \int_0^d C_N^2\,(s)\,ds < 10^{-0.55}\,\mathrm{pc\,m}^{-20/3}$, where d is the thickness of the shell.

Beside the SM, other integrated measures are also used to describe the electron density and its fluctuations along the line of sight. These are the following.

- Dispersion measure, the path integral of the electron density:

$$\mathrm{DM} = \int_0^D n_\mathrm{e}\,ds\,\mathrm{pc\,cm}^{-3}, \tag{2.5}$$

where n_e is the number density of free electrons along the line of sight. DM values

are obtained from measurements of the differential arrival times of pulsars pulses at different frequencies.

- Emission measure, path integral of the squared electron density:

$$\mathrm{EM} = \int_0^D n_\mathrm{e}^2 \, ds \, \mathrm{pc\,cm^{-6}} \tag{2.6}$$

EM can be measured from recombination line and free-free absorption or observations of Hα.

- Rotation measure, the path integral of the parallel component of the magnetic field ($B_\parallel$) multiplied by the electron density along the line of sight from the source to the observer:

$$\mathrm{RM} = 812 \int_0^D n_\mathrm{e} \, B_\parallel \, ds \, \mathrm{rad\,m^{-2}}, \tag{2.7}$$

where $B_\parallel$ is in mG. RM is sensitive to the correlation of electron density and magnetic field. Observations suggest that magnetic field fluctuations accompanying or driving the density fluctuations are responsible for scattering. In magneto-hydrodynamical (MHD) turbulence, the density fluctuations are expected to be aligned with the direction of the magnetic field and thus to show anisotropy. Effects of anisotropy were observed in the case of several highly scattered sources, such as Cyg X-3 (Wilkinson et al. 1994) and NGC 6334B (Trotter et al. 1998).

2.2.2 Scattering regimes

This subsection is based mainly upon the paper of Narayan (1992), which reviews and summarizes the scattering regimes of scintillation.

For an assumed originally unit amplitude wavefront from a radio source, the Fresnel-Kirchhoff integral describes the amplitude received at the observer plane (in the point (X, Y)) after the wavefront crosses the scattering screen at a distance L from the observer:

$$\psi(X,Y) = \frac{e^{-i\pi/2}}{2\pi r_\mathrm{F}^2} \iint \exp\left(i\phi(x,y) + i\frac{(x-X)^2 + (y-Y)^2}{2r_\mathrm{F}^2} \right) dxdy, \tag{2.8}$$

here $\phi(x,y)$ is the phase change introduced by the scattering medium at a point (x,y), λ is the wavelength, r_F is the Fresnel scale:

$$r_\mathrm{F} = \sqrt{\frac{\lambda L}{2\pi}}. \tag{2.9}$$

For observations at 1 m wavelength over a length scale of 1 kpc, the Fresnel scale is $r_\mathrm{F} \sim 10^{-8}$ pc. The second term in the exponential of equation 2.8 is the contribution to the phase due to the additional path length between (x,y) and (X,Y).[2] When there is no

[2] In the limit of small scale scattering, i.e.: $|x - X| \ll L$ and $|y - Y| \ll L$.

scattering, $\phi(x,y) = 0$, $\psi(x,y) = 1$. When scattering occurs, random phase fluctuations are introduced to the wavefront. If there is a transverse velocity between the scattering medium and the observer-source line-of-sight, then temporal variations will be observed.

Besides the Fresnel scale, another basic length scale in the theory of scintillation is the diffractive scale r_{diff}. This is the transverse separation over which the induced phase variations are coherent within one radian. With these two length scales the different scattering regimes can be defined.

Weak scattering

Weak scattering (WISS) occurs, when $r_{\mathrm{diff}} \gg r_{\mathrm{F}}$. $\psi(X,Y)$ experiences only weak perturbations, which consequently means that the measured flux variations are small. A source is point-like in this regime if its size is smaller than the Fresnel angle, determined from the Fresnel scale as: $\theta_{\mathrm{F}} = r_{\mathrm{F}}/L$. The scintillation time-scale and the modulation index are given by:

$$t_{\mathrm{scint}} \approx \frac{r_{\mathrm{F}}}{v} \tag{2.10}$$

$$m_{\mathrm{p}} \approx \left(\frac{r_{\mathrm{F}}}{r_{\mathrm{diff}}}\right)^{\frac{5}{6}} < 100\,\%, \tag{2.11}$$

where v is the transverse velocity between the scattering medium and the source's line-of-sight.

If the angular size of the source is larger than the Fresnel angle then the scintillations are dampened:

$$t_{\mathrm{scint}} \approx t_{\mathrm{F}}\frac{\theta_{\mathrm{S}}}{\theta_{\mathrm{F}}} \tag{2.12}$$

$$m_{\mathrm{e}} \approx \left(\frac{r_{\mathrm{F}}}{r_{\mathrm{diff}}}\right)^{\frac{5}{6}}\left(\frac{\theta_{\mathrm{F}}}{\theta_{\mathrm{S}}}\right)^{\frac{7}{6}} < m_{\mathrm{p}} < 100\,\%, \tag{2.13}$$

where θ_{S} refers to the scintillating source size. For example pulsars are subject to WISS at cm wavelengths and the extrinsic explanation of IDV of extragalactic radio sources also involves WISS of compact AGN.

Strong scattering

Strong scattering is characterized by $r_{\mathrm{diff}} \ll r_{\mathrm{F}}$. The Fresnel scale loses its relevance in this regime, as the phase fluctuations vary by many radians over r_{F}. Instead, r_{diff} becomes the characteristic scale, as this is the scale on which the phase may be assumed to be constant (within 1 rad). The spectrum of flux density variations in this regime has two peaks at two widely separated length scales. The diffractive scale defines the branch of diffractive scintillation, while the longer refractive scale corresponds to weaker scintillations, and this branch is referred to as refractive scintillation. The refractive length scale is defined as: $r_{\mathrm{ref}} = r_{\mathrm{F}}^2/r_{\mathrm{diff}}$.

The most important feature in the diffractive regime is the so-called multi-path propagation. Each (X,Y) point in the observer plane receives radiation from numerous (x,y)

points of the scattering screen. The scattering screen can be visualized as a sum of large number of coherent patches (each surrounding the points of stationary phase), with a size of $\sim r_{\rm diff}$. Each of them scatters the radiation into a diffraction cone of angle: $\theta_{\rm scat} \sim \lambda/r_{\rm diff} \sim r_{\rm ref}/L$. Therefore, as the observer receives rays from a range of angles $\sim \theta_{\rm scat}$, the image of a point source will be scatter broadened by this angle. The rays contributing in forming a point in the observer plane have random phases; they interfere with each other and produce a random interference pattern.

Again a source is treated as point-like if its angular size is smaller than the diffractive scale defined angle: $\theta_{\rm diff} = r_{\rm diff}/L$. In that case, the scintillation time-scale and the modulation index are:

$$t_{\rm scint} \approx \frac{r_{\rm diff}}{v} \tag{2.14}$$

$$m_{\rm p} \approx 100\,\%. \tag{2.15}$$

If the source is extended, the scintillation will be suppressed:

$$t_{\rm scint} \approx t_{\rm diff}\frac{\theta_{\rm S}}{\theta_{\rm diff}} \tag{2.16}$$

$$m_{\rm p} \approx \frac{\theta_{\rm diff}}{\theta_{\rm S}} < 100\,\%. \tag{2.17}$$

When the inhomogeneities of the scattering screen are larger, on a length scale of $\approx r_{\rm ref}$, then refractive scintillation occurs. In that branch, the observer receives radiation from a large number of $r_{\rm diff}$-sized coherent patches; if the phase fluctuations have a focusing profile then the received flux is larger, if they have defocusing profile then the received flux is smaller. A source is point-like if it is smaller than the scattering size (defined by the refractive scale): $\theta_{\rm S} < \theta_{\rm scat} = r_{\rm ref}/L$. The scintillation time-scale and the modulation index are:

$$t_{\rm scint} \approx \frac{r_{\rm ref}}{v} \tag{2.18}$$

$$m_{\rm p} \approx \left(\frac{r_{\rm diff}}{r_{\rm F}}\right)^{\frac{1}{3}} < 100\,\%. \tag{2.19}$$

For an extended source, the time-scale becomes longer and the modulation index is reduced:

$$t_{\rm scint} \approx t_{\rm ref}\frac{\theta_{\rm S}}{\theta_{\rm scat}} \tag{2.20}$$

$$m_{\rm p} \approx \left(\frac{r_{\rm diff}}{r_{\rm F}}\right)^{\frac{1}{3}} \frac{\theta_{\rm scat}}{\theta_{\rm S}}^{\frac{7}{6}} < m_{\rm p} < 100\,\%. \tag{2.21}$$

The source size requirement is much more stringent in the case of diffractive scintillation: for a typical path length through the ISM at metre wavelengths gives a $\theta_{\rm diff} \approx 10^{-6}$ arsec Therefore only pulsars are small enough to experience not just refractive but diffractive scintillation as well. The observed time-scales of DISS in pulsars are in the order of ~ 100 s. Because of the much larger extent of extragalactic radio sources, they do not exhibit diffractive scintillation. There is only one quasar J 1819+385 that showed

some evidence of diffractive scintillation caused flux density variability (Macquart & de Bruyn 2005).

Although AGN are too extended to display DISS-induced flux density variations, their angular diameters can be comparable to $\theta_{\rm scat}$ implying that they can show angular broadening.

Moreover, they are also subject to refractive strong and weak scintillation. For a point-like source in the refractive strong regime, the strength of scintillation (the modulation index) increases with increasing frequency: $m \sim \nu^{17/30}$ (e.g. Goodman 1997). However, above a transition frequency weak scattering takes place, where the modulation index goes as: $m \sim \nu^{-2}$. This transition frequency, in the case of high Galactic latitude sources, is thought to be between 1 GHz and 8 GHz, whilst it is higher for sources closer to the Galactic plane (Walker 1998, 2001). In almost all cases the intrinsic source size is larger than the Fresnel scale (at frequencies $\geq$ 1 GHz and scattering screen beyond the Solar system). Therefore the scintillations are quenched as described above.

2.2.3 Annual modulation

One consequence of the scintillation theory is the annual modulation. An annual cycle in the observed variability time-scale is caused by the changes of the relative velocity between the Earth and the scattering screen as the Earth orbits the Sun. When both move in similar direction, the relative speed is low, hence the variations are slow. Six months later, when the Earth moves in the opposite direction, the variations are faster (for examples see Fig. 2.3, and Fig.2.4; for details see Sect. 3.6.2).

Apart from being a perfect tool to prove the extrinsic origin of short-time-scale variations, annual modulation can provide information on the velocity and distance to the scattering screen and anisotropy of the scattering material. The observations of the seasonal changes in the time-scale can be accomplished theoretically for larger samples of sources. However, practical difficulties exist since accurate sampling of the time-scale at different times of the year is necessary and the observations should continue during a couple of years to provide sufficient data to constrain the model.

2.2.4 Observational evidence in favour of extrinsic explanations

The two most convincing pieces of observational evidence in favour of the extrinsic origin of IDV are the time delay in the variability pattern arrival time and the annual cycle of the characteristic time-scale of the variability. Measurements of the time delay at two widely-spaced radio telescopes are feasible only for sufficiently rapid sources. Thus, these measurements were carried out for only the three most extreme ("intra-hour") variable sources: PKS 0405-385 (Jauncey et al. 2000), J 1819+3845 (Dennett-Thorpe & de Bruyn 2002), and PKS 1257-326 (Bignall et al. 2003).

Annual cycles have now been found in three sources: J 1819+3845 (Dennett-Thorpe & de Bruyn 2003, see Fig.2.3 and 2.4) PKS 1257-326 (Bignall et al. 2003; Bignall 2003), and PKS 1519-273 (Jauncey et al. 2003). There is increasing evidence that S4 0954+658 also shows an annual modulation (L. Fuhrmann priv. comm.). Kraus et al. (1999) reported a remarkable slow-down in the variability of S5 0917+624 and predictions of an annual cycle were performed by Rickett et al. (2001) and Jauncey & Macquart (2001). However,

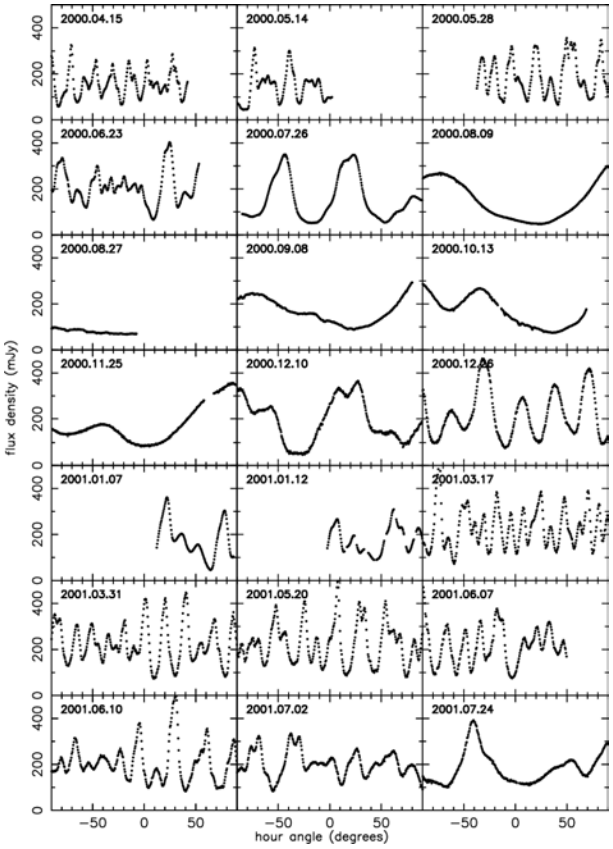

Figure 2.3: Monitoring observations of J1819+3845 at 5 GHz over 15 months from 2000 until 2001, performed by Dennett-Thorpe & de Bruyn (2003) with the Westerbork Synthesis Radio Telescope (WSRT). The annual change in the time-scale of the modulations is clearly apparent. Each panel covers up 12 hours. The time-scale when the source is most rapid can be as short as $\sim$ 15 min. Between August and December it slows down, then the variability time-scale is $\sim$ 120 min.

the fast variations in S5 0917+624 have not restarted since September 2000 (Fuhrmann et al. 2002b).

A similar problem occurs in the case of the above mentioned extra rapid variable PKS 0405-385. It shows short-lived phases (lasting several months) of fast variations followed by a slow flux density evolution during years (Kedziora-Chudczer et al. 2001a). These episodic IDV events can be attributed to source intrinsic changes or changes in the scattering material. Changes in the source structure, e.g. ejection of a new component or expansion of the scintillating component can severely influence the observed variations, since the time-scale and modulation index are functions of the intrinsic source size (see Sect. 2.2.2).

Additional support for ISS comes from the strong frequency dependence of variations observed in IDV, which is mostly (however not entirely) consistent with the predictions of ISS. In most of the cases the variability modulation index has a maxima around 3 GHz to 5 GHz, and the variations are reduced both below and above this value. This frequency behaviour is expected from ISS theory. Above a transition frequency, the observed variability can be described as weak scattering (and it gets weaker with increasing frequency).

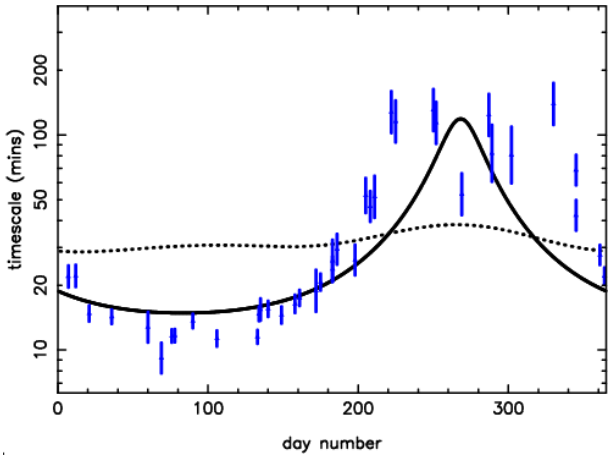

Figure 2.4: The time-scale of the variations in J1819+3845 as a function of observation date (taken from Dennett-Thorpe & de Bruyn 2003). The slow-down can be clearly seen at around days $\sim$ 240 to 280. The dotted line corresponds to the prediction if the scattering plasma has no peculiar velocity. The solid line gives the best fit to the data if the plasma is allowed to have a peculiar velocity. The screen velocity in declination is 31 km s^{-1}, in right ascension is -1 km s^{-1}.

Below this transition frequency strong scattering takes place, and the variability strengthens with increasing frequency.

Rickett et al. (2005) identified variations with time-scales of 5 days to 50 days at 2 GHz, which they interpreted also as ISS phenomenon, an intermediate stage between LFV and IDV.

Using the results of the MASIV survey (Lovell et al. 2003) and publicly available VLBA images, Ojha et al. (2004) studied the morphological differences between scintillating and non-scintillating sources. The scintillating sources have a larger portion of their flux in a compact core, and have smaller angular sizes than the non-scintillating sources. Low and high flux density scintillators do not show different morphologies. These results are consistent with the ISS theory.

2.3 Summary

Apart from observational evidence, another argument in favour of ISS-induced IDV is that even intrinsic explanations of the variability introduce source sizes so small that they have to experience ISS as well.[3] Thus, the ISS surely plays a role in IDV.

On the other hand, even though ISS provides very convincing explanation for IDV in general, numerous intriguing problems remain. The strongest argument against the extrinsic origin of IDV is the observed correlated variations over wide frequency ranges. Quirrenbach et al. (1991) and Wagner et al. (1996) report on correlated optical and radio variations in S5 0716+714 (see Fig. 2.1). Also a correlation between radio and optical flares were detected in S4 0954+658 by Wagner et al. (1993). Whilst changes in the radio

[3] Exceptions are those intrinsic theories, that introduce new radiation procedures. However these theories are not confirmed by any other observed phenomena.

regime can be explained via ISS, variations at the much shorter wavelength – in the optical – cannot be caused by scattering.

Similarly, the IDV phenomenon has also been observed in the millimetre regime, and the variations were too large compared to the prediction of ISS theory (Kraus et al. 2003). In several sources the frequency dependence of the modulation index did not follow the prediction of ISS even at centimetre wavelengths (Krichbaum et al. 2002). For example, S4 0954+658 instead of a peak, exhibits a minimum modulation index in the range of 3 GHz to 5 GHz, and m increases with increasing frequency above 8 GHz.

In explaining the changes in polarization flux density and polarization angles within the framework of ISS, sources had to be described by multiple component models with different polarization characteristics. For example in PKS 0405-385 see Rickett et al. (1995, 2002), or in S5 0917+624 see Quirrenbach et al. (1989); Qian et al. (2002, 2001). But still these fairly complicated models were not able to describe all the observed variability characteristics.

These phenomena either imply that the theory of ISS in its present form is not yet developed enough to account for all the observations (for example inhomogeneities in the scattering material, non-Kolmogorov type turbulence), or – especially at higher frequencies – source intrinsic changes play an important role as well. Episodic changes in the IDV time-scale (discussed in Sect. 2.2.4) support the idea that IDV is a complex mixture of ISS and variations in the source itself.

Although, extrinsic explanation avoids unreasonably high Doppler factors, in some cases it requires such small (scintillating) source sizes, that the calculated brightness temperatures are in excess of the Compton limit in the range of $T_{\rm B} \sim 10^{13}$ K to 10^{14} K and so still require Doppler boosting factors of ~ 10 to 100. For example, in the extremely fast source PKS 0405-385 the derived brightness temperature is $T_{\rm B} = 5 \cdot 10^{14}$ K. and in J1819+3845 Macquart & de Bruyn (2005) also report on the observed diffractive scintillation and a brightness temperature of 10^{14} K.

In calculating the scintillating source size and hence the brightness temperature values, the distance to the scattering screen is a very important parameter. More reasonable values can be obtained for the "intra-hour" variables assuming nearby scattering screens, less than 100 pc. These distances are: ≤ 12 pc in the case of J 1819+3845 (Dennett-Thorpe & de Bruyn 2003), 10 pc to 15 pc in the case of PKS 1257-326 (Bignall et al. 2003), and ~ 25 pc in the case of PKS 0405-385 (Rickett et al. 2002). However in "normal" (slower) IDV sources, where time-delay measurements are not feasible, the estimates of scattering screen distances are cruder.

If IDV is caused by scattering of the radio waves in the turbulent ISM of the Milky Way, naively one can expect to see a Galactic-latitude dependence of the observed variability characteristics and the distribution of IDV sources on the sky. In the case of LFV such dependence was detected. Also the early observations by Heeschen & Rickett (1987) showed a correlation with Galactic latitude. However, the already known IDV sources do not show a clear correlation of variability characteristics with the Galactic latitude. This also supports the idea that the scattering screens responsible for scintillation are nearby, therefore one cannot expect to see the reflection of the large-scale distribution of the Galactic material on the locations of the observed IDV sources. If this is the case in most IDV sources, then the scattering material is more likely to be connected to the local interstellar medium (LISM) for example to the boundary of the Local Bubble. The Local

Bubble is a hot, low-density structure, irregular shaped void (Cox & Reynolds 1987). Unfortunately, still not much is known about the amount of ionized material within the Local Bubble, and the nature of its boundary.

Fuhrmann (2004) investigated the possible connection between different H regions, Galactic loop structures, and the positions of known IDV sources, and tried to detect directly the screens in front of IDV sources via spectral line observations. Altogether six IDV sources (out of surveyed 15) were found to exhibit intervening CO material along their lines of sight (e.g. S4 0954+658 Fuhrmann et al. 2002a).

In the future, the Square Kilometre Array (SKA) will provide a huge amount of data on scintillating radio sources (Lazio et al. 2004) and thus help to better constrain the model of ISM and the LISM and consequently to understand more thoroughly the connection between IDV and ISS and to better disentangle intrinsic and ISS-induced short time-scale variations.

3 Intraday Variability observations

3.1 Investigations of galactic latitude dependence of IDV source positions

The distances to the scattering screens of IDV sources are very crucial parameters in the extrinsic explanations of the IDV phenomenon (see Sect. 2.3). The farther away the screen from the observer, the longer the time-scale of the variations will be, assuming the same scintillating source size and same velocity for the scattering screen.

From pulsar dispersion-measure studies Nordgren et al. (1992) reported that the Galactic scattering medium follows a well defined latitude dependence. If IDV is caused by RISS in the turbulent ISM of the Milky Way, one would similarly expect to detect a Galactic latitude dependence in the distribution of IDV sources on the sky. Quirrenbach et al. (1992) presented a statistical analysis of results of IDV observations performed at 6 cm and found no dependence of the strength of Intraday variations on Galactic latitude, and that the effect is not confined to a certain region in the sky. Shapirovskaya & Larchenkova (1995) examined the modulation index dependence on Galactic latitude. Their statistical analysis was based mainly upon the observational data of low frequency variability (Simonetti & Cordes 1990), "flickering" of extragalactic radio sources (Heeschen 1984; Heeschen & Rickett 1987) and IDV data of Quirrenbach et al. (1992). They found a correlation between the modulation index and Galactic latitude. However, this correlation does not follow the one predicted by the RISS theory of Rickett (1986) to be $m \sim (\sin b)^{-1/2}$, where b is the Galactic latitude. Based upon these results, they noted there should be a much stronger correlation between m of IDV sources and the Galactic latitude than was observed.

Kedziora-Chudczer et al. (2001b) reported that, from the Australia Telescope Compact Array (ATCA) IDV survey, the distribution of IDV sources with respect to the Galactic plane is not random, but does not follow the simple predictions of the ISS theory.

Cimó (2003) statistically analyzed the results of IDV monitoring projects performed with the Effelsberg 100 metre radio telescope and with the Very Large Array (VLA) from 1985 to 2000. He found no any evidence for a latitude dependence of the strength of the variability. He argued that the observed features of IDV are not caused by the global distribution of matter in the ISM, but rather by local clouds.

Fuhrmann (2004) introduced a new approach: direct detection clouds in front of known IDV sources. Observations of radio recombination lines of hydrogen did not yield results (four IDV source positions were checked). However, CO lines were detected towards four known IDV sources out of a sample of 13 (e.g. in the direction of S4 0954+658, see Fuhrmann et al. 2002a) and a literature search revealed that CO clouds

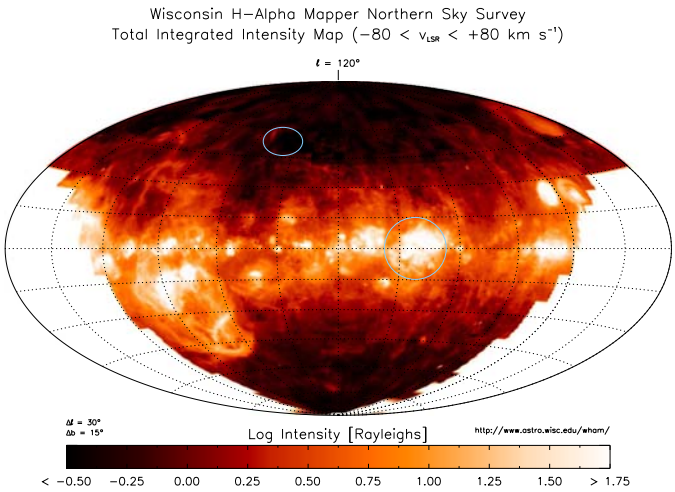

Figure 3.1: Velocity integrated images from the WHAM Northern Sky Survey (Haffner et al. 2003). The superimposed circles indicate the locations of the two regions (the Lockman Hole and the Cygnus region) towards which IDV observation was conducted.

had been detected towards two additional IDV sources. Fuhrmann (2004) also reported that a good correlation is often seen between IDV positions and enhanced CO and dust emission. He argues that various components of the LISM (the wall of the Local Bubble, adjacent bubble/loop structures and their turbulent interaction zones) – based upon their distance estimations and turbulent, clumpy structures – are most likely to be connected to IDV phenomena.

3.2 New observations

To investigate, the influence of the Galactic distribution of ISM on the occurrence of IDV sources, an observation was carried out with the Effelsberg 100 metre radio telescope of two samples of compact radio sources. The two samples are located in different parts of the sky: towards the Cygnus region and in the direction of the Lockman Hole. Lines of sight passing through these two regions are significantly different in the amount of interstellar matter. The Lockman Hole is well known as the region with the lowest neutral atomic hydrogen column density ($N_{\rm H} = 4.5{\times}10^{19}{\rm cm}^{-2}$) on the sky (Lockman et al. 1986). WHAM (Wisconsin Hα Mapper)[1] measurements showed that this region of the sky is also depleted in H ; Hausen et al. (2002) reported $N_{\rm H} = 2 \times 10^{19}{\rm cm}^{-2}$. In contrast, towards the Cygnus region, several heavily scattered lines of sight can be found. To illustrate the different amount of H , a picture created by the WHAM Northern Sky Survey is shown in Fig. 3.1 and the two observed regions are indicated by circles.

The observed sources were chosen from the Cosmic Lens All Sky Survey (CLASS) catalogue (Myers et al. 2003), and the Jodrell Bank VLA Astrometric Survey (JVAS) catalogue (Patnaik et al. 1992; Browne et al. 1998; Wilkinson et al. 1998). The first area

[1]The WHAM H-α survey maps the distribution of the warm, ionized ISM. It has a resolution of 1°. The Wisconsin H-Alpha Mapper is funded by the National Science Foundation.

towards the Cygnus region is located within the following coordinates: $70^\circ < l < 100^\circ$ and $|b| < 15^\circ$. The second area in the Lockman Hole direction: $140^\circ < l < 170^\circ$ and $45^\circ < b < 65^\circ$.

The flat spectrum ($|\alpha| \leq 0.6$) candidate sources were three days prior to the main campaign observed to select those that were bright enough ($S_{5\,\mathrm{GHz}} \geq 200\,\mathrm{mJy}$) and whether that were not confused by neighbouring sources or large scale structure. Because of these initial sample selecting observations a three-day-long gap can be seen in most of the light curves. The final Cygnus sample consisted of 14 sources; the final Lockman sample consisted of 15 sources. The coordinates of the sources are listed in Table 3.1. (In the subsequent tables and figures, the catalogue designations of the sources are dropped for clarity reason).

The observations were performed with the Effelsberg 100 metre radio telescope at 4.85 GHz, between December 25 and 31 2004. The Cygnus region sources were observed for the time when they were visible and the sources toward the Lockman Hole region were observed for the remaining time, since they are circumpolar.

The observations were performed using a cross-scan technique. The telescope was moved in azimuth and in elevation over the source position and a Gaussian was fit to the resulting slice across the source to measure the source strength. Weak sources required longer integration time and we found eight (sub)scans, providing approximately four minutes on-source in total, were enough to obtain flux density measurements. A scan had a length of four to five times the half-power beamwidth (HPBW) of the telescope. Thus the off-source position provided adequate information to determine the off-source sky signal level. The cross-scan technique enables one to correct for pointing offsets during the observations.

The 4.85 GHz receiver consists of two feeds; one of them normally observing the source plus the sky ("main feed"), the other the empty sky ("weather feed"). The difference between the signal strengths in the two feeds provided the source strength. This architecture allows removing the time dependent effects due to changes of the atmosphere.

The incoming signal was split by a circular transducer into the left-hand circular (LHC) and right-hand circular (RHC) components of the radiation. A polarimeter derives from the LHC and RHC signals the Stokes parameters (I, Q, U, V). The output of the receiver consists of four signals:

$$\mathrm{SIG}_1 = S_{\mathrm{LHC}} \cdot S_{\mathrm{LHC}} \tag{3.1}$$
$$\mathrm{SIG}_2 = S_{\mathrm{LHC}} \cdot S_{\mathrm{RHC}} \sin\Theta \tag{3.2}$$
$$\mathrm{SIG}_3 = S_{\mathrm{LHC}} \cdot S_{\mathrm{RHC}} \cos\Theta \tag{3.3}$$
$$\mathrm{SIG}_4 = S_{\mathrm{RHC}} \cdot S_{\mathrm{RHC}}, \tag{3.4}$$

where Θ are the phase shift between the two components of polarization. The Stokes parameters related to these signals as:

$$I = \mathrm{SIG}_1 + \mathrm{SIG}_4 \tag{3.5}$$
$$V = \mathrm{SIG}_1 - \mathrm{SIG}_4 \tag{3.6}$$
$$Q = 2 \cdot \mathrm{SIG}_2 \tag{3.7}$$
$$U = 2 \cdot \mathrm{SIG}_3 \tag{3.8}$$

Table 3.1: Equatorial coordinates and Galactic coordinates of the sources included in the observation of December 2004. In the first part the sources toward the Lockman Hole are listed, in the second part, the sources toward the Cygnus region are listed, in the third part, steep spectrum sources of this two regions are listed. (These were included for calibration purposes.) In the last part, the standard calibrators are listed. Column 2 and Col. 3 gives the right ascension and declination in J2000.0 epoch. Column 3 and Col. 4 gives the Galactic latitude and Galactic longitude. Col. 5 gives the spectral index (between 0.4 GHz and 8 GHz).

Name	R.A.	Dec.	l [°]	b [°]	α
GB6 J 1017+6116	$10^h17^{min}25.8875^{sec}$	+61°16′27.496″	149.10	47.27	+0.3
CLASS J 1035+5652	$10^h35^{min}06.239^{sec}$	+56°52′57.90″	152.53	51.69	−0.5
GB6 J 1033+6051	$10^h33^{min}51.4289^{sec}$	+60°51′07.334″	147.79	49.11	−0.2
GB6 J 1035+5040	$10^h35^{min}06.0194^{sec}$	+50°40′06.101″	161.28	55.07	+0.1
GB6 J 1035+5628	$10^h35^{min}07.0403^{sec}$	+56°28′46.798″	158.78	56.48	−0.2
GB6 J 1041+5233	$10^h41^{min}46.781639^{sec}$	+52°33′28.23127″	157.52	54.97	−0.1
GB6 J 1046+5354	$10^h46^{min}24.038372^{sec}$	+53°54′26.23600″	154.91	54.75	+0.0
GB6 J 1048+6008	$10^h48^{min}33.771^{sec}$	+60°08′45.76″	146.72	50.93	−0.6
GB6 J 1058+5628	$10^h58^{min}37.7261^{sec}$	+56°28′11.180″	149.59	54.43	−0.1
GB6 J 1102+5941	$11^h02^{min}42.7630^{sec}$	+59°41′19.571″	145.18	52.49	−0.3
GB6 J 1104+5752	$11^h04^{min}12.9568^{sec}$	+57°52′12.848″	146.99	53.96	−0.1
JVAS J 1104+6038	$11^h04^{min}53.6954^{sec}$	+60°38′55.295″	143.82	51.94	+0.2
GB6 J 1110+4403	$11^h10^{min}46.3428^{sec}$	+44°03′25.939″	166.41	63.63	−0.2
GB6 J 1110+6028	$11^h10^{min}13.088110^{sec}$	+60°28′42.56689″	143.17	52.49	+0.0
GB6 J 1128+5925	$11^h28^{min}13.340684^{sec}$	+59°25′14.79921″	141.14	54.67	0.2
JVAS J 1949+5041	$19^h49^{min}43.492332^{sec}$	+50°41′31.97269″	84.09	12.18	+0.0
JVAS J 1955+5131	$19^h55^{min}42.7382^{sec}$	+51°31′48.546″	85.30	11.76	−0.2
JVAS B 2005+403	$20^h07^{min}44.944851^{sec}$	+40°29′48.60414″	76.82	4.30	+0.4
GB6 J 2010+3322	$20^h10^{min}49.7233^{sec}$	+33°22′13.810″	71.16	4.30	+0.5
NVSS J 2015+3710	$20^h15^{min}28.729820^{sec}$	+37°10′59.51480″	74.87	1.22	−0.1
JVAS J 2022+6136	$20^h22^{min}06.6817^{sec}$	+61°36′58.804″	96.08	13.78	+0.4
JVAS J 2023+5427	$20^h23^{min}55.844017^{sec}$	+54°27′35.82879″	90.09	9.66	−0.0
JVAS J 2023+3153	$20^h23^{min}19.0173^{sec}$	+31°53′02.305″	71.40	−3.10	+0.2
JVAS J 2025+3343	$20^h25^{min}10.8420^{sec}$	+33°43′00.214″	13.00	−2.37	+0.3
JVAS J 2052+3635	$20^h52^{min}52.0619^{sec}$	+36°35′35.303″	78.86	−5.12	+0.0
JVAS J 2115+2933	$21^h15^{min}29.4135^{sec}$	+29°33′38.367″	76.62	−13.31	0.4
GB6 J 2113+4012	$21^h13^{min}29.553^{sec}$	+40°12′51.61″	84.27	−5.76	+0.3
JVAS J 2114+3130	$21^h14^{min}50.53^{sec}$	+31°30′20.7″	78.00	−11.90	−0.5
JVAS J 2140+3911	$21^h40^{min}16.9471^{sec}$	+39°11′44.855″	87.27	−10.09	−0.2
GB6 J 1023+5904	$10^h23^{min}38.829^{sec}$	+59°04′49.12″	151.12	49.17	−0.8
GB6 J 1058+5843	$10^h58^{min}31.577^{sec}$	+58°43′29.93″	146.91	52.83	−0.7
JVAS J 2002+4725	$20^h02^{min}10.4182^{sec}$	+47°25′28.773″	82.22	8.79	+0.8
S5 0836+710	$08^h41^m24.3652^s$	+70°53′42.173″	143.54	34.43	−0.3
M 82	$09^h55^m52.219^s$	+69°40′46.93″	141.41	40.57	−0.5
NGC 7027	$21^h07^m01.70^s$	+42°14′11.0″	84.93	−3.50	+1.9
3C 286	$13^h31^m08.2879^s$	+30°30′32.958″	56.53	80.68	−0.4
3C 48	$01^h37^m41.2994^s$	+33°09′35.134″	133.96	−28.72	−0.8

Than the polarized intensity and polarization angle of the source can be obtained from the Stokes parameters:

$$P = \sqrt{Q^2 + U^2} \tag{3.9}$$

$$\chi = \frac{1}{2} \arctan \frac{U}{Q} \tag{3.10}$$

NGC 7027, 3C 48, S5 0836+710[2], and 3C 286 were observed as primary calibrators. Additionally several steep spectrum sources were included in both samples as secondary calibrators to ensure reliable flux density calibration allowing to correct instrumental and atmospheric effects (tho coordinates of the steep spectrum calibrators are listed in Table 3.1). The residual scatter in the final light curves of the secondary calibrators defines the level (1σ) on which variability can be detected, thus representing the final accuracy of the calibration. Since the single measurement errors (the errors of the Gaussian fit analysis) were usually smaller than the residual scatter of the secondary calibrators, an additional error was applied to each data-point. These were derived from the average scatter of the secondary calibrators around their mean values. Thus, the final flux density errors incorporate the statistical errors from the Gaussians fits and the contribution from the systematics seen in the secondary calibrators; they are in the order of $\sim$ 0.5 % (at 4.85 GHz).

Because the Cygnus sources are not circumpolar, this naturally introduced gaps in the time series of flux density measurements. Additional, the measurements were interrupted several times because of weather (snow and storms). This reduced the observing time by $\approx$ 15 h, and made the sampling more uneven. The sampling interval was $\approx$ 2.4 h during an undisturbed observing run of one sample. Taking all these effects into account and using the formulae described in Sect. 3.4 leads to 35 % to 50 % statistical uncertainty in m. Naturally these problems also greatly influence the variability time-scale estimations (see Sect. 3.4).

3.3 Data reduction

The data reduction was performed following the procedure described by Kraus et al. (2003). The standard 2 program (from the MPIfR Toolbox software package) was used to fit Gaussian profiles to each subscan (after subtracting the weather feed from the main feed measurements). These fits provided: the amplitude, which is proportional to the source brightness, the pointing offset and the HPBW. Bad sub-scans with errors in these values of $\geq$5 % to 10 % could then be recognized and flagged. After correcting the amplitudes for the pointing offsets, the subscans were averaged, giving one measurement value for each scan.

In the following steps systematic elevation-dependent and time-dependent gain changes from the amplitude measurements were removed by using polynomial fits to the observations of the secondary calibrators. The elevation-dependent gain correction is necessary since the telescope aperture efficiency changes with elevation as the surface of the dish deforms due to gravity. Time-dependent corrections remove the influences of changing

[2] In the following, we refer to this source as B 0836+710

weather conditions, drifts in the receivers and structural changes in the telescope due to, for example, temperature gradients.

The flux densities were then calibrated relative to the absolute flux density scale (Baars et al. 1977; Ott et al. 1994) using the primary calibrator observations. To a more detailed description of the standard reduction steps, refer to Fuhrmann (2004).

The observed signal can be represented by the following vector of the Stokes parameters: $\boldsymbol{S}_{\rm obs}\,(I_{\rm obs}, Q_{\rm obs}, U_{\rm obs}, V_{\rm obs})$. The fourth Stokes parameter, V, describing circular polarization is neglected in the following, since circular polarization of the observed sources were less than 0.5 %. The observed signal is related to the true signal via the 3×3 Müller matrix ($\boldsymbol{M}$):

$$\boldsymbol{S}_{\rm obs}\,(I_{\rm obs}, Q_{\rm obs}, U_{\rm obs}) = \boldsymbol{M}\cdot\boldsymbol{S}_{\rm true}\,(I_{\rm true}, Q_{\rm true}, U_{\rm true})\,. \tag{3.11}$$

Following Turlo et al. (1985), $\boldsymbol{M}$ can be decomposed into the terms (matrices) describing the time-dependent polarization due to the changes of parallactic angle q and the instrumental polarization ($\boldsymbol{T}$):

$$\boldsymbol{M} = \boldsymbol{T}\cdot\begin{pmatrix} 1 & 0 & 0 \\ 0 & \cos(2q) & \sin(2q) \\ 0 & -\sin(2q) & \cos(2q) \end{pmatrix} \tag{3.12}$$

The parallactic angle is defined as

$$q = \arctan\left(\pm\frac{\cos\varphi\sin H}{\sin\varphi\cos\delta' - \cos\varphi\sin\delta'\cos H}\right), \tag{3.13}$$

where φ is the latitude of the observer, H is the hour angle of the source, δ' is the declination of the source. The argument of the arcus-tangent is positive when $0 < H < 12$ and negative for $12 < H < 24$. Fig. 3.2 illustrates the definition of the parallactic angle. In the alt-azimuth mounted Effelsberg telescope, the parallactic angle is the orientation of the feeds with respect to the source. As the Earth rotates the sources trace circles in the sky and the polarization vector changes orientation. Therefore, the observed polarization angle ($\chi_{\rm obs}$) is related to the true polarization angle ($\chi_{\rm tru}$) as $\chi_{\rm obs} = \chi_{\rm true} - q$.

In reducing the polarization data, corrections for the parallactic angle and the leakage terms had to be carried out. From a set of known calibrator sources, the elements of $\boldsymbol{M}$ were derived. Inverting $\boldsymbol{M}$ lead to the true polarization vector. There were non-variable highly polarized calibrator sources, such as 3C 286 and B 0836+710 and unpolarized calibrators such as M 82. In Fig. 3.3, the uncalibrated, and the calibrated Stokes Q and U signals of B 0836+710 are compared. After applying the corrections for the instrumental polarization and the correction for the parallactic angle, the points at the QU-plane shrank to the point corresponding the polarization characteristics of B 0836+710. For a detailed description of polarization calibration, refer to Kraus (1997).

During the data reduction, two steep spectrum sources, J 1058+5843 and J 2002+4725, which were included originally for calibration, showed variability. Therefore, they were not used as secondary calibrators. This did not affect the reliability of the calibration process, since there were sufficient non-varying sources to use as secondary calibrators.

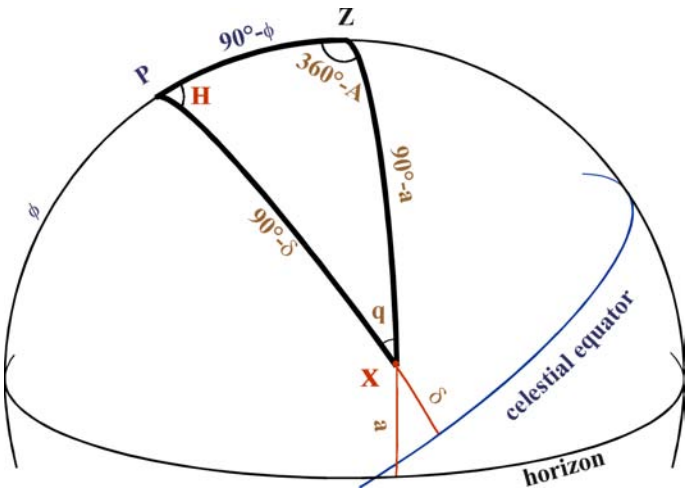

Figure 3.2: The parallactic angle of a source at point X. Z stands for zenith, P is the North Celestial Pole. δ is the source declination, H is the local hour angle of the source, A is the azimuth of the source, a is the altitude of the source. ϕ is the latitude of the observer. Image is obtained from the website `http://star-www.st-and.ac.uk/~fv/webnotes/chapter7.htm`.

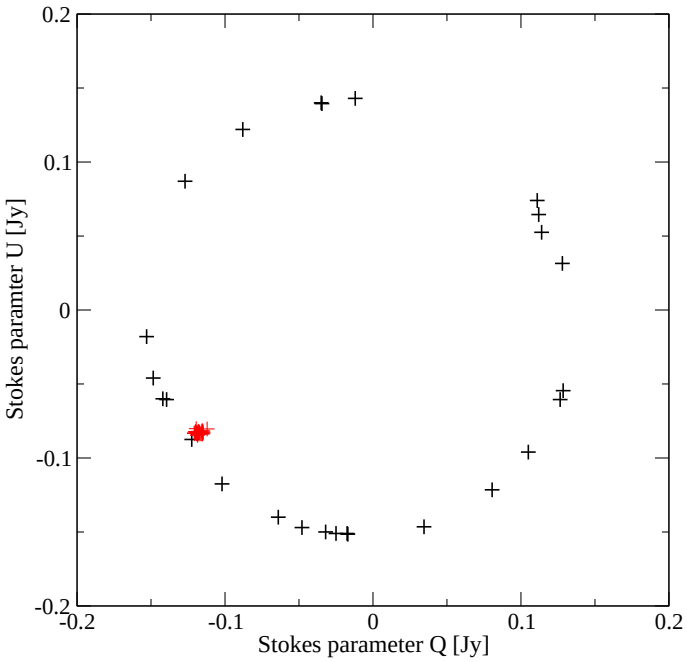

Figure 3.3: Observations of the strongly polarized, polarization calibrator, B 0836+710 in the observing campaign in December 2004. The observed Stokes parameters Q and U of B 0836+710 denoted by the black crosses. After calibrating the polarization using the inverse Müller matrix, the calibrated Q and U values (denoted by the red crosses) shrank to the point $(Q, U) \approx (-0.11, -0.08)$.

3.4 The tools of variability analysis

For the variability analysis of the data, modulation index (m) and variability amplitude (Y) (described in Sect. 2 and in detail Quirrenbach et al. 2000) were calculated for the sources.

The factors contributing to the error in m are related to the measurement accuracy, to the finite observing time and to the typical sampling interval. The limited accuracy of the measurements is absorbed in the mean flux density error. An observing period shorter than the time-scale of the variations can lead to the underestimation of m, introducing an error, Δn of $0.85 \cdot n^{-1/2}$, where n denotes the number of variability cycles, detected in the measurements. The factor 0.85 originates from the analytic solution of this statistical problem, described in Jenkins & Watts (1969). With an under-sampled light curve, fast variations can be missed. Following Cimó (2003), assuming that significant variations can appear within three data points, the error contribution can be expressed as $3 \cdot \langle t_s \rangle / T_{\rm obs}$, where $t_{\rm s}$ is the sampling interval and $T_{\rm obs}$ is the length of the observation.

Usually a χ^2 test (e.g. Bevington & Robinson 1992) is used to test whether a source displays variability. The reduced χ^2 value, which is the χ^2 divided by the numbers of degree of freedom, is the following:

$$\chi_r^2 = \frac{1}{N-1} \sum_{i=1}^{N} \left(\frac{S_i - \langle S \rangle}{\Delta S_i} \right)^2 , \tag{3.14}$$

where S_i are the individual flux density measurements, ΔS_i are the errors on those, and N is the number of measurements. The closer the value of χ_r^2 to 1, the better the data measurements can be fitted with a constant value. Sources for which the probability of fitting with a constant value is less than 0.1%, are considered to be variable.

To extract the characteristic time-scale of the variations from the measured light curve, the structure function analysis is used here. The first order discrete structure function (SF) is defined as (Simonetti et al. 1985):

$$\mathrm{SF}\,(\tau) = \langle (S\,(t) - S\,(t+\tau))^2 \rangle, \tag{3.15}$$

where $S\,(t)$ is the flux density time series, τ is the time lag, and $\langle\rangle$ denotes the time average. For a time series of $S(t_i)$ Simonetti et al. (1985) define the discrete structure function as:

$$\mathrm{SF}(\tau_j) = \frac{1}{N_{ij}} \sum_{i=1}^{n} w\,(i)\, w\,(i+j) \left[S\,(t_i) - S(t_i + \tau_j) \right]^2 . \tag{3.16}$$

where N_{ij} is the normalization and $w(i)$ is the weighting function. For the weighting function, $w(i)w(i+j) > 0$ for two measurements obtained at t_i and at $t_i + \tau_i$. The SF is related to the autocorrelation function. The definition of the autocorrelation function (e.g. Edelson & Krolik 1988):

$$\rho(\tau) = \langle S\,(t) \cdot S\,(t-\tau) \rangle. \tag{3.17}$$

Therefore the SF can be given as:

$$\mathrm{SF}\,(\tau) = 2\,[\rho(0) - \rho(\tau)] \tag{3.18}$$

Above the noise level, SF can be described by a power law: $\mathrm{SF} = A \cdot \tau^b$. At larger time lags, SF reaches its maximum at a "plateau" level of $2m^2$. Fitting the power law and the plateau level of the SF leads to the characteristic variability time-scale. The time-scale can be taken at the point where the power law fit reaches this maximum value.An example is shown in Fig. 3.4. The blue line is the fitted power law, the red line corresponds to the

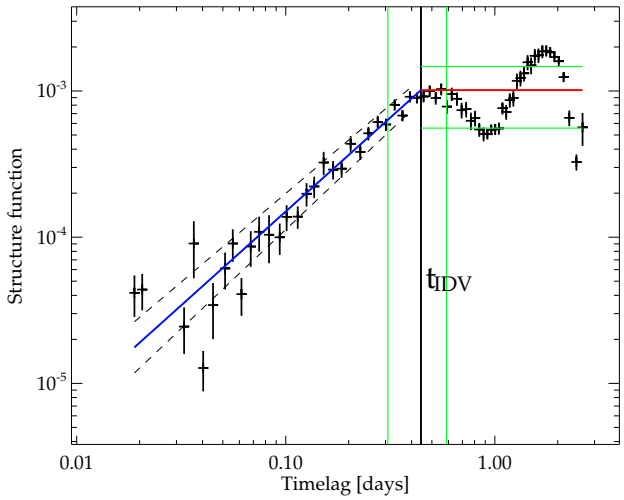

Figure 3.4: A typical SF with fitted power law and plateau level at the first maximum. This SF was constructed for J 1128+5925 from observations performed at 4.85 GHz in September 2005.

first maximum of SF (the plateau). The characteristic variability time-scale is marked by the black vertical line at the point where the power law fit crosses the plateau, that is given as $A \cdot \tau^b = 2m^2$, so the time-scale is $t_{\rm IDV} = (2m^2/A)^{1/b}$. The errors are displayed as green horizontal and vertical lines. Horizontal lines correspond to errors of m and vertical lines to errors of $t_{\rm IDV}$. The two dashed lines represent the error of the power law fit.

However, this procedure requires light curves which are long enough to include several variability cycles. IDV observations often do not meet this requirement. In "normal" IDV sources, the necessary duration of observation is five days or more. The case is more complicated when an IDV source experiences annual modulation. In this case, the variability time-scale can be significantly different at different times of the year. Additionally, in many IDV sources several variations can be superimposed on each other, thus producing a SF without a clearly pronounced maximum, or with having several maxima, or without a clear plateau level. These effects complicate the fitting procedure and often introduce extremely high errors for the derived values of the time-scale and m. Therefore, in the observations discussed below, errors sometimes as high as 100 % appear. To check the reliability of the fits, the values derived from the light curves were compared with the results of the SF analysis. In light curves, the time-scales were estimated from the time interval between subsequent maxima and minima.

3.5 Results

3.5.1 Total flux density variations

The light curves measured during our Effelsberg IDV campaign are displayed in Appendix A.2. The average flux densities ($\langle S \rangle$), the standard deviation (σ), the modulation indices (m), the variability amplitudes (Y), and the reduced χ^2 are given in Table 3.2. In each epoch, m_0, the modulation index of an assumed non-varying source is given. m_0

was chosen conservatively: we adopted for m_0 the highest modulation index among the several secondary calibrators, 0.42 % instead using the average value for m_0, which was 0.33 %. Out of the three steep spectrum sources, which were included as additional calibrators, two showed variability. J 2002+4725 displayed a constant rise in its light curve. J 1058+5843 showed short time-scale variations with $m \approx 2$ %. However, to keep the consistency of the sample and use only flat spectrum sources, J 1058+5843 was not included in the subsequent analysis.

Naively, one would expect to see greater variability on lines of sight that include longer path length through the Galactic disk, as such sight lines pass through more ionized interstellar matter. However, the results obtained do not agree with this expectation. On the contrary, more variations were detected at high Galactic latitudes. In the direction of the Lockman Hole (towards high Galactic latitude), 12 out of 15 sources (80 %) were variable according to the χ^2 test. In the direction of the Cygnus region (towards low Galactic latitude) 5 out of 14 sources (36 %) showed variability. Applying a stricter criterion for variability and regarding a source as variable if its modulation index derived from IDV analysis was higher than 1 %, 9 of 15 sources (60 %) showed IDV in the first sample and 4 of 14 sources (29 %) showed IDV in the second sample.

A "Difference of Two Proportions" test (Glantz e.g. 1992 and see A.1) shows that the null hypothesis, that the two samples comes from the same parent population is true at a significance level of 2 %. Applying the stricter criterion of variability for the observed sources, the difference between the two samples are not significant, the null hypothesis can be accepted at a level of significance of 9 %. However, this statistical test is valid for continuous distribution of data. Here it is not the case, the number of detected IDV sources can only be integer values, therefore the "Yates correction" (Glantz e.g. 1992 and see A.1 for details) has to be applied. This test show no significant difference in the IDV detection rate in the two samples of sources. The hypothesis that the two samples do not differ can be accepted at a significance level of 4 % in the first case and at a significance level of 18 % in the second case.

In Fig. 3.5, the observed source positions are plotted in Galactic coordinates together with the Hα intensity measurements of the WHAM Northern Sky Survey. Correlation cannot be seen between the positions of IDV sources and the ionized hydrogen intensity content of the nearest line of sight.

Linear regression to the two samples showed that the correlation is indeed low (see Fig. 3.6). The highest correlation coefficients (in absolute value) were obtained in the Cygnus region for those variable sources which have a $m > 1$ %, so it is calculated only with using four datapoints. In the Cygnus region, the trend suggested by the linear regressions is that the sources are more variable towards those line of sights, where the Hα intensity is lower. This trend might be explained with the following. The ISS in the Cygnus region (at a distance of $\sim$ 1 kpc to 2.5 kpc) causes scatter-broadening in many lines of sight (e.g. Desai & Fey 2001, and references therein). Those already scatter broadened sources, however, exhibit only quenched scintillation, because of their (apparent) larger extent in the LISM.[3]

Towards the Lockman Hole the correlation coefficients between Hα intensity and Y are much closer to zero. The variability amplitude of those IDV sources, which have a

[3] In B 2005+403 quenched scattering was observed in a previous measurements performed at 1.6 GHz, with much denser time sampling. Those results are discussed in detail in Sect.4.5.2.

Table 3.2: Variability characteristics of individual sources. Column 2 gives the number of measurements, Col. 3 the average flux density, Col. 4 the standard deviation, Col. 5 the modulation index, Col. 6 the variability amplitude, and Col. 7 gives the reduced χ^2. This table is divided into three parts. In the first part the sources toward the Lockman Hole are listed, in the second part, the sources toward the Cygnus region are listed, and in the last part the three most frequently observed calibrators are listed for comparison.

Name	N	$\langle S \rangle$ [Jy]	σ [Jy]	m [%]	Y [%]	χ^2_r	$m_{\rm SF}$ [%]	$t_{\rm SF}$ [day]
$\nu = 4.85\,$GHz, $m_0 = 0.42\%$								
J 1017+6116	26	0.657	0.004	0.55	1.06	1.583	–	–
J 1035+5652	21	0.259	0.010	3.95	11.78	70.454	1.7 ± 0.7	$1.1^{+0.5}_{-0.4}$
J 1033+6051	26	0.402	0.003	0.82	2.10	3.270	0.5 ± 0.2	$0.1^{+0.2}_{-0.1}$
J 1035+5040	25	0.245	0.003	1.02	2.80	4.283	0.4 ± 0.2	$2.7^{+2.4}_{-3.5}$
J 1035+5628	25	1.203	0.007	0.55	1.07	1.597	–	–
J 1041+5233	26	0.704	0.006	0.90	2.38	4.201	1.1 ± 0.3	$3.6^{+2.8}_{-3.0}$
J 1046+5354	26	0.163	0.004	2.53	7.50	20.014	0.7 ± 0.3	$0.2^{+0.9}_{-0.2}$
J 1048+6008	26	0.367	0.003	0.89	2.36	3.872	0.5 ± 0.2	$0.3^{+2.0}_{-0.3}$
J 1058+5628	26	0.190	0.006	3.03	9.01	30.635	1.0 ± 0.3	$1.9^{+0.7}_{-0.8}$
J 1102+5941	25	0.324	0.003	1.06	2.91	5.193	0.7 ± 0.3	$1.0^{+1.0}_{-0.9}$
J 1104+5752	26	0.133	0.004	3.03	8.99	21.779	0.6 ± 0.2	$0.3^{+0.3}_{-0.5}$
J 1104+6038	24	0.167	0.002	1.16	3.25	3.957	0.4 ± 0.1	$1.5^{+0.2}_{-0.3}$
J 1110+4403	22	0.175	0.005	2.59	7.67	21.576	0.7 ± 0.2	1.1 ± 0.7
J 1110+6028	25	0.405	0.003	0.62	1.36	1.915	–	–
J 1128+5925[a]	24	0.570	0.062	10.88	32.62	649.705	9.8 ± 3.5	$\left(1.2^{+0.4}_{-0.6}\right)$
J 1949+5041	24	0.235	0.007	2.79	8.26	29.771	0.7 ± 0.2	$0.2^{+0.4}_{-0.2}$
J 1955+5131	24	0.956	0.011	1.17	3.29	7.253	1.8 ± 0.5	$1.1^{+0.1}_{-0.2}$
B 2005+403[b]	23	2.549	0.012	0.45	0.50	1.075	–	–
J 2010+3322	23	1.302	0.004	0.33	–	0.579	–	–
J 2015+3710	22	2.183	0.025	1.14	3.19	6.515	5.0 ± 2.0	$0.5^{+0.7}_{-0.4}$
J 2022+6136	20	3.038	0.010	0.32	–	0.543	–	–
J 2023+5427	23	1.035	0.010	0.93	2.48	4.502	1.6 ± 0.5	$2.0^{+0.4}_{-0.6}$
J 2023+3153	23	1.137	0.006	0.54	1.03	1.555	–	–
J 2025+3343	23	2.194	0.013	0.61	1.33	1.938	–	–
J 2052+3635	27	3.341	0.010	0.29	–	0.439	–	–
J 2115+2933	21	0.863	0.032	3.65	10.89	72.146	5.6 ± 1.4	$1.8^{+0.3}_{-0.4}$
J 2113+4012	23	0.492	0.002	0.46	0.53	1.081	–	–
J 2114+3130	21	0.231	0.001	0.57	1.16	1.273	–	–
J 2140+3911	18	0.452	0.002	0.54	1.02	1.528	–	–
J 1023+5904	26	0.492	0.003	0.57	1.14	1.670	–	–
J 1058+5843[c]	21	0.161	0.003	1.88	5.50	11.241	0.7 ± 0.4	0.2 ± 2.0
J 2002+4725	22	0.708	0.012	1.71	4.98	15.305		> 5[d]
B 0836+710	31	2.547	0.008	0.31	–	0.507		
M 82	25	3.290	0.011	0.32	–	0.570		
NGC 7027	33	5.447	0.017	0.30	–	0.487		

[a] The variability characteristics of this source are discussed in detail in Sect.3.6.

[b] In different epochs this source showed IDV, see Sect. 4.5.2.

[c] Although this source showed IDV, it was not included in the final analysis to keep the consistency of the data.

[d] The source showed a monotonous increase in flux density during the observations, a time-scale can thus not be derived.

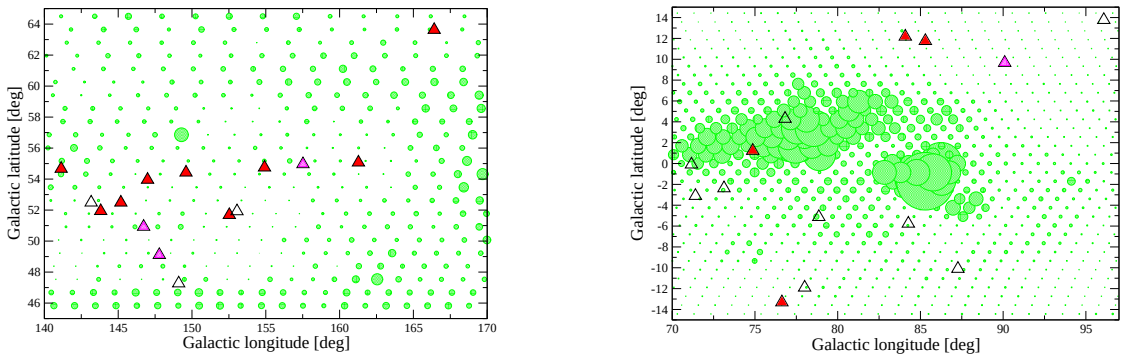

Figure 3.5: The observed radio sources in Galactic coordinates. Filled, red triangles are for those variable sources which have $m > 1\,\%$, partially filled magenta triangles are for those variable sources which have $m < 1\,\%$, open triangles are for non-variable sources. On the left hand side, the Lockman Hole area is displayed, on the right hand side the Cygnus region. The sizes of the green circles are proportional to the Hα intensity measured in a particular line of sight by the WHAM-NSS but different multiplicative factors were used in the two plots. Since the electron density in the Lockman Hole region (left plot) are much lower than in the Cygnus (right plot), therefore a circle with the same size denotes 75 times smaller Hα in the left plot than in the right plot.

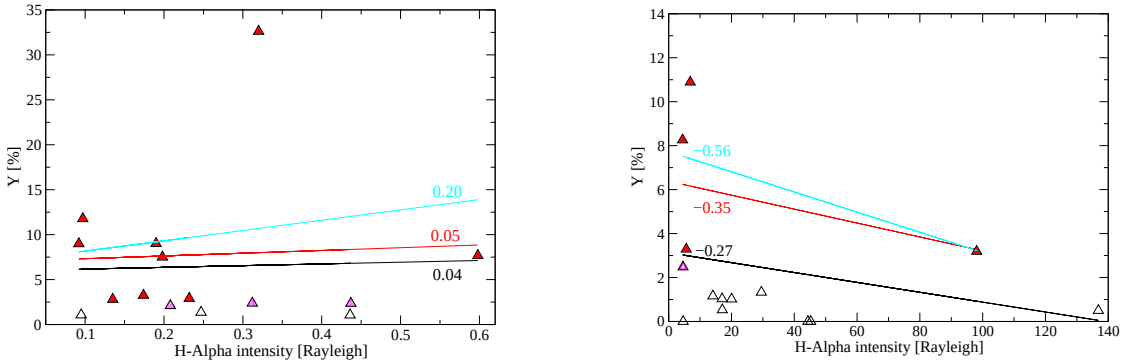

Figure 3.6: The variability amplitude of observed sources versus Hα intensity. Filled, red triangles are for the variable sources which have $m > 1\,\%$, open triangles are for non-variable sources. Partially filled magenta triangles are for those variable sources where $m < 1\,\%$. Black lines regression to all sources, red line regressions to sources which showed IDV according to the χ^2-test, turquoise lines regressions to those IDV sources, where $m > 1\,\%$. On the left hand side, the Lockman Hole area is displayed, on the right hand side the Cygnus region. Next to each line the corresponding correlation coefficient are displayed.

$m > 1\,\%$ might suggest a trend, that the variability amplitude is higher at line of sights where Hα intensity is higher. This is opposite to that was observed in the Cygnus region.

In Fig. 3.7, Y values for the variable sources in both sample are plotted versus the absolute value of Galactic latitude. (The highest value of J 1128+5925 is not displayed for clarity). Linear regression to the combined samples suggest a trend that at larger $|b|$ values the Y is larger, however if the highly variable source, J 1128+5925 is excluded, dependence on Galactic latitude cannot be detected. Naturally, the same applies if only

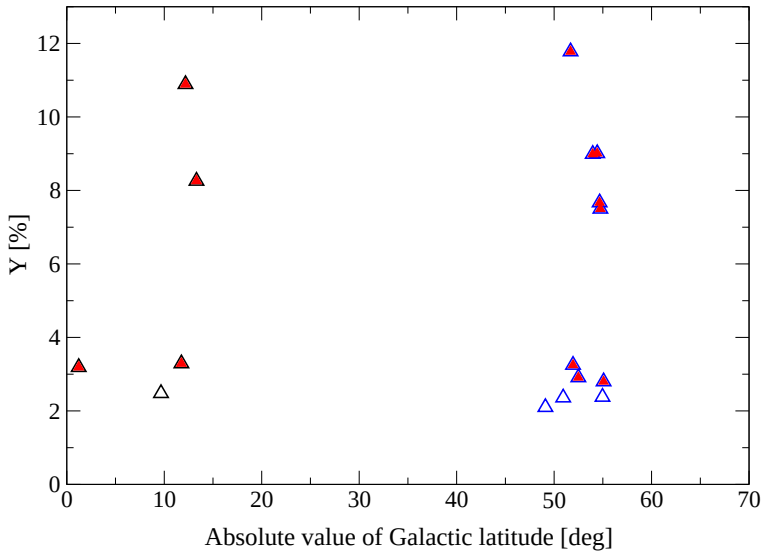

Figure 3.7: The variability amplitude, Y, of the variable sources versus the absolute value of Galactic latitude. The extremely variable J 1128+5925 is not shown for clarity, see Sect. 3.6 for a detailed analysis of this source. Black symbols: Cygnus region sample, blue symbols: Lockman Hole sample. The filled red symbols denote the variable sources which have $m > 1\,\%$.

the Lockman Hole sources are included in the linear regression. The IDV sources towards the Cygnus region suggest a trend of higher Y with larger $|b|$ values, however this depends upon a smaller sample of four and five sources.

In summary, the observation showed no significant difference between variability characteristics of the two samples of sources. Surprisingly, a slightly larger fraction of sources showed IDV towards the Lockman Hole, toward which less ionized hydrogen is seen, than towards the Cygnus region. However, the statistical tests showed, that there is no significant difference between the IDV detection rates between the samples. These results are consistent with the picture that the interstellar material responsible for IDV is nearby, at a distance of $\sim 100\,$pc or less (as it was calculated in the case of some IDV sources, see Sect. 2.3) and does not depend on the larger scale Galactic distribution of the ISM.

Nonetheless, these two regions are very different in the structure of the LISM towards them. Lallement et al. (2003) investigated the shape of the Local Bubble in different Galactic directions. They found that the boundary of the Local Bubble in the Galactic plane is $\sim 60\,$pc, but it appears to be open-ended in both Galactic hemispheres up to at least $\sim 250\,$pc in the so called Local Interstellar Chimney (LC). The axis of this rarefied cavity ($N_{\rm H} < 2 \cdot 10^{19}\,{\rm cm}^{-2}$) is oriented towards $l = 155^\circ$ and $b = +58^\circ$ in the northern Galactic hemisphere (toward the direction of the Lockman Hole), with a diameter of $\sim 25^\circ$. Welsh et al. (2004) reported column densities of Ca ranging $(10 \text{ to } 40) \cdot 10^{10}\,{\rm cm}^{-2}$ towards five lines of sight in this region. They suggest, that the LC is filled mainly with clouds of warm and ionized interstellar Ca gas at least from $\sim 185\,$pc upward from the Galactic disk. However, they also failed to detect any boundary, or "end" to the LC. From these observations, it seems plausible, that the IDV phenomena detected in sources toward this region of the sky are probably caused by these ionized clouds, whereas the IDV

observed towards the Cygnus region may be connected to the interaction in the boundary region of the Local Bubble.

3.5.2 Polarized flux density variations

Propagation of the radiation through the ISM can cause Faraday rotation of the polarization angle. This phenomenon occurs because the two circular polarized components of the wave travel through the magnetized plasma with different speeds, shifting the phase of the two components with distance, which causes rotation of the polarization vector. In some cases the detected variations are so fast that assuming changing Faraday rotation in the ISM as an explanation implies very fast, physically not plausible changes in the intervening medium.

In several such cases, the sources were modelled with multiple components with different polarization characteristics. For example, in the case of S5 0917+624 Qian et al. (2002) introduced a two-component model of the source and thus was able to explain some of the polarization characteristics of the variability. Rickett et al. (2002) and Rickett (2001) used a similar model to describe the extremely rapid variations detected in PKS 0405-385. These models can explain several observed features in the polarized variability, but still are not able to reproduce some of the polarization angle changes.

Most of the observed sources in our campaign were only weakly polarized, or not polarized at all. In several weakly polarized sources, the Gaussian fit to the observed signal did not provide believable amplitudes for the Stokes Q and U flux densities in numerous scans, therefore those scans had to be discarded in the further data analysis. Examples for discarded and for good scans are shown in Fig. 3.8.

In Table 3.3, the variability parameters of the sources are listed which have polarized flux density larger than 10 mJy and where the Gaussian fits were acceptable at least for half of the scans. The respective light curves are shown in Appendix A.2, in figures A.6 and A.7.

All target sources which have significantly large polarized flux density, showed variations. Even some sources which did not exhibit IDV in total flux density showed variability in polarization. As can be seen from the table and the figures, the variations in polarization are higher than in total flux density. However significant fraction of measurements had to be discarded during the analysis of the polarization data of the target sources, which causes larger errors in m_{p} and Y_{p}. Therefore, the polarization measurements are not sufficient (in quantity and in quality) to make detailed analysis of the two different samples or to compare them thoroughly.

3.5.3 Summary

Observations of IDV sources in two regions of the sky were carried out with the Effelsberg 100 metre radio telescope. These two parts of the sky differ in the amount of interstellar matter detected towards them. The Lockman Hole has the lowest column densities of H and H , whilst the Cygnus region is well known for the large amount turbulent ionized material in the line of sight.

According to the RISS theory, IDV of flat-spectrum AGN is caused by the intervening turbulent, ionized ISM. Therefore, naively one might expect to see a larger fraction of

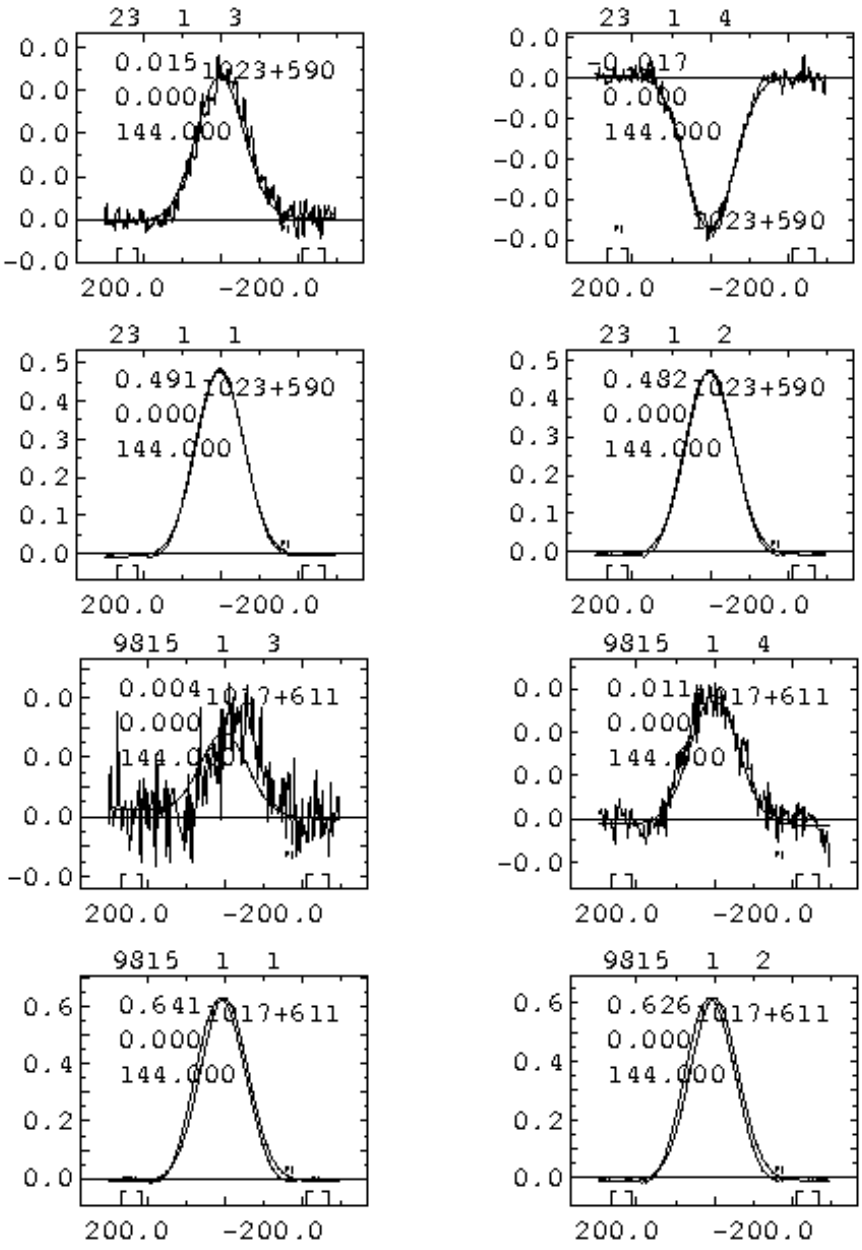

Figure 3.8: The top four plots displays the Gaussian fits to the scans of J 1023+5904 in elevation. The bottom four plots displays the Gaussian fits to the scans of J 1017+6116 in elevation. The plots denoted by the number 3 and 4 in their header displays the channels of Stokes *Q* and Stokes *U* signals. The plots denoted by the number 1 and 2 in their header displays the right und left circularly polarized channels of the total intensity. The scan of J 1017+6116 had to be discarded in the polarization analysis of the data because of the ambiguous Gauss fit to the Stokes *Q* and *U* data. The plots were created by the 2 software.

Table 3.3: Variability characteristics of polarized sources ($P > 10$ mJy). Column 1 gives the source name, Col. 2 the number of measurements, Col. 3 the average polarized flux density, Col. 4 the standard deviation, Col. 5, 6 and 7 the modulation index, the variability amplitude and the reduced χ^2 of the polarized intensity. In Col. 8, 9 and 10 the mean polarization angle, its error, and its reduced χ^2 are given.

Name	N	$\langle P \rangle$ [mJy]	σ_P [mJy]	m_P [%]	Y_P [%]	$\chi^2_r(P)$	χ [°]	σ_χ [°]	$\chi^2_r(\chi)$
$\nu = 4.85$ GHz, $m_{P0} = 1.7\%$, $\sigma_{\chi 0} = 1.0°$									
J 1017+6116	13	12.1	1.5	12.04	35.75	213.36	34.7	2.8	152.534
J 1023+5904	17	20.2	1.3	6.45	18.66	164.39	20.9	1.5	102.512
J 1035+5652*	14	19.0	2.1	11.10	32.90	444.1	52.2	3.0	366.267
J 1033+6051*	14	14.0	1.7	12.11	35.96	287.10	84.8	3.7	303.420
B 2005+403	18	45.9	1.1	2.44	5.24	4.14	40.4	0.7	5.368
B 0836+710	26	144.2	2.0	1.26	0.00	6.08	107.7	0.1	2.590
3C 286	16	817.7	14.1	0.91	0.00	15.47	33.1	0.0	1.829

*According to the χ^2 test, showed variability in total flux density.

IDV sources towards lines of sight where the amount of turbulent ionized material is larger. However, the observations presented here revealed a no significant difference in the IDV detection rate between the two samples of sources. These observations showed no evidence that the strength of variability depends on Galactic latitude. These results are consistent with the picture derived from the measurement of fast scintillators (see Sect. 2.3) that IDV is caused by the LISM and therefore that the large-scale distribution of Galactic ISM has no influence on IDV rate of occurrence.

No significant correlation between the Y and the Hα intensity (measured by WHAM) was found. Towards the Cygnus region, a trend suggested by the linear regressions is that the sources are more variable towards those line of sights, where the Hα intensity is lower. This finding might be the result, that in the Cygnus region, the ISS causes scatter-broadening in many lines of sight. However, those already scatter broadened sources exhibit only quenched scintillation because of their larger apparent extent in the LISM.

3.6 The source J 1128+5925

J 1128+5925 is a compact quasar - see the VLBI images displayed in Fig. 3.9 from the Caltech-Jodrell Bank Survey (Taylor et al. 1994). Its redshift is 1.799 ± 0.003 (Britzen et al. 2006, in prep.). It has a flat spectrum, with a spectral index of $\alpha_{8\,\mathrm{GHz}}^{0.365\,\mathrm{GHz}} \approx 0.33$. [4] No previous IDV observations of this source have been published.

J 1128+5925 was the mostly variable source in the Effelsberg observing campaign in December 2004. Its modulation index was $\sim 11\,\%$ and it showed 20 % flux- density changes during 6 h to 7 h. These variations imply an apparent variability brightness tem-

[4] In calculating the spectral index, flux density measurements of Taylor et al. (1994); Patnaik et al. (1992); Gregory & Condon (1991); Becker et al. (1991); White & Becker (1992); Douglas et al. (1996) were used.

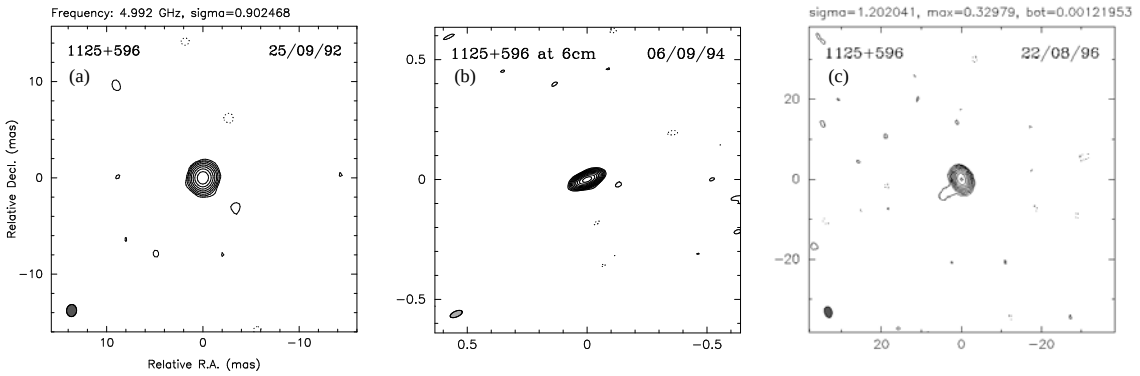

Figure 3.9: VLBI images of J 1128+5925 from the Caltech-Jodrell Bank Survey (Taylor et al. 1994) performed at 4.85 GHz at the epochs of 1992.74, 1994.68 and 1996.64.

perature of $\sim 6 \cdot 10^{19}$ K, which, if the variations were intrinsic, would require a Doppler boosting factor of ~ 400 (or in the case of the equipartition limit $\delta \sim 800$).

3.6.1 Follow-up observations of J 1128+5925

To investigate the frequency dependence of the variations and to obtain more adequately sampled measurements, J 1128+5925 was observed in May 2005 at 4.85 GHz and at 10.45 GHz with the Effelsberg 100 metre radio telescope over three days. To check the variability characteristics and a possible systematic variation of the variability time-scale, the source was observed several times during 2005. The details of all measurements are shown in Table 3.4. Four epochs of observations were performed with the Effelsberg 100 metre radio telescope, one observation was carried out with the Urumqi (China) 25 metre radio telescope. The latter was a test experiment of the 4.85 GHz receiver provided to the Urumqi telescope by the MPIfR.

During the Effelsberg observation in 2005 December, because of bad weather conditions, the calibration of the 10.45 GHz data are difficult. This will be accomplished in the near future. Therefore the results of the observations performed only at 4.85 GHz and 2.6 GHz are discussed here.

The calibration of the Effelsberg data were carried out in the same way as described in Sect. 3.3. Additionally, opacity corrections were applied for the 10.45 GHz dataset obtained in May 2005 and for the 4.85 GHz dataset obtained in December 2005. The Urumqi dataset was reduced by P. Müller and T. P. Krichbaum.

The 4.85 GHz light curves from May 2005, August 2005, September 2005, and December 2005 are displayed in Fig. 3.10. The light curves are shifted by the appropriate amounts in time so the observations from different epochs are overlaid. Along with J 1128+5925, a secondary calibrator (M 82) is also shown (from epoch May 2005). The quality of the Urumqi data differs from the quality of the Effelsberg data due to the smaller

Table 3.4: Summary of observations of J 1128+5925. The table lists the epochs the observing frequencies, the observing radio telescope, the total duration of the observations, and the mean sampling intervals of J 1128+5925.

Epoch	Frequency [GHz]	Instrument	Duration [h]	Mean sampling interval [h]
25-31 December 2004	4.85	Effelsberg	125	5.0
13-16 May 2005	4.85	Effelsberg	67	1.2
13-16 May 2005	10.45	Effelsberg	55	1.5
14-17 August 2005[a]	4.85	Urumqi	67	2.8
16-19 September 2005[b]	4.85	Effelsberg	64	0.7
28-31 December 2005[c]	2.70	Effelsberg	29	1.0
28-31 December 2005[c]	4.85	Effelsberg	30	0.5
28-31 December 2005[d]	10.45	Effelsberg	30	0.5

[a]Data reduction was done by P. Müller and T. P. Krichbaum.
[b]Observation of T. P. Krichbaum.
[c]Only preliminary results are given here.
[d]The results of this measurement are not discussed here.

size of the Urumqi dish (25 m diameter compared to 100 m for Effelsberg implying a sensitivity one sixteenth that of Effelsberg). Additionally, the preliminary data reduction software did not provide accurate errors, therefore conservatively large errors were assumed (priv. comm. T. P. Krichbaum). The different variability time-scales observed at different epochs are obvious, for discussion see Sect. 3.6.2.

In Fig. 3.11 the 10.45 GHz light curves of J 1128+5925 and of a secondary calibrator, B 0836+710 from May 2005 are shown. The observation at 10.45 GHz was interrupted due to rain between 2453504.973 and 2453505.511 for 12 hours.

The 2.6 GHz light curve from December 2005 is displayed in Fig. 3.12.

In Table 3.5, the variability characteristics (modulation index, variability amplitude, variability time-scale) of J 1128+5925 are summarized. The modulation index was derived from the light curve and from the structure function. The time-scale estimates result from the structure function analysis (see Sect. 3.4). Except for the first epoch, the time-scale estimates are consistent within the error with the time-scale estimates obtained from the light curves. However, in December 2004, because of the uneven sampling and the limited number of data points, the resulting time-scale from the structure function analysis was inconsistent with the light curve (see Fig. A.1): the latter suggests a variability time-scale of 6 h to 7 h.

3.6.2 Annual modulation in J 1128+592?

According to the ISS model of IDV, the Earth moves in a scintillation pattern projected to the Earth plane (see illustration in Fig. 3.13). The relative velocity between the Earth and the scattering screen changes through the year, as the Earth orbits around the Sun. When the Earth and the scattering medium moves parallel with each other, the relative velocity is low, hence the observed variability time-scale lengthens, the variations are slow. Six

Table 3.5: The variability parameters of J 1128+5925 from the observations from 2004 and 2005 performed with the Effelsberg telescope and with the Urumqi telescope. Col. 1 shows the source name, col. 2 the number of flux density measurements. Col. 3 shows the mean flux density in Jy, col. 4 the standard deviation, col. 5 the modulation index, col. 6 the variability amplitude col. 7 the reduced χ^2. In the last two columns, the modulation index and time-scale are given, which are obtained from structure function analysis of the data. Except for the first epoch, the time-scale estimates from the structure functions provide values consistent with those obtained from light curves. In the first epoch the uneven sampling and very few data points caused the time-scale derived from structure function to be poor.

Name	N	$\langle S \rangle$ [Jy]	σ [Jy]	m [%]	Y [%]	χ^2_r	m_{SF} [%]	t [day]
December 2004, $\nu = 4.85$ GHz, $m_0 = 0.42$ %								
J 1128+5925	24	0.570	0.062	10.88	32.62	649.705	9.8 ± 3.5	$\sim 0.27^*$
B 0836+710	31	2.547	0.008	0.31	0	0.507		
M 82	25	3.290	0.011	0.32	0	0.570		
May 2005, $\nu = 4.85$ GHz, $m_0 = 0.46$ %								
J 1128+5925	54	0.611	0.013	2.20	6.44	19.932	2.1 ± 0.7	$0.8^{+0.6}_{-0.5}$
B 0836+710	61	2.346	0.008	0.34	0	0.498		
M 82	59	3.318	0.010	0.31	0	0.401		
4C +67.22	27	0.889	0.004	0.45	0	0.886		
May 2005, $\nu = 10.45$ GHz, $m_0 = 0.63$ %								
J 1128+5925	29	0.730	0.028	3.78	11.17	11.875	5.0 ± 2.0	1.0 ± 0.4
B 0836+710	26	1.610	0.011	0.54	0	0.235		
M 82	29	1.833	0.011	0.62	0	0.319		
August 2005, $\nu = 4.85$ GHz, $m_0 = 0.61$%								
J 1128+5925	20	0.682	0.040	5.85	17.51	4.291	7.0 ± 3.0	0.8 ± 0.5
8C 1148+592	91	0.473	0.003	0.61	0.20	1.394		
September 2005, $\nu = 4.85$ GHz, $m_0 = 0.46$%								
J 1128+5925	91	0.719	0.021	2.91	8.61	14.815	4.0 ± 0.1	0.6 ± 0.2
B 0836+710	93	2.212	0.008	0.37	0	0.241		
M 82	132	3.295	0.015	0.46	0	0.368		
December 2005, $\nu = 4.85$ GHz, $m_0 = 0.42$%								
J 1128+5925	64	0.725	0.052	7.17	21.49	237.791	5.3 ± 1.7	0.16 ± 0.1
B 0836+710	22	2.184	0.007	0.33	0	0.518		
M 82	26	3.311	0.013	0.38	0	0.719		
8C 1203+645	60	1.152	0.005	0.41	0	0.787		
December 2005, $\nu = 2.70$ GHz, $m_0 = 0.25$ %								
J 1128+5925	31	0.532	0.036	6.81	20.42	102.584	6.1 ± 1.9	$0.6^{+0.3}_{-0.2}$
B 0836+710	11	2.817	0.007	0.25	0.13	0.158		
M 82	13	5.011	0.012	0.25	0	0.147		
8C 1203+645	28	2.120	0.005	0.23	0	0.120		

*The given variability time-scale is derived from the light curve, since the time-scale obtained from the SF analysis was not consistent with the light curve. SF indicated a variability time-scale of $1.2^{+0.4}_{-0.6}$.

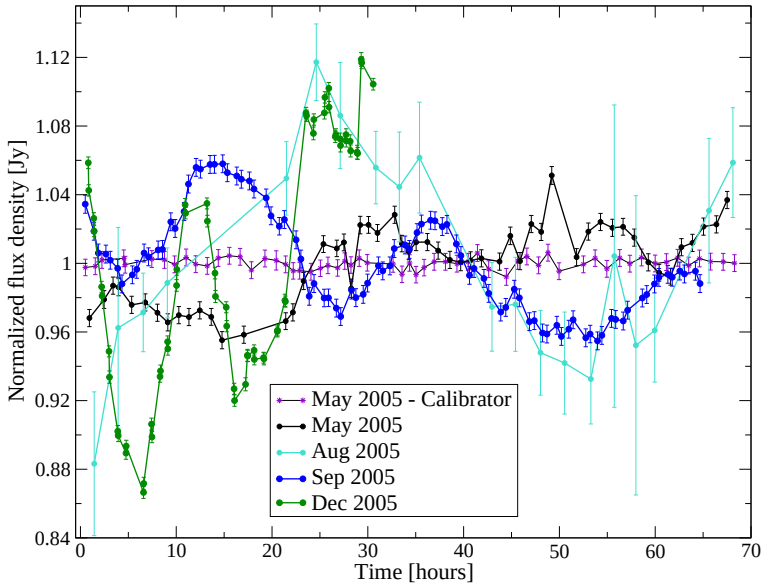

Figure 3.10: 4.85 GHz light curves of J 1128+5925 measured in four different epochs, denoted by differently coloured circles. A secondary calibrator M 82 from one epoch (May 2005) is also shown (denoted by asterisks). The light curves are shifted in time with an arbitrary value, so that the x axis gives a "relative" time-scale.

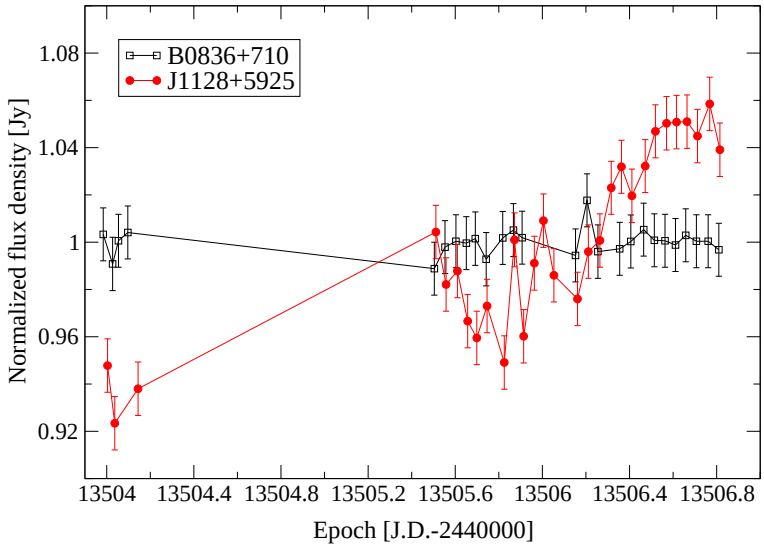

Figure 3.11: 10.45 GHz light curves of J 1128+5925 (red circles and red line) measured in May 2005 along with a secondary calibrator, B 0836+710 (black squares and black line). The missing measurements in the middle are due to rain.

months later, when the Earth moves in the opposite direction as the scattering medium, the relative velocity is high, hence the observed variability time-scale shortens, the variations are fast.

In calculating the changes of the variability time-scale through the year with the annual modulation scenario, the spatial scale of the "scintles" and the relative speed between

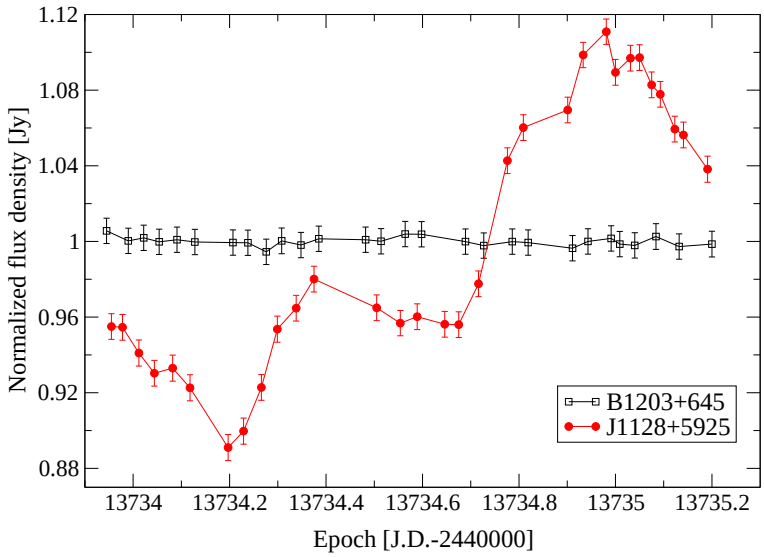

Figure 3.12: 2.70 GHz light curves of J 1128+5925 (red circles and line) measured in December 2005 along with a secondary calibrator, B 1203+645 (black squares and line).

the Earth and the scattering medium are required.

The relative speed between the Earth and the scattering medium

The relative motion of the Earth with respect to the scattering medium consists of the following velocity components: the velocity of the Earth's orbital motion around the Sun ($\boldsymbol{V}_{\rm Earth}$), the Sun's motion towards the solar apex[5] with respect to the Local Standard of Rest (LSR) frame of the Milky Way ($\boldsymbol{V}_{\odot}$) and the velocity of the scattering screen with respect to the LSR ($\boldsymbol{V}_{\rm screen}$)[6]. The proper motion of the extragalactic radio source is negligible. Thus, the total velocity vector between the Earth and the scattering screen is

$$\boldsymbol{V} = \boldsymbol{V}_{\rm Earth} + \boldsymbol{V}_{\odot} - \boldsymbol{V}_{\rm screen}. \tag{3.19}$$

To calculate these velocities, following Qian & Zhang (2001) and Fuhrmann (2004), we assume an equatorial coordinate system, with its origin at the centre of the Sun. The X axis points towards the equinox, the Y axis points towards the terrestrial equator at R. A. $6^{\rm h}$ and the Z axis points towards the north pole. Thus, the relations between the equatorial coordinates of R. A. (α') and Dec. (δ') and the X Y and Z coordinates are given as

$$\cos X = \cos\alpha' \cos\delta' \tag{3.20}$$
$$\cos Y = \cos\delta' \sin\alpha' \tag{3.21}$$
$$\cos Z = \sin\delta'. \tag{3.22}$$

[5]The B 1950 coordinates of the solar apex are 267° in R. A. and 28° in Dec. (Gilmore & Zeilik 2000).

[6]In this deduction, we neglect the possibility that the scattering is caused by multiple layers with different speeds which are located at different distances. Here, one scattering screen is assumed to be responsible for the scattering.

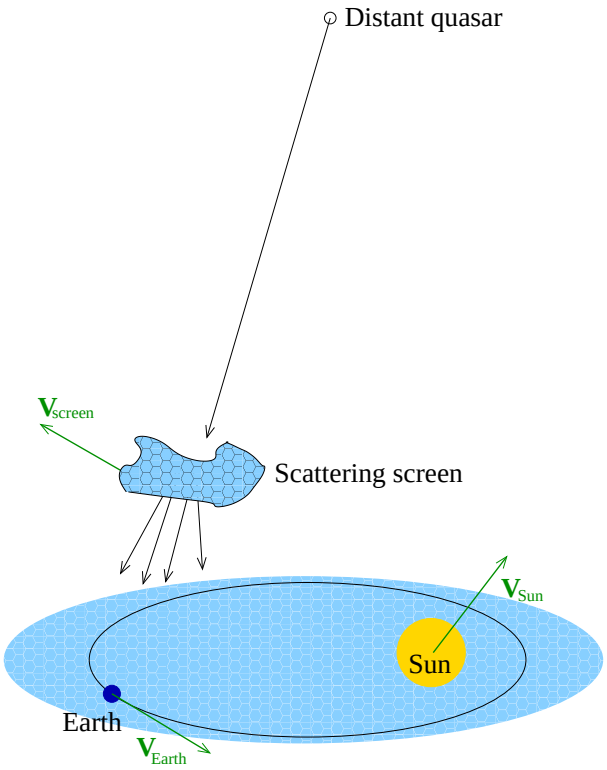

Figure 3.13: A sketch of annual modulation model. The screen creates a scintillation pattern via focusing and defocusing the light of the distant quasar. The Earth moves through this scintillation pattern projected onto its orbit (indicated by the light-blue pattern). As the observer moves through this spatial scintillation pattern, it observes flux density variations. The time-scale of the observed variations depends upon the relative velocity between the Earth and the scattering screen. Thus, it depends upon the vector sum of the three velocity vectors (indicated by green lines in the figure).

In this reference frame the R. A. and Dec. of the Earth are

$$\alpha'_{\text{Earth}} = \alpha'_{\odot} + 180^{\circ} \tag{3.23}$$
$$\delta'_{\text{Earth}} = -\delta'_{\odot}, \tag{3.24}$$

where $\alpha'_{\odot}$ and $\delta'_{\odot}$, the R. A. and Dec. of the Sun in the usual geocentric coordinate system. They can be calculated using the Astronomical Almanac of year 1999 (U. S. Naval Observatory & Royal Greenwich Observatory 1998) in the following way:

$$n = \text{doy} - 1.5 \tag{3.25}$$
$$L = 280.460^{\circ} + 0.985647 \cdot n \tag{3.26}$$
$$g = 357.528^{\circ} + 0.9856003 \cdot n \tag{3.27}$$
$$\lambda = L + 1.915^{\circ} \cdot \sin g + 0.020^{\circ} \cdot \sin(2g) \tag{3.28}$$
$$\epsilon = 23.439^{\circ}, \tag{3.29}$$

where doy is the day of the year, L is the mean longitude of the Sun, g is the mean anomaly, λ is the ecliptic longitude and ϵ is the angle of the ecliptic with respect to the

Sun's plane. Defining

$$f = 180^\circ/\pi \tag{3.30}$$
$$t = \tan^2 \epsilon/2 \tag{3.31}$$

we obtain

$$\alpha'_\odot = \lambda - ft\sin(2\lambda) + 0.5ft^2\sin(4\lambda) \tag{3.32}$$
$$\delta'_\odot = \arcsin(\sin\epsilon\sin\lambda). \tag{3.33}$$

Then the spatial velocity of the Earth's orbital motion around the Sun can be calculated as

$$\begin{aligned}\boldsymbol{V}_{\rm Earth} &= |\boldsymbol{V}_{\rm Earth}|\times \\ &\left(-\frac{\sin\delta'_{\rm Earth}}{\sin\epsilon}\cdot\boldsymbol{X_0} + \cos\alpha'_{\rm Earth}\sin\delta'_{\rm Earth}\cos\epsilon\cdot\boldsymbol{Y_0} + \cos\alpha'_{\rm Earth}\cos\delta'_{\rm Earth}\sin\epsilon\cdot\boldsymbol{Z_0}\right),\end{aligned} \tag{3.34}$$

where the absolute value of the velocity of the Earth is $29.8\,\mathrm{km\,s^{-1}}$ (Gilmore & Zeilik 2000) and $\boldsymbol{X_0}$, $\boldsymbol{Y_0}$ and $\boldsymbol{Z_0}$ are the unit vectors along the respective axes.

The Sun's motion in the LSR frame can be given as

$$\boldsymbol{V}_{\rm Sun} = |\boldsymbol{V}_{\rm Sun}|\left(\cos\alpha'_{\rm apex}\cdot\boldsymbol{X_0} + \sin\alpha'_{\rm apex}\cos\delta'_{\rm apex}\cdot\boldsymbol{Y_0} + \sin\delta'_{\rm apex}\cdot\boldsymbol{Z_0},\right) \tag{3.35}$$

where the absolute value of the velocity of the Sun is $16.6\,\mathrm{km\,s^{-1}}$ (Gilmore & Zeilik 2000).

The velocity of the scattering screen can be represented by two velocity components, one along the R. A. of the source and one along the Dec. of the source. Motion along the line of sight is not considered, since only of the transverse velocity of the Earth through the scintillation pattern is involved in the scintillation theory. Thus the velocity of the scattering screen is

$$\boldsymbol{V}_{\rm screen} = \boldsymbol{V}_{\alpha'\,\rm screen} + \boldsymbol{V}_{\delta'\,\rm screen}, \tag{3.36}$$

where $\boldsymbol{V}_{\alpha'\,\rm screen}$ and $\boldsymbol{V}_{\delta'\,\rm screen}$ are

$$\begin{aligned}\boldsymbol{V}_{\alpha'\,\rm screen} &= |\boldsymbol{V}_{\alpha'\,\rm screen}|\,(-\sin\alpha'_{\rm screen}\cdot\boldsymbol{X_0} + \cos\alpha'_{\rm screen}\cdot\boldsymbol{Y_0}) \\ \boldsymbol{V}_{\delta'\,\rm screen} &= |\boldsymbol{V}_{\delta'\,\rm screen}|\times \\ &\qquad(-\cos\alpha'_{\rm screen}\sin\delta'_{\rm screen}\cdot\boldsymbol{X_0} + \sin\alpha'_{\rm screen}\sin\delta'_{\rm screen}\cdot\boldsymbol{Y_0} + \cos\delta'_{\rm screen}\cdot\boldsymbol{Z_0})\end{aligned} \tag{3.37}$$

Combining all the velocity components together (see Equation 3.19), one obtains the components (V_X, V_Y and V_Z) of the Earth relative velocity with respect to the scattering medium:

$$\begin{aligned}V_X &= -|\boldsymbol{V}_{\rm Earth}|\frac{\sin\delta'_{\rm Earth}}{\sin\epsilon} + |\boldsymbol{V}_{\rm Sun}|\cos\alpha'_{\rm apex}\cos\delta'_{\rm apex} + |\boldsymbol{V}_{\alpha'\,\rm screen}|\sin\alpha'_{\rm screen} + \\ &\quad |\boldsymbol{V}_{\delta'\,\rm screen}|\cos\alpha'_{\rm screen}\sin\delta'_{\rm screen} \\ V_Y &= |\boldsymbol{V}_{\rm Earth}|\cos\alpha'_{\rm Earth}\sin\delta'_{\rm Earth}\cos\epsilon + |\boldsymbol{V}_{\rm Sun}|\sin\alpha'_{\rm apex}\cos\delta'_{\rm apex} - |\boldsymbol{V}_{\alpha'\,\rm screen}|\cos\alpha'_{\rm screen} + \\ &\quad |\boldsymbol{V}_{\delta'\,\rm screen}|\sin\alpha'_{\rm screen}\sin\delta'_{\rm screen} \\ V_Z &= |\boldsymbol{V}_{\rm Earth}|\cos\alpha'_{\rm Earth}\cos\delta'_{\rm Earth}\sin\epsilon + |\boldsymbol{V}_{\rm Sun}|\sin\delta'_{\rm apex} - |\boldsymbol{V}_{\delta'\,\rm screen}|\cos\delta'_{\rm screen}\end{aligned} \tag{3.38}$$

Assuming ζ to be the angle between the sum of velocities ($\boldsymbol{V}$) and the line of sight of the IDV source, the transverse speed of the Earth with respect to the scattering screen can be represented as

$$V_{\perp} = |\boldsymbol{V}| \sin\zeta, \tag{3.39}$$

$\sin\zeta$ is equal to $\sqrt{(1-\cos^2\zeta)}$ and $\cos\zeta$ can be expressed as

$$\cos\zeta = \frac{V_X}{|\boldsymbol{V}|}\cos\alpha'_{\rm screen}\cos\delta'_{\rm apex} + \frac{V_Y}{|\boldsymbol{V}|}\sin\alpha'_{\rm screen}\cos\delta'_{\rm screen} + \frac{V_Z}{|\boldsymbol{V}|}\sin\delta'_{\rm screen} \tag{3.40}$$

The properties of the scattering medium

As described in Sect. 2.2.2, the variability time-scale inversely proportional to the relative velocity of the observer through the pattern transverse to the line of sight and proportional to the length scale of the scintillation pattern. The length sale of the scintillation pattern depends upon the distance to the scattering screen (L) and the effective source size ($\theta_{\rm eff}$). The latter is the convolution of the intrinsic surface brightness distribution of the source ($\theta_{\rm int}$) with the scatter-broadened image of a point source (or the diffractive angle, $\theta_{\rm diff}$). Thus, following Goodman (1997), $\theta_{\rm eff}$ is given as:

$$\theta_{\rm eff} = \sqrt{\theta_{\rm int}^2 + (0.71\theta_{\rm diff})^2 + (0.85\theta_{\rm F})^2}, \tag{3.41}$$

where $\theta_{\rm F}$ is the Fresnel angle, which allows one to use the formula in both weak and strong regimes of scattering. The diffractive angle and the Fresnel angle given as:

$$\theta_{\rm diff} = 2.93\left(\frac{\nu}{10\,{\rm GHz}}\right)^{-2.2}\left(\frac{\rm SM}{10^{-3.5}\,{\rm m}^{-20/3}\,{\rm kpc}}\right)^{0.6}\mu{\rm as} \tag{3.42}$$

$$\theta_{\rm F} = 2.57\left(\frac{\nu L_{\rm kpc}}{10\,{\rm GHz}}\right)^{-0.5}\mu{\rm as} \tag{3.43}$$

Thus, knowing the effective size, the distance to the scattering screen and transverse velocity the time-scale can be calculated for different day of the year (Goodman 1997):

$$t = 14 L_{\rm kpc}\left(\frac{\theta_{\rm eff}}{10\,\mu{\rm as}}\right)\left(\frac{V_{\perp}}{30\,{\rm km\,s^{-1}}}\right)^{-1}{\rm h} \tag{3.44}$$

Application of the model to the source J 1128+5925

The measurements suggest that J 1128+5925 experienced different variability time-scales during a year (see Fig. 3.10 and Table 3.5). In May and August the source slowed down compared to its variability in December. However, the two observations performed in December with one year difference, showed remarkably consistent variability time-scale estimates.

The prediction of the annual modulation model with different input parameters were calculated by the program of L. Fuhrman (Fuhrmann et al. 2002b and Fuhrmann 2004) which is based upon the paper of Qian & Zhang (2001) and Goodman (1997) and was presented in the previous sections. In this model, the screen is assumed to be thin, and SM is approximated as $0.5\overline{C_N^2}\cdot L_{\rm kpc}$. The average scattering amplitude of the screen is

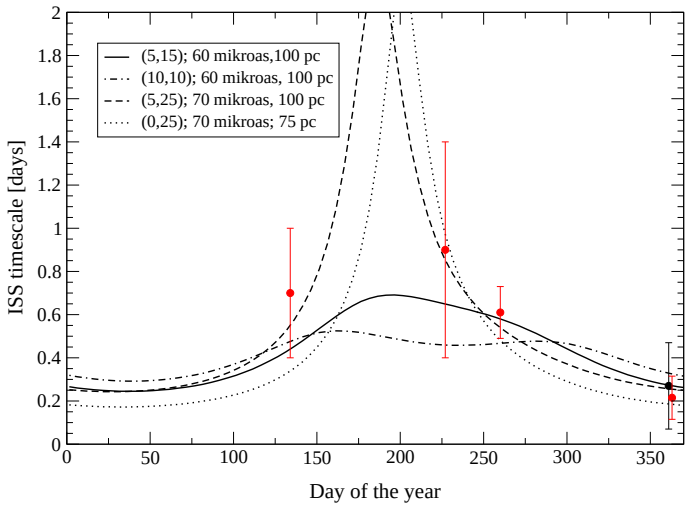

Figure 3.14: The IDV time-scale of J 1128+5925 throughout the year measured at 4.85 GHz, with four different sets of parameters of annual modulation model. The calculations of the annual modulation curves were done with the program of L. Fuhrmann (Fuhrmann 2004). The model parameters are shown in the upper right side. The first two number are the screen velocity components in R. A. and in Dec. in km s^{-1}, the third is the upper limit of the intrinsic source size and the last one is the distance of the scattering screen. The red circles denote observations took place in 2005, the black circle denote observation took place in 2004.

given as, $\overline{C_N^2} = 0.5\,\mathrm{m}^{-20/3}$ kpc. In the model calculation, 70 μas and 60 μas were assumed for θ_{int}, 100 pc and 75 pc were assumed for the screen distance, and 0 km s^{-1} to 10 km s^{-1} were assumed for the screen LSR velocity in R. A., and 10 km $^{-1}$ to 25 km s^{-1} for the velocity in Dec.

The model calculations with the measured time-scales of J 1128+5925 are displayed in Fig. 3.14. (The time-scales and their errors were calculated using the estimates from the SF analysis and from the light curves.) The four different annual modulation models cannot be distinguished by the five data points in Fig. 3.14. Additional observations - preferably in summer - are needed.

The θ_{int} basically gives an the upper limit of the intrinsic source size, since the intrinsic source size can be smaller than this to show scintillation, but sources with larger extent than θ_{int} cannot display scintillation. Using the mean flux density of all our 4.85 GHz observations of J 1128+5925 (0.66 Jy) and the assumed upper limit of the intrinsic source size (60 μas) one can calculate a lower limit of the brightness temperature. The obtained lower limit of the brightness temperature is $2.6 \cdot 10^{12}$ K. This is slightly higher than the inverse-Compton limit. A moderate Doppler boosting factor ($\delta \sim 1.4$) would be needed to reduce the brightness temperature in the source frame to the inverse-Compton limit (10^{12} K) or $\delta \sim 3$ to reduce the brightness temperatures to the equipartition limit (10^{11} K).

The annual modulation scenario explains changes in the time-scale, and it predicts that m should be constant. However, in J 1128+5925 at 4.85 GHz, m seems to be varying. The modulation indices derived from the structure function analysis versus observing epoch are displayed in the right hand side of Fig. 3.15). The average m_{SF} is $\sim$ 3.1 %; the measured values display a large scatter around the mean. No clear trend or correlation

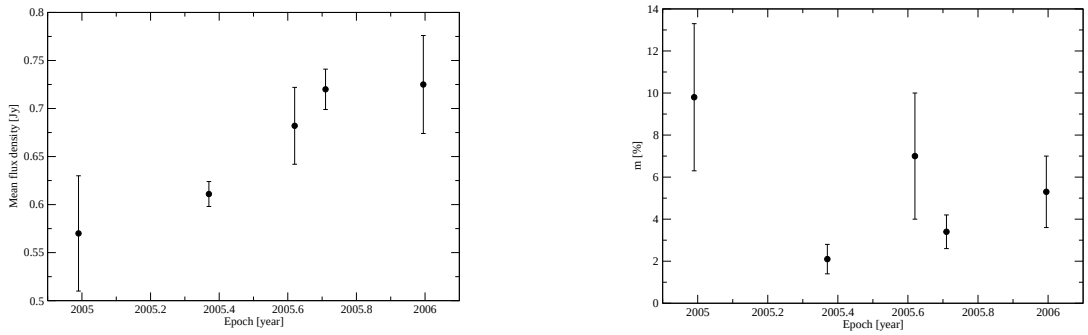

Figure 3.15: The mean flux density of J 1128+5925 at the different epochs (left), and the modulation indices (right). The annual modulation scenario predicts constant modulation index. The varying *m* can be caused either by changes in the scattering screen, or in the source itself.

can be detected. The varying *m* can be caused either by changes in the scattering screen, or in the source itself. However, observations with shorter duration can significantly underestimate the modulation index (Sect. 3.4), and consequently may explain the observed apparent changes in *m*.

The mean flux density exhibit an increase through the epochs (see left hand side of Fig. 3.15). This can be a sign of a longer-term trend, however the errors are large and only few data points are yet available.

Further observations aimed directly to confirm or falsify the annual modulation scenario will be needed not just to better constrain the time-scale changes through the year but to provide evidence for or against a changing in *m*.

3.6.3 Frequency dependence of the modulation index and the variability amplitude

Different variability behaviour is expected, according to the ISS explanation of IDV, in the different scattering regimes(see Sect. 2.2.2). In the strong scattering regime (below a transition frequency), the modulation index increases with increasing frequency (Goodman 1997):

$$m_{\mathrm{strong}} \sim \frac{\nu}{\nu_{\mathrm{tr}}}^{17/30}, \tag{3.45}$$

where ν_{tr} is the transition frequency. In the weak scattering regime (above this transition frequency), the modulation index decreases with increasing frequency:

$$m_{\mathrm{weak}} \sim \frac{\nu}{\nu_{\mathrm{tr}}}^{-2}. \tag{3.46}$$

In both regimes, the time-scale of the variations decreases with increasing frequency. However, in the strong regime this time-scale decrease is much faster than in the weak regime (Walker 1998):

$$t_{\mathrm{strong}} \sim 2\left(\frac{\nu_{\mathrm{tr}}}{\nu}\right)^{\frac{11}{5}}, \tag{3.47}$$

Table 3.6: The observed and predicted modulation indices ($m_{\rm obs}$ and $m_{\rm predict}$) and time-scales ($t_{\rm obs}$ and $t_{\rm predict}$) of J 1128+5925 at different frequencies. The transition frequency is assumed to be 10.45 GHz. The calculations are based upon equations 3.45 and 3.47. In Col. 3, the modulation index of the secondary calibrator is given.

Epoch	ν [GHz]	m_0 [%]	$m_{\rm obs}$ [%]	$m_{\rm predict}$ [%]	$t_{\rm obs}$ [day]	$t_{\rm predict}$ [day]
May 2005	4.85	0.46	2.20	2.4 ± 0.1	$0.8^{+0.6}_{-0.5}$	(1.1 ± 1.2) *
May 2005	10.45	0.63	3.78	3.7 ± 0.2	1.0 ± 0.4	(0.2 ± 0.2) *
Dec 2005	4.85	0.23	7.17	8.0 ± 1.1	0.16 ± 0.1	0.16 ± 0.01
Dec 2005	2.70	0.46	6.81	5.7 ± 0.7	$0.6^{+0.3}_{-0.2}$	0.59 ± 0.01

*The measured time-scales in this epoch contradict to the expected decrease in time-scale with increasing frequency, therefore the calculated timescales have huge errors.

where $\nu_{\rm tr}$ is the transition frequency. In the weak regime the time-scale is:

$$t_{\rm weak} \sim 2\sqrt{\frac{\nu_{\rm tr}}{\nu}}. \tag{3.48}$$

The IDV observations suggest that the transition frequency usually is ~ 5 GHz.

The observations indicate that J 1128+5925 experiences IDV at all the three observing frequencies (2.70 GHz, 4.85 GHz, and 10.45 GHz), with different modulation indices and time-scales. Naturally, only the simultaneous multi-frequency observations can be compared. Therefore in the epoch in May 2005 the variability behaviour at 4.85 GHz and 10.45 GHz can be compared, and (independently from this) in December 2005 the variability at 2.70 GHz and 4.85 GHz can be compared.

In May 2005 m was higher at 10.45 GHz than m at 4.85 GHz. In December 2005, m was higher at 4.85 GHz than the m at 2.70 GHz. These results suggest a lower limit of 10.45 GHz for the transition frequency. If 10.45 GHz is assumed to be the transition frequency, one can check whether equation 3.45 correctly describes m at other frequencies. The result of this comparison is shown in Table 3.6.

The predicted and measured values of m and variability time-scales are in agreement within the error bars. The assumption that the transition frequency is 10.45 GHz does not contradict to the most of the derived parameters of the observations. Only the measured time-scale at 10.45 GHz disagrees with the RISS expectations, as the variability time-scale decreases with increasing frequency. However, the time-scale measurements are very crude at this frequency due to the inadequate sampling and small amount of data (because of bad weather conditions, see Fig. 3.11).

The transition frequency can be written as (Goodman 1997):

$$\nu_{\rm tr} \approx 178.8 \cdot {\rm SM}^{\frac{6}{17}} L^{\frac{5}{17}}\ {\rm GHz}, \tag{3.49}$$

where L is the distance to the scattering screen measured in kpc. Assuming the distance to be between 75 pc and 100 pc (from the annual modulation scenario), SM ranges between $2.2 \cdot 10^{-3}\ {\rm m}^{-20/3}$ kpc and $2.8 \cdot 10^{-3}\ {\rm m}^{-20/3}$ kpc.

If instead of the thin-screen approximation, one assumes that the scintillation in the source J 1128+5925 is caused by an extended, thick screen with thickness comparable to

its distance, then the SM can be approximated as: SM = $\overline{C_N^2} \cdot L$. Using the above calculated SM and this assumption, $\overline{C_N^2}$ ranges between $2.2 \cdot 10^{-2}\,\mathrm{m}^{-20/3}$ and $3.7 \cdot 10^{-2}\,\mathrm{m}^{-20/3}$.

This $\overline{C_N^2}$ is a factor of thousand larger than that proposed by Bhat et al. (1998) for the cavity of the Local Bubble ($(2 \text{ to } 6) \cdot 10^{-5}\,\mathrm{m}^{-20/3}$). Using the $\overline{C_N^2}$ values of the (Bhat et al. 1998) model, a path length of 2.5 kpc to 4.5 kpc would be needed to produce the SM value inferred from the assumed transition frequency. However, to reproduce the same time-scale of variations with a screen distance of the order of couple of kpc would require either the scintillating source size must be in the order of μas or the speed of the scattering screen must be of the order of several hundred $\mathrm{km\,s^{-1}}$. The latter is not very plausible, since the Galactic rotation velocity is $\sim 220\,\mathrm{km\,s^{-1}}$. A scintillating angular size in the order of 1 μas is also much smaller, than the ones usually obtained for IDV sources. It is comparable to the size calculated by Macquart & de Bruyn (2005) for J 1819+3845 in which they observed diffractive scintillation. This is not the case in J 1128+5925. Therefore it can be safely assumed that the ISM causing the observed variations in J 1128+5925 can be modelled by a thin screen, thus it can be connected to the clouds of ionized material in the LC (Welsh et al. 2004).

Nevertheless, observation performed at frequencies higher than the assumed transition frequency, 10.45 GHz are needed to confirm that the modulation index indeed peaks at 10.45 GHz. If the variations were intrinsic to the source, one would expect to see stronger variations at higher frequencies. Therefore, the frequency dependence of *m* derived from the available data can be still consistent with source intrinsic variations.

3.6.4 Summary

The observations presented here revealed a new, highly variable IDV source, J 1128+5925. They showed that the variability time-scale of the source changes over the year. Two observations separated by one year showed remarkably similar time-scales and thus confirm each other. Based upon these measurements, the time-scale changes of J 1128+5925 most likely can be explained by the annual modulation scenario. J 1128+5925 might be the fifth IDV source (besides J 1819+3845 (Dennett-Thorpe & de Bruyn 2003) PKS 1257-326 (Bignall et al. 2003; Bignall 2003) PKS 1519-273 (Jauncey et al. 2003) and S4 0954+658 (L. Fuhrmann priv. comm.)) showing evidence for annual modulation. However to confirm the annual modulation scenario and to distinguish between different models, more densely sampled flux-density measurements will be necessary, preferably at those times of the year when J 1128+5925 was not previously observed (e.g. in June or July).

J 1128+5925 showed evidence for IDV at three frequencies (2.70 GHz, 4.85 GHz and 10.45 GHz). Based upon the limited amount of observational data, it is probable, that the transition frequency between weak and strong scattering regimes is higher than 5 GHz (which is the transition frequency in most IDV sources). However, the frequency dependence of *m* derived from the available data may also indicate that, the variations are intrinsic to the source. Simultaneous, multi-frequency observations are essential to check the variability behaviour at different frequencies and thus answer the question, where the variability of J 1128+5925 originates from.

4 The scatter-broadened quasar B 2005+403

4.1 The importance of scatter-broadening

The ISM of the Milky Way affects point-like Galactic and extragalactic radio sources in several ways (see Sect. 2.2.2). In the previous chapter, I presented observations of IDV in quasars and discussed to what extent RISS can explain the results. In this chapter, I focus on scatter-broadening, another phenomenon related to ISS.

There are several examples of scatter-broadened extragalactic sources, of those NGC 6334B (Trotter et al. 1998, and references therein) and B 1849+005 (Lazio 2004) are the most strongly-scattered examples. From angular-broadening measurements of extragalactic sources, the Scattering Measure (SM, see Sect. 2.2.1) value can be evaluated. By comparing SM values along different lines of sight, the angular distribution of scattering material can be obtained.

Combining the SM values of extragalactic and Galactic radio sources with the measurements of other scattering induced phenomena (DM values of pulsars, pulse broadening in pulsars, EM values) is a powerful approach to produce a three-dimensional model for the Galactic distribution of interstellar plasma. The most up-to-date model of this kind was created by Cordes & Lazio (2002) (hereafter NE2001). Fig. 4.1 displays the electron density according to the NE2001 model. Like its predecessors, it describes the large-scale structure of the Galaxy with a thin and thick disk, and spiral arms. However, the novelty of NE2001, is that it also introduces "clumps" and "voids", regions of enhanced and low electron density (or scattering). Thus it models not just the overall structure of the Milky Way, but the middle-sized structure of the ISM (e.g. H regions) as well.

Additionally, angular broadening provides information on the power spectral index of the density fluctuations (see Sect. 2.2.1). The relation between the apparent angular size and the observing frequency depends on the actual slope of the power law of the ISM, β. In the case of a Kolmogorov type turbulence ($\beta = 11/3$), the apparent angular size of an extragalactic source scales as: $\theta \sim \nu^{-2.2}$ (Rickett 1990). Significant deviation from this value may indicate that the electron density fluctuations do not follow a Kolmogorov turbulence. Or it may imply that the inner scale of the turbulence is greater than the scales sampled by the interferometer baseline. Thus, the longest baseline used in the observation places a lower limit to the inner scale.

If the density fluctuations are elongated, scattering observables would be affected (e.g. scattering disk of sources would be anisotropic). In magneto-hydrodynamical (MHD) turbulence, it is expected that the density fluctuations would be aligned along the field di-

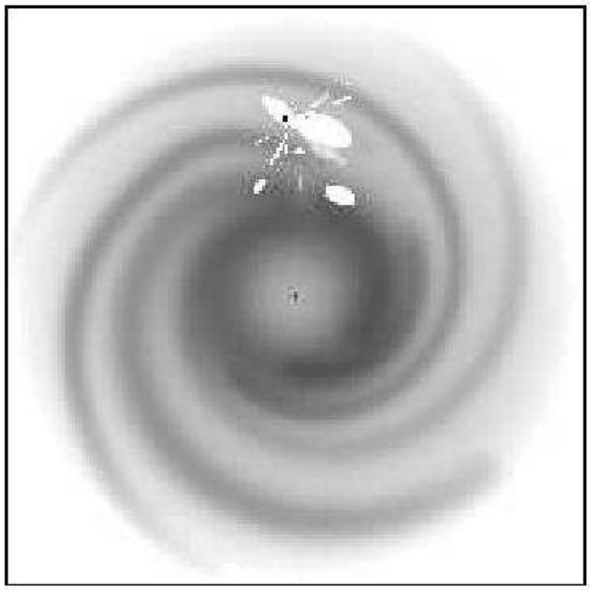

Figure 4.1: The Galactic distribution of electron density as described by NE2001 model of Cordes & Lazio (2002). The most prominent large-scale features are the spiral arms, a thick disk and a molecular ring component. The Galactic centre component appears as a small dot. The small scale, white features represent the local ISM of the Solar System and the underdense regions. The small dark region embedded in one of the underdense region is the Gum Nebula and the Vela supernova remnant. (The size of the figure is 30 kpc times 30 kpc.)

rections and potentially be highly anisotropic. Thus measurements of the scattering disks of scatter-broadened sources can provide information on the orientation and organization of the magnetic field in the ISM on sub-parsec scales.

Probably the best-known scattered source is the Galactic centre, Sgr A* (e.g. Lo et al. 1998; Lazio & Cordes 1998). Lo et al. (1998) managed to disentangle the intrinsic source structure of Sgr A* from the scattering. They performed VLBA observations nearly simultaneously at five wavelengths between 6 cm and 7 mm. At 7 mm, they detected that the measured minor axis diameter of Sgr A* differs significantly from the scattering diameter predicted by the lower frequency measurements. Thus they were able to estimate the intrinsic source size, the elongation of the source and give a brightness temperature limit at 7 mm.

To reveal the characteristics of angular broadening in B 2005+403

Multi-frequency VLBI observations of scatter broadened extragalactic sources can shed light on the characteristics of the intervening Galactic ISM, and can as well make it possible to study the intrinsic source structure. To disentangle propagation and source intrinsic effects, a wide range of observing frequencies is required. As scattering increasing with decreasing frequency, only high-frequency observations are free of scattering influences and can probe the internal source characteristics.

In this chapter, I describe the study of a scatter-broadened extragalactic radio source, B 2005+403. The wide frequency coverage of the observations (from 1.6 GHz to 43 GHz)

made it possible to investigate the interplay between the frequency-dependent scattering effects, which dominate below 8 GHz, and the source-intrinsic structure and variability, which is best seen at and above 15 GHz.

The organization of this chapter is as follows: In Sect. 4.2, the results of earlier studies of B 2005+403 are summarized. In Sect. 4.3, a brief description of the VLBI technique is given. In Sect. 4.4, the observations and data reduction steps are summarized. In Sect. 4.5.1, the angular broadening of B2005+403, in Sect. 4.5.2 its short time-scale variations are discussed. In Sect. 4.5.3, the intrinsic source structure of B2005+403, and kinematics of the jet features are presented. In Sect. 4.5.4, I focus on the flux density evolution and position of the VLBI core. Additionally, in Sect. 4.5.5 the polarization data are presented.

4.2 Introducing B 2005+403

B 2005+403 is a flat spectrum quasar ($\alpha_{5\,\mathrm{GHz}}^{0.365\,\mathrm{GHz}} = 0.3$; Becker et al. 1991) at a redshift of 1.736 (Boksenberg et al. 1976). It is located close to the Galactic plane at $l = 76.82°$, $b = 4.29°$ behind the Cygnus super-bubble region.

Fey et al. (1989) and Desai & Fey (2001) studied several extragalactic lines of sight seen through the Cygnus region. B 2005+403 turned out to be one of the most scattered quasars in their sample (see Fig. 4.2). Their studies showed that interstellar scattering (ISS) affects the source image, causing angular broadening at frequencies from 0.6 GHz to 5 GHz. Spangler & Reynolds (1990) measured the Hα emission towards eight of the sources studied by Fey et al. (1989). B 2005+403 showed the highest Hα intensity of 130 Rayleigh, which corresponds to an emission measure of 294 cm^{-6} pc (assuming an electron temperature of 8000 K). They concluded that the line of sight of B 2005+403 is intercepted by an H region.

A more recent, all-sky Hα survey, the Virginia Tech Spectral-Line Survey (VTSS, Dennison et al. 1998)[1] provides higher angular resolution (approximately the resolution is 1 arc-minute). For the line of sight of B 2005+403, the reported emission measure is 147.8 cm^{-6} pc (see `http://www.phys.vt.edu/~halpha/`).

B 2005+403 was incorporated in the NE2001 model because of its heavily scattered line of sight. Cordes & Lazio (2002) using the SM measurements of Desai & Fey (2001) calculated the characteristics of the "clump" of material responsible for the measured angular broadening of B 2005+403. With an assumed electron density of 1 cm^{-3} and a fluctuation parameter of 20, they obtained a path length through the scattering material of $d \approx 18$ pc. The distance they assumed to this scattering region is $L \approx 2.35$ kpc.

B 2005+403 was observed within the Green Bank Interferometer (GBI) flux density monitoring program between 1982 and 1996 at 2 GHz and 8 GHz (Lazio et al. 2001). One of the main goals of those observations was to identify extreme scattering events (ESE). In the case of B 2005+403 no such event was detected. However, Rickett et al. (2005) recently analyzed the GBI observations in order to separate the long-term intrinsic variations from the more rapid ISS caused flux-density changes. They report a variation of $\sim 4\,\%$ on a time-scale of ≈ 12 d at 8 GHz in B 2005+403, and they suggest that it is caused by ISS. (Further discussion on this topic is presented in Sect. 4.5.1.)

[1] The VTSS is supported by the National Science Foundation.

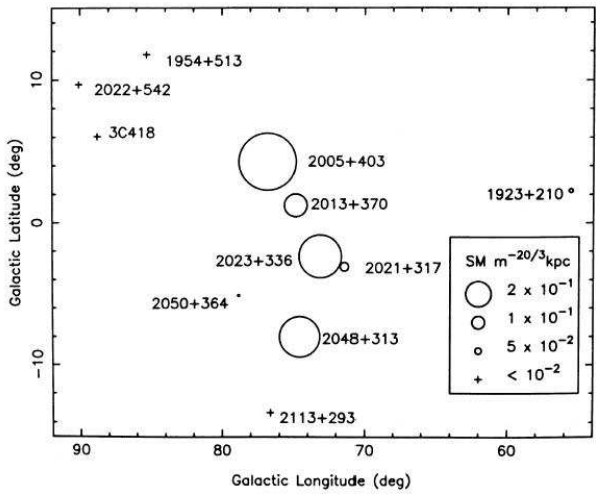

Figure 4.2: Fey et al. (1989) studied several extragalactic lines of sight through the Cygnus region. They plotted the different SM values in the direction of different sources. The sizes of the circles are proportional to the SM values, as indicated by the legend. They measured the highest SM value towards B 2005+403. It can be seen that the SM changes significantly within only a few degrees, e.g. with a factor of ≈ 2.5 over $\approx 4^\circ$ between B 2005+403 and B 2013+370, or ≈ 4 over $\approx 2^\circ$ between B 2023+336 and B,2021+317.

B 2005+403 had not been intensively studied with VLBI at higher frequencies (15 GHz, 22 GHz and 43 GHz). The high frequency VLBI data presented here cover a time range of 15 yr (from 1992 to 2005) and thus allowed us to study the structural evolution of the VLBI core and the pc-scale jet.

4.3 Very Long Baseline Interferometry

The angular resolution ϑ of an astronomical instrument is given as:

$$\vartheta \sim \frac{\lambda}{D}, \tag{4.1}$$

where λ is the observing wavelength and D is the diameter of the telescope. It is clear from equation 4.1, that radio astronomy working at wavelength four to six orders of magnitude longer than optical astronomy would require enormous telescopes to achieve the same resolution. However, using interferometer, radio astronomy can overcome this wavelength handicap and can reach better angular resolution than any other (Earth-based) instrument.

The simplest interferometer consists of two antennas (Figure 4.3), which observe the same, distant radio source at the same frequency band. The received signals are coherently combined (correlated). The interferometer works as if it were a single antenna with an aperture diameter equal to the distance between the two elements.

In VLBI, the elements of the interferometer are not connected directly. The data are recorded on disks (or tapes) at the observing stations, then shipped to the correlator, where the data are played back and correlated. However, this will change in the future with the

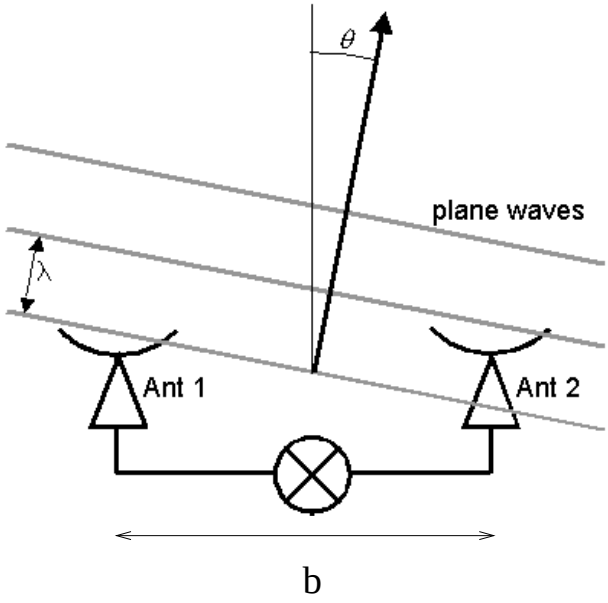

Figure 4.3: Schematic diagram of a connected two-element interferometer

completion of the e-VLBI project (see Whitney 2005, and references therein), which will provide high bandwidth connections between the telescopes.[2]

Frequently used VLBI arrays are, for example, the European VLBI Network (EVN), the Very Long Baseline Array (VLBA) in the US, the Japanese VLBI Exploration of Radio Astronomy (VERA) and the Global mm VLBI Array (GMVA).

The advantage of such "un-connected" interferometer is that the length of the longest baseline is only limited by the size of the Earth itself. (The resolution can be increased by making use of a space antenna, see Sect. 5.1 details). Thus the resolution achievable with VLBI is in the order of 50 μas. The drawback of such long baselines is the difficult phase stabilization. One of the main reasons of loss of phase information in VLBI is the independent Local Oscillators at the stations. Since their relative phase is unknown, the absolute position information is lost. Moreover, at every antenna site, the atmospheric conditions can be different, moreover every antenna sees through different amounts of the atmosphere. Additionally, unlike the connected, shorter baseline arrays (such as the VLA for example), the Earth rotation and the geophysical effects have significant influences as well. The wavefront from the source arrives at the antennas at different times (delay) and – because they move with different speeds – the signal is Doppler shifted (fringe rate). To estimate and remove these effects, a geometrical model is introduced in the correlator. An overview of the most important terms of this model is given in Table 22-1 in Walker (1999).

After correlation, the data are sent to the PI, and the calibration and the log files are made available. Then a post-processing software package – usually the AIPS (Astronom-

[2]The first trans-Atlantic eVLBI image was produced on 10th September in 2004 using four telescopes: Cambridge (UK), Toruń (Poland) Westerbork (Netherlands), Arecibo (Puerto Rico) (Momjian et al. 2004).

ical Image Processing System) – is used to reduce the dataset. This process can be divided into three main stages:

- Applying the calibration and editing information provided with the data. This involves the calibration of the data amplitude using the gain curve and system temperature information, correcting for atmospheric absorption (at higher frequencies), and correcting for the effect of parallactic angle. Corresponding AIPS tasks are for example: , , , , .
- Improving calibration with using the data itself and further editing. This involves fringe fitting, a priori amplitude calibration, bandpass calibration, etc. Corresponding AIPS tasks are for example: , , , .
- Self-calibration and imaging (hybrid mapping). Corresponding AIPS tasks are for example: , .

4.3.1 VLBI observations and scattering effects

The visibility function of a point source seen through a turbulent medium, sampled by a radio interferometer can be written as:

$$V(|\boldsymbol{r}|) = S\, e^{-1/2 D_\phi(|\boldsymbol{r}|)}, \tag{4.2}$$

where S is the integrated flux density of the source, $D_\phi(|\boldsymbol{r}|)$ is the phase structure function, and $|\boldsymbol{r}|$ is the interferometer baseline length. The phase structure function is given as (Spangler & Cordes 1998):

$$D_\phi(|\boldsymbol{r}|) = 8\pi^2 r_e^2 f(\beta)\, \lambda^2\, |\boldsymbol{r}|^{\beta-2} \int_0^L dz\, C_N^2(z), \tag{4.3}$$

where r_e the classical electron radius, $f(\beta)$ is a constant of the order of unity, z is a coordinate along the line of sight from the observer to the source and β is the exponent of the power law spectrum of the turbulence. The integration is performed over the extent of the turbulent medium along the line of sight.

Models of the visibilities of a scatter-broadened source

However, this equation is valid only in the most ideal case, i.e. for a perfect point source is observed with a perfectly calibrated interferometer through an isotropic turbulent medium. To include the properties of anisotropic scattering, instead of the baseline length the so called "rotundate baseline" is introduced (Spangler & Cordes 1998): $(x^2 + \rho\, y^2)^{1/2}$, where $\rho \leq 1$ is the anisotropy parameter, and y is a coordinate in the sky-plane parallel to the major axis of the scattering disk.

In a simple approach, the components of a source are described as Gaussian brightness distributions, and the scattering and intrinsic source size are combined in quadrature to give the observed size.

A more detailed formalism is given by Desai & Fey (2001), who defined models with various complexity to account for the intrinsic source structure. In the simplest one, they consider a single scatter-broadened component. The visibility can be modelled as

$$V = S \exp\left[2\pi i\left(\delta_x r_x + \delta_y r_y\right) - \frac{1}{2}\left(\frac{\pi\theta_{\rm int} b_{\rm int}}{\lambda\sqrt{\ln 4}}\right)^2 + \frac{1}{2}\left(\frac{\pi\theta_{\rm c} b_{\rm s}}{\lambda\sqrt{\ln 4}}\right)^{\beta-2}\right], \tag{4.4}$$

where S is the correlated flux density, $\theta_{\rm int}$ is the intrinsic size of the Gaussian component, $b_{\rm int}$ and b_s are the rotundate baselines reflecting the orientation and elongation of the intrinsic source structure (given in units of $10^6\lambda$), δ_x and δ_y are the positional offsets in R.A. and declination, and θ_c is the angular size which corresponds to the "coherence scale". The "coherence scale" is where the phase structure function equals one, i.e. the visibility amplitude is reduced by $e^{-0.5}$. The last two terms in Equation 4.4 can be gathered into a single expression, and hence the visibility can be expressed as:

$$V_{\rm obs} = S \exp\left[2\pi i\left(\delta_x r_x + \delta_y r_y\right) - \frac{1}{2}\left(\frac{\pi\,\theta\, b}{\lambda\sqrt{\ln 4}}\right)^{\alpha}\right]. \tag{4.5}$$

In this equation, θ includes the intrinsic source size, therefore it can give only an upper limit on the scattering disk size. At longer wavelengths, usually the intrinsic source size is much smaller than the "coherence scale", therefore $\theta \approx \theta_c$. When $\beta = 4$ and the elongation and the orientation of the scattering disk are the same as the elongation and orientation of the intrinsic source structure, then $\theta = \sqrt{\theta_{\rm int}^2 + \theta_{\rm c}^2}$.

Another model of Desai & Fey (2001) includes two components with one common scattering disk. The observed visibilities can be expressed, similarly to the previous case, as:

$$\begin{aligned} V_{\rm obs} = &\left(S_1 \exp\left[2\pi i\left(\delta_{x1} r_x + \delta_{y1} r_y\right)\right] + S_2 \exp\left[2\pi i\left(\delta_{x2} r_x + \delta_{y2} r_y\right)\right]\right) \\ &\times \exp\left[-\frac{1}{2}\left(\frac{\pi\,\theta}{\lambda\sqrt{\ln 4}}\right)^{\alpha}\right]. \end{aligned} \tag{4.6}$$

These two models are implemented in the AIPS task written by Desai & Fey (2001). fits nonlinear models directly to the visibilities, like the DIFMAP model-fitting procedure. However, allows one to fit a wider variety of components than DIFMAP and provides error estimates for the model parameters. For the analysis of scatter-broadening properties of B 2005+403 (see Sect. 4.5.1), the "MUK" and "KOL" components types were used. "KOL" represents a single point-like component with a single scattering disk. Equation 4.5 describes this model. The fitted parameters are: the flux density of the point-like component (S), the position of the point-like component ($\delta_{\rm x}$ and $\delta_{\rm y}$), the size of the scattering disk (θ), the axial ratio of the scattering disk, the position angle of the scattering disk and α. "MUK" consists of two point-like component and a single scattering disk in the form as described by equation 4.6. The fitted parameters are: the flux densities of the two point-like components (S_1 and S_2), the position of the two point-like components (δ_{x1}, δ_{y1}, δ_{x2} and δ_{y2}), the size of the scattering disk (θ), the position angle of the scattering disk, the axial ratio of the scattering disk and α.

Variability in flux density

ISS can also give rise to flux-density variations (as discussed in Sect. 2). Since constant sky brightness is a basic assumption in creating an image with a synthesis array, flux-density changes on a time-scale shorter than the duration of the observation can cause severe problems; the image obtained is not the convolution of the average source brightness and the dirty beam. Various artifacts (side-lobes) can degrade the image quality. However, the simulations of Hummel (1987) showed that IDV during VLBI observations only reduces the achievable dynamic range without changing the source structure. Typical source variations of the order of few percent are usually larger than the uncertainties arising from system temperature measurements, which are used to calibrate the amplitudes. Therefore, the effect of IDV during an 8 to 12 hours-long VLBI observation can be neglected.

4.4 VLBI datasets of B 2005+403 and data reduction

Nineteen VLBI observations of B 2005+403 from 16 different observing epochs obtained during 1992 to 2005 were analyzed. The details of the various observations are summarized in Table 4.1.

B 2005+403 was observed as part of the Cygnus A VLBI monitoring program (Krichbaum et al. 1998; Bach et al. 2003, 2004). These observations were performed at frequencies between 1.6 GHz and 43 GHz. The data were complemented by regular VLBI observations at 15 GHz performed within the 2 cm Survey (Kellermann et al. 2004, and references therein) and by three observations of the source in the MOJAVE survey[3] (Lister & Homan 2005).

After correlation at the VLBI correlators in Socorro (NRAO) or Bonn (MPIfR), a priori amplitude calibration using system temperature measurement and fringe-fitting were performed using the standard AIPS analysis tasks. Editing, phase and amplitude self-calibration and imaging were performed using AIPS and the Caltech DIFMAP packages (Shepherd 1997). For the previously published observations (from the 2 cm Survey, the MOJAVE data and the datasets from epoch 2003.04), the self-calibration and the imaging were redone for consistency of data handling for all epochs.

Eight observations were performed with full polarization (see Table 4.1). In the polarization analysis, the feed leakage terms for the antennas (D-terms) were determined in the usual way using the AIPS task (Leppänen et al. 1995). At 15 GHz, I used the University of Michigan (UMRAO) database[4] (Aller et al. 2003) to calibrate the orientation of the electric vector position angle (EVPA). (Except for the epochs of MOJAVE data, which were already calibrated.) The total and correlated flux density (in total intensity and in polarization) matched within 10 % accuracy, therefore the existence of a large-scale polarized structure can be ruled out. The single-dish observations could be used for the EVPA calibration. At 22 GHz and 43 GHz, the EVPA could not be calibrated following the same procedure since no single-dish polarization measurements were available

[3]The MOJAVE project is supported under National Science Foundation grant 0406923-AST.

[4]The University of Michigan Radio Astronomy Observatory has been supported by the University of Michigan and the National Science Foundation.

Table 4.1: Summary of the epochs, frequencies, and arrays of the VLBI observations of B 2005+403. In Col. 4, the polarization mode of the observation is indicated. In Col. 5, references of previously published data are given.

Epoch	Frequency	Instrument	Pol.	Reference
1992.44*	22 GHz	EVN (8 stations)	LL	Gabányi et al. (2006)
1994.17*	22 GHz	VLBA (8 stations) + VLA + EVN (4 stations)	LL	Gabányi et al. (2006)
1995.27	15 GHz	VLBA (2 cm Survey)	RR	Kellermann et al. (2004)
1995.96	15 GHz	VLBA (2 cm Survey)	LL	Kellermann et al. (2004)
1996.73*	43 GHz	VLBA+EB	full	Gabányi et al. (2006)
1996.73*	22 GHz	VLBA+EB	full	Gabányi et al. (2006)
1996.73*	15 GHz	VLBA+EB	full	Gabányi et al. (2006)
1996.82*	5 GHz	EVN (8 stations)	LL	Gabányi et al. (2006)
1996.83*	8 GHz	EVN (8 stations)	RR	Gabányi et al. (2006)
1997.19*	15 GHz	VLBA (2 cm Survey)	LL	Gabányi et al. (2006)
1998.14*	1.6 GHz	EVN (9 stations)	LL	Gabányi et al. (2006)
1999.01	15 GHz	VLBA (2 cm Survey)	LL	Kellermann et al. (2004)
2001.17	15 GHz	VLBA (2 cm Survey)	LL	Kellermann et al. (2004)
2001.98	15 GHz	VLBA (2 cm Survey)	LL	Kovalev et al. (2005)
2003.04	22 GHz	VLBA	full	Bach (2004)
2003.04	15 GHz	VLBA	full	Bach (2004)
2003.16	15 GHz	VLBA (MOJAVE)	full	Lister & Homan (2005); Kovalev et al. (2005)
2004.61	15 GHz	VLBA (MOJAVE)	full	Kovalev et al. (2005)
2005.36	15 GHz	VLBA (MOJAVE)	full	Kovalev et al. (2005)

*A priori calibration and fringe-fitting was done by T. Krichbaum.

at these frequencies of the source. The other sources (Cygnus A and calibrator source), observed together with B 2005+403, did not show polarization. The RM measurements of Zavala & Taylor (2003) and Clegg et al. (1992) were used to calibrate the EVPA at these frequencies. Using these RM values, we interpolated the EVPA from the known frequency (15 GHz) to the unknown frequencies (22 GHz and 43 GHz). We assumed that the RM calculated between 8 GHz and 15 GHz by Zavala & Taylor (2003) and between 1.4 GHz and 1.7 GHz by Clegg et al. (1992) can be used at 22 GHz and 43 GHz.

The results of the VLBI imaging are presented in Fig. 4.4, Fig. 4.12, and Fig. 4.11. The CLEAN maps obtained at 1.6 GHz, 5 GHz, and 8 GHz are shown in Fig. 4.4. The CLEAN maps obtained at 15 GHz are displayed in Fig. 4.11. The CLEAN maps obtained at 22 GHz and 43 GHz are shown in Fig. 4.12. Figure 4.11 and Fig. 4.12 show images with the electric vectors superimposed in epochs. The details of the resulting images are listed in Table 4.2. The images will be discussed in detail in Sect. 4.5.3.

To measure the structural changes, the VLBI images were parameterized using Gaussian components. Gaussian components were fitted to the calibrated visibility data using the DIFMAP program. The resulting model-fit parameters are listed in table B.1, in Ap-

Table 4.2: The parameters of the images in Figures 4.4, 4.12 and 4.11. In Col. 3 the integration time in hours is listed. Col. 4 gives the image peak flux density, Col. 5 the beam size, Col. 6 the beam position angle and Col. 7 the residual noise of the images.

Epoch	Frequency [GHz]	Int. [h]	$S_{\rm peak}$ [Jy/beam]	Beam size and P.A. [mas×mas]	[°]	Residual noise [mJy/beam]
1992.44	22	1.6	0.584	0.52×0.19	−22.3	2.0
1994.17	22	1.4	0.448	0.46×0.19	−17.8	1.6
1995.27	15	7.1	1.020	0.90×0.51	−11.6	1.5
1995.96	15	7.1	1.078	0.90×0.55	11.4	0.7
1996.73	43	1.0	0.368	0.58×0.47	18.5	1.8
1996.73	22	1.1	0.316	0.50×0.20	−18.0	1.5
1996.73	15	0.8	0.523	0.58×0.37	−16.7	1.7
1996.82	5	0.8	1.550	4.16×2.87	−76.9	2.2
1996.83	8	1.7	1.080	1.36×0.88	25.9	3.3
1997.19	15	7.1	0.749	0.97×0.64	−10.8	2.0
1998.14	1.6	0.8	0.464	13.1×13.0	49.8	4.8
1999.01	15	0.7	0.372	0.81×0.52	−2.4	0.6
2001.17	15	7.1	1.360	0.87×0.46	−7.6	2.3
2001.98	15	7.1	1.300	0.98×0.54	−5.7	2.0
2003.04	22	11.5	1.200	0.57×0.40	7.1	1.4
2003.04	15	11.5	1.430	0.86×0.58	2.0	1.1
2003.16	15	3.9	1.560	0.77×0.52	1.2	0.8
2004.61	15	4.6	0.985	0.73×0.49	4.1	0.7
2005.36	15	1.9	0.701	0.74×0.46	−15.4	0.6

pendix B. The measurement errors listed in the table were estimated from the internal scatter obtained during the process of imaging and model-fitting and is described in more detail e.g. in Krichbaum et al. (1998). During the process of model fitting, the number of independent variables was reduced by fitting only circular Gaussian components. For those cases where circular Gaussian model fits did not give satisfactory results and produced unacceptably large reduced χ^2 values, elliptical Gaussian components were fitted. Most of the 22 GHz and 43 GHz data were fitted best with elliptical Gaussians. In Figure B.1, B.3, and B.2 (in Appendix B) the VLBI images resulting from the Gaussian model fitting are shown. The circles seen in this figure denote for the positions and sizes of the individual model fit components. The contour lines result from the convolution of the model-fit components with the observing beam and the addition of the underlying (noise limited) residuals.

To study the scattering effects following Fey et al. (1989), I measured the total angular source size as a function of observing frequency by fitting the visibility data of B 2005+403 at all frequencies with *one* Gaussian component within DIFMAP. The result of these size measurements are listed in Table 4.3.

To investigate more thoroughly the scattering effects I also explored the range of model types and the fitting procedure used by (see Sect. 4.3.1). For the starting model values, the results of the multiple-component DIFMAP model-fitting were

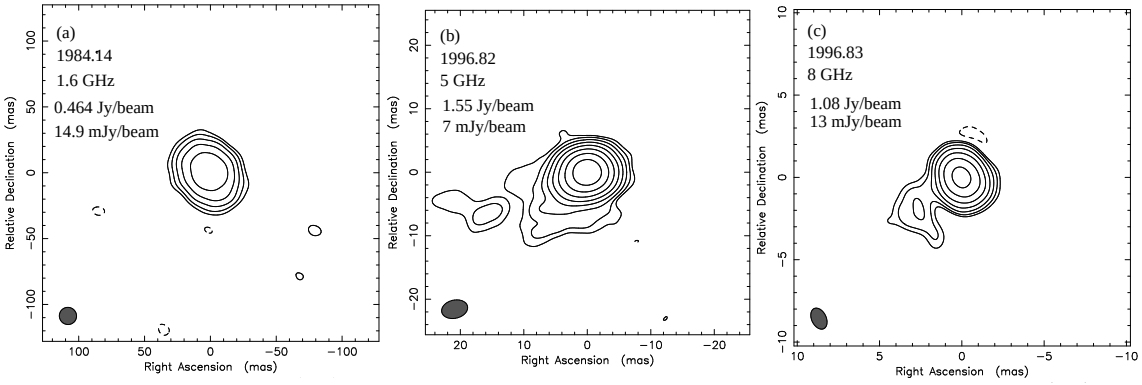

Figure 4.4: EVN CLEAN maps of B 2005+403 at 1.6 GHz, 5 GHz, and 8 GHz at different observing epochs. Epoch, frequency, peak flux density and the lowest (positive) contour are given in the upper left corner of each image. Contours are in percent of the peak flux and increase by factors of two. The beam size is shown in the bottom left corner of each image. (Images were created in DIFMAP.)

used (see Table B.1). At both 5 GHz and 8 GHz, the two-component model plus a scattering disk provided the best fits. At 1.6 GHz, the simpler one-component model plus a scattering disk representation was able to describe the source structure, however the two-component model gave more stable fits and smaller error bars. This contradicts the model-fit results obtained with DIFMAP at 1.6 GHz. At 1.6 GHz in DIFMAP, there was no indication of second component. Nevertheless, the parameters (position and flux density) of this additional feature fitted with at 1.6 GHz are consistent with the parameters of one of the component (denoted as M3 in Table B.1 in Appendix B) fitted with DIFMAP to the 5 GHz dataset. The resulting parameters from the model-fits are given in Table B.2 in Appendix B and discussed in the following section (Sect. 4.5.1).

4.5 Results and discussion

In this section I discuss the results of the VLBI observations together with single-dish flux-density measurements from the literature.

First, I focus on the propagation effects seen in the observable properties in B 2005+403 and what can be learned from these about the properties of the ISM.

Second, I present the VLBI study of B 2005+403 at high frequencies in combination with single-dish flux-density measurements.

4.5.1 Propagation effect I: Scatter broadening of B2005+403

In Figure 4.4, the 1.6 GHz image illustrates the effect of scatter broadening: the measured source size (36 mas) is three times larger than the size of the observing beam (13 mas).

I constrained the inner scale of the fluctuations, the spectral index of the power spectrum and the scattering measure which are the most important scattering parameter values.

I combined those with the measurements of Hα surveys in order to learn more about the characteristics of the scattering plasma. Moreover, having high frequency VLBI observations made it possible to complete the previous results in a way that source intrinsic influences on the scattering could be studied as well.

Scattering in the ISM is also closely connected to flux-density variability. The expected time-scale of the variability in B 2005+403 is tens to hundred days, however mild variations on a time-scale of less than a day were observed with the 100-meter Effelsberg radio telescope. I describe a possible multiple scattering scenario as well.

Scattering parameters: α, β, and the inner scale

The angular source size of B 2005+403 versus frequency is plotted in Fig. 4.5, using our data and including previous measurements from the literature. The corresponding values are given in Table 4.3. To quantify the scatter broadening, which dominates at lower frequencies, a power law was fitted to the size-frequency relation in the frequency range from 0.67 GHz to 8 GHz, yielding

$$\theta = (77.1 \pm 4.0) \cdot (\nu/1\,\mathrm{GHz})^{-(1.91\pm0.05)}\,\mathrm{mas} \tag{4.7}$$

This fit is shown as the black line in Figure 4.5. Excluding the data point at 8 GHz does not change the slope significantly, yielding: $\theta = (77.7 \pm 4.0) \cdot (\nu/1\,\mathrm{GHz})^{-1.92\pm0.06}$. The slope of the power-law (the so called size spectral index, γ) differs significantly from the slope of -2.2, one would expect for Kolmogorov type density fluctuations in the ISM. For wavelengths where the diffractive scale is smaller than the inner scale of the turbulence, the size spectral index is given as $\gamma = -(1 + 2/\alpha)$ (Trotter et al. 1998). Thus the size spectral index obtained from the power-law fit to the angular sizes ($\gamma = -1.91 \pm 0.05$) implies $\alpha = 2.2 \pm 0.1$[5].

The best-fit model parameters given by are listed in Table B.2 in Appendix B. The α values acquired from the fitting task are close to two at all frequencies. This also indicates a deflection from the Kolmogorov value, however the difference between the Kolmogorov value and the obtained α is not as big as in the previous case. This may be caused by the different approaches in model-fitting. In DIFMAP, only one fitted Gaussian component was used to describe the observed structure and then a power-law fit to the size of these fitted components yielded the value for α. In , the intrinsic source structure modelled as two point-like components. Such point-like components are not physical, in reality the characteristics of the fitted scattering disk in still influenced by the intrinsic structure of the source. However, this influence from the intrinsic structure can be still lower, than the one introduced by the DIFMAP approach.

Nevertheless, these results show that α is not equal to the Kolmogorov value. According to Trotter et al. (1998), this implies either that the power law distributions of the fluctuations have an exponent of $\beta = 4$, or that the inner scale of the fluctuations is greater than the scales sampled by the interferometer baselines. The latter case would mean that the inner scale is most likely greater than the longest baseline in the observation. The longest baseline of the EVN observation performed at 1.6 GHz was 8100 km. This lower

[5]For a Kolmogorov turbulence one expects $\alpha = 5/3$.

Table 4.3: The measured angular sizes of B 2005+403 at different frequencies. Col. 1 shows the observing frequency, Col.2 the observing epoch, Col. 3 the major axis size of the fitted Gaussian component. In Col. 4 references for previously published data are given.

ν [GHz]	Epoch	θ [mas]	Reference
0.6	Oct 1986	225.0 ± 58.0	Fey et al. (1989)
1.6	1998.14	29.8 ± 0.5	Gabányi et al. (2006)
1.7	Mar 1986	26.4 ± 4.7	Fey et al. (1989)
1.7	Jan 1997	31.0 ± 0.8	Desai & Fey (2001)
2.3	Jan 1997	17.6 ± 0.5	Desai & Fey (2001)
5	Oct 1985	3.5 ± 0.4	Fey et al. (1989)
5	1996.82	3.5 ± 0.1	Gabányi et al. (2006)
5	Jan 1997	3.4 ± 0.1	Desai & Fey (2001)
8	1996.83	1.6 ± 0.1	Gabányi et al. (2006)
15	1996.73	0.8 ± 0.1	Gabányi et al. (2006)
22	1996.73	0.6 ± 0.1	Gabányi et al. (2006)
43	1996.73	0.5 ± 0.1	Gabányi et al. (2006)

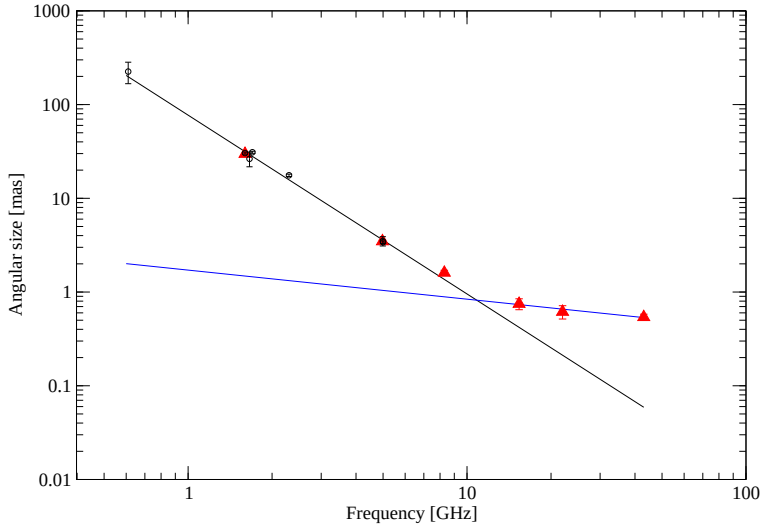

Figure 4.5: The measured angular size plotted versus observing frequency. The black line represents a power law fit to the data in the range from 0.6 GHz to 8 GHz. The slope of the line is -1.91 ± 0.05. The blue line represents a power law fitted to the data in the range from 15 GHz to 43 GHz. The slope of the line is -0.31 ± 0.07. Black circles denote data from the literature (Fey et al. 1989; Desai & Fey 2001), red triangles denote our data.

limit on the inner scale of this value is larger than the values of 5000 km reported earlier for the Cygnus region by Fey et al. (1989) and Wilkinson et al. (1994).

A frequency dependence of the axial ratios and position angles of the fitted Gaussian components were observed in some other scatter-broadened extragalactic radio sources (NGC 6334B by Trotter et al. 1998 and B 1849+005 by Lazio 2004). This is interpreted as anisotropy in the scattering. Moreover, scattering observations of Galactic sources in

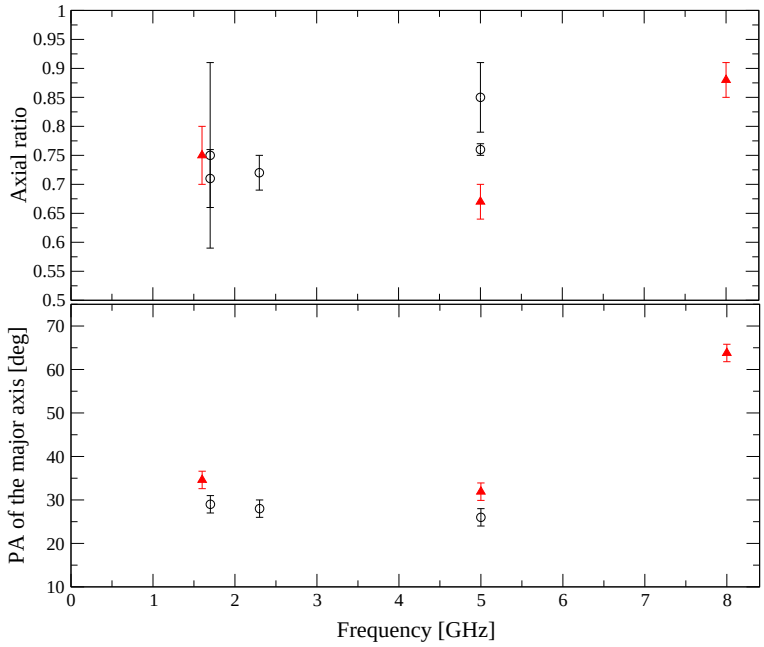

Figure 4.6: The axial ratios and position angles of the fitted Gaussian components of B 2005+403 plotted versus frequency in the range from 0.6 GHz to 8 GHz. Black circles denote data from the literature (Fey et al. 1989; Desai & Fey 2001), red triangles denote our data.

the Cygnus region (most notably that of Cygnus X-3 by Wilkinson et al. 1994 and Molnar et al. 1995) reveal anisotropic scattering in the very region through which B 2005+403 can be seen. A possible elongation is also seen in B 2005+403. For example at 1.6 GHz (Fig. 4.4) the source is elongated in the position angle of $\sim 37°$ whilst the restoring beam is almost a perfect circle. Fey et al. (1989) also saw evidence for an elliptical scattering disk, but were unable to perform an unambiguous measurement. The axial ratios and position angles reported in the literature and derived from these observations are presented in Figure 4.6. The observations agree on an axial ratio that is not unity and (except for one) on a position angle of 30°. No clear trend can be recognized with different frequency. The most outlying point is at 8 GHz dataset, at which frequency the intrinsic structure of the source is becoming visible.

The influence of the intrinsic structure

Above 8 GHz, the extrapolated scattering size becomes smaller than the measured source size. This indicates that towards higher frequencies scattering effects are less dominant and that the intrinsic structure of the sources shines through. The differences between the extrapolated scattering size and the measured source size at all three frequencies (15 GHz, 22 GHz, and 43 GHz) are of the order of 0.4 mas. To characterize the frequency dependence of the intrinsic source size, a power law was fitted to the size-frequency relation above 8 GHz, yielding

$$\theta_{\mathrm{int}} = (1.7 \pm 0.4) \cdot (\nu/1\,\mathrm{GHz})^{-(0.31\pm0.07)}\,\mathrm{mas}. \tag{4.8}$$

The blue line in Fig. 4.5 shows this fit. With this line, it was possible to obtain an upper limit on the intrinsic source size at lower frequencies where direct size measurements with VLBI are not possible. Hence lower limit on the brightness temperature could also be calculated. At 1.6 GHz, 5 GHz, and 8 GHz the intrinsic source sizes are $\theta_{\rm int} \leq (1.5 \pm 0.6)$ mas, $\theta_{\rm int} \leq (1.0 \pm 0.3)$ mas, and $\theta_{\rm int} \leq (0.9 \pm 0.2)$ mas, respectively. The corresponding lower limits to the brightness temperatures are $T_{\rm B} \geq (0.6 \pm 0.5) \cdot 10^{12}$ K, $T_{\rm B} \geq (0.14 \pm 0.09) \cdot 10^{12}$ K, and $T_{\rm B} \geq (0.08 \pm 0.04) \cdot 10^{12}$ K. These numbers are in accordance with typical brightness temperatures measured with VLBI (e.g. Kovalev et al. 2005) and neither strongly violate the inverse-Compton limit nor do they indicate excessive Doppler-boosting.

Scattering measure

The size of the scattering disk at a given frequency can be estimated via the deconvolution formula: $\theta_{\rm scat} = \sqrt{\theta^2_{\rm obs} - \theta^2_{\rm int}}$. From the power law fit (Equation 4.7), the scattering size at 1 GHz $\theta_{1\,\rm GHz}$ is (77.1 ± 4.0) mas. Following Taylor & Cordes (1993) and assuming a Kolmogorov turbulence, the scattering measure is

$$\mathrm{SM} = \left(\frac{\theta_{\rm scat}}{128\,\mathrm{mas}} \right)^{5/3} \cdot \nu^{11/3}_{\rm GHz}. \tag{4.9}$$

The derived SM of $(0.43 \pm 0.04)\mathrm{m}^{-20/3}$ kpc is in good agreement and consistent with the previous measurement of Fey et al. (1989), though with much improved accuracy.

In the NE2001 model Cordes & Lazio (2002), modelled the clump material responsible for the scatter broadening of B 2005+403 with an electron number density, $n_{\rm e}$, of $1\,\mathrm{cm}^{-3}$ and fluctuation parameter, F of 20. The fluctuation parameter is defined as:

$$F = \epsilon^2 l_0^{-2/3}, \tag{4.10}$$

where ϵ^2 is the fractional variation of the electron density in the clump and l_0 is the outer scale in units of AU. According to the model, the SM of the clump is given as:

$$\mathrm{SM} = C_{\rm SM} F n_{\rm e}^2 d, \tag{4.11}$$

where d is the thickness of the medium in kpc, and $C_{\rm SM} = 10.2[3\,(2\pi)^{1/3}]^{-1}\mathrm{m}^{-20/3}\,\mathrm{cm}^6$. With these equations, using the parameters of NE2001 and our SM value, the thickness of the medium, d, is found to be 12 pc. Since the SM is given as $\mathrm{SM} = \overline{C_N^2} d$, the line of sight average of the coefficient of electron density fluctuations power law is $\overline{C_N^2} = 35.8\,\mathrm{m}^{-20/3}$.

According to Haffner et al. (2003), the Hα intensity in [Rayleigh] is related to the SM through l_0 and ϵ:

$$I_{\mathrm{H}\alpha} = 0.198 \cdot T^{-0.9} \epsilon^{-2} (1 + \epsilon^2) l_0^{-2/3}, \tag{4.12}$$

where T is the temperature. Spangler & Reynolds (1990) report an EM of $294\,\mathrm{cm}^{-6}$ pc, while the more recent and higher-resolution all-sky Hα survey, the VTSS, gives the much lower EM for the line of sight to B 2005+403 of $147.8\,\mathrm{cm}^{-6}$ pc. Thus, using equations 4.10, 4.11, 4.12 and the measured SM and EM values, F, ϵ^2 and l_0 can be calculated. By fixing $n_{\rm e}$ or d, the other parameters can be obtained. The results are listed in Table 4.4 assuming $T = 8000$ K. The values obtained for F are significantly different from those of the NE2001 model. This can be caused by the inaccuracy of the model; the parameters for

Table 4.4: The ISM parameters derived from the EM measurements of Spangler & Reynolds (1990) (in Col. 1) and from the VTSS (in Col.2) assuming $T = 8000$ K. Following Spangler & Reynolds (1990) it is assumed that the main contribution to the EM is caused by the same clump of material that causes the angular broadening of B 2005+403.

EM	294 cm^{-6} pc	147.8 cm^{-6} pc
F	0.794	1.579
l_0	25.5 AU	158.3 AU
ϵ^2	6.9	46.21
If $d = 12$ pc, then n_e	5 cm^{-3}	3.5 cm^{-3}
If $n_e = 1$, then d	294 pc	148 pc

the line of sight to B 2005+403 were derived from only one measurement of one source. (For example, had a pulsar been observed close to this line of sight, at the appropriate distance, its DM value would provide additional constraints on the clump material. See e.g. the case of B1849+005 Lazio 2004.) Another reason for the discrepant F values could be that the assumption that the EM is due mostly to the same material that causes the angular broadening, was wrong.

Throughout these calculations, Kolmogorov turbulence was assumed[6]. However, along the line of sight to B 2005+403, a flatter wavenumber spectrum was found. Romani et al. (1986) tabulate numerical estimates of scintillation parameters for different power-law spectra of electron density fluctuations. I used the equation from Table 1 of Romani et al. (1986) with a power law index of -2, since this index describes most adequately the angular broadening observation presented here. From this, $C_N^2 d = 15.16\,\mathrm{m}^{-20/3}$ kpc was obtained. With a thickness of the screen of 12 pc the calculated C_N^2 was $1263\,\mathrm{m}^{-20/3}$. However, this is not an entirely consistent approach, as d was obtained assuming a Kolmogorov spectrum.

Flux-density variability caused by the scattering material in the Cygnus region

The screen responsible for the angular broadening of B 2005+403 can also cause variations in the observed flux density of B 2005+403 on time-scales of tens to hundreds of days at low GHz frequencies (up to 8 GHz). The scintillation time-scale in days is given by Rickett et al. (2005) as

$$t = 18 \cdot \theta_{\mathrm{scat}} \cdot L \cdot \left(\frac{v}{50\,\mathrm{km\,s^{-1}}} \right)^{-1}, \tag{4.13}$$

where L is the distance to the scattering screen in kpc, v is the transverse velocity of the medium relative to the Earth in km s^{-1} and θ_{scat} is in units of mas.

Rickett et al. (2005) analyzed the data from the Green Bank Interferometer flux density monitoring program to search for flux-density variations on time-scales of 2 days to 50 days. They reported on variations in B 2005+403 at 8 GHz with a time-scale of $\sim$ 12 days

[6]Even the definition of SM is only meaningful in the case of a Kolmogorov turbulence.

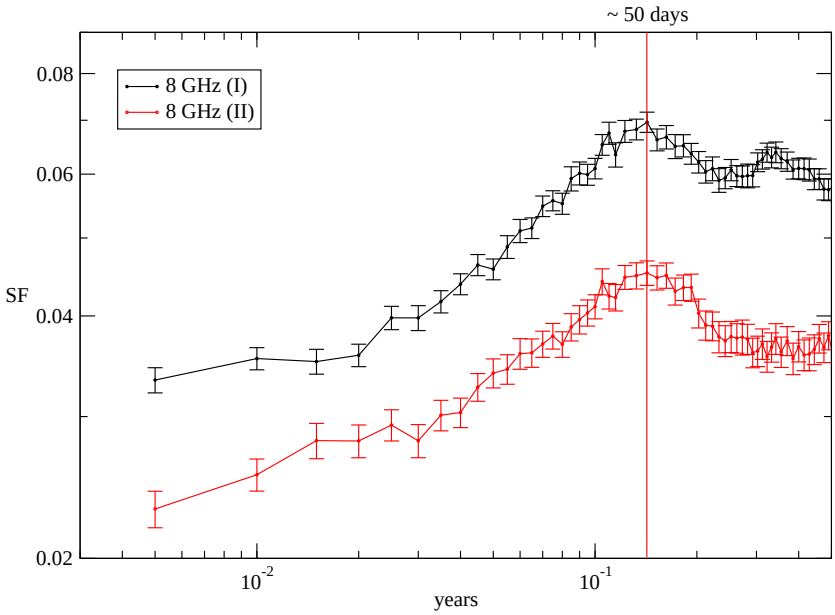

Figure 4.7: The structure function of B 2005+403 derived from the Green Bank Interferometer monitoring data. The 12 year-long observation contained a gap of approximately two years. Therefore two continuous time series were analyzed independently and the SFs were determined for both time series (labelled I and II). The black points and line represent the SF of the data between 1983 and 1988 (I), the red line and points represent the SF of the data between 1991 and 1996 (II). The vertical red line marks the time-scale of 52 days found from the SFs.

(see Sect. 4.2). If these variation are caused by the same screen at a distance of ~ 2.4 kpc as is responsible for angular broadening and adopting $\theta_{\rm scat} = 1.15$ mas from the 8 GHz angular broadening measurements, then the transverse velocity is ≈ 200 km/s, which is higher than the velocities usually inferred from ISS caused flux density variations, but still smaller than the Galactic rotation velocity of 220 km/s.

Rickett et al. (2005) smoothed the time series of B 2005+403 to separate the long-term intrinsic variations from the rapid changes. We reanalyzed the GBI 8 GHz dataset[7], and explored other smoothing functions using shorter time lengths than those used by Rickett et al. (2005). The structure function analysis resulting of the smoothed light curve indicated variability with a time-scale of 52 days (see Fig. 4.7). This time-scale implies a transverse velocity between the Earth and the scattering medium of 47 km/s, which is in agreement with velocities obtained from similar ISS induced variability time-scales. Note however, that Rickett et al. (2005) mention systematic errors in the observations that mimicked a one-year-long time-scale variation in the 2 GHz light curve. Therefore, we cannot be sure of the validity of the time-scale estimations.

4.5.2 Propagation effect II: IDV behaviour of B 2005+403

In November and December 2003 the flux-density variability of B 2005+403 was monitored with the Effelsberg 100 metre radio telescope with high time resolution. In Fig. 4.8

[7]The GBI data are publicly available at the web-site `http://ese.nrl.navy.mil/GBI/GBI.html`

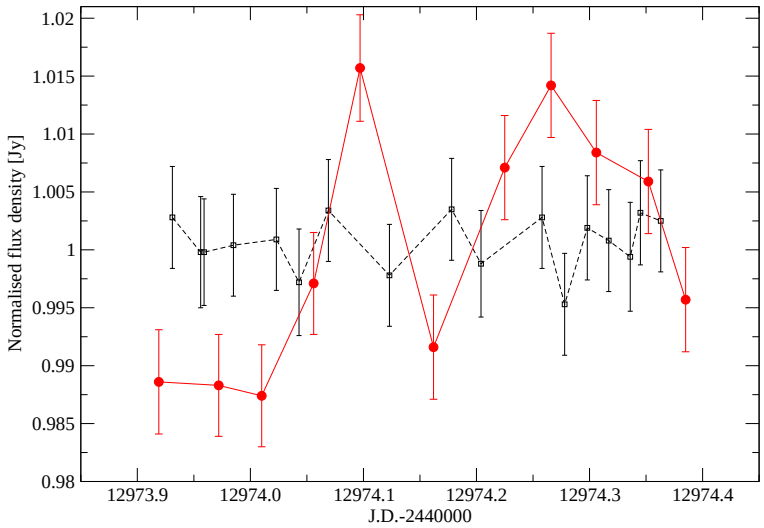

Figure 4.8: The light curve of B 2005+403 at 1.6 GHz in November 2003, observed with the Effelsberg 100 metre radio telescope. Filled red circles connected by a red line denote B 2005+403, open squares connected by a dashed line denote the calibrators NGC 7027 and B 2021+614. The modulation indices of the secondary calibrators are a measure of the calibration uncertainty, which is $m_0 \leq 0.25$ %. The modulation index of B 2005+403 is $m = 1.01$ %.

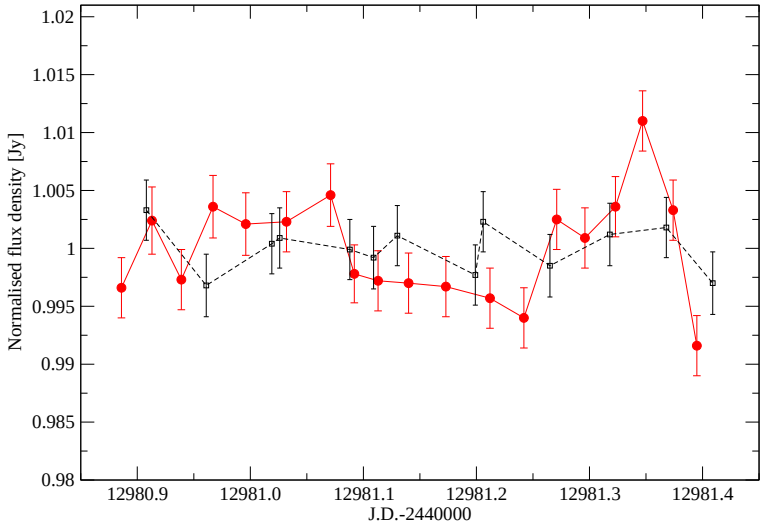

Figure 4.9: The light curve of B 2005+403 at 5 GHz in December 2003, observed with the Effelsberg 100 metre radio telescope. Filled red circles connected by a red line denote B 2005+403, open squares connected by a dashed line denote the calibrator NGC 7027. The modulation index of the calibrator is $m_0 = 0.20$ %, the modulation index of B 2005+403 is $m = 0.45$ %.

and Fig. 4.9 the variability curves are plotted at 1.6 GHz and 5 GHz, respectively.

In Table 4.5, the results from these measurements are summarized. To characterize the variability amplitudes and their significance, the methods described in Sect. 3.3 have been followed. From Table 4.5 and Figures 4.8 and 4.9 one can see that the variability amplitude of B 2005+403 decreases with frequency. Formally, the measured modulation

Table 4.5: The variability parameters of B 2005+403 and the secondary calibrators at 1.6 GHz (top) and 5 GHz (bottom). Col. 2 shows the mean flux density in Jy, col. 3 its standard deviation, col. 4 the modulation index, col. 5 the noise-bias corrected variability amplitude and col. 6 the reduced χ^2_r.

Source name	$\langle S \rangle$ [Jy]	σ [Jy]	m [%]	Y [%]	χ^2_r
$\nu = 1.6$ GHz, $m_0 = 0.25$ %					
B 2005+403	2.430	0.024	1.01	2.93	5.593
NGC 7027	1.906	0.004	0.19	0	0.197
B 2021+614	2.193	0.006	0.25	0	0.365
$\nu = 5$ GHz, $m_0 = 0.20$ %					
B 2005+403	2.905	0.013	0.45	1.18	3.107
NGC 7027	5.489	0.011	0.20	0	0.621

indices are $m = 1.01$ % at 1.6 GHz and $m = 0.45$ % at 5 GHz. At 5 GHz, the detection of IDV is only marginal. The model of refractive interstellar scintillation in the weak regime predicts a decrease of the modulation index with increasing frequency (e.g. Rickett 1990). This is consistent with these observations.

The characteristic variability time-scales derived from the light curves in Figures 4.8 and 4.9 range between 0.09 days and 0.13 days at 1.6 GHz and 0.05 days and 0.12 days at 5 GHz. Adopting a source-intrinsic interpretation for the variability, the light travel-time argument can be applied to derive, via the source size, an apparent brightness temperature (see Sect. 1.3.1). Using equations 1.4, 1.16 and 1.15, the apparent brightness temperatures are found to be in the range of (10^{17} to 10^{19}) K. This can be reduced to the inverse-Compton limit with Doppler-factors of a few hundreds. Since these values appear unreasonably high and are not consistent with the results from VLBI or with theoretical expectations (e.g. Begelman et al. 1994), one can probably rule out, that source-intrinsic effects are responsible for the observed rapid variations.

The source size and the apparent brightness temperature can be determined from the interstellar scintillation model, assuming that the main reason for the observed variability is the motion of the Earth through the scintillation pattern (as described in Sect 2.2.2). In this scenario the variability time-scale in days is given by equation 4.13.

A screen located at kpc distance, as proposed by Cordes & Lazio (2002), is not able to explain the observed short variability time-scale. With a scattering size of $\theta_{\rm scat} = 30$ mas at 1.6 GHz, a screen distance of 2.35 kpc and typical Galactic velocities of ≤ 220 km/s, one would expect to see variations on time-scales greater than 288 days.

To reproduce a variability time-scale of 0.1 day at 1.6 GHz with the above equations, the following constraints for the scattering size and the screen distance are obtained: $\theta_{\rm eff} L \leq 2.4 \cdot 10^{-2}$ mas kpc. For the measured scattering size of ~ 30 mas, this leads to an unreasonably nearby screen of ≤ 1 pc. The only way out of this dilemma is a smaller scattering size. Adopting a minimum screen distance of at least 10 pc as required for the interpretation of the ultra fast scintillators (e.g. Dennett-Thorpe & de Bruyn 2002, 2003), one obtains $\theta_{\rm scat} \leq 2.4$ mas.

An upper limit on the distance of the screen is obtained from the restriction of the source size via the inverse-Compton limit of $T_{\rm B}^{\rm IC} = 10^{12}$ K. The requirement that the

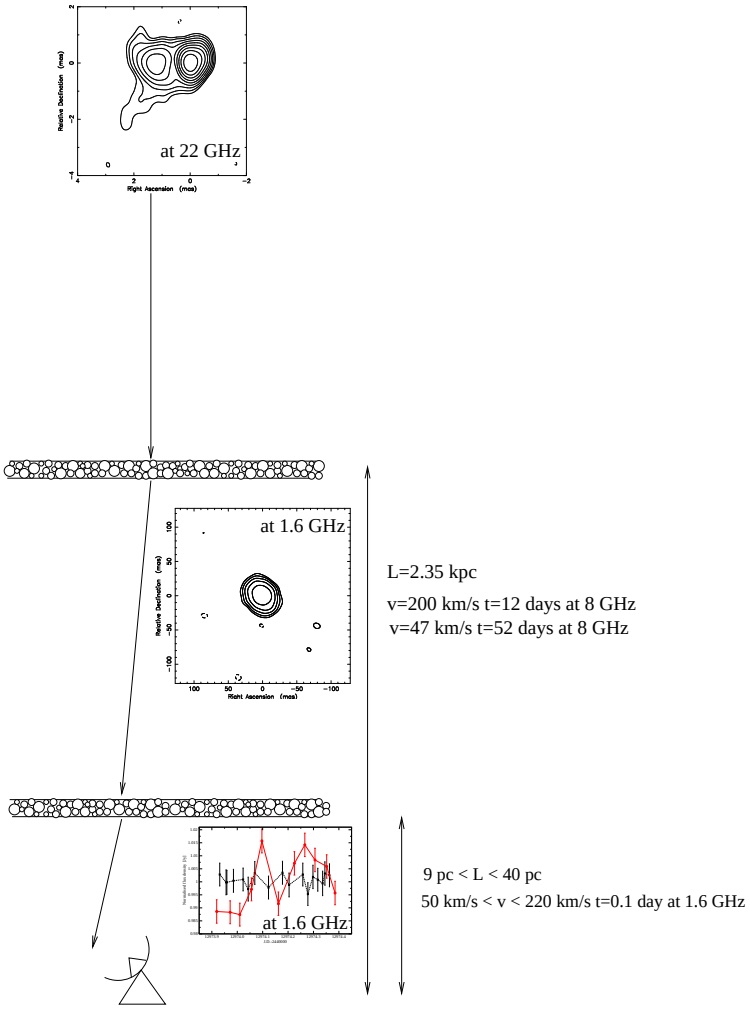

Figure 4.10: A sketch of the scattering effects that influence the image of B 2005+403 and the resulting time series of flux density observed for the source.

brightness temperature be lower than this leads to a source size of

$$\theta_{\rm int} = \sqrt{1.77 \cdot 10^{12} S_\nu \nu^{-2} T_{\rm B}^{-1} \delta^{-1} (1+z)} \geq 0.6\,{\rm mas}, \tag{4.14}$$

where $S_{1.6\,{\rm GHz}} = 2.4\,{\rm Jy}$ is adopted from Table 4.5 and $\delta \simeq 10$ for the Doppler factor and ν is in the units of GHz. Approximating $\theta_{\rm scat}$ with this size and using equation 4.13 leads to an upper limit on the screen distance of $0.185v\,{\rm pc}$ or with a relative screen velocity in the range (50 to 220) km/s, an upper limit in the range (9 to 41) pc.

Therefore, the observed IDV can be explained with a screen located at a distance less than or equal to 41 pc that can be characterized by a scattering size of $0.6\,{\rm mas} \leq \theta_{\rm scat} \leq 1.5\,{\rm mas}$. The corresponding scattering measure at 1.6 GHz then is in the range of $(1\text{ to }3)\cdot 10^{-3}\,{\rm m}^{-20/3}\,{\rm kpc}$. These values are considerably lower than the scattering measure of the more distant screen, which is thought to be responsible for the scatter broadening in B 2005+403. Therefore the observed IDV is not caused by this distant screen. Most likely, one has multiple scattering by at least two spatially and physically very different

plasma screens (see the illustration in Fig. 4.10). In this scenario the first screen leads to a significant scatter broadening of the source image, which then by the second screen leads to only very weak scattering due to large quenching effects ($\theta_{\rm source} >> \theta_{\rm scat}$). This quenched scattering (e.g. Rickett 1986) by the second screen can explain the relatively low variability amplitudes of ≤ 1 % observed in the IDV experiments at 5 GHz and 1.6 GHz. Quantitatively this can be verified using equation (20) of Goodman (1997), which relates the variability index, the scattering measure, the effective source size and the screen distance. With the parameters from above, a modulation index of $m \leq 1$ % is obtained, in good agreement with the observations.

4.5.3 The intrinsic structure of B 2005+403

To examine the source structure without scattering effects, high-frequency VLBI observations were analyzed. The VLBI images of at 15 GHz, 22 GHz and 43 GHz showed an east-west oriented core-jet structure with several embedded components (Fig. 4.11 and Fig. 4.12). The central 1 mas region is best described by three Gaussian components C1, C2, and C3. The relative alignment of these three components varied over the time spanned by the observations. In most images, the components C1, C2 and C3 are aligned along a slightly northern bent path. Beyond 1 mas core separation and oriented to the south-east, a faint and partially resolved region of diffuse emission was visible. It could be fitted by one or two Gaussian components of large extent (C4 and C5).

At lower frequencies (1.6 GHz, 5 GHz and 8 GHz), the central region of B 2005+403 (denoted M1, see in Table B.2 in Appendix B) could not be resolved in such detail. However, one or two extended features appeared in the jet direction, towards south-east (M2 and M3) which were visible in the images obtained at 5 GHz and at 8 GHz and could be model-fitted with DIFMAP. At 1.6 GHz only one component could be seen in the image, however the AIPS task was able to fit one additional feature consistent with M3 found at 5 GHz (see table B.1 and B.2 in Appendix B).

The VLBI core

In VLBI, the information about absolute position is lost. Therefore it is difficult to find a stationary reference point to which the orientation of the VLBI components is referenced. In B 2005+403, the complications arise because there are two components apparently stationary relative to each other and both of them experience dramatic flux-density variability. Fortunately, simultaneous multi-frequency (15 GHz, 22 GHz and 43 GHz) measurements helped to calculate the spectral indices of the different components. This helped to distinguish the optically thin jet components from the optically thick VLBI core.

In epoch 1996.73 the VLBI observations were performed at three frequencies simultaneously. In epoch 2003.04 the VLBI observations were performed at two frequencies simultaneously. Thus, for these two epochs, spectral indices of the components could be calculated and are given in Table 4.6. In 1996.73 and 2003.04, component C1 shows an inverted spectrum between 15 GHz and 22 GHz. Between 22 GHz and 43 GHz, the spectrum steepens. Components C2 and C3 show an optically-thin synchrotron spectrum with similar spectral indices of $\alpha \sim -0.7$ consistently measured in both observations. The spectral shape of C1 can be explained via synchrotron-self-absorption. This, in combina-

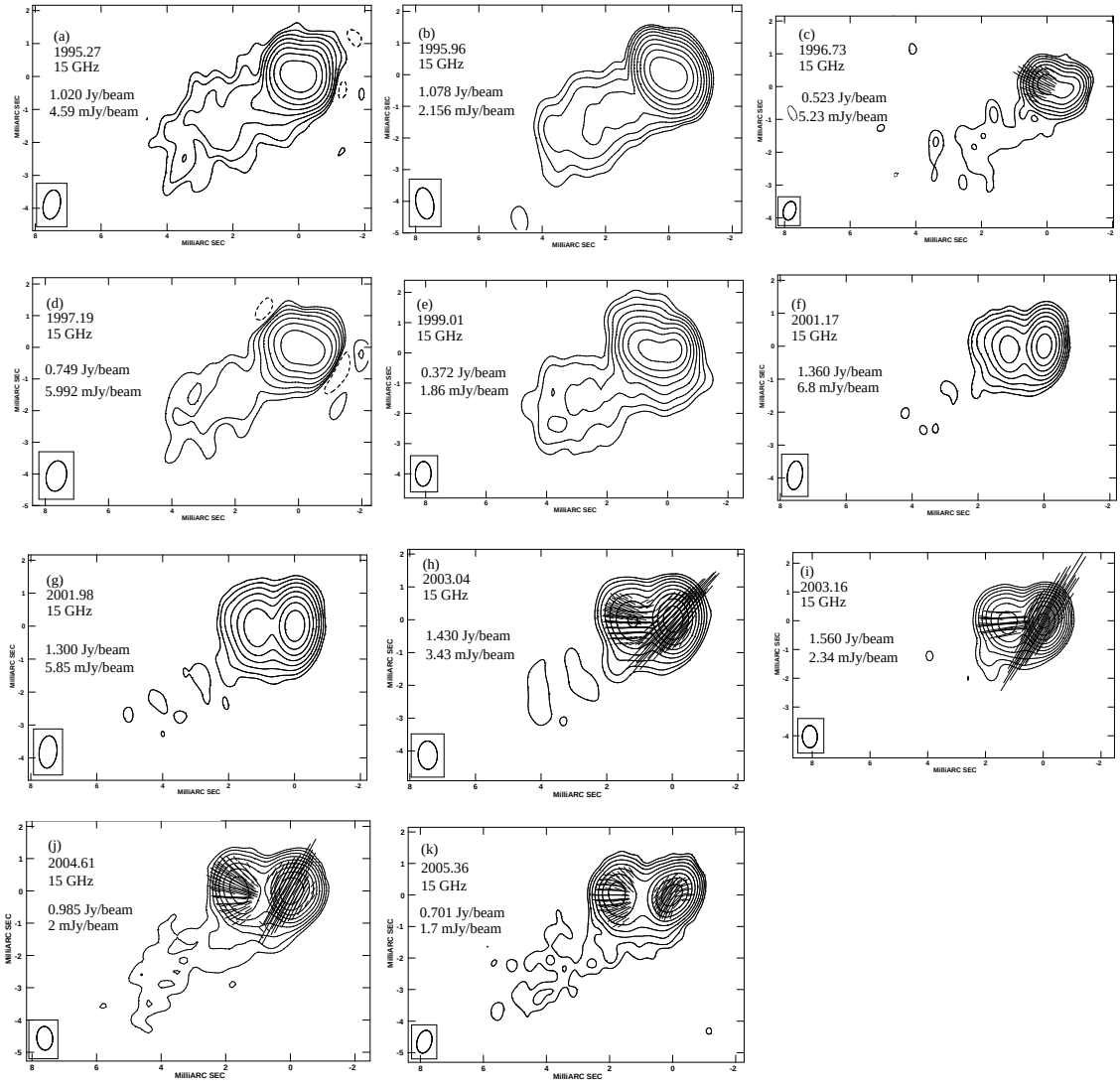

Figure 4.11: VLBI CLEAN maps of B 2005+403 at 15 GHz shown at the different observing epochs. Epoch, frequency, peak flux density and the lowest (positive) contour are given in the upper left corner of each image. Contours are in percent of the peak flux density and increase by factors of two. The beam size is shown in the bottom left corner of each image. 1 mas length of the superimposed polarization vectors corresponds to 25, 12.5, 10, 10, 10 mJy/beam in images (c) to (k), respectively. (Images were created in AIPS.)

tion with its high compactness seen in the model fits indicates that C1 should be identified with the synchrotron-self-absorbed jet base, which commonly is called the VLBI core.

Despite its optically thin spectrum, component C2 shows the most dramatic flux-density variability (see Figure 4.16). This is somewhat atypical, as pronounced flux-density variability is usually seen in jet components with much flatter spectra. The flux density increase at 15 GHz of 1.3 Jy in 2.16 yr between 1999.01 and 2001.17 leads via the light travel-time argument to an apparent brightness temperature of $2.2 \cdot 10^{12}$ K, which violates the inverse Compton limit. The calculation leads to a lower limit for the Doppler fac-

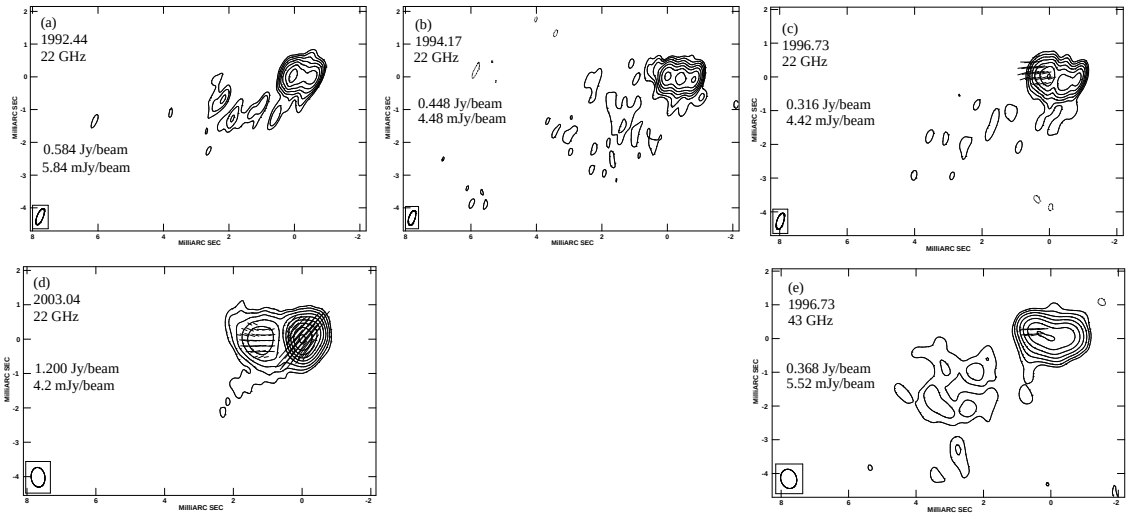

Figure 4.12: VLBI CLEAN maps of B 2005+403 at 22 GHz and 43 GHz shown at the different observing epochs. Epoch, frequency, peak flux density and the lowest (positive) contour are given in the upper left corner of each image. Contours are in percent of the peak flux density and increase by factors of two. The beam size is shown in the bottom left corner of each image. 1 mas length of the superimposed polarization vectors corresponds to 25 mJy/beam in images (c), (d), and (e). (Images were created in AIPS.)

Table 4.6: Spectral indices of the components C1, C2, and C3.

Epoch	C1	C2	C3
1996.73	$\alpha_{15}^{22} = 1.34$	$\alpha_{15}^{43} = -0.70$	$\alpha_{15}^{43} = -0.70$
	$\alpha_{22}^{43} = -0.35$		
2003.04	$\alpha_{15}^{22} = 1.46$	$\alpha_{15}^{22} = -0.65$	$\alpha_{15}^{22} = -0.67$

tor of 3.6 that would be required to reduce the observed brightness temperature to 10^{12} K. It is therefore very likely that the variability is mainly caused by differential Doppler boosting in combination with motion along a curved path. The relatively large variability and the apparent stationarity of C2 strongly indicate motion more or less directly towards the observer, i.e. an angle to the line of sight close to zero degrees. A similar interpretation to explain apparent stationarity has been made also for other sources, e.g. for 4C 39.25 (Alberdi et al. 2000).

The spectral shape of C1 indicates the existence of a spectral maximum near 22 GHz (Table 4.6). If this is identified with the synchrotron turnover of a homogeneous synchrotron self-absorbed component, the magnetic field strength can be estimated using the measured size of component C1. Following Marscher (1983), the magnetic field strength is:

$$B = 10^{-9}\delta\frac{b(\alpha)\theta^4\nu^5}{S^2(1+z)}\,\mathrm{T}$$

where δ is the Doppler factor, θ is the component size in units of mas, ν is the turnover frequency in GHz, S (in Jy) is the flux density at the turnover frequency and $b(\alpha)$ is a spectral

Table 4.7: The apparent speed and the corresponding apparent proper motion of components C2, C3, C4 and C5 measured from Fig 4.13.

Component	Apparent speed [mas yr^{-1}]	Apparent proper motion in units of c
C2	$(-0.3 \pm 3.0)\,10^{-3}$	≤ 0.02
C3	0.106 ± 0.008	8.08 ± 0.61
C4	0.14 ± 0.03	9.91 ± 2.12
C5	0.20 ± 0.02	15.25 ± 1.53

index dependent tabulated parameter (see Table 1 in Marscher 1983). Substituting the corresponding values of C1 from the epoch 1996.73 ($S = 0.434$ Jy and $\theta = 0.29$ mas) and for $b(\alpha) = 2.48$ (which was obtained from the tabulated values via logarithmic interpolation for $\alpha = -0.35$), the magnetic field obtained is: $1.8 \cdot 10^{-4}\delta$ T.

Jet kinematics

In Fig. 4.13, the relative separation of the components C2 to C5 from C1 is plotted versus time. C1 is assumed to be the VLBI core owing to its inverted spectrum, compactness and variability (Sect. 4.5.3). In the figure, straight lines result from a linear fit to the motion of each component. The slope of each line measures the angular separation rate. These rates and the corresponding apparent speeds are summarized in Table 4.7.

With the exception of component C2, which appears to be stationary within the measurement errors, the components C3 to C5 move with apparent superluminal speeds. For these three components a systematic increase to their apparent velocities – from 8.1c for component C3, to 9.9c for C4 and 15.3c for C5 – can be observed. In the 2 cm survey (Kellermann et al. 2004), B 2005+403 is characterized by a two component model only, with the secondary component moving with an apparent speed of $(12.3 \pm 3.0)\,c$. Based on its core-separation, this component may be identified with a blending of components C4 and C5 in this analysis.

The minimum Lorentz factor ($\gamma_{\rm min}$) of the jet and the corresponding viewing angle ($\psi_{\gamma_{\rm min}}$) can be estimated from the maximum observed component speed (see equation 1.10 and 1.11). Thus calculating for C5: $\gamma_{\rm min} = 15.3 \pm 1.5$ and $\psi_{\gamma_{\rm min}} = 3.8^\circ \pm 0.4^\circ$, corresponding a Doppler boosting factor of $\delta \approx 15$.

Lähteenmäki & Valtaoja (1999) calculate the Doppler boosting factor for a sample of active galactic nuclei using the total flux density monitoring data of the Metsähovi observatory. They decompose the radio light curves into exponential flares. From the variability time-scales obtained, the apparent brightness temperatures and the Doppler boosting factors were calculated. For B 2005+403, they report a variability Doppler boosting factor of 8.63, which translates to 10.9, for the cosmological parameters used in this thesis (see page 7). The derived Doppler-factor places a lower limit on the true Doppler-factor because of the light travel time argument used by Lähteenmäki & Valtaoja (1999). With the proper motions obtained from VLBI, one may calculate the viewing angle and the

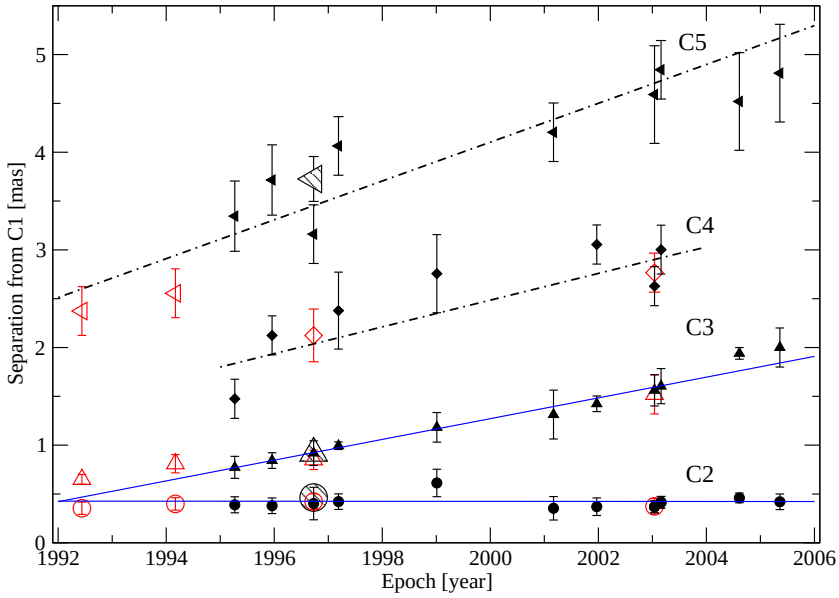

Figure 4.13: Core separation as a function of time for components: C2 (circles), C3 (triangles), C4 (diamonds), C5 (left triangles). Filling and colour of a symbol denotes the frequency of the observation: open red for 22 GHz, filled black for 15 GHz, larger and striped for 43 GHz. Solid lines indicate linear regression to reliable identifications (C2 and C3). The dashed-dotted lines show a regression performed on two tentative identifications. Component speeds are given in Table 4.7.

Lorentz factor of the jet:

$$\psi_{\mathrm{var}} = \arctan \frac{2\beta_{\mathrm{app}}}{\beta_{\mathrm{app}}^2 + \delta_{\mathrm{var}}^2 - 1}$$

$$\gamma_{\mathrm{var}} = \frac{\beta_{\mathrm{app}}^2 + \delta_{\mathrm{var}}^2 + 1}{2\delta_{\mathrm{var}}}$$

$\psi_{\mathrm{var}} \leq 5.0°$ and $\gamma_{\mathrm{var}} \geq 16.2 \pm 2.1$. These values are consistent with those determined from the jet kinematics.

The apparent acceleration observed for components C2 to C5 may result from an intrinsic acceleration of the jet, from a systematic bending of the jet, or from a combination of both effects. As $\psi_{\gamma_{\mathrm{min}}}$ and ψ_{var} are both very small, a jet bending of less than a few degrees could easily explain the observed increase of the apparent velocities. In Fig. 4.14, the apparent variations of the position angle of the radius vector for each component are shown. The plot indicates that component C2 and C3 move along similar and spatially bent trajectories with position angle changes in the range of $\sim 20°$ to $40°$. Between 1992 and 2003 the position angle difference between C2 and C3 increased, indicating similar but spatially offset paths. For components C4 and C5 the situation is less clear, as much smaller variations of the position angles are observed and the scatter in the data is larger. Therefore, one can conclude that at least the components C2 and C3 move on non-ballistic and spatially bent trajectories.

This is also illustrated in Fig. 4.15, where the trajectories of the components are displayed. (C1 is assumed to be at the origin.) The radial distance of C2 from C1 did

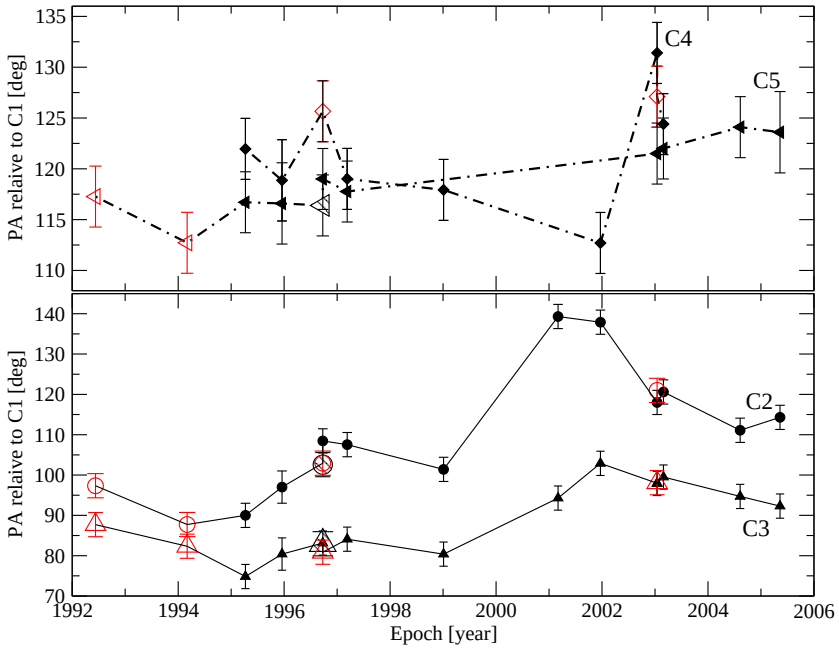

Figure 4.14: Component position angles as a function of time. Same symbols and lines are used as in Figure 4.13. Lines guide the eye.

not change significantly, however C2 shows movement on a circular path. In the case of C3 the bent trajectory is obvious, while the outer features, C4 and C5, move on relatively straight paths.

4.5.4 Long-term flux density evolution of B 2005+403

B 2005+403 was included in two single-dish monitoring programs (at UMRAO at 5 GHz, 8 GHz and 15 GHz and at the Mestähovi radio telescope at 22 GHz and at 37 GHz). These programs are dedicated to follow the long-term flux density evolution of quasars and blazars. In combination with observations performed at other wavebands and VLBI imaging measurements, the flux-density monitoring helps to better understand the physical properties of jet outflows in these systems.

B 2005+403 is particularly interesting as, during 13 years of VLBI observations, no new component ejection happened. However, the individual jet components show complex flux density variations (see Fig. 4.16). The flux density of C1 mainly decreased until 1999 and increased afterwards. C2 experienced a dramatic increase between 1999 and 2001, reaching its maximum brightness two years later and afterwards faded rapidly. C3 also showed a decrease in flux density in 1999. After a brightening in 2001, it also faded.

In Figure 4.17 the radio light curves of B 2005+403 are shown at 5 GHz, 8 GHz, 15 GHz, 22 GHz and 37 GHz during the time interval covered by the VLBI observations. The summed flux densities of the VLBI components combined in each of the epochs are also indicated with black circles connected by lines (at 15 GHz and at 22 GHz). The single-dish flux- density measurements and the respective VLBI observations are in good agreement.

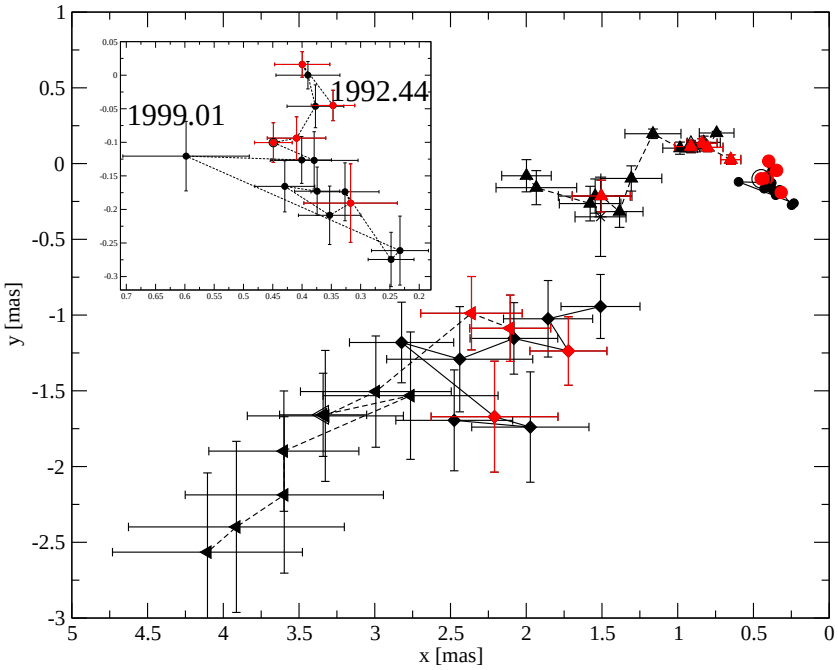

Figure 4.15: Trajectories of the jet components C2, C3, C4 and C5, relative to C1, which is assumed to be the core. The same symbols are used as in Figure 4.13. Lines guide the eye.In the diagram at the top left corner, the trajectory of C2 is shown in detail. Three epochs are labelled.

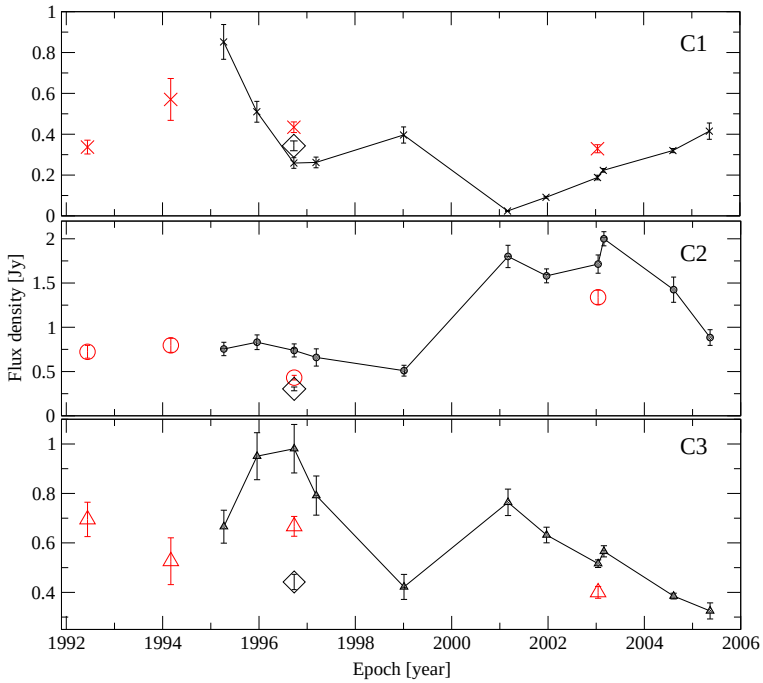

Figure 4.16: The flux density evolution of individual jet components C1, C2 and C3 is shown. Filled, black symbols denote 15 GHz data, open red symbols denote 22 GHz data, and open diamonds denote the 43 GHz data.

Table 4.8: The mean flux density, the standard deviation and the modulation indices for the flux-density variability of B 2005+430 at different frequencies between 1990 and 2004.

Frequency [GHz]	$\langle S \rangle$ [Jy]	σ [Jy]	m [%]
5	2.86 ± 0.02	0.217	7.61
8	3.03 ± 0.02	0.369	12.15
15	2.63 ± 0.02	0.374	14.24
22	1.95 ± 0.03	0.500	25.67
37	1.84 ± 0.03	0.363	19.81

The data clearly show the long-term variability of the source. A feature of particular interest is the apparent decrease of the flux density observed between 1992 and 1999. Between 1999 and 2001, the flux density increased again. This flux density 'trough' is best seen and more pronounced at the higher frequencies. At 5 GHz, the decline begins at 1996.5 and the flux density drops by 16 % reaching its lowest value around 1999.4. At 8 GHz, a flux density decrease of 30 % is observed during approximately the same time interval. At 15 GHz, the flux density drops by 47 % from 1996.6 till the beginning of 1999. At the two highest observed frequencies (22 GHz and 37 GHz), the decrease is even more pronounced: 54 % and 60 % respectively. This systematic frequency dependence of the variability amplitude is accompanied by a systematic and frequency dependent shift of the time of the flux density minimum. The flux-density minimum and the subsequent rise of the flux density appear earlier at the higher frequencies. In Fig. 4.17 this frequency dependence is illustrated by a solid line, which guides the eye.

To quantify the variations at the different frequencies, the modulation index was used (see definition in Seq. 2). The mean flux density and the corresponding modulation indices are summarized in Table 4.8. It is seen that at 22 GHz the modulation index is largest.

In the following, I discuss possible explanations for the observed "trough" in the long-term flux density light curves.

1. Extreme scattering event

"Extreme scattering events" (ESEs, see Fiedler et al. 1994) are flux density variations at GHz frequencies caused by strong ray path distortions due to moving discrete plasma clouds in the ISM, which partially obscure the source for a limited time. The first ESEs were observed in quasar light curves (Fiedler et al. 1987). Later, ESEs were observed in a few pulsars as well (e.g. Maitia et al. 2003, and references therein). Depending on size, distance and relative velocity of the scatterer, time-scales between a few days, months and perhaps even years are possible (see also Cimó 2003; Pohl et al. 1995).

Since B 2005+403 is located in a region of the sky with prominent scattering effects, the interpretation of the observed flux density trough via such an extreme scattering event provides an attractive possibility.

ESEs display a wide variety of shapes, their strong frequency dependence however, is characteristic. Amplitudes of the variations, time-scales, and amplitudes of the two surrounding maxima decrease with increasing frequencies. Fiedler et al. (1994) reported

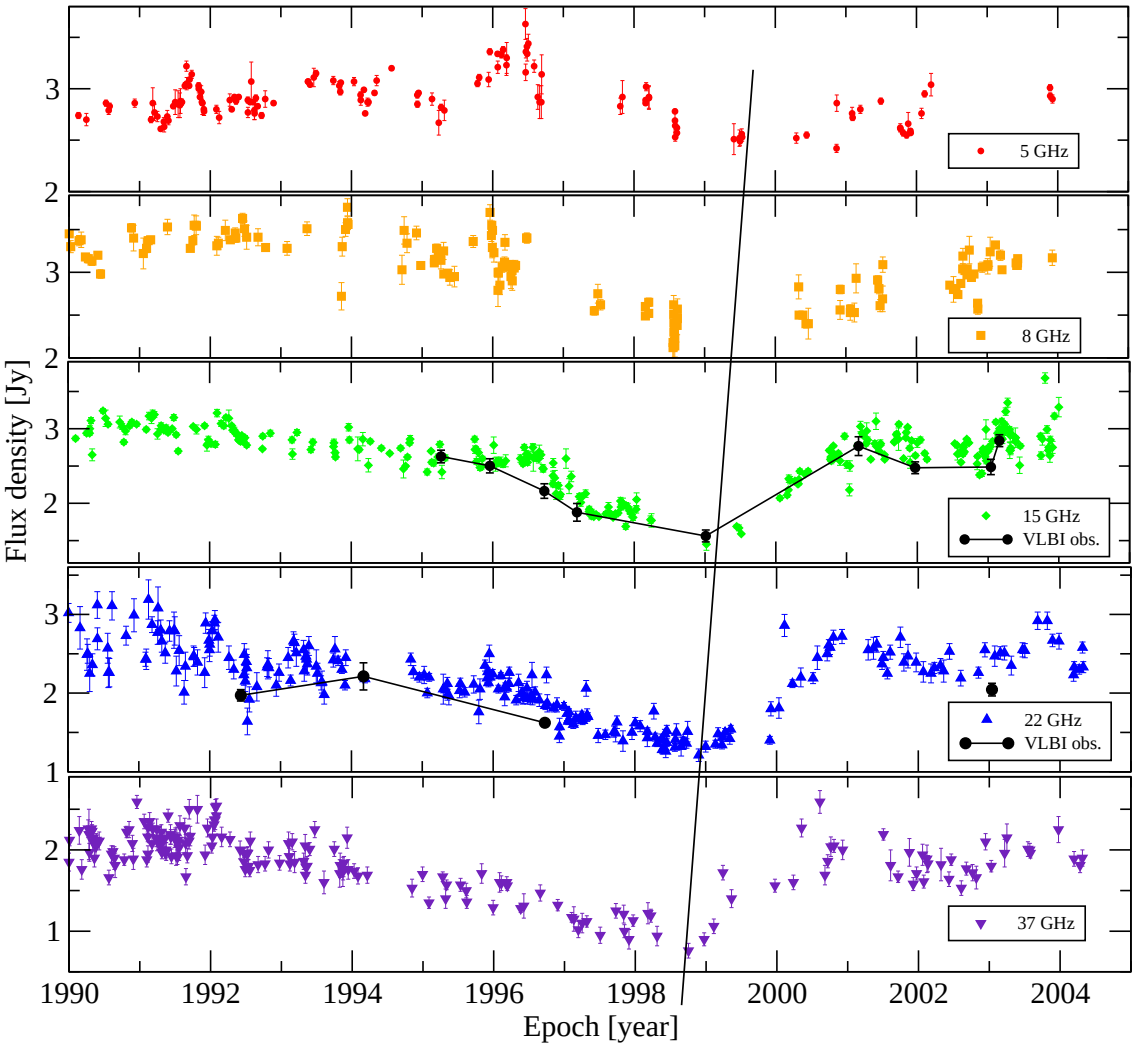

Figure 4.17: Light curves of B 2005+403 at 5 GHz, 8 GHz, 15 GHz, 22 GHz, and 37 GHz from the monitoring data of the University of Michigan Radio Astronomy Observatory, and the Metsähovi 14 metre radio telescope. The straight line connects the minima. The dark circles and lines denote the sum of flux density of the model-fit components from the VLBI observations at 15 GHz and 22 GHz.

that variations observed at 2 GHz have often no counterpart at 8 GHz and when changes at higher frequency are detected, the light curves are very dissimilar. An example light curve is shown in Fig. 4.18.

However, the frequency dependence and variability time-scales seen in B 2005+403 are different from those expected for an ESE. Typical ESEs show more pronounced and more rapid variations towards longer wavelengths, opposite to that observed in B 2005+403 (see Table 4.8). Also the frequency dependence of the flux density minimum observed in the trough of B 2005+403 is not consistent with an ESE event, which, owing to the geometrical occultation, should not show any frequency shifts.

Even though the low frequency VLBI observations performed in 1996.8 at 5 GHz and 1998.1 at 1.6 GHz coincided with the times of the decrease of the total flux density, the

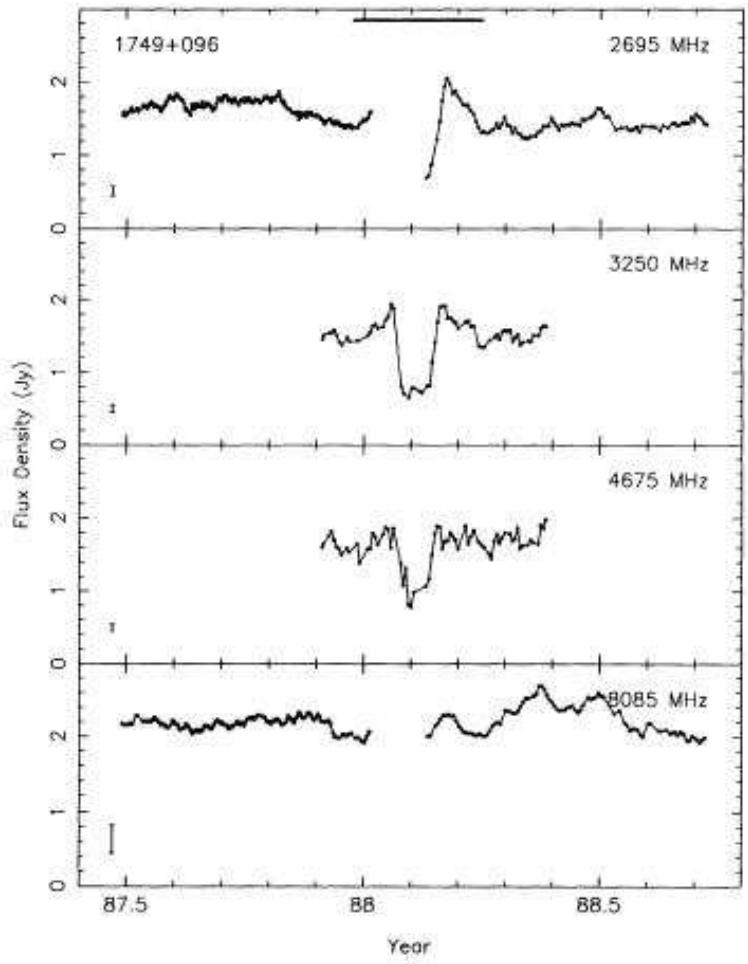

Figure 4.18: The light curve of a typical extreme scattering event from Fiedler et al. (1994). It shows a deep, flat minimum, bracketed by large peaks. The amplitude of the maxima and the depth of the minimum both decrease with increasing frequency.

observed angular source sizes at those times were not significantly different from the sizes observed previously (in 1985 and 1986) at the same frequencies by Fey et al. (1989), long before the flux density trough. Thus, the angular broadening was persistent and therefore was not related to the observed flux-density variability.

2. Variability of the jet components

Alternatively, the observed flux-density trough can be explained by the sum of the flux densities of the variable VLBI components. In Figure 4.17, the sum of the flux density of three model-fit components (C1+C2+C3) from the VLBI observations at 15 GHz and 22 GHz are displayed (as dark circles and lines). Particularly at 15 GHz, where the time coverage of the VLBI experiments covers the full time range of the trough, there is an excellent agreement between the single-dish flux-density measurements and the summed VLBI component flux densities. Examining the flux densities of the individual components (see Fig. 4.16), it appears that the combination of the declining trend of C1 and

Table 4.9: Polarization characteristics of B 2005+403 obtained from the VLBI images. The table lists the epoch, the frequency of the observation, the name of the component, the polarized flux density in mJy, and the polarization angle in degrees.

Epoch	ν [GHz]	ID	P [mJy]	χ[°]
2003.04	15	C2	59 ± 14	138 ± 2
2003.04	22	C2	59 ± 15	116 ± 4
2003.16	15	C2	67 ± 14	144 ± 3
2004.61	15	C2	44 ± 10	151 ± 3
2005.36	15	C2	11 ± 4	147 ± 7
1996.73	15	C3	42 ± 5	93 ± 8
1996.73	22	C3	29 ± 6	100 ± 4
1996.73	43	C3	13 ± 5	98 ± 4
2003.04	15	C3	38 ± 4	85 ± 8
2003.04	22	C3	22 ± 2	92 ± 6
2003.16	15	C3	26 ± 4	89 ± 9
2004.61	15	C3	29 ± 4	67 ± 8
2005.36	15	C3	17 ± 4	76 ± 7

the increasing trend of C2 are mainly responsible for the shape of the flux-density trough. Therefore, the peculiar shape of the total flux density light curve of B 2005+403 is a result of a blending of the independently varying flux densities of the inner jet components.

The flux-density increase of one of the jet components, C2, between 1999.01 and 2001.17 indicated Doppler boosting (see Sect. 4.5.3). Therefore it is very likely that the flux-density changes of the individual jet components is mainly caused by differential Doppler boosting as they move along a curved path. This is consistent with the trajectories described in the previous section.

4.5.5 Polarization

The VLBI study of the polarization of AGN is an extremely useful tool to understand the shock-in-jet models, and to follow the source evolution. VLBI shocks leave clear signatures in images of the polarized flux density, therefore providing critical tests for the shock-in-jet models. Moreover, magnetic fields are crucial indicators of the underlying jet physics. Therefore, to study oblique shocks, boundary layer interactions, turbulence and instabilities, it is often straightforward to image the source in polarized intensity.

In Fig. 4.11 the polarization vectors are superimposed on the VLBI images for those epochs on which polarization data were available. The lengths of the vectors represent the polarized flux density. The polarized flux density and the polarization position angles derived from the VLBI observations are displayed in Table 4.9. The measured polarization characteristics at 15 GHz are in agreement with the UMRAO single-dish measurements.

Component C2 was unpolarized in 1996.73, however this was the most prominent polarized feature in 2003 and 2004, with comparable polarized flux density at 15 GHz and 22 GHz. By 2005, its polarized intensity dropped by 75 %.

The polarized flux density of C3 decreased through all the epochs and also decreased

with increasing frequency. Similar to C2, it experienced its biggest decrease between the last two epochs ($\sim 40\,\%$ decrease in polarized flux density).

The polarization position angles of C2 did not change significantly with time. It is roughly parallel (within 30°) with the position angle of C2 measured from the core. C2 is an optically thin jet component (see Sect. 4.5.3), therefore the magnetic field is perpendicular to the EVPA, thus the magnetic field is roughly perpendicular to the jet direction between C2 and C1.

The polarization angle of C3 changed by $\approx 15^\circ$ between 2003.16 and 2004.61. The EVPA of C3 is roughly parallel with the jet direction. C3 is an optically thin jet component (Sect. 4.5.3), so the magnetic field is perpendicular to the EVPA. Therefore, the magnetic field is perpendicular to the jet axis at the position of C3.

4.6 Summary

B 2005+403 is located in the Cygnus region and is known as one of the most scatter-broadened extragalactic sources in this region of the sky. Here, combined multi-frequency flux density monitoring data and VLBI imaging observations have been presented. In addition, the results of high time resolution flux density monitoring observations were discussed.

The VLBI images at lower frequencies (1.6 GHz, 5 GHz and 8 GHz) show a scatter-broadened source. Combining the new size measurements with published data from earlier observations allowed us to study the frequency dependence of the source size in greater detail. Below 8 GHz, this dependence was best described by a non-Kolmogorov power law with slope of -1.9. Above 8 GHz, the measured sizes were larger than the prediction from the scattering law, and the internal source structure became visible. Based on the observed scatter broadening, several parameters of the scattering medium (scattering size, scattering measure, electron density) were determined and found to be agree with previously published estimates (NE2001, Cordes & Lazio 2002). The NE2001 model places the scattering screen at a distance of 2.35 kpc. (Towards the direction of B 2005+403 there is a degree-size extended supernova remnant, G78.2+2.1. It has a patchy, inhomogeneous structure at optical, X-ray and radio wavelengths (Bykov et al. 2004, and references therein). Its distance is (1.5 ± 0.5) kpc (Landecker et al. 1980), which is compatible with the scattering model.)

Densely time-sampled variability measurements performed with the 100 m Effelsberg telescope showed only weak intra-day variability in B 2005+403. The low variability indices ($m = 1\,\%$ at 1.6 GHz, $m = 0.5\,\%$ at 5 GHz) and the short variability time-scale of ~ 0.1 days cannot be explained by scattering effects from the kpc-screen, which is responsible for the scatter broadening. Instead, another and much closer scatterer was required. Using the thin screen approximation for refractive interstellar scintillation, the likely range of distance of the scattering screen is determined, $9\,\mathrm{pc} \leq L \leq 41\,\mathrm{pc}$. For B 2005+403 a scattered-broadened image (due to kpc-screen) is scattered a second time (pc-screen) and the combination of both effects limits the accuracy of low-frequency flux-density variability measurements to about 0.5 % to 1 % and the angular the resolution of VLBI observations to a few mas.

High frequency VLBI imaging observations (at 15 GHz, 22 GHz and at 43 GHz) span-

ning 13 years (between 1992 and 2005) revealed a one sided and bent core-jet structure, with at least five embedded VLBI components. The inner jet components separated from the stationary assumed core (C1) with apparent superluminal speeds of 8c to 15c. The component nearest to the core (C2), however, appeared to be stationary ($\beta_{\rm app} \leq 0.02$). The flux-density variation of this stationary and steep spectrum component apparently violates the inverse-Compton limit, indicating Doppler-boosting of $\delta = 3.6$. This can be explained by a component path oriented at a smaller angle to the line of sight than those of the other jet components. A systematic increase of the component speeds with increasing core separation is observed. The paths of the inner-most jet components are curved and their motion was not ballistic, suggesting a spatially curved (helical) jet. Beyond 2 mas core-separation, however, the components moved on linear (ballistic) trajectories. Future VLBI monitoring will be necessary to determine their paths more accurately.

The observed long-term flux-density variability curves at GHz frequencies were discussed. The light curves showed a remarkable flux-density "trough" between 1996 and 2001. A tentative interpretation via a possible "scattering event" similar to the "extreme scattering events" observed in other sources, could be excluded on the basis of the observed frequency dependence of the variability (the variability was more pronounced at higher frequencies). Instead, the "trough" could be explained by the summed flux-density variability of the (independently) varying VLBI components (C1, C2, and C3). In contrast to other sources, which often show correlations between jet component ejection and flux-density variability (e.g. Savolainen et al. 2002, and references therein; see also Sect. 1.3.1), such a relation was not seen in B 2005+403. In this source, at least some (if not most) of the observed flux-density variability resulted from the blending of the evolving jet components.

5 Space-VLBI observations of B 2007+777

B 2007+777 is a blazar at $z = 0.342$ (Stickel et al. 1989). B 2007+777 belongs to the complete and flux-density limited S5 polar cap sample (Eckart et al. 1986). Its kpc-scale morphology has been studied by, for example Antonucci et al. 1986, Kollgaard et al. 1992 and Murphy et al. 1993. The images presented here reveal a jet-like feature at least 6″ long extended towards southwest from the brightest compact central component. Another bright compact component is located at 10″ to the east of the brightest component (see Fig. 5.1). At pc-scales, all VLBI images show emission west of the main component, extending out to 40 mas at 2.3 GHz (Fey & Charlot 1997) and 20 mas at 5 GHz (Xu et al. 1995) at a position angle of $-95°$. One of the embedded components separates form the core with $\mu = (0.223 \pm 0.015)$ mas/yr, corresponding to $\beta_{\rm app} = 5.78 \pm 0.38$. (Gabuzda et al. 1994). Homan et al. (2001) analyse six epochs of VLBI observations of B 2007+777 at 22 GHz and at 15 GHz during the year 1996. They found no moving component in the source. The detected displacement of one of the jet features but this could most probably be attributed to a shift of the centroid of brightness in a large low surface brightness component. Gabuzda et al. (1994) reported that the dominant magnetic field in B 2007+777 is transverse, typical for radio-selected BL Lacs, though they also observed one component that has a longitudinal magnetic field.

The observations of Quirrenbach et al. (1992) revealed that B 2007+777 is an IDV source. VLA observations by Quirrenbach et al. (2000) showed time-scales of a few days both at 6 cm and 11 cm. Variability in polarized flux density and polarization angle was also observed. To investigate the nature of IDV in B 2007+777, the source was observed at several wavebands simultaneously from the optical to the infrared (IR) within a campaign in 1997. Peng et al. (2000) reported on rapid variations in almost all wavebands. According to the authors, the time-scale and the modulation indices did not support an extrinsic explanation of this IDV. The authors argued that the observed characteristics favour the shock-in-jet model. In the high energy regime, B 2007+777 was detected by the Einstein Observatory (High Energy Astrophysical Observatory, HEAO-2) in the 0.1 keV to 3.5 keV energy band with a flux density of 3.64 μJy at 1 keV (Worrall & Wilkes 1990). Additionally, it was observed by ROSAT in a pointed mode at 0.1 keV to 2.0 keV twice in 1992; in the first observation the source was below the detection limit, in the second, the flux density was 0.17 μJy at 1 keV (Urry et al. 1996). This is 20 times weaker than in the HEAO-2 observation, suggesting variations also at this band.

B 2007+777 has been monitored with the UMRAO radio telescope since 1982. Its total and polarized intensity light curves and the changes in the polarization angle are

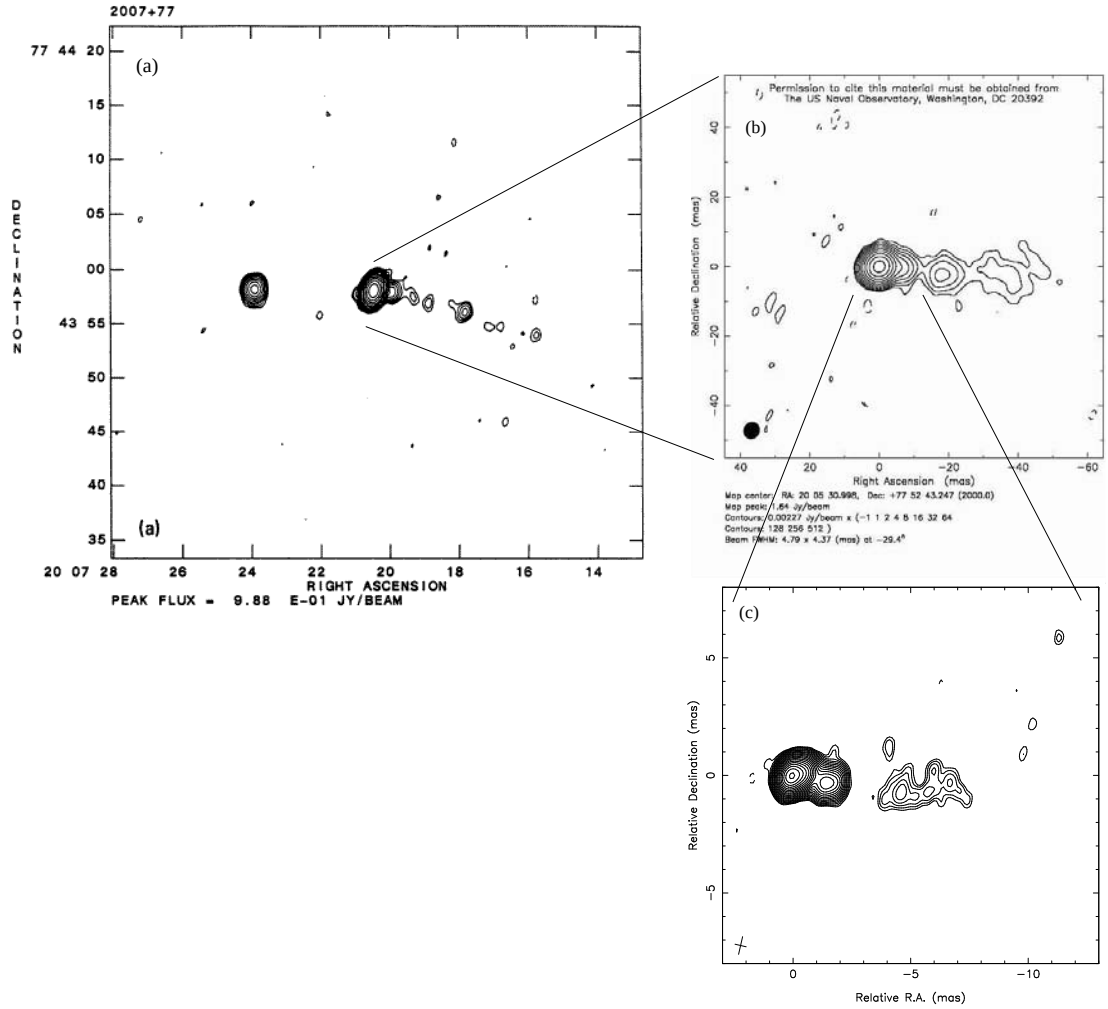

Figure 5.1: B 2007+777 at different wavelengths and resolutions. (a) shows a VLA image made at 1.5 GHz at epoch 1985 by Antonucci et al. (1986). (b) shows a VLBA image at 2.3 GHz from Fey & Charlot (1997) at epoch 1995. (c) shows a 15 GHz image from the 2 cm Survey from 1998 (Kellermann et al. 2004).

shown in Fig. 5.2. The typical BL Lac characteristics – highly variable total and polarized flux density – are illustrated by these plots. B 2007+777 displayed several flares at all three observed frequencies, The flares were more or less simultaneous at the different wavelengths with a slight tendency for the high-frequency variations to be followed by the lower frequency variations, typical for source-intrinsic variations.

5.1 Space-VLBI observations of IDV sources

Several of the most compact IDV sources were observed by VLBI Space Observatory Program (VSOP, Hirabayashi et al. 2000).

The main aim of these observations was to look for the origin of the variability with the highest achievable resolution at cm wavelengths. These observations were planned so

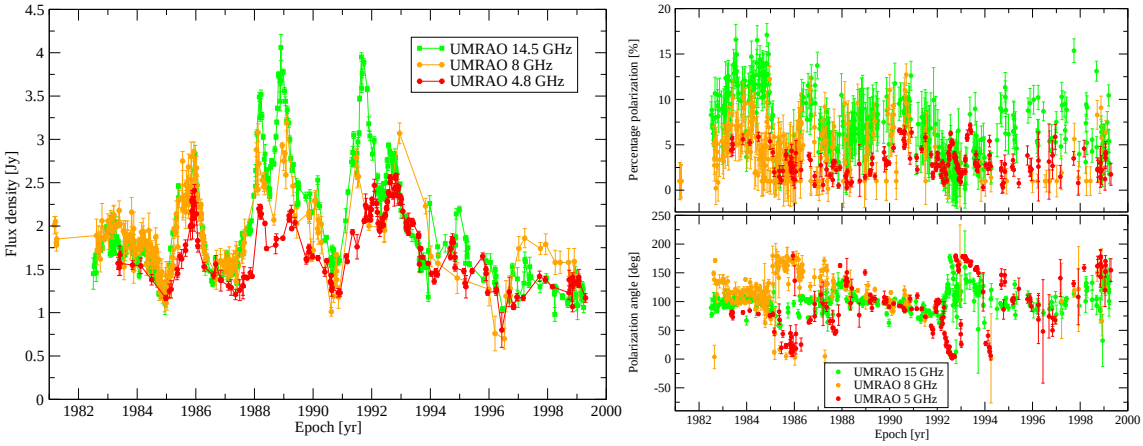

Figure 5.2: The UMRAO monitoring data of B 2007+777 at different wavelengths: 4.8 GHz (red), 8 GHz (orange), and 14.5 GHz (green). At the left hand side the total intensity data are shown, at the right side, the percentage polarization (top) and the polarization angle (bottom) changes are displayed versus time.

that one could distinguish from the measurements whether the short time-scale variations can be attributed to the core or the jet of the particular radio source. They were performed at three or four epochs, which were separated by a few days and some weeks to allow to detect significant changes on short time-scales. The observed sources are well known for showing substantial short time-scale changes in polarized intensity and some of them also displayed rapid polarization angle swings. The observations were performed in full polarization[1] to reveal the origin of these variations. The closely-spaced epochs made it feasible to search for any high speed motion of the components. If any motion was detected between the epochs of the observation, it would imply atypically fast apparent superluminal motions of the components, and thus would confirm the extremely high Doppler factors, obtained from light-travel time arguments of IDV.

The observed sources included the BL Lac objects S5 0716+714 (Bach et al. 2005), S4 0954+658 (Bernhart et al. 2006, in preparation) and B 2007+777. In S5 0716+714, the observations showed that the IDV is associated with the VLBI-core region and not with the mas jet. This was already reported by Gabuzda et al. (2000a) for S5 0917+624 and S4 0954+658 on the basis of previous ground-based VLBI observations. Bach et al. (2005) concluded, that the detected variations in polarization in S5 0716+714 can be attributed to compact sub-components in the core, which exhibit different polarization properties.

The orbiting radio telescope HALCA was launched in February 1997. The pointing control was lost in October 2003. Officially its observations ended in November 2005. HALCA's diameter was 8 m, so its sensitivity was much lower than the ground based antennas. HALCA's orbit was elliptical with an apogee height of 21375 km and a perigee height of 556 km; the maximum baseline lengths obtained with ground based arrays were $\sim$ 33000 km. This is approximately three times longer than can be achieved by ground

[1]The orbiting space antenna is able to measure only the left hand circular polarization. However, VLBI polarimetry is possible if enough ground telescopes of the array can provide full polarization measurements. This subject is discussed in more detail in Sect 5.1.3.

Table 5.1: Details of the VSOP observations of B 2007+777. Col. 1 shows the observing epoch (all observations took place in 1999). Col. 2 gives the source name, Col. 3 the total integration time in hours, Col. 4 the mutual observing time with HALCA.

Epoch		Designation	Source names	Int. time [hrs]	HALCA [hrs]
Sep. 5	1999.679	W044F1	B 2007+777	8.2	6.4
			J 1800+7828	0.9	–
			J 1825+5651	0.8	–
Sep. 7[a]	1999.685	W044F2	B 2007+777	8.7	6.2
			J 1800+7828	0.9	–
			J 1824+5651	0.8	–
Oct. 2[b]	1999.753	W044F3	B 2007+777	8.9	5.0
			J 1800+7828	0.8	–
			J 1824+5651	0.8	–
Oct. 4	1999.759	W044F4	B 2007+777	8.6	6.7
			J 1800+7828	0.8	–
			J 1824+5651	0.8	–

[a] In this epoch, the Los Alamos antenna did not observe due to a loss of freon in the air conditioning system. For one of the tracking stations of HALCA (UZ, Usuda, Japan) no fringes were found. Approximately 35 minutes of HALCA time were lost.

[b] For one of the tracking stations of HALCA (UZ, Usuda, Japan) no fringes were found. Lost HALCA time was approximately 2.3 hours.

based arrays. HALCA was able to observe at 1.6 GHz and at 5 GHz with a maximum bandwidth of 32 MHz.

5.1.1 The observations of B 2007+777

In the space-VLBI observing campaign, B 2007+777 was observed in seven epochs in 1998 and 1999. Here are presented the four observations that took place in 1999. In all cases the array consisted of the ten antennas of the VLBA, the Effelsberg 100 metre telescope, and the 8 metre orbiting radio telescope, HALCA. The observations were performed at 5 GHz. Three or four tracking stations of HALCA were used. B 2007+777 was classified as a type (“slower”) IDV source (Quirrenbach et al. 1992; Kraus et al. 2003). The VSOP observations were planned accordingly: the epochs were separated by two days and a month to make it possible to detect changes on time-scales from days to weeks. The details of these observations are summarized in Table 5.1.

In two epochs (September 7 and October 2) at one of the HALCA tracking stations no fringes were found, therefore the given HALCA observing times are slightly shorter than in other epochs. On Sep. 7th, Los Alamos antenna of the VLBA did not observe due to a loss of freon gas in the air conditioning system. The two calibrators in the observations were J 1800+7828 and J 1824+5651. They were observed by the ground array only, since it was not possible to slew HALCA to different source positions during one observation. HALCA observed only the target, B 2007+777.

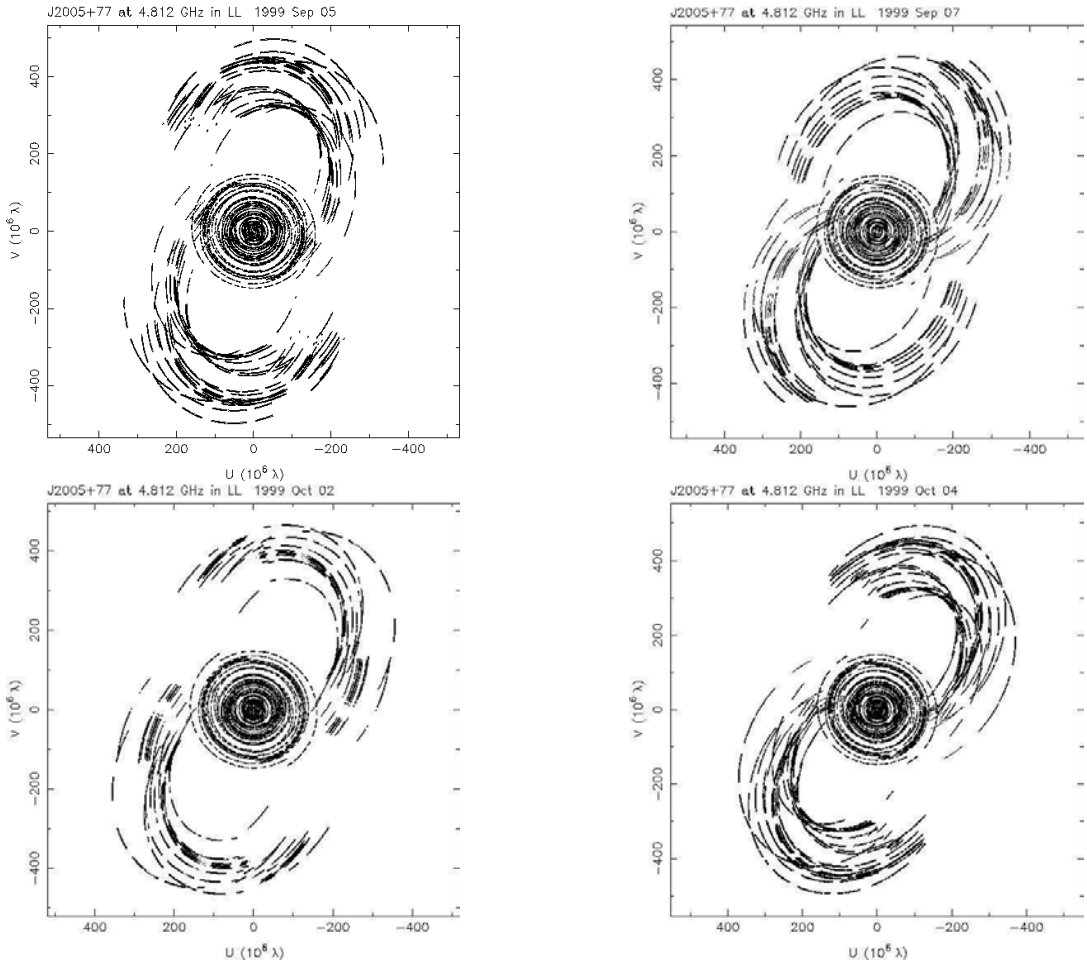

Figure 5.3: (u, v) coverage of B 2007+777. From left to right and top to bottom: Sep 5th., Sep 7th., Oct 2nd., Oct 4th, 1999. The coverages are very similar; therefore the resulting images from the different epochs can be reliably compared.

The (u, v) coverage of B 2007+777 in the different observations is displayed in Fig. 5.3. The central densely covered regions correspond to the baselines of the ground based telescopes; the more extended elliptical tracks represent the much longer HALCA baselines.

5.1.2 Reduction of the total intensity data

The data reduction was done within AIPS following standard procedure. This is very similar to that described briefly in Sect. 4.3. The important differences in the data reduction steps – because of the orbiting antenna – are the following:

- There may be discontinuities in the recorded data for a variety of reasons, such as tracking station handoffs, or clock glitches, etc. In those cases it is recommended to force scan boundaries at such events. In these observations, the necessary input files for the task were provided by the correlator.

- The table containing the details of each antenna (table) had to be modified using the task. This determines the mean orbital elements using the spacecraft positions and velocities and accordingly updates the table.

- For the VLBA antennas the gain and system temperature calibration are provided from the correlator along with the datasets. For HALCA and the Effelsberg antenna these data have to be loaded into AIPS separately, for this the task is used.

- As HALCA – unlike the ground based telescopes – does not provide pulse-cal information with the data, "manual" phase calibration is needed to remove the offsets between IFs. (This is necessary if one wants to average the IFs later.) For this the task is used. This step has to be performed for each tracking station individually, using a short (few minutes long) section of the data within a single scan of the target source.

- Fringe fitting can be much more challenging for the space baselines than in "ground-only" observations, mainly because the sensitivity of HALCA is much lower than that of the ground radio antennas. Moreover, as HALCA can observe only one source during the measurement, the target has to be strong enough to provide fringes. Additionally, the location of fringes for HALCA is dependent on the accuracy of the orbit. Several "tricks" are proposed in the AIPS Cookbook to overcome these difficulties and to enable to search for fringes even in those cases when they were not initially seen at the correlator. Although, in those epochs where no fringes were detected to one of the tracking stations, even employing these suggestions we were not able to find fringes.

The next step, the data editing, was done within DIFMAP. Self calibration and total intensity imaging was performed within DIFMAP (for the ground array data only) and within AIPS (including the space data as well). AIPS provides more sophisticated methods in imaging, with the possibilities of using very different weighting schemes – through the robustness parameter (Briggs 1995) – between the two "extremities", the natural (equal weight for each visibility point) and uniform (weights are corrected for the local density of the points) weightings. This is extremely useful in the case of heterogeneous array, which includes such different sensitivity antennas (HALCA with a diameter of 8 m and Effelsberg with a diameter of 100 m). Model-fitting of the final calibrated datasets were performed within DIFMAP.

5.1.3 Reduction of the polarization data

Polarization calibrations involve the following steps.

- Removal of the effect of changing parallactic angle with the task .

- Determination of right-left multi-band and single-band delay corrections. (The phase and delay corrections obtained using the RR and LL data can remove only right-right and left-left offsets.) is available to determine these offsets.

- Feed D-term calibrations. The so-called D-terms or leakage terms are the complex response of each feed to the orthogonally polarized radiation. The calibrator source can be unpolarized, then all the measured polarization is due to instrumental polarization. However, unpolarized sources are rare. To distinguish the instrumental and source polarization in a polarized calibrator, one has to provide an adequate model of the calibrator source. The sub-models determined from the total intensity images are regarded similar to the structures in the linear polarization. Therefore, a proper total intensity image of the calibrator is essential. This model can be divided into separate subcomponents with the task . Then the task can determine the D-terms of different antennas, by analysing the changes of the polarization angle of the "separated" components at different parallactic angles.[2] Therefore a good (polarized) polarization calibrator source has to be bright and has to have fairly simple structure on VLBI scales (having limited number of discrete subcomponents).

- Electric vector position angle (EVPA) calibration. Correction for phase offset between the orthogonal polarizations at the reference antenna. This was set to zero during fringe fitting. At this step, the recovered polarized flux density has to be compared to simultaneous single-dish measurements. If the measurements are comparable, then the EVPA can be corrected via the polarization-angle measurements provided by single-dish observations.

These steps were followed in reducing the polarization data of the ground array. Both of the calibrators were polarized. The D-terms were calculated using both sources and different total intensity models were explored. The D- terms obtained did not differ significantly in the different approaches.

During the VLBI observations Effelsberg took part not only as a member of the array, but in the gaps of the VLBI scans, as a single antenna it measured the flux densities of the observed sources to improve the calibration. In Table 5.2, the Effelsberg and the ground array polarized flux density (P) and polarization angle (χ) measurements for the calibrators are displayed for all epochs. To compare the VLBI measurements to the single dish data, the source model was convolved with a large beam (larger than the VLBI structure of the particular source). The tasks and were used to determine the "average" value of P and χ. The VLBI and Effelsberg measurements are comparable. From Table 5.2, it is clear that the EVPA correction values ($\chi_{\rm Eff} - \chi_{\rm VLBI}$) are slightly different for the two calibrators. The differences are of the order of a few degrees, which probably reflects the measurement accuracy of the EVPA.

Polarization reduction of the HALCA data

As mentioned before, HALCA can detect only left circular polarization (LCP). However, VLBI polarimetry is still possible: the HALCA LCP data can be cross-correlated with the RCP data of the ground array. Normally, from the LL, RR, RL and LR correlations all four Stokes parameter (I, U, Q, V) can be derived, and then U and Q can be imaged separately and deconvolved in the same way as the total intensity image, for example with the task . However, in space-VLBI observations the sampling function is

[2]Instrumental contributions are unaffected by the parallactic angle, whereas contributions from the source itself do depend on the parallactic angle.

Table 5.2: The polarization characteristics (polarized flux density and polarization angle) of the calibrators at different epochs, measured by the Effelsberg 100 metre telescope (columns 3 and 4) and in the VLBI observations (columns 5 and 6).

Epoch	Source name	$P_{\rm Eff}$ [mJy]	$\chi_{\rm Eff}$ [°]	$P_{\rm VLBI}$ [mJy]	$\chi_{\rm VLBI}$ [°]
1999.679	J 1800+7828	132.5 ± 3.4	88.8 ± 1.5	125.8 ± 13.3	46.5 ± 2.5
1999.679	J 1824+5651	85.8 ± 2.5	34.1 ± 1.4	68.5 ± 6.9	−15.6 ± 3.1
1999.685	J 1800+7828	133.2 ± 3.6	87.0 ± 0.9	112.6 ± 14.0	−72.6 ± 2.3
1999.685	J 1824+5651	84.4 ± 2.5	33.7 ± 1.7	77.5 ± 6.0	46.6 ± 1.7
1999.753	J 1800+7828	110.5 ± 8.6	90.4 ± 1.3	103.1 ± 21.0	−66.4 ± 3.0
1999.753	J 1824+5651	81.3 ± 4.2	33.3 ± 3.1	76.9 ± 7.2	49.9 ± 3.5
1999.759	J 1800+7828	118.3 ± 6.3	88.1 ± 0.9	107.3 ± 10.0	−86.0 ± 2.0
1999.759	J 1824+5651	79.0 ± 5.0	29.0 ± 3.4	69.4 ± 10.0	31.1 ± 2.0

asymmetric (because one of the two "mixed" polarization signal is missing), consequently the Fourier transform of the sampling function, the dirty beam is complex. To analyze the polarization measurements of HALCA, complex imaging and complex deconvolution of $U + iQ$ has to be done. This results in a complex image for which the real part represents the Q emission and the imaginary part the U emission (Cotton 1993). The AIPS tasks produces the complex beam and complex dirty map; the task does the complex clean and creates the U and Q images.

Another important aspect is that HALCA cannot "switch" between sources and therefore can observe only the target source and not the calibrator. Thus, during polarization calibrations, the D-terms and the corrections of EVPA were derived from the data of the target source, B 2007+777.

5.2 Results

5.2.1 Ground baselines

In Fig. 5.4 the images of B 2007+777 are displayed (details of the images are given in Table 5.3). The left panels show the total-intensity images with superimposed polarization vectors, the right panels show the polarized intensity contours with two contours of total intensity.

During the four, in time closely-spaced epochs, no significant structural changes were detected in total intensity. The source has a bright compact central region (A0) from which a 7 mas-long jet emerges westward which ends in a rather compact knot-like feature (A1). One more faint feature is visible at 18 mas from the centre, which suggests that the jet bends slightly towards the south at larger separation.

The knot-like feature in the jet is also visible in polarized intensity. (However the other, farther emission is below the detection limit.) The peak in polarized intensity is slightly displaced from the position of the peak in total intensity. The position angles of the polarization vectors are different in A0 and in A1 by 100° to 140°.

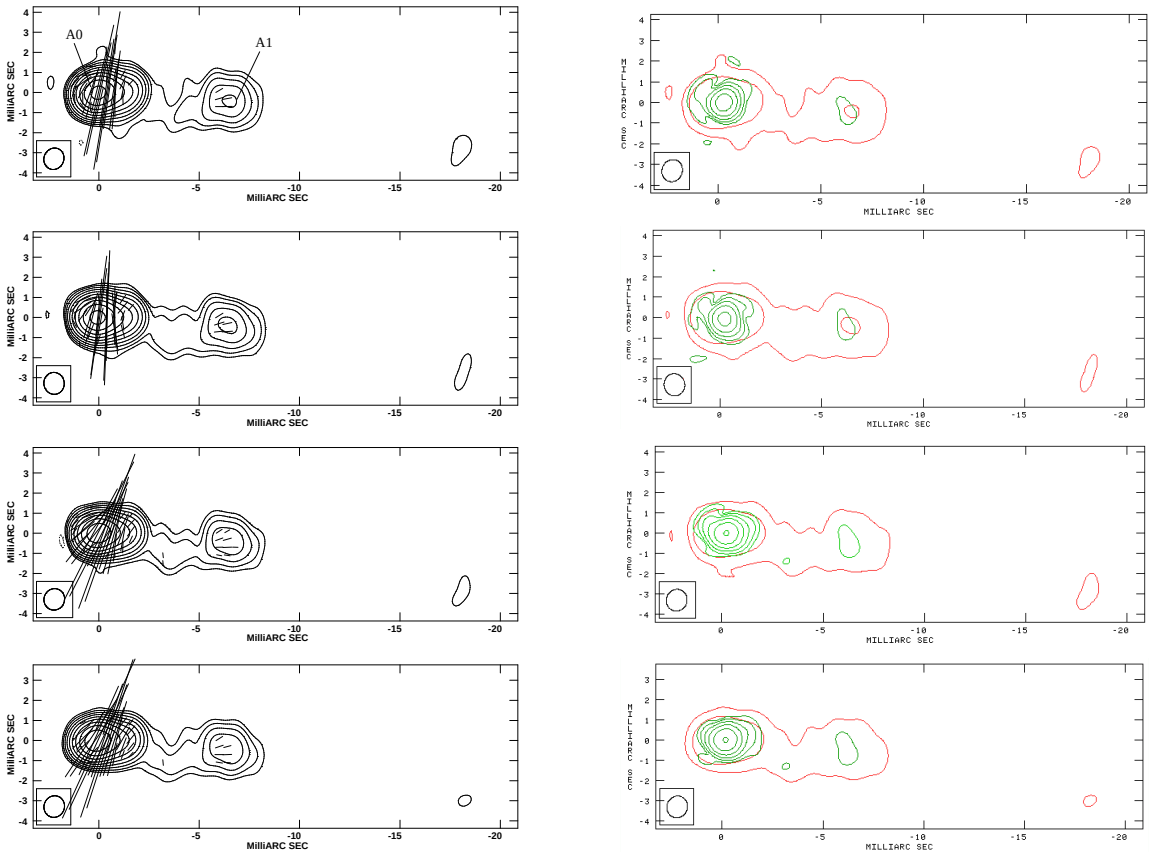

Figure 5.4: Ground based polarization images of B 2007+777. From top to bottom the epochs are: 1999.679, 1999.685, 1999.753 and 1999.759. Left panels: total intensity contours with the polarization vector superimposed. 1 mas length of the polarization vector corresponds to 3.33 mJy/beam. Right panels: contour images of the polarized intensity (green) with two contours of the total intensity (red) superimposed. The beams are displayed in the lower left corner of each image, the beam size in all cases is 1.1×1 mas. Peaks and contour levels of the images are displayed in Table 5.3.

In the optically thin emission regions, the magnetic field is perpendicular to the observed polarization angle. Thus, in B 2007+777, the magnetic field is perpendicular to the jet direction in A1. This is typical in low-energy-peaked, radio-selected BL Lacs (see e.g. Gabuzda et al. 2000b, and references therein). Whether the region A0 can be assumed to be optically thin is not clear. If it is optically thin, then the magnetic field is parallel to the jet direction (the jet position angle can be seen more clearly in the higher-resolution VSOP images, see Sect. 5.2.2). On the other hand, Gabuzda & Pashchenko (2002) reported that there is evidence that the spectrum may flatten near this region, implying a transverse magnetic field.

In component A0, beside the "dominant" polarization, finer structure is suggested by the polarization images. This is confirmed by the higher resolution of HALCA data, see Sect. 5.2.2 for a discussion.

With the AIPS tasks and , the polarized and total intensity and the average value of the polarization angles of A0 and A1 were obtained. The data are sum-

Table 5.3: The details of the ground-based polarization and total-intensity images displayed in Fig. 5.4. Col. 2 and 5 are the peak flux densities of the total-intensity, and polarized-intensity images respectively. Col. 3 and 6 are the lowest positive contour in percentage of the peak flux density in the total-intensity and polarized-intensity images respectively. The contour levels increase by factors of two. Col. 4 and 7 are the residual noise of the total-intensity and the polarized intensity images respectively.

Epoch	I map			P map		
	Peak	Contour	Noise	Peak	Contour	Noise
	[mJy/beam]	[%]	[mJy/beam]	[mJy/beam]	[%]	[mJy/beam]
1999.679	629.0	0.15	0.1	28.3	4.0	0.05
1999.685	671.1	0.15	0.1	22.1	4.8	0.06
1999.753	634.7	0.22	0.1	29.7	3.0	0.05
1999.759	638.7	0.20	0.1	31.4	3.0	0.05

Table 5.4: Total intensity and polarized intensity and polarization angle of B 2007+777 as measured in ground-based images in two distinct regions (see 5.4) and with the Effelsberg 100 metre telescope during the VLBI observations. In the rows denoted as "Sum", the vector sum of the polarization and the scalar sum of the total intensity is displayed. Col. 3 is the total intensity, Col. 4 is the polarized intensity and Col. 5 is the polarization angle, measured from north to east.

Epoch	Comp.	I [mJy]	P [mJy]	χ [°]
1999.679	A0	842.1 ± 12.6	24.0 ± 4.1	−10.3 ± 1.5
1999.679	A1	26.3 ± 6.8	2.0 ± 0.7	96.9 ± 1.1
	Sum	868.4 ± 19.4	23.5 ± 14.9	−5.6 ± 1.4
Effelsberg		1124.9 ± 6.6	30.5 ± 1.2	−4.2 ± 1.5
1999.685	A0	855.5 ± 15.4	21.1 ± 3.2	0.5 ± 2.5
1999.685	A1	31.1 ± 8.0	1.9 ± 0.4	104.8 ± 3.1
	Sum	886.6 ± 23.4	20.7 ± 7.0	5.6 ± 2.6
Effelsberg		1144.1 ± 16.0	25.7 ± 2.4	−2.8 ± 1.8
1999.753	A0	844.6 ± 10.6	30.2 ± 1.7	−28.0 ± 3.0
1999.753	A1	29.2 ± 7.2	1.7 ± 0.3	105.0 ± 4.5
	Sum	873.8 ± 17.8	29.1 ± 5.2	−25.6 ± 2.2
Effelsberg		1085.4 ± 12.6	31.4 ± 1.6	−19.5 ± 1.8
1999.759	A0	851.5 ± 7.9	32.8 ± 5.0	−27.7 ± 5.0
1999.759	A1	26.2 ± 6.1	1.3 ± 0.4	113.1 ± 6.1
	Sum	877.7 ± 14.0	31.8 ± 18.4	−26.2 ± 3.7
Effelsberg		1098.4 ± 13.5	31.8 ± 4.1	−17.3 ± 4.4

marized in Table 5.4 for components A0 and A1 separately, for the summed the components (vector sum of polarized intensity and the scalar sum of total intensity) and for the measurements with the Effelsberg telescope.

Between the first two epochs the total intensity increased by ~ 20 mJy. Although the summed total intensities in the VLBI images are lower than the single-dish values (~ 77 %

of the single-dish flux density was recovered by VLBI measurements), the changes between the two epochs are remarkably similar (difference is only 1 mJy). Both features show an increase in the total intensity. Component A1 reveals a higher percentage of change in total flux density than A0, however the relative error of 25 % is large in comparison with to that of component A0 2 % and so the change in A1 is not as significant as the change in A0. In polarized intensity, there was a decrease during the same time. This change can be seen in the VLBI (in component A0) as well as in the single-dish measurements. The changes in the polarization angle are not significant in both VLBI and single dish measurements.

Between September and October (between epochs 1999.685 and 1999.753) the total intensity decreased and this intensity drop was more pronounced in A0 than in A1. The polarized-intensity increase can be attributed to changes of the polarization flux density of A0. The polarization angle changed significantly, which can also be related to A0 (see Fig. 5.4).

During the last two epochs no significant changes occurred either in total intensity or in polarized intensity.

In summary, the ground-based images revealed that the changes in polarization and in total flux density are related to A0, the central region rather then the jet feature (A1). No significant variations can be seen on the short, two-day-long time-scales either in total intensity or in polarized intensity. However, variations occurred between the September and October epochs, on time-scales of 25 days. The total intensity decreased while polarization increased. Significant changes in the polarization angle (of A0) also occurred between epoch 1999.685 and 1999.753.

5.2.2 Space-VLBI data

Total intensity

In Fig. 5.5 the space-VLBI total intensity images of B 2007+777 are displayed (details of the image are given in Table 5.5). In the much higher resolution, space-VLBI data, the central region (A0) can be resolved into four or five subcomponents in total intensity. The emission located 6.5 mas from the centre corresponds to A1. The rest of the jet is resolved out and.

To parameterize the total intensity data, the visibilities were model-fitted using the DIFMAP software. Circular Gaussian components were used to reduce the number of independent variables. The reduced χ^2 of the model-fits were in all epochs in the range between 3 and 4. To illustrate the positions of the components, one image is shown in Fig.5.6 (epoch 1999.685). All epochs can be fitted by using seven Gaussian components: five in the central part and two fainter jet components at larger core separations (designated as Im and I5). The results of the model-fitting are displayed in Table C.1.

Based upon the model fit results, the jet as seen at the space-VLBI images (modelled by Im and I5) was not variable during the observations. Since the flux density of the jet did not vary, then it can be used to normalize the flux density of the core components in the space-VLBI measurements from different epochs. Unfortunately, the model component Im is the largest and so the least well-defined feature of the map. Therefore I5 was used for the normalization. (The result of the normalization is not significantly different if the

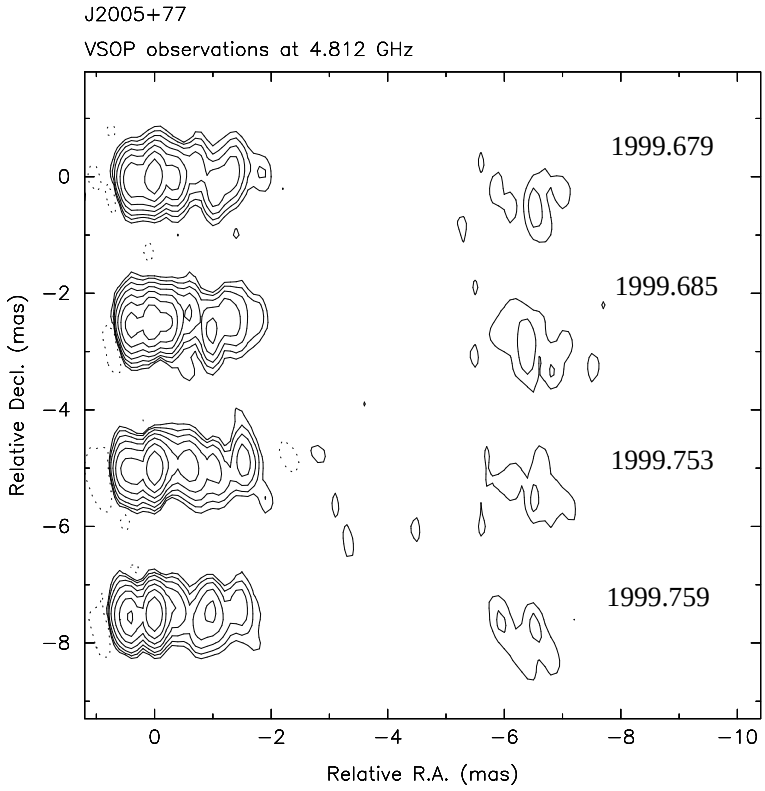

Figure 5.5: Total-intensity images of B 2007+777 at four different epochs. The beam size in all images is 0.6 mas × 0.2 mas at a position angle of 0°. The details of the images can be seen in Table 5.5. At the right side the epochs of the observations are displayed. 1 mas corresponds to 4.85 pc in the source frame.

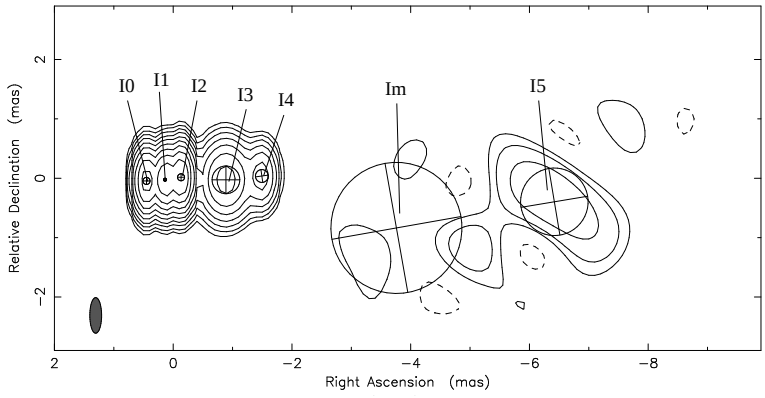

Figure 5.6: Image of Gaussian model-fit of B 2007+777 in epoch 1999.685. Circles characterize the positions and sizes of individual model-fit components. Contours result from the convolution with the observing beam. The peak flux density is 0.691 Jy/beam, the contours are in percentage of the peak and increase by a factor of two (lowest contour is 0.2 % of the peak flux density). The beam is displayed in the lower left corner of the image. The beam size is 0.95 mas × 0.76 mas at a position angle of −35°.

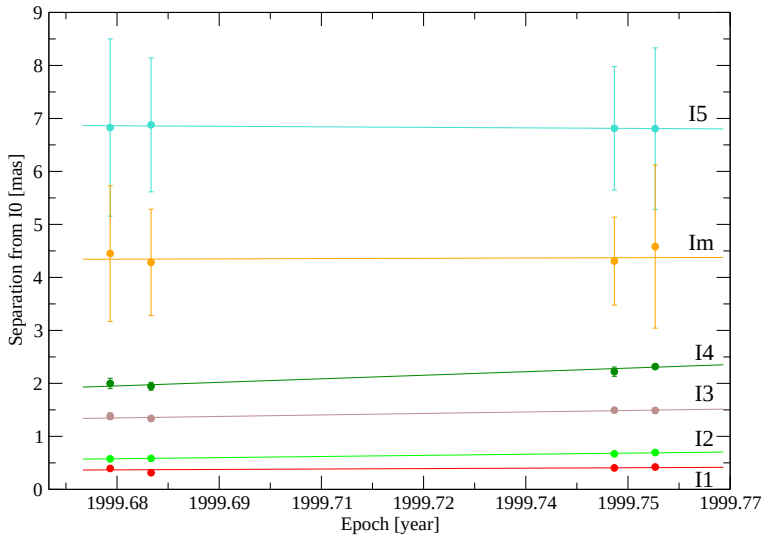

Figure 5.7: Component separations from the easternmost component as a function of time. Different colours represent different components. Lines are linear regressions to the data.

sum of I5 and Im components are assumed to be non-variable through all four epochs.) In table C.1 in Appendix C, the normalized flux-density values are given. After these corrections, the changes of the flux densities of the components were checked. Almost all the inner components (I0, I1, I2, I4) showed flux density changes. However, these changes were in almost all epochs and all components are within the errors of the flux density measurements. There is no clear trend, the components show independent variations; for example I0 and I1 decreased between 1999.679 1999.685, whilst I2 and I4 increased. If the variations are real, the assumed core I0 and the component I2 experienced the biggest flux density changes (30 % and 20 %, respectively) on a timescale of one day. The derived brightness temperatures are for component I0 $4 \cdot 10^{15}$ K and for component I2 $2 \cdot 10^{15}$ K. The Doppler factors required to reduce them to the inverse-Compton limit are 16 and 13, respectively.

The component position angles (measured from north through east) suggest that the jet starts in a direction of $-85°$ and at larger separations of 5 mas and 7 mas turns toward $-100°$ and $-90°$. Comparing the model-fit results to the total intensity images, it is clear that the fitted components cannot describe perfectly the complex inner morphology of the source. Especially the images from September suggest that the fitted components I3 and I4 are likely to be a blending of multiple subcomponents.

The core separation of the components are displayed in Fig. 5.7. The positions of the outer components Im and I5 are not well defined because of their larger extent, they are partly resolved out on the HALCA baselines. Three of the inner components (I2, I3, and I4) showed significant position changes during the observing period of one month. If these are real, they imply apparent superluminal speeds for component I2 29.7 ± 2.3, for component I3 37.7 ± 7.9 and for component I4 even as high as 92.0 ± 14.4. (The last value would imply a minimum Lorentz factor of $\gamma_{\mathrm{min}} = 92.0 \pm 14.4$ and $\psi_{\gamma_{\mathrm{min}}} = 0.6° \pm 0.1°$, see equations 1.10 and 1.11.)

However, these large values can be the result of the above-mentioned blending of

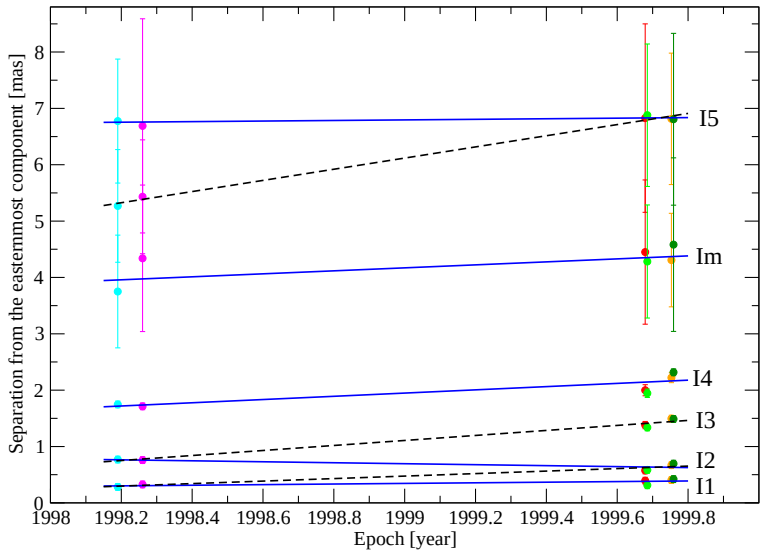

Figure 5.8: Component separations from the easternmost component as a function of time. Different colours represent different epochs: cyan 1998.19, magenta 1998.26, red 1999.679, light green 1999.685, orange 1999.753 and dark green 1999.759. Lines are linear regressions to the data. Solid blue and dashed black lines represent different identification scenarios.

multiple subcomponents. To confirm the apparent speeds of the components, previous VSOP observations of the source (epoch 1998) were model-fitted[3]. The source could be best described by seven components in those datasets as well, however the identification of the components after a year is not straightforward. In Fig. 5.8, possible identification scenarios are displayed as linear regression to the components. It is clear, that more data at intervening epochs would be needed, to unambiguously determine the motions of the components.

In the scenario represented by solid blue lines in the figure, the components move with moderate apparent superluminal speeds, ranging from (0.05 ± 0.03) mas/yr to (0.3 ± 0.08) mas/yr, which correspond to $\beta_{\rm app} = 1.2 \pm 0.5$ and $\beta_{\rm app} = 6.2 \pm 1.6$, respectively. (There is one component, which seems to be moving backwards with an apparent speed of (0.09 ± 0.03) mas/yr, corresponding to $\beta_{\rm app} = -1.8 \pm 0.7$.) The minimum Lorentz factor of the jet and the corresponding viewing angle can be estimated from the maximum observed component speed (see equation 1.10 and 1.11). In this scenario, the minimum Lorentz factor and the corresponding viewing angle of the jet are: $\gamma_{\rm min} = 6.3 \pm 1.6$ and $\psi_{\gamma_{\rm min}} = 9.2^\circ \pm 2.3^\circ$.

However, in this scenario, I3 would be identified with a new component as it does not have predecessor in 1998. Additionally there is one outer component in 1998 which was not detected in 1999. The dashed black lines in Fig. 5.8 represent another possible identification for these two components. Because the highest apparent speed ($\beta_{\rm app} = 33.5 \pm 6.6$) is obtained for a large, partly resolved component, in calculating the minimum Lorentz factor and corresponding angle of the jet, the fastest inner jet component value is used. This is (0.45 ± 0.03) mas/yr corresponding to $\beta_{\rm app} = 9.5 \pm 0.6$. This implies

[3]Data reduction was done by T. P. Krichbaum

Table 5.5: The details of the HALCA polarization and total intensity images displayed in Fig. 5.9. Col. 2 and 5 are the peak flux densities of the total-intensity images and polarized-intensity images respectively. Col. 3 and 6 are the lowest positive contour in percentage of the peak flux density in the total-intensity images and polarized-intensity images respectively. The contour levels increase by factors of two. Col. 4 and 7 are the residual noise of the total-intensity and polarized-intensity images respectively.

Epoch		*I* map			*P* map	
	Peak	Contour	Noise	Peak	Contour	Noise
	[mJy/beam]	[%]	[mJy/beam]	[mJy/beam]	[%]	[mJy/beam]
1999.679	289.0	1.0	0.3	18.8	3.0	0.04
1999.685	246.3	1.0	0.3	22.1	2.2	0.03
1999.753	321.2	1.0	0.4	18.7	3.0	0.03
1999.759	318.0	0.8	0.3	18.7	3.0	0.03

$\gamma_{\rm min} = 9.6 \pm 0.6$ and $\psi_{\gamma_{\rm min}} = 6.0^\circ \pm 0.4^\circ$.

Neither of these identification scenarios show apparent speeds of the inner jet components as large as was suggested by the four 1999 epochs. These discrepancies can indicate that the chosen reference point (the easternmost component) is not stable, and/or that the innermost components may move on bent trajectories.

Polarization data

In Fig. 5.9 the polarized intensity structure of B 2007+777 as revealed by the space-VLBI data is displayed. The left panels show the total intensity images with superimposed polarization vectors, the right panels show the polarized intensity contours with two contours of total intensity. Details of the images are given in Table 5.5.

As described in the previous section, the polarized intensity and the total intensity and the average value of the polarization angles of the polarized components were measured. Here, however, the polarized-intensity and total-intensity components barely coincide, therefore the total intensity given in Table 5.6 was integrated over the same region in the total intensity images, as in the polarized images regardless of the total intensity structure of the source. The data are given in Table 5.6. In different epochs, different numbers of polarization features appear. However, features P2, P3 and P4 are visible through all the epochs.

For component A1 the polarization is very close to the detection limit at this resolution. Polarization in this component was detected (and denoted as P5) in two epochs out of the four (1999.685 and 1999.759). The measured values of P and χ are consistent with the values measured using the the ground array.

At the position of component A0, several polarized subcomponents (denoted as P0, P1, P2, P3 and P4) are seen in the high resolution images. P2 gives the largest contribution to the polarized intensity in all the epochs and is also the dominant polarized component in the ground baseline images. Now with the higher resolution images, it is clear that P2 does not coincide with any of the total-intensity features but rather is located between the components I1 and I2.

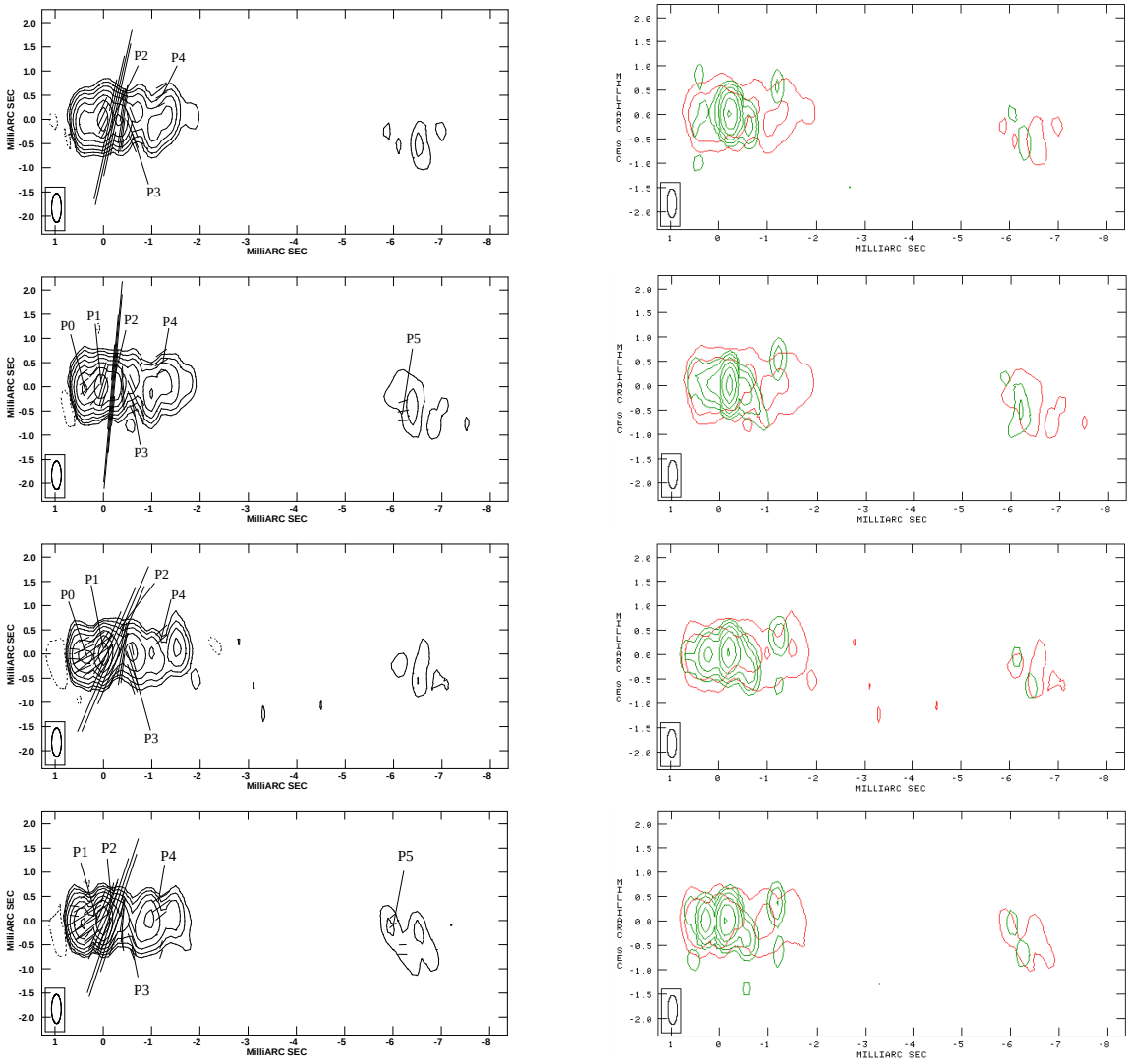

Figure 5.9: HALCA polarization images of B 2007+777. From top to bottom the epochs are: 1999.679, 1999.685, 1999.753 and 1999.759. Left panels: total intensity contours with polarization vectors superimposed. 1 mas corresponds to 5 mJy/beam. Right panels: contour images of the polarized intensity (green) with two contours of the total intensity (red) superimposed. The beams are displayed in the lower left corner of each image, the beam sizes in all cases are 0.6×0.2 mas. Peaks and contour levels of the images are displayed in Table 5.5.

The EVPA in P2 is $-10°$ to $-20°$. To the east of P2, in the direction of the assumed core, the EVPAs are significantly different: $-35°$ and $-55°$ in P1 and $-80°$ in P0. If P2 is assumed to be an optically thin inner jet component, then the magnetic field is perpendicular to the EVPA, and hence the magnetic field is roughly parallel to the inner jet direction at this location. However, Gabuzda & Pashchenko (2002) report that there is evidence that the spectrum flattens roughly at this position, which then implies an optically thick component, where magnetic fields are perpendicular to the jet direction. Longitudinal fields have been thought to reflect the interaction between the jet and the surrounding medium, whilst transverse magnetic fields have usually been interpreted as relativistic shocks in

Table 5.6: Total intensity and polarized intensity and polarization angle of B 2007+777 measured including the space baselines (see 5.9). Col. 2 is the total intensity, Col. 3 is the polarized intensity and Col. 3 is the polarization angle, measured from north to east.

Epoch	Comp.	I [mJy]	P [mJy]	χ [°]
1999.679	P2	370.3 ± 17.4	25.7 ± 3.7	−12.0 ± 2.8
1999.679	P3	80.9 ± 7.2	5.7 ± 1.6	16.5 ± 13.0
1999.679	P4	9.9 ± 4.5	1.2 ± 0.6	−76.0 ± 17.9
1999.685	P0	124.8 ± 36.4	1.5 ± 0.4	−71.3 ± 14.0
1999.685	P1	307.8 ± 34.2	4.0 ± 0.8	−34.7 ± 2.5
1999.685	P2	319.7 ± 26.1	22.4 ± 2.0	−5.3 ± 4.9
1999.685	P3	171.3 ± 43.7	7.4 ± 3.0	21.6 ± 6.7
1999.685	P4	18.9 ± 4.2	1.5 ± 0.6	−48.4 ± 13.0
1999.685	P5	12.4 ± 1.0	1.6 ± 0.3	101.8 ± 2.7
1999.753	P0	105.1 ± 33.4	2.0 ± 0.6	−84.4 ± 34.0
1999.753	P1	407.9 ± 39.4	9.5 ± 0.9	−55.3 ± 3.7
1999.753	P2	352.7 ± 19.2	25.6 ± 1.2	−21.1 ± 4.8
1999.753	P3	78.2 ± 9.7	5.9 ± 1.2	12.1 ± 11.9
1999.753	P4	19.3 ± 8.9	2.2 ± 0.4	−46.5 ± 9.7
1999.753	P5	9.7 ± 1.5	1.2 ± 0.2	91.3 ± 7.9
1999.759	P1	339.1 ± 30.4	8.9 ± 1.9	−55.1 ± 20.9
1999.759	P2	347.1 ± 47.3	28.0 ± 2.1	−16.9 ± 4.6
1999.759	P3	42.3 ± 11.6	4.4 ± 0.6	14.8 ± 7.8
1999.759	P4	28.9 ± 4.1	2.4 ± 0.6	−48.9 ± 6.4
1999.759	P5	9.6 ± 2.5	1.3 ± 0.2	113.3 ± 6.0

the VLBI jets, that enhance the magnetic field component in the plane of compression, perpendicular to the direction of the propagation of shocks (Laing 1980; Hughes et al. 1989). The observed polarization of P2 is more suggestive of a shock-induced polarization enhancement.

In the case of P1, the orientation of the magnetic field with respect to the jet direction is not clear, it does not seem to be either parallel or perpendicular to the jet direction.

If P0 originates in the optically thick core (as suggested by the VSOP images), then the direction of the magnetic field is parallel to the EVPA, and hence the magnetic field is parallel to the jet axis at this point. Otherwise, were the core optically thin then the magnetic field would be perpendicular to the jet direction. Alternating aligned and orthogonal polarization vectors were observed in other BL Lac objects: Gabuzda & Gómez (2001) reported on the VSOP polarization observations of OJ 287 and Gabuzda (2003) on B 1418+546.

The components P3 and P4 are suggestive of a so-called “edge-brightening” in polarization. These components appear only in polarization at the outer edges of the jet, one to the south and one to the north. They do not coincide with total-intensity features. They do not show significant polarization angle variations and, in polarized intensity, the changes are also within the error bars. They may result from the interaction between the jet and the surrounding medium or from the jet instabilities (as seen for example in 3C 273 Lobanov

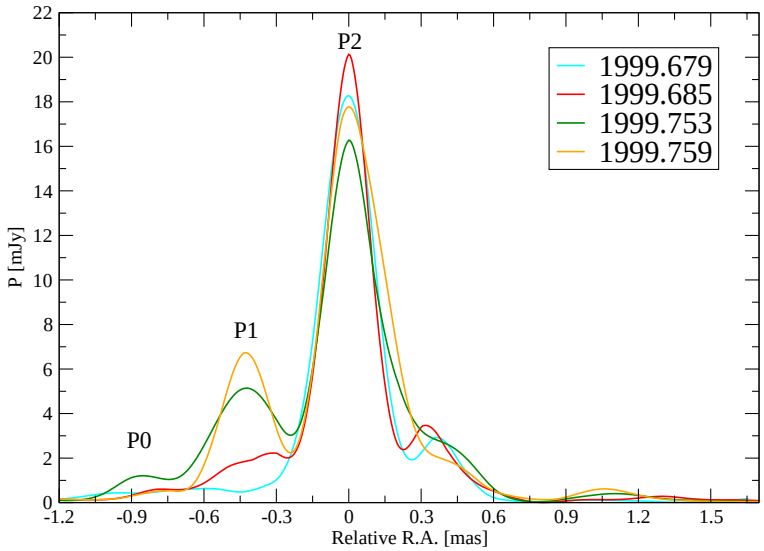

Figure 5.10: Slices through linear polarization intensity VSOP images of the central region of B 2007+777. Different colours correspond to different epochs (see legend). The curves are shifted in a way that the maximum corresponds to zero R. A. in the diagram.

Table 5.7: The variations in polarized intensity of the components P0 and P1. The epochs, components name, the average polarized intensity, its standard deviation, the calculated brightness temperatures are listed. In the last two columns the Doppler factors are listed, which required to reduce the apparent brightness temperatures to the inverse-Compton (δ^{iC}) or to the equipartition limit (δ^{eq}).

Epoch	Comp.	$\langle P \rangle$ [mJy]	ΔP [mJy]	T_{B} [K]	δ^{iC}	δ^{eq}
1999.679-1999.685	P0	1.05	0.67	$1.3 \cdot 10^{14}$	5.1	10.9
1999.679-1999.685	P1	2.30	2.40	$8.5 \cdot 10^{14}$	9.5	20.4
1999.753-1999.759	P0	1.28	1.02	$2.7 \cdot 10^{17}$	64.6	139.3
1999.753-1999.759	P1	9.20	0.42	$6.6 \cdot 10^{12}$	1.9	4.0

& Zensus 2001).

Fig. 5.10 shows profiles of the polarization along the inner jet of B 2007+777. The slices were made at a position angle of 90° through P0, P1 and P2 polarized features. The figure illustrates the systematic polarization increase of P1 and an increase followed by a decrease of P2. In the first epoch no polarization could be detected at the position of P0, however in the following epochs the polarized intensity increased significantly. An increase in polarized intensity of P1 was detectable within the two days time between the first two observational epochs, and a month later the polarized flux density of P1 increased by more then 50 %. The sudden appearance of P1 (and P0) can be related to a component ejection. The resolution was not sufficient to detect this assumed component and it was not bright enough to significantly change the total intensity values, but it was still able to introduce detectable (with high resolution VSOP observations) polarization. In that context, one can imagine that a component moved along the jet until it reached the steady shock P2 and caused the changes in the polarization angle that we observed.

Assuming that the polarization variability originates in the source within a compact component, the brightness temperature can be calculated from the polarized flux density variations (see Sect. 1.3). On September 5 neither P0 nor P1 could be seen. Assuming that the minimum detectable polarization is 0.6 mJy[4] the mean polarized intensity between 5th and 7th of September ($\langle P \rangle$) and the standard deviations (ΔP) can be calculated for P0 and P1. The resulting brightness temperatures, using equations 1.4, 1.16, and 1.15, are both in excess of the inverse-Compton limit (see Table 5.7). To reduce these values to the inverse-Compton limit in the source frame, the Doppler factors of 5.1 and 9.5 are needed for components P0 and P1 respectively. Using the equipartition limit the necessary Doppler factors are roughly doubled.

There was significant variation in P1 between October 2 and 4 as well implying a lower brightness temperature than that in September but still above the inverse-Compton limit (see Table 5.7). The Doppler factor required to reduce this to the inverse-Compton limit is 1.9, or using the equipartition limit the Doppler factor is 4.0. In the last epoch, P0 could not be detected as it was very close to the noise limit. From the image of the polarized variability the upper limit to its polarized flux density can be estimated to be 0.6 mJy. Thus its rate of decrease of polarized intensity corresponds to a brightness temperature of $2.7 \cdot 10^{17}$ K. The Doppler factor required to reduce this to the inverse-Compton limit 65, or using the equipartition limit is 140.

5.3 Conclusions

To reveal the origin of the variability in the IDV source, B 2007+777 was observed in four closely-spaced epochs separated by two days, 25 days and 2 days, respectively in 1999 with VSOP. These observations were part of a larger project in which a couple of IDV sources were observed with space-VLBI to search for changes in total intensity and in polarization of the source at highest achievable resolution and on the shortest time-scales.

In this campaign, the VSOP observations of S5 0716+714 revealed fast variations in polarization within the core of the source and showed that the IDV is associated with the core region. The polarization angle variations in this source suggest that the observed polarization is the result of more than one compact sub-component on scales smaller than the beam size (Bach et al. 2005).

During the VSOP observations in 1999, B 2007+777 did not display such dramatic changes as S6 0716+714. The mild variations seen in total intensity were produced by the variations of the individual inner jet components resolved by the VSOP data.

In polarization, larger variations were detected. Two polarized features close to the core appeared in the second epoch and increased (and decreased) in flux density through the later epochs. Additionally, the polarization angle of the dominant polarized feature, P2, changed significantly by 16° between September 7 and October 2, 1999.

The appearance of the polarized subcomponent, P1 in the epoch September 7, 1999 could be the result of the ejection of a new component that was not separated enough from the core to be resolved and could therefore be observed only through its polarization. An

[4]This is conservative upper limit value using the minimum polarization of P4 (1.2 mJy to 0.6 mJy), see Table 5.6.

ejection of a new component can increase the pressure in the jet and the compression can result in stronger magnetic field which can be detected as increase in polarization.

The brightness temperatures deduced from the variations in polarized intensity require Doppler factors in the range of 2 to 65 to reduce them to the invserse-Compton limit. Assuming the equipartition limit instead of the inverse-Compton limit, the required Doppler factors are roughly doubled.

To determine the total-intensity components' speed and the jet viewing angle, the four epochs analyzed here were combined with two epochs of VSOP observations obtained one year earlier (1998). However, the component identification turned out to be difficult. Apparent speeds from $1.2\,c$ to $9.5\,c$ are obtained depending on the identification scenario. The minimum Lorentz speed of the jet and the derived Doppler boosting factors (5.6 and 9.5) are consistent with most of the values obtained from the polarization variations. There were indications of changes in the component positions even during 25 days, which would imply even higher Doppler factors. However those apparent speeds were not confirmed by the long-term (one year) data. A better constraint on the speeds could be obtained if additional intervening epochs were available. Possibly, the publicly available data of the 2 cm Survey of the source will help.[5]

A lower limit to the brightness temperature was obtained from the Gaussian model-fit of the brightest unresolved component, I1. This was in between $8.9 \cdot 10^{12}$ K and $12.6 \cdot 10^{12}$ K, requiring a Doppler boosting factor of two, or a Doppler factor of five in the case of using the equipartition limit.

[5]Ground based 15 GHz observations have roughly the same resolution as the 5 GHz VSOP data.

6 Summary and outlook

In this thesis, the different aspects of propagation effects on radio loud AGN were investigated. Flux-density variations of flat spectrum extragalactic radio sources on different time-scales were discussed and the study of a scatter-broadened compact quasar were presented.

The theory of refractive interstellar scintillation of the IDV phenomenon provided explanations for a number of the observed variability characteristics. However, some difficulties remain. The observed discrepancy of the frequency dependence of the variability from the the predictions of RISS can indicate source-intrinsic contributions to the variability. The RISS model might not yet be developed enough to explain all of the observations.

IDV sources at different Galactic latitudes. The distance to the scattering material is one very important parameter. An observation was carried out in order to compare lines of sight passing through very different amounts of interstellar matter. Short time-scale variations of the flux density of flat spectrum extragalactic radio sources were measured towards the Cygnus region and the Lockman Hole. No significant differences between the variability characteristics of the two samples of sources were detected. This result is consistent with the picture that the interstellar material responsible for IDV is nearby (at a distance of $\lesssim 100\,\mathrm{pc}$).

Towards the Cygnus region, the measurements suggested that the higher the Hα intensity the lower is the variability amplitude. This, however, might be the result of the large-scale distribution of Galactic material. Those sources, whose lines of sight pass through more Galactic material, are more probably subject to scatter broadening. The scatter-broadened, sources however, experience quenched scintillation because of their apparently larger extent.

Studies of the local interstellar medium and particularly the shape of the Local Bubble revealed that, in the direction of the Lockman Hole, the Local Bubble is open-ended, no boundary was observed at least up to 250 pc. Therefore, the IDV observed in that direction cannot be associated with the boundary of the Local Bubble as it is often assumed in the case of other IDV sources. The observed IDV in that direction alternatively may be caused by the ionized clouds in this Local Chimney.

The source J 1128+5925. The most variable IDV source in this observation was detected in the Lockman Hole direction. J1128+5925 showed $\sim$ 20 % peak-to-peak variations during $\sim$ 7 h. Subsequent observations high time-sampling revealed that the variability time-scale of the source changed. The measurements were consistent with an annual modulation of the variability, caused by the orbital motion of

the Earth. Particularly the two observations in December, separated by one year, yielded remarkably similar time-scales and suggested that the source is fastest in winter. J 1128+5925 is a promising new candidate for further studies of seasonal cycles.

Scatter broadening of B 2005+403. The highly scatter-broadened quasar B 2005+403 provides an interesting opportunity to study the interplay between source-intrinsic and source-extrinsic effects. The ISM causes scatter-broadening of the source image up to 8 GHz. At higher frequencies, however, the underlying intrinsic source structure can be studied. The low-frequency VLBI observations presented here provided the size of the scattering disk, the Scattering Measure and the exponent of the power law of the density fluctuations. The non-canonical value ($\beta = 4$) of this exponent implies either a non-Kolmogorov power spectrum or a lower limit to the inner scale, which would be 60 % larger than the previously reported value for this region.

Quenched IDV in B 2005+403. Densely time-sampled variability measurements revealed that B 2005+403 exhibits weak IDV at 1.6 GHz. The measured time-scale was not consistent with a scattering screen located at 2.35 kpc, proposed to cause the angular broadening. Most probably, in the case of B 2005+403, multiple scattering occurs; the already scatter-broadened image is scattered a second time at a closer screen at a distance of a few pc.

Intrinsic structure of B 2005+403. VLBI observations spanning 13 years, performed at high frequencies, revealed the intrinsic structure of B 2005+403. B 2005+403 has a bent core-jet structure with superluminally moving (with apparent speeds range between 8 c and 15 c) and stationary components. The VLBI core of B 2005+403, atypically of most of the quasars, is not the brightest component and it is not the one exhibiting the biggest flux-density changes. The brightest, most varying component is stationary and could be explained as a sharp bend in the jet.

Long-term flux-density variability in B 2005+403. B 2005+403 is also unusual in the sense that no component ejection was detected during 13 years. However, long-term, multi-frequency single-dish flux density monitoring revealed remarkable changes of its total flux density. B 2005+403 is heavily influenced by scattering. However, these variations in flux density could not be described as an "extreme scattering event". It was well explained by the summed flux density variability of the independently varying VLBI components.

VSOP observation of the IDV blazar, B 2007+777. Several blazars showing IDV were observed with the high angular resolution of space-VLBI. These observations were aimed to reveal changes in the total intensity and polarization structure of the sources on time-scales of days to weeks.

In this thesis, observations at four epochs of the blazar B 2007+777 were analyzed and discussed. Significant changes in polarization appeared during a two day-long time-scale and a 25 day-long time-scales. The calculated variability brightness temperatures are in excess of the inverse-Compton limit, and thus require Doppler

boosting factors in the range of 2 to 11 and one as high as 65 to bring the intrinsic brightness temperatures below the inverse-Compton limit. The physical cause of this polarization variability is unclear and further data at additional frequencies are needed for a better understanding.

In total intensity, the flux-density changes were not dramatic. The apparent speeds of the VLBI-components were derived by combining the data with previous measurements. The calculated apparent speeds and required minimum Lorentz factors and Doppler factors were consistent with most (except the highest) Doppler factors obtained from the variations of polarized flux density.

Future projects

It is most probable that the main cause of the IDV phenomenon is the refractive interstellar scintillation of radio waves in the turbulent ISM of the Milky Way. However, as was demonstrated in this thesis, source intrinsic contributions can play an important role as well. Moreover, even the different scattering phenomena can work against each other, i.e. scatter broadened sources experience only quenched IDV in the Local ISM. Distinguishing between source-intrinsic and extrinsic propagation-induced variability is essential, especially in those particularly interesting IDV sources that do not follow the prediction of RISS theory.

New, frequent, densely-sampled measurements of J 1128+5925 are desirable to better constrain the parameters of the so-called annual modulation scenario. This can provide information on the characteristics of the scattering screen responsible for the IDV. Observations primarily aimed to confirm the annual modulation scenario would also answer the question, whether the detected variations in the modulation index of are real. Changes in the modulation index cannot be explained in the framework of this scenario and may indicate contributions to the observed IDV from source-intrinsic changes.

The flux-density monitoring of J 1128+5925 should be accompanied with VLBI imaging of the source in the near future. Since very little is known about the source itself, these observations would allow one to distinguish possible intrinsic contributions to the RISS induced IDV.

B 2005+403 has been observed within the MOJAVE survey. New epochs of observations can help to better understand the jet and the component trajectories as well as their flux-density evolution. The MOJAVE observations are performed in full polarization, which should provide even more insight to the variable source structure.

The four epochs of space-VLBI observations of B 2007+777 presented here indicate an unusually high apparent speed of some components. These were not seen in earlier observations. However, component identifications through all the six epochs were not unambiguous. Therefore, a more thorough analysis of preferably in combination with archive ground-based VLBI observations at 15 GHz, is worthwhile.

A IDV observations

A.1 The statistical tests

The "Difference of Two Propostions" test and the "Yates Correction" were used in testing whether the observed difference of IDV detection rate in the two different samples of sources are significant.

The probability of detection IDV sources is given by the binomial distribution. The binomial distribution can be approximated by normal distribution if the sample is sufficiently large (e.g. Glantz 1992). That means, if $Np > 5$ and $N(1-p) > 5$, where N is the size of the sample and p is the probability of the detection.

We tested the null hypothesis, that the two samples are come from the same parent population and the detection rate of IDV in the two samples are the same $H_0 : n_\mathrm{L}/N_\mathrm{L} = n_\mathrm{C}/N_\mathrm{C}$, where $n_\mathrm{L}/N_\mathrm{L}$ is the IDV detection rate in the Lockman Hole area and $n_\mathrm{C}/N_\mathrm{C}$ is the IDV detection rate in the Cygnus area. $n_\mathrm{L}/N_\mathrm{L}$ and $n_\mathrm{C}/N_\mathrm{C}$ have approximately normal distribution, thus $n_\mathrm{L}/N_\mathrm{L} - n_\mathrm{C}/N_\mathrm{C}$ has also approximately normal distribution, and according to the null hypothesis it has approximately zero mean. The test statistics estimating the standard deviation of the distribution $n_\mathrm{L}/N_\mathrm{L} - n_\mathrm{C}/N_\mathrm{C}$ is (e.g. Glantz 1992):

$$z = \frac{\dfrac{n_\mathrm{L}}{N_\mathrm{L}} - \dfrac{n_\mathrm{C}}{N_\mathrm{C}}}{\sqrt{p\,(1-p)\left(\dfrac{1}{N_\mathrm{L}} + \dfrac{1}{N_\mathrm{C}}\right)}}, \tag{A.1}$$

where p is the best estimate of the detection rate, given as $p = (n_\mathrm{L} + n_\mathrm{C}) \,/\, (N_\mathrm{L} + N_\mathrm{C})$. The table of normal curve was used to determine the level of significance for the test.

This test statistic in the normal table is assumed to be a continuous variable, however the number of detected IDV sources can only take integer values. The assumption of continuity can make to seem the test more significant. The "Yates Correction" correct for this effect. Using this correction the test statistic becomes:

$$z = \frac{\left|\dfrac{n_\mathrm{L}}{N_\mathrm{L}} - \dfrac{n_\mathrm{C}}{N_\mathrm{C}}\right| - \dfrac{1}{2}\left(\dfrac{1}{N_\mathrm{L}} + \dfrac{1}{N_\mathrm{C}}\right)}{\sqrt{p\,(1-p)\left(\dfrac{1}{N_\mathrm{L}} + \dfrac{1}{N_\mathrm{C}}\right)}} \tag{A.2}$$

In Sect. 3.5.1, the significance calculated with and without the "Yates correction" are both given. It is shown, that with the "Yates correction" the result of the test changes, the usage of this correction is important.

A.2 IDV light curves

Light curves from IDV observation performed in December 2004 with the Effelsberg 100 metre radio telescope at 5 GHz. In Fig. A.1, A.2, A.3 and A.5, the top lines of the plots list the source names, the mean intensities and the standard deviations. The left ordinates show the absolute intensities in Jy, the right ordinates show the normalized intensities.

In Fig. A.6 and A.7 the light curves of those sources shown in which significant polarized flux densities were detected. The first panel displays the total flux density, the second panel the polarized flux density (P), the third panel the polarization angle (χ). In the header of every plot the source name, the average value and the standard deviation of the plotted observable are displayed. The left ordinates show the absolute values in Jy or degrees, the right ordinates show the normalized values.

The abscissa in every cases display a modified Julian date (J.D.-2450000).

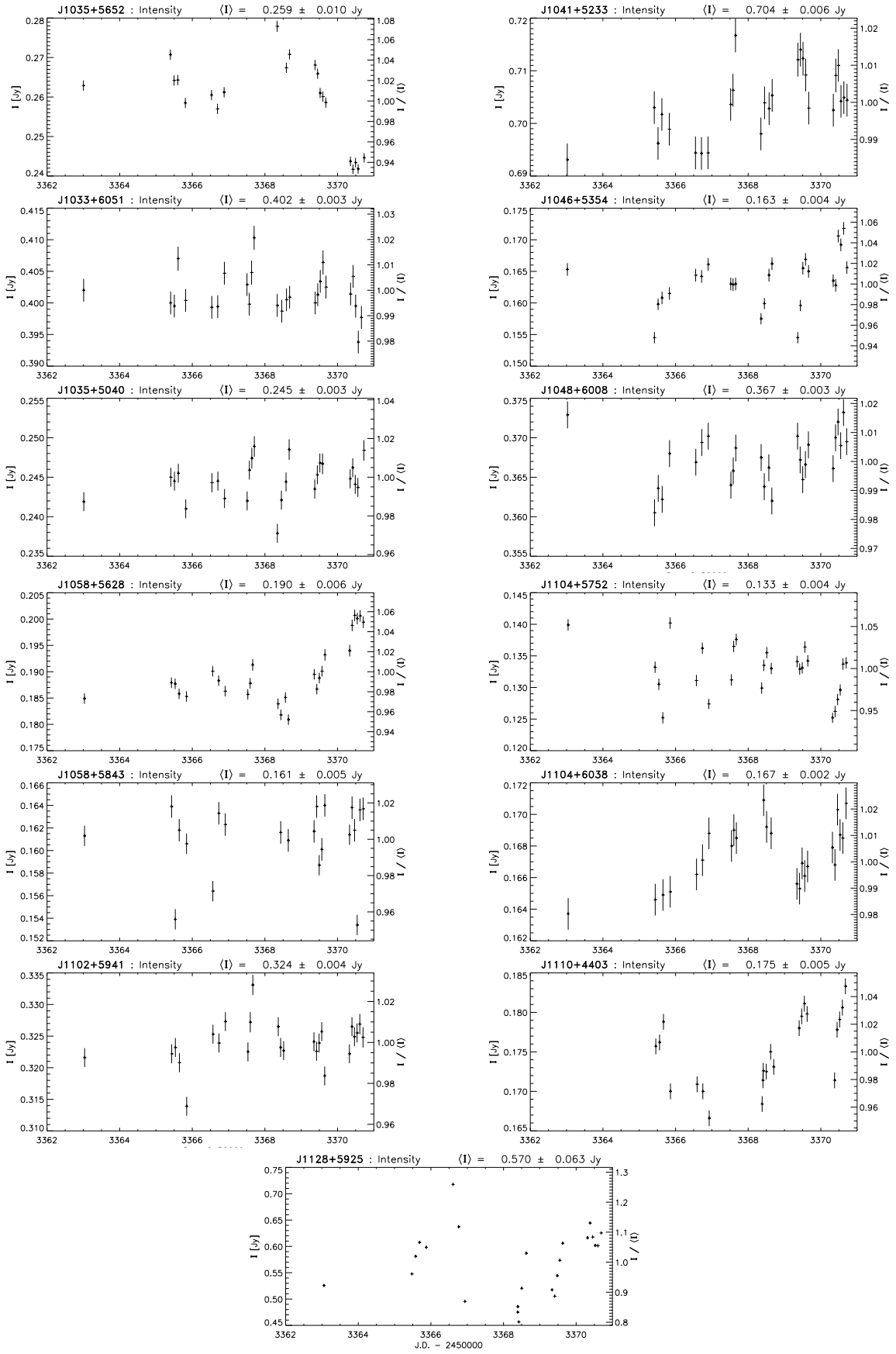

Figure A.1: Light curves of the sources seen towards the Lockman Hole region.

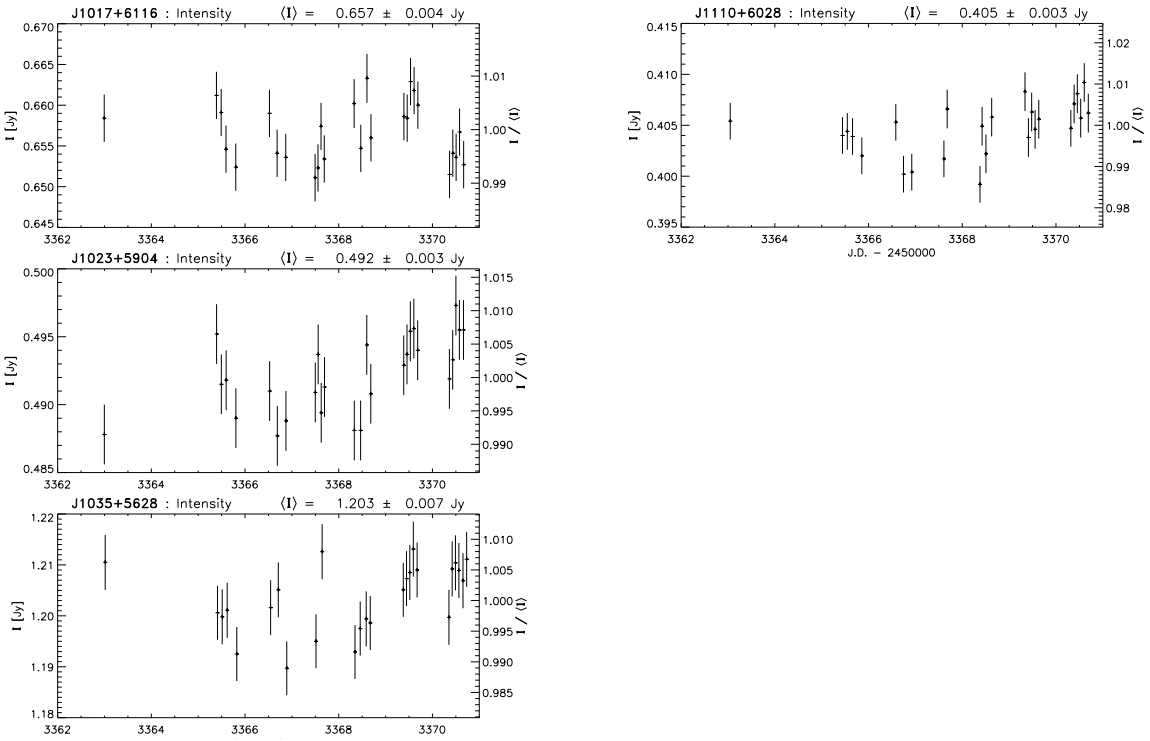

Figure A.2: Light curves of the sources seen towards the Lockman Hole region (cont).

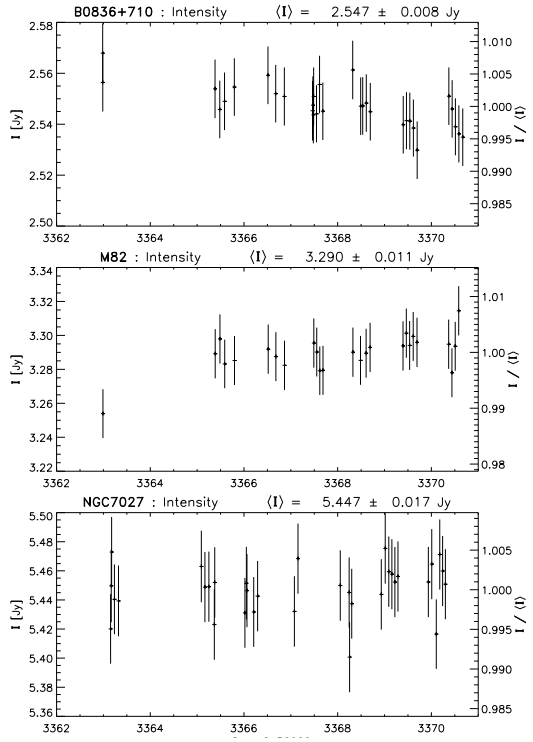

Figure A.3: Light curves of three secondary calibrators.

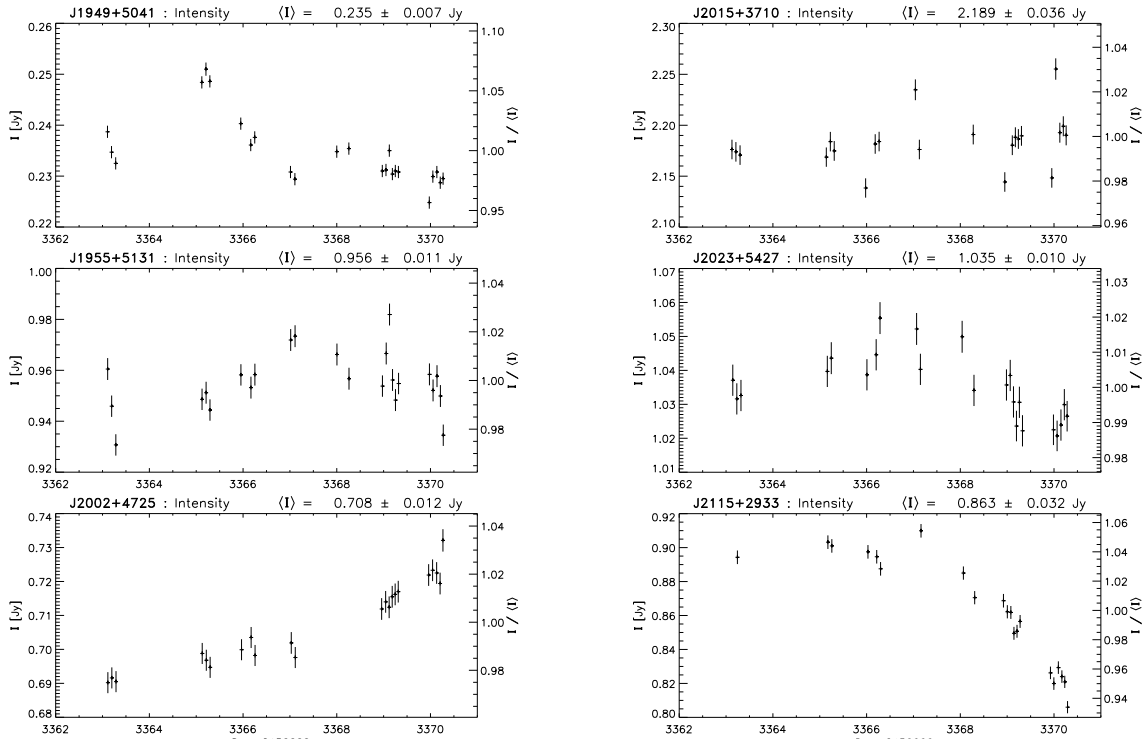

Figure A.4: Light curves of the sources seen towards Cygnus region.

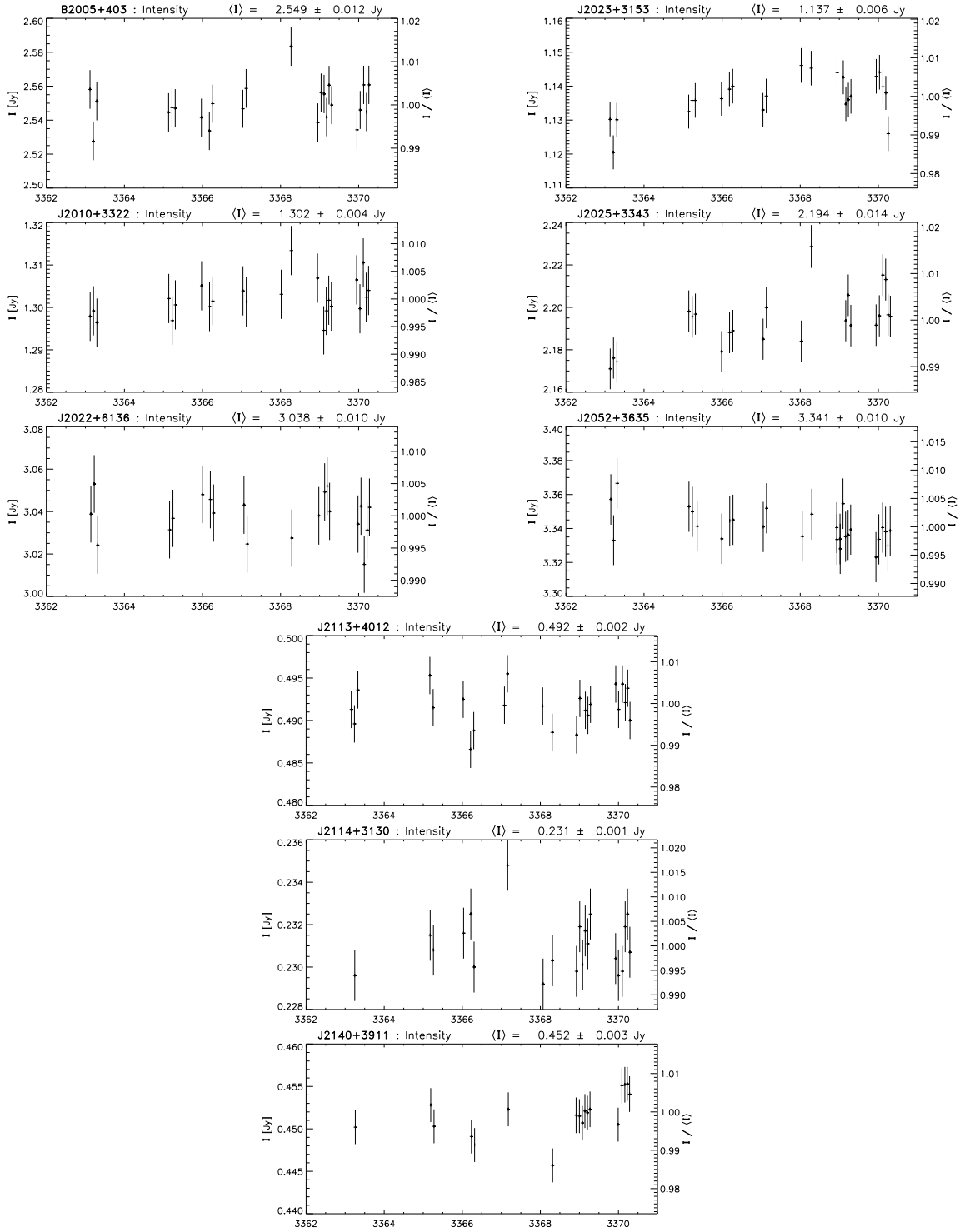

Figure A.5: Light curves of the sources seen towards the Cygnus region (cont).

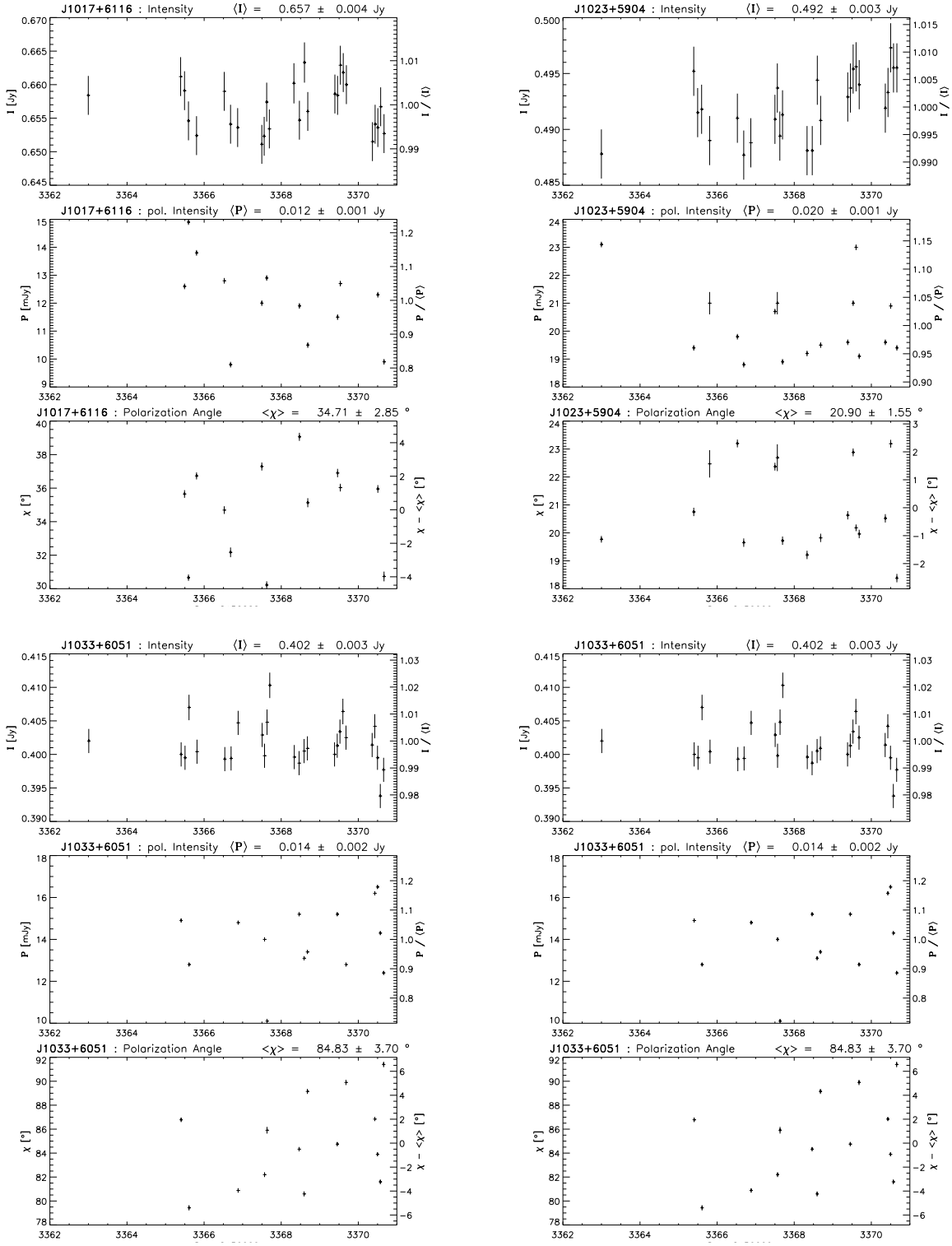

Figure A.6: Total and polarized flux density light curves and variations in the polarization angles of four sources.

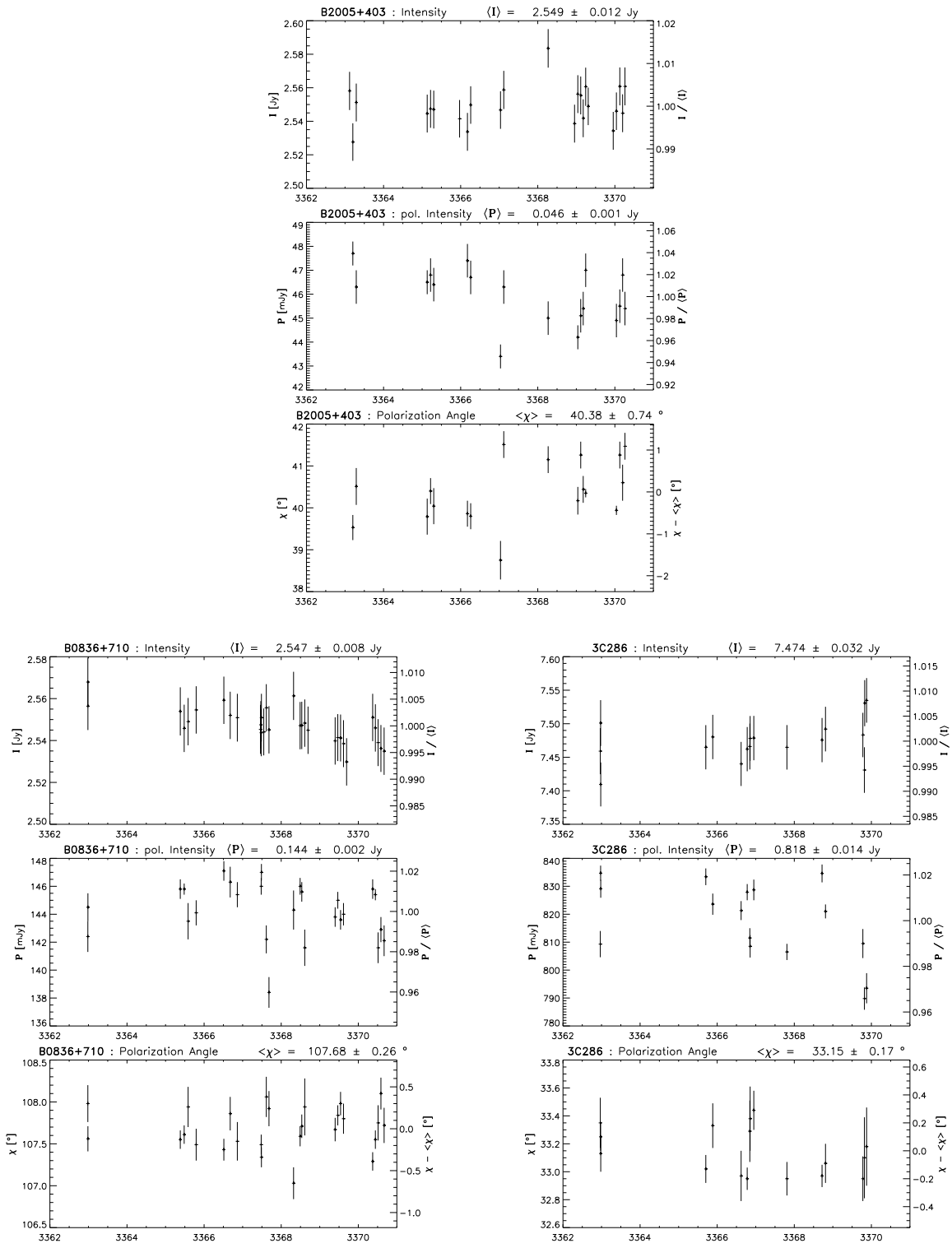

Figure A.7: Total and polarized flux density light curves and variations in the polarization angles of four sources. The two plots at the bottom are polarized calibrator sources.

B B 2005+403 model-fitting results

The results of the Gaussian model-fits with DIFMAP and by the AIPS task are displayed in this appendix. The tables contain the parameters of the model components. The figures show the maps of the Gaussian model-fits.

Table B.1: The parameters of the Gaussian model-fits. The table contains the following information: Col. 1 gives the observing epoch, frequency and VLBI array, Col. 2 identifies the VLBI components by letters and numbers, Col. 3 gives the flux density of each VLBI component (S), Col. 4 its radial distance (r) relative to component C1, Col. 5 the position angle (θ), Col. 6 the FWHM major axis (a), Col. 7 the ratio of minor to major axis (b/a), Col. 8 the position angle of the major axis (ϕ), and Col. 9 the reduced χ^2 (χ^2_r) to characterise the goodness of the model-fit. The positional information (Columns 4 and 5) is relative to the westernmost component, denoted as C1.

Epoch, array and frequency	Comp.	S [Jy]	r [mas]	θ [°]	a [mas]	b/a	ϕ [°]	χ^2_r
(1)	(2)	(3)	(4)	(5)	(6)	(7)	(8)	(9)
1998.14	M1	2.365	0.00	–	29.76	0.8	37.5	4.5
EVN								
1.6 GHz								
Errors		4 %			7 %	3 %	3°	
1996.82	M1	2.572	0.00	–	3.48	0.70	32.1	2.6
EVN	M2	0.488	2.67	129.7	3.24	1.00	–	
5 GHz	M3	0.069	8.10	138.3	6.95	1.00	–	
Errors		10 %	12 %	4°	5 %	10 %	4°	
1996.83	M1	3.418	0.00	–	1.51	0.86	65.4	1.0
EVN	M2	0.297	3.06	127.0	2.13	0.69	44.7	
8 GHz								
Errors		11 %	6 %	3°	6 %	10 %	5°	
1995.27	C1	0.852	0.00	–	0.40	1.00	–	1.0
VLBA	C2	0.755	0.39	90.0	0.37	1.00	–	
15 GHz	C3	0.666	0.77	74.8	0.37	1.00	–	
	C4	0.170	1.78	122.0	1.44	1.00	–	
	C5	0.185	3.35	116.7	1.79	1.00	–	
Errors		10 %	14 %	3°	12 %			

Table B.1: continued

Epoch, array and frequency	Comp.	S	r	θ	a	b/a	ϕ	χ^2_r
		[Jy]	[mas]	[°]	[mas]		[°]	
(1)	(2)	(3)	(4)	(5)	(6)	(7)	(8)	(9)
1995.96	C1	0.510	0.00	–	0.31	1.00	–	0.3
VLBA	C2	0.831	0.38	97.0	0.35	1.00	–	
15 GHz	C3	0.951	0.84	80.4	0.40	1.00	–	
	C4	0.106	2.12	118.9	1.34	1.00	–	
	C5	0.104	3.72	116.6	1.55	1.00	–	
Errors		10 %	12 %	4°	10 %			
1996.73	C1	0.260	0.00	–	0.28	1.00	–	0.3
VLBA+EB	C2	0.738	0.40	108.5	0.44	1.00	–	
15 GHz	C3	0.981	0.92	83.1	0.45	1.00	–	
	C5	0.185	3.16	119.0	2.38	1.00	–	
Errors		10 %	18 %	3°	10 %			
1997.19	C1	0.262	0.00	–	0.25	1.00	–	2.0
VLBA	C2	0.659	0.42	107.5	0.47	1.00	–	
15 GHz	C3	0.791	0.99	84.1	0.48	1.00	–	
	C4	0.075	2.38	119.0	1.44	1.00	–	
	C5	0.092	4.07	117.8	1.73	1.00	–	
Errors		15 %	11 %	3°	7 %			
1999.01	C1	0.396	0.00	–	0.38	1.00	–	0.5
VLBA	C2	0.510	0.61	101.4	0.68	1.00	–	
15 GHz	C3	0.422	1.18	80.4	0.67	1.00	–	
	C4	0.234	2.76	117.9	3.62	1.00	–	
Errors		12 %	17 %	3°	3 %			
2001.17	C1	0.024	0.00	–	0.17	1.00	–	3.5
VLBA	C2	1.800	0.35	138.3	0.39	0.80	38.2	
15 GHz	C3	0.764	1.31	94.3	0.83	0.69	47.0	
	C5	0.179	4.21	121.3	4.14	1.00	–	
Errors		7 %	15 %	3°	3 %	4 %	5°	
2001.98	C1	0.091	0.00	–	0.20	1.00	–	1.6
VLBA	C2	1.581	0.37	137.9	0.45	0.70	36.0	
15 GHz	C3	0.632	1.42	102.9	0.77	0.74	27.2	
	C4	0.172	3.06	112.7	3.66	1.00	–	
Errors		5 %	10 %	3°	6 %	4 %	4°	
2003.04	C1	0.188	0.00	–	0.2	1.0	–	0.3
VLBA	C2	1.714	0.37	118.0	0.40	0.79	24.2	
15 GHz	C3	0.516	1.56	97.9	0.86	0.81	29.0	
	C4	0.008	2.63	131.4	0.27	1.00	–	
	C5	0.061	4.59	121.5	2.23	1.00	–	
Errors		6 %	15 %	3°	6 %	4 %	4°	
2003.16	C1	0.223	0.00	–	0.34	0.45	30.3	1.5
VLBA	C2	2.000	0.41	120.6	0.41	0.79	25.1	
15 GHz	C3	0.566	1.60	99.5	0.85	0.89	40.7	

Table B.1: continued

Epoch, array and frequency	Comp.	S	r	θ	a	b/a	ϕ	χ^2_r
		[Jy]	[mas]	[°]	[mas]		[°]	
(1)	(2)	(3)	(4)	(5)	(6)	(7)	(8)	(9)
	C4	0.017	3.00	124.4	0.99	1.00	–	
	C5	0.034	4.84	122.0	1.63	1.00	–	
Errors		4 %	12 %	3°	4 %	5 %	4°	
2004.61	C1	0.320	0.00	–	0.31	1.00	–	1.5
VLBA	C2	1.425	0.46	111.1	0.43	1.00	–	
15 GHz	C3	0.385	1.94	94.7	0.97	0.74	26.2	
	C5	0.072	4.52	124.1	2.87	1.00	–	
Errors		3 %	10 %	3°	4 %	5 %	4°	
2005.36	C1	0.415	0.00	–	0.33	1.00	–	1.3
VLBA	C2	0.884	0.42	114.3	0.42	1.00	–	
15 GHz	C3	0.325	2.00	92.3	0.75	0.81	10.2	
	C3b	0.272	1.55	103.1	0.94	1.00	–	
	C5	0.049	4.81	123.6	2.53	1.00	–	
Errors		10 %	8 %	3°	4 %	6 %	3°	
1992.44	C1	0.337	0.00	–	0.21	0.63	88.3	2.5
EVN	C2	0.723	0.35	97.4	0.43	0.79	37.4	
22 GHz	C3	0.695	0.65	87.7	0.20	0.77	71.2	
	C5	0.217	2.37	117.3	2.29	0.10	86.0	
Errors		10 %	10 %	3°	10 %		5°	
1994.17	C1	0.570	0.00	–	0.27	0.68	−54.3	6.3
VLBA+	C2	0.796	0.40	87.7	0.28	0.56	62.8	
+VLA+EVN	C3	0.526	0.81	82.4	0.24	0.85	22.7	
22 GHz	C5	0.157	2.56	112.7	2.32	0.92	−2.7	
Errors		18 %	12 %	3°	18 %		4°	
1996.73	C1	0.434	0.00	–	0.29	0.65	−53.1	4.1
VLBA+EB	C2	0.431	0.42	102.9	0.27	0.69	33.1	
22 GHz	C3	0.667	0.85	80.9	0.35	0.91	53.1	
	C4	0.212	2.12	125.7	4.53	0.28	−72.4	
Errors		6 %	11 %	3°	18 %		5°	
2003.04	C1	0.329	0.00	–	0.20	1.0	–	0.9
VLBA	C2	1.339	0.37	121.0	0.21	0.77	27.2	
22 GHz	C3	0.400	1.52	98.1	0.78	0.89	28.2	
	C4	0.015	2.77	127.1	0.41	1.0	–	
Errors		6 %	15 %	3°	8 %		3°	
1996.73	C1	0.343	0.00	–	0.30	0.57	−36.3	0.6
VLBA+EB	C2	0.304	0.46	102.6	0.23	0.67	−0.2	
43 GHz	C3	0.442	0.92	83.0	0.33	0.84	36.2	
	C5	0.191	3.73	116.4	3.01	0.66	35.5	
Errors		7 %	6 %	3°	12 %		5°	

Table B.2: The parameters of the model-fits performed using the task . The table contains the following information: Col. 1 gives the observing epoch, and frequency, Col. 2 identifies the VLBI components by letters and numbers, Col. 3 gives the flux density of each VLBI component (S), Col. 4 its radial distance r relative to component C1, Col. 5 the position angle (θ), Col. 6 the FWHM major axis (a), Col. 7 the ratio of minor to major axis (b/a), Col. 8 the position angle of the major axis (ϕ), and Col. 9 the α value (introduced in Sect. 4.3.1, in the simplest case it equals with $\beta - 2$). The positional information (Columns 4 and 5) are relative to the westernmost component, denoted as M1.

Epoch and frequency	Comp.	S [Jy]	r [mas]	θ (°)	a [mas]	b/a	ϕ (°)	α
(1)	(2)	(3)	(4)	(5)	(6)	(7)	(8)	(9)
1998.14	M1	2.235 ± 0.027	0	–	30.46 ± 0.34	0.75 ± 0.01	34.6 ± 0.17	1.97 ± 0.03
1.6 GHz	M3	0.189 ± 0.007	12.23 ± 0.68	105.1 ± 3.0				
				Estimated model-fit residuals: 57 mJy				
1996.82	M1	2.660 ± 0.011	0	–	3.46 ± 0.01	0.67 ± 0.01	31.9 ± 0.4	1.98 ± 0.02
5 GHz	M2	0.458 ± 0.009	2.90 ± 0.04	128.5 ± 4.0				
				Estimated model-fit residuals: 51 mJy				
1996.83	M1	3.202 ± 0.006	0	–	1.60 ± 0.01	0.88 ± 0.01	63.8 ± 0.6	1.99 ± 0.01
8 GHz	M2	0.219 ± 0.003	3.29 ± 0.02	125.6 ± 3.2				
				Estimated model-fit residuals: 47 mJy				

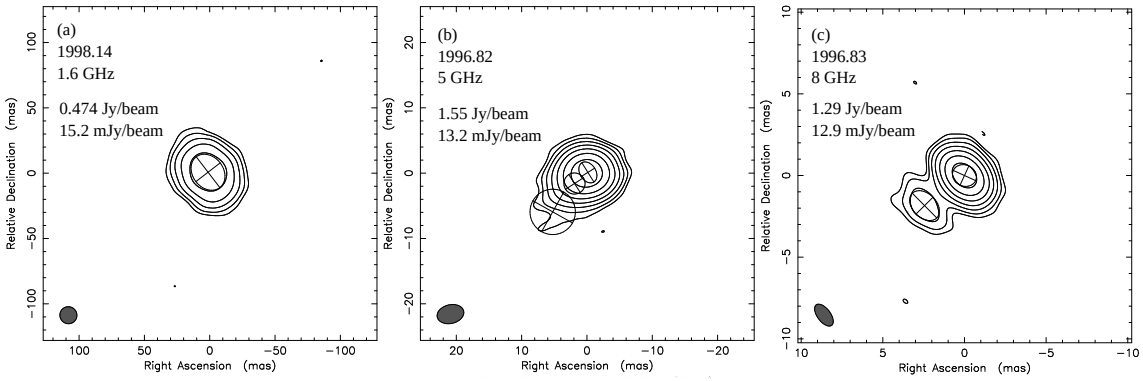

Figure B.1: Images of Gaussian model-fits of B 2005+403 at 1.6 GHz, 5 GHz, and 8 GHz at the different observing epochs. The circles characterise positions and sizes of the individual model-fit components. Epoch, frequency, peak flux density and the lowest (positive) contour level are given in the upper left corner of each image. Contours correspond to the model-fits, they are in percent of the peak flux and increase by factors of two. (Images were created in DIFMAP.)

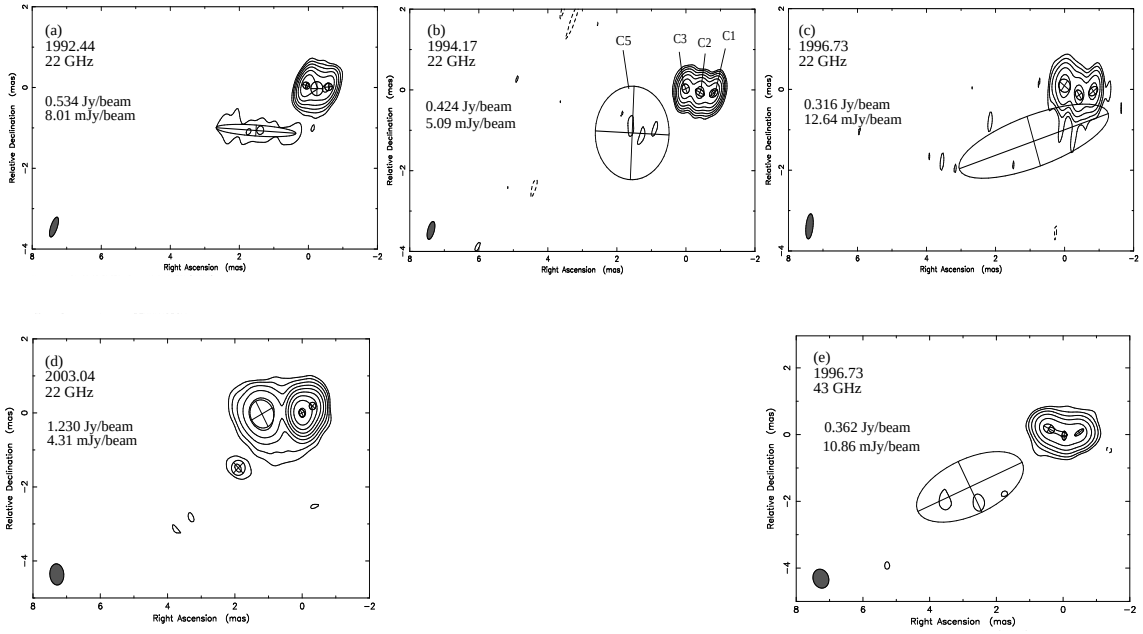

Figure B.2: Images of Gaussian model-fits for B 2005+403. The circles characterise positions and sizes of the individual model-fit components. Epoch, frequency, peak flux density and the lowest (positive) contour level are given in the upper left corner of each image. Contours correspond to the model-fits, they are in percent of the peak flux and increase by factors of two. As in Fig. 4.11, the VLBI observations were performed at 22 GHz, and 43 GHz. (Images were created in DIFMAP.)

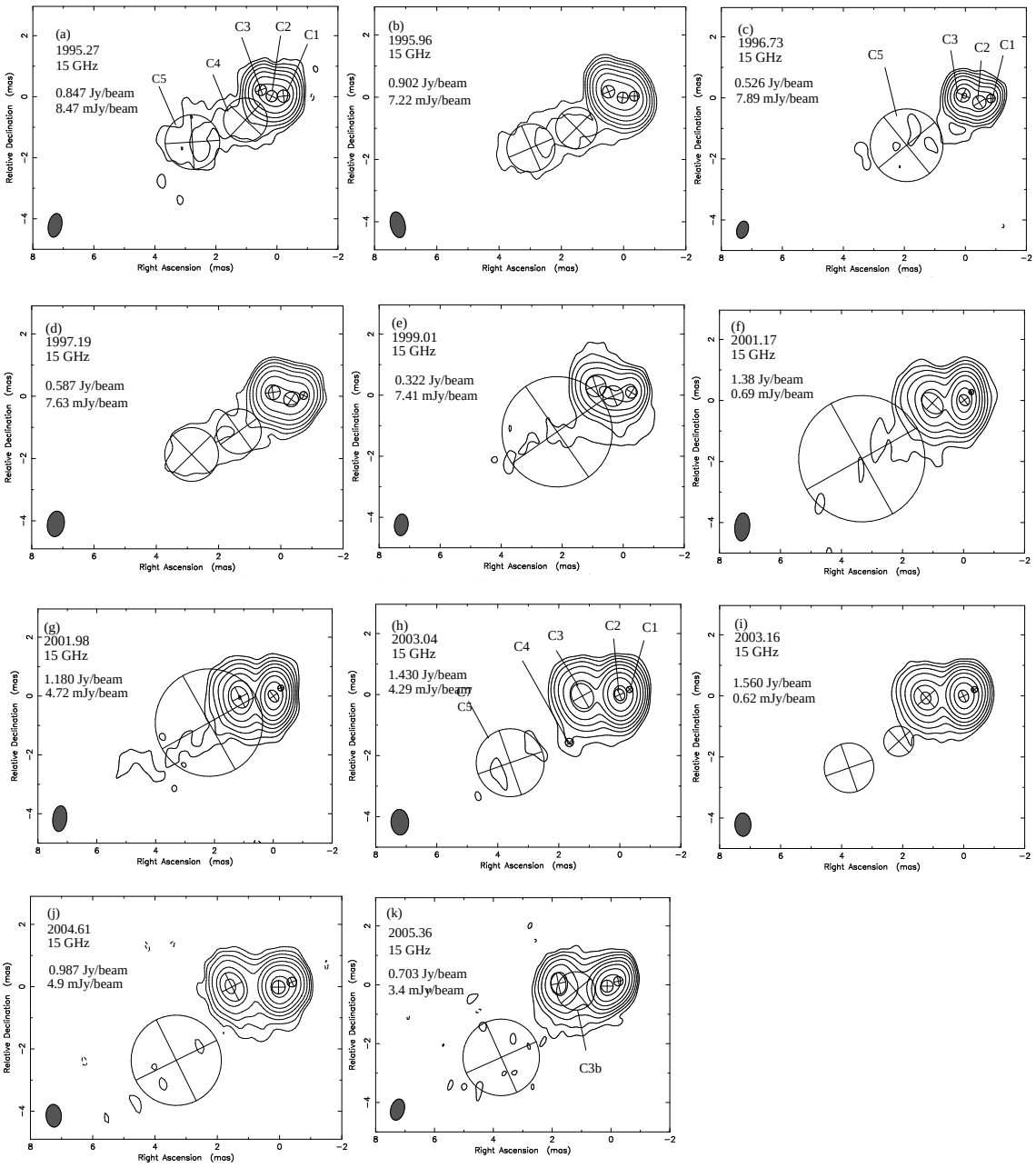

Figure B.3: Images of Gaussian model-fits for B 2005+403. The circles characterise positions and sizes of the individual model-fit components. Epoch, frequency, peak flux density and the lowest (positive) contour level are given in the upper left corner of each image. Contours correspond to the model-fits, they are in percent of the peak flux and increase by factors of two. As in Fig. 4.11, the VLBI observations were at 15 GHz. (Images were created in DIFMAP.)

C B 2007+777 model-fitting results

The results of the DIFMAP model-fitting procedures to the total intensity VSOP data of B 2007+777 are displayed in this appendix.

Table C.1: The parameters of the Gaussian model-fits. Col. 1 is the epoch, Col. 2 is the component's name, Col. 3 is the flux density in Jy, Col. 4 the major axis in mas, Col. 5 the radial distance from I0 in mas and Col. 6 the position angle. The positions of the outer components, Im and I5, are not well defined, because they are partly resolved out on the HALCA baselines.

Epoch	Comp.	S [Jy]	a [mas]	r [mas]	θ [°]
1999.679	I0	0.317 ± 0.030	0.08 ± 0.02	0	–
1999.679	I1	0.260 ± 0.021	0.05 ± 0.02	0.394 ± 0.060	−84.8 ± 4.0
1999.679	I2	0.250 ± 0.020	0.19 ± 0.06	0.575 ± 0.060	−83.4 ± 2.0
1999.679	I3	0.144 ± 0.008	0.43 ± 0.01	1.380 ± 0.064	−89.6 ± 6.0
1999.679	I4	0.024 ± 0.005	0.33 ± 0.10	1.999 ± 0.098	−85.7 ± 2.0
1999.679	Im	0.014 ± 0.005	1.92 ± 0.08	4.450 ± 1.280	−103.9 ± 3.0
1999.679	I5	0.045 ± 0.020	1.17 ± 0.08	6.827 ± 1.672	−93.3 ± 2.0
1999.685	I0	0.212 ± 0.100	0.12 ± 0.05	0	–
1999.685	I1	0.248 ± 0.080	0.05 ± 0.02	0.313 ± 0.060	−86.2 ± 2.0
1999.685	I2	0.315 ± 0.060	0.12 ± 0.05	0.585 ± 0.060	−84.0 ± 4.0
1999.685	I3	0.139 ± 0.010	0.47 ± 0.03	1.338 ± 0.060	−89.2 ± 2.0
1999.685	I4	0.036 ± 0.006	0.22 ± 0.11	1.945 ± 0.074	−87.6 ± 2.0
1999.685	Im	0.019 ± 0.004	2.21 ± 0.50	4.283 ± 1.003	−100.7 ± 2.0
1999.685	I5	0.045 ± 0.020	1.14 ± 0.06	6.879 ± 1.264	−92.9 ± 2.0
1999.753	I0	0.280 ± 0.010	0.05 ± 0.02	0	–
1999.753	I1	0.270 ± 0.060	0.05 ± 0.02	0.406 ± 0.060	−84.8 ± 5.0
1999.753	I2	0.197 ± 0.050	0.05 ± 0.02	0.670 ± 0.060	−85.7 ± 2.0
1999.753	I3	0.124 ± 0.014	0.35 ± 0.02	1.495 ± 0.060	−88.9 ± 2.0
1999.753	I4	0.009 ± 0.005	0.17 ± 0.02	2.221 ± 0.088	−86.8 ± 2.0
1999.753	Im	0.014 ± 0.014	1.79 ± 0.60	4.308 ± 0.830	−102.4 ± 2.0
1999.753	I5	0.045 ± 0.016	1.18 ± 0.01	6.814 ± 1.166	−93.0 ± 2.0
1999.759	I0	0.295 ± 0.070	0.05 ± 0.02	0	–
1999.759	I1	0.322 ± 0.033	0.05 ± 0.02	0.421 ± 0.060	−85.8 ± 4.0
1999.759	I2	0.146 ± 0.020	0.05 ± 0.02	0.695 ± 0.060	−87.1 ± 2.0
1999.759	I3	0.125 ± 0.020	0.32 ± 0.12	1.488 ± 0.060	−89.3 ± 3.0
1999.759	I4	0.010 ± 0.005	0.54 ± 0.20	2.317 ± 0.060	−87.0 ± 3.0
1999.759	Im	0.015 ± 0.004	1.15 ± 0.10	4.582 ± 1.540	−101.9 ± 4.0
1999.759	I5	0.045 ± 0.010	1.82 ± 0.18	6.807 ± 1.524	−92.9 ± 2.0

Bibliography

Abraham, Z., Carrara, E. A., Zensus, J. A., & Unwin, S. C. 1996, A&AS, 115, 543

Alberdi, A., Gómez, J. L., Marcaide, J. M., Marscher, A. P., & Pérez-Torres, M. A. 2000, A&A, 361, 529

Aller, H. D., Aller, M. F., Latimer, G. E., & Hughes, P. A. 2003, American Astronomical Society Meeting Abstracts, 202

Antonucci, R. R. J., Hickson, P., Olszewski, E. W., & Miller, J. S. 1986, AJ, 92, 1

Armstrong, J. W., Rickett, B. J., & Spangler, S. R. 1995, ApJ, 443, 209

Baars, J. W. M., Genzel, R., Pauliny-Toth, I. I. K., & Witzel, A. 1977, A&A, 61, 99

Bach, U. 2004, Ph.D. Thesis, Rheinischen Friedrich-Wilhelms-Universität Bonn

Bach, U., Kadler, M., Krichbaum, T. P., et al. 2003, in Proceedings of the Second ENIGMA Meeting, ed. C. M. Raiteri & M. Villata, 216–223

Bach, U., Krichbaum, T. P., Kraus, A., Witzel, A., & Zensus, J. A. 2005, ArXiv Astrophysics e-prints, astro-ph/0511761

Bach, U., Krichbaum, T. P., Middelberg, E., et al. 2004, in European VLBI Network on New Developments in VLBI Science and Technology, ed. R. Bachiller, F. Colomer, J.-F. Desmurs, & P. de Vicente, 155–156

Becker, R. H., White, R. L., & Edwards, A. L. 1991, ApJS, 75, 1

Beckert, T. 2005, Memorie della Societa Astronomica Italiana, 76, 150

Begelman, M. C., Blandford, R. D., & Rees, M. J. 1980, Nature, 287, 307

Begelman, M. C., Ergun, R. E., & Rees, M. J. 2005, ApJ, 625, 51

Begelman, M. C., Rees, M. J., & Sikora, M. 1994, ApJ, 429, L57

Bender, R., Kormendy, J., Bower, G., et al. 2005, ApJ, 631, 280

Benford, G. 1992, ApJ, 391, L59

Bernhart, S., Krichbaum, T. P., Bach, U., et al. 2006, in preparation, to be published in A&A

Bevington, P. R. & Robinson, D. K. 1992, Data reduction and error analysis for the physical sciences (New York: McGraw-Hill, 2nd ed.)

Bhat, N. D. R., Gupta, Y., & Rao, A. P. 1998, ApJ, 500, 262

Bhat, N. D. R., Gupta, Y., & Rao, A. P. 1999, ApJ, 514, 249

Bignall, H. E. 2003, Ph.D. Thesis, The University of Adelaide

Bignall, H. E., Jauncey, D. L., Kedziora-Chudczer, L. L., et al. 2002, Publications of the Astronomical Society of Australia, 19, 29

Bignall, H. E., Jauncey, D. L., Lovell, J. E. J., et al. 2003, ApJ, 585, 653

Blandford, R. D. & Königl, A. 1979, ApJ, 232, 34

Boksenberg, A., Briggs, S. A., Carswell, R. F., Schmidt, M., & Walsh, D. 1976, MNRAS, 177, 43P

Briggs, D. S. 1995, Bulletin of the American Astronomical Society, 27, 1444

Britzen, S., Krichbaum, T. P., Strom, R. G., et al. 2005, A&A, 444, 443

Britzen, S., Roland, J., Laskar, J., et al. 2001, A&A, 374, 784

Britzen, S., Vermeulen, R., Taylor, G., et al. 2006, in preparation, to be published in A&A

Britzen, S., Witzel, A., Krichbaum, T. P., et al. 2000, A&A, 360, 65

Browne, I. W. A., Wilkinson, P. N., Patnaik, A. R., & Wrobel, J. M. 1998, MNRAS, 293, 257

Bykov, A. M., Krassilchtchikov, A. M., Uvarov, Y. A., et al. 2004, A&A, 427, L21

Camenzind, M. 2002, Lecture Notes, Heidelberg

Camenzind, M. 2005, Memorie della Societa Astronomica Italiana, 76, 98

Camenzind, M. & Krockenberger, M. 1992, A&A, 255, 59

Cimó, G. 2003, Ph.D. Thesis, Rheinischen Friedrich-Wilhelms-Universität Bonn

Clegg, A. W., Cordes, J. M., Simonetti, J. M., & Kulkarni, S. R. 1992, ApJ, 386, 143

Cohen, M. H., Cannon, W., Purcell, G. H., et al. 1971, ApJ, 170, 207

Cordes, J. M. & Lazio, T. J. W. 2002, ArXiv Astrophysics e-prints, astro-ph/0207156

Cordes, J. M., Weisberg, J. M., & Boriakoff, V. 1985, ApJ, 288, 221

Cotton, W. D. 1993, AJ, 106, 1241

Cox, D. P. & Reynolds, R. J. 1987, ARA&A, 25, 303

Dennett-Thorpe, J. & de Bruyn, A. G. 2000, ApJ, 529, L65

Dennett-Thorpe, J. & de Bruyn, A. G. 2002, Nature, 415, 57

Dennett-Thorpe, J. & de Bruyn, A. G. 2003, A&A, 404, 113

Dennison, B., Simonetti, J. H., & Topasna, G. A. 1998, Publications of the Astronomical Society of Australia, 15, 147

Desai, K. M. & Fey, A. L. 2001, ApJS, 133, 395

Desai, K. M., Gwinn, C. R., & Diamond, P. J. 1994, Nature, 372, 754

Dewangan, G. C. & Griffiths, R. E. 2005, ApJ, 625, L31

Douglas, J. N., Bash, F. N., Bozyan, F. A., Torrence, G. W., & Wolfe, C. 1996, AJ, 111, 1945

Eckart, A., Witzel, A., Biermann, P., et al. 1986, A&A, 168, 17

Edelson, R. A. & Krolik, J. H. 1988, ApJ, 333, 646

Fabian, A. C. 1979, Royal Society of London Proceedings Series A, 366, 449

Fanaroff, B. L. & Riley, J. M. 1974, MNRAS, 167, 31P

Fanti, C., Fanti, R., Ficarra, A., et al. 1981, A&AS, 45, 61

Fey, A. L. & Charlot, P. 1997, ApJS, 111, 95

Fey, A. L., Spangler, S. R., & Mutel, R. L. 1989, ApJ, 337, 730

Fiedler, R., Dennison, B., Johnson, K. J., Waltman, E. B., & Simon, R. 1994, ApJ, 430, 581

Fiedler, R. L., Dennison, B., Johnston, K. J., & Hewish, A. 1987, Nature, 326, 675

Fuhrmann, L. 2004, Ph.D. Thesis, Rheinischen Friedrich-Wilhelms-Universität Bonn

Fuhrmann, L., Cimò, G., Krichbaum, T. P., et al. 2002a, in Proceedings of the 6th EVN Symposium, ed. E. Ros, R. W. Porcas, A. P. Lobanov, & J. A. Zensus, 73

Fuhrmann, L., Krichbaum, T. P., Cimò, G., et al. 2002b, Publications of the Astronomical Society of Australia, 19, 64

Gabányi, K. E., Krichbaum, T. P., Britzen, S., et al. 2006, A&A, in press

Gabuzda, D. C. 2003, New Astronomy Review, 47, 599

Gabuzda, D. C. & Gómez, J. L. 2001, MNRAS, 320, L49

Gabuzda, D. C., Kochenov, P. Y., Kollgaard, R. I., & Cawthorne, T. V. 2000a, MNRAS, 315, 229

Gabuzda, D. C., Mullan, C. M., Cawthorne, T. V., Wardle, J. F. C., & Roberts, D. H. 1994, ApJ, 435, 140

Gabuzda, D. C. & Pashchenko, I. N. 2002, in Proceedings of the 6th EVN Symposium, ed. E. Ros, R. W. Porcas, A. P. Lobanov, & J. A. Zensus

Gabuzda, D. C., Pushkarev, A. B., & Cawthorne, T. V. 2000b, MNRAS, 319, 1109

Ghisellini, G., Padovani, P., Celotti, A., & Maraschi, L. 1993, ApJ, 407, 65

Ghisellini, G., Tavecchio, F., & Chiaberge, M. 2005, A&A, 432, 401

Gilmore, G. F. & Zeilik, M. 2000, Allen's Astrophysical Quantities (New York: Springer-Verlag)

Glantz, S. A. 1992, Primer of Biostatistics (New York: McGraw-Hill)

Gómez, J.-L., Marscher, A. P., Alberdi, A., & Gabuzda, D. C. 1999, ApJ, 519, 642

Goodman, J. 1997, New Astronomy, 2, 449

Gopal-Krishna, Dhurde, S., & Wiita, P. J. 2004, ApJ, 615, L81

Gopal-Krishna & Wiita, P. J. 1992, A&A, 259, 109

Gopal-Krishna & Wiita, P. J. 2000, A&A, 363, 507

Gregory, P. C. & Condon, J. J. 1991, ApJS, 75, 1011

Gupta, Y., Rickett, B. J., & Coles, W. A. 1993, ApJ, 403, 183

Haffner, L. M., Reynolds, R. J., Tufte, S. L., et al. 2003, ApJS, 149, 405

Hausen, N. R., Reynolds, R. J., Haffner, L. M., & Tufte, S. L. 2002, ApJ, 565, 1060

Heeschen, D. S. 1984, AJ, 89, 1111

Heeschen, D. S., Krichbaum, T., Schalinski, C. J., & Witzel, A. 1987, AJ, 94, 1493

Heeschen, D. S. & Rickett, B. J. 1987, AJ, 93, 589

Hirabayashi, H., Hirosawa, H., Kobayashi, H., et al. 2000, PASJ, 52, 955

Homan, D. C., Ojha, R., Wardle, J. F. C., et al. 2001, ApJ, 549, 840

Hughes, P. A., Aller, H. D., & Aller, M. F. 1985, ApJ, 298, 301

Hughes, P. A., Aller, H. D., & Aller, M. F. 1989, ApJ, 341, 68

Hummel, C. A. 1987, Diploma Thesis, Rheinischen Friedrich-Wilhelms-Universität Bonn

Jauncey, D. L., Johnston, H. M., Bignall, H. E., et al. 2003, Ap&SS, 288, 63

Jauncey, D. L., Kedziora-Chudczer, L. L., Lovell, J. E. J., et al. 2000, in Astrophysical Phenomena Revealed by Space VLBI, Proceedings of the VSOP Symposium, held at the Institute of Space and astronautical Science, Sagamihara, Kanagawa, Japan, January 19 - 21, 2000, Eds.: H. Hirabayashi, P.G. Edwards, and D.W. Murphy, Published by the Institute of Space and Astronautical Science, p. 147-150., 147–150

Jauncey, D. L. & Macquart, J.-P. 2001, A&A, 370, L9

Jenkins, G. M. & Watts, D. G. 1969, Spectral analysis and its applications (Holden-Day Series in Time Series Analysis, London: Holden-Day, 1969)

Junor, W., Biretta, J. A., & Livio, M. 1999, Nature, 401, 891

Kaastra, J. S. & Roos, N. 1992, A&A, 254, 96

Kedziora-Chudczer, L., Jauncey, D. L., Wieringa, M. A., Tzioumis, A. K., & Bignall, H. E. 2001a, Ap&SS, 278, 113

Kedziora-Chudczer, L., Jauncey, D. L., Wieringa, M. H., et al. 1997, ApJ, 490, L9

Kedziora-Chudczer, L. L., Jauncey, D. L., Wieringa, M. H., Tzioumis, A. K., & Reynolds, J. E. 2001b, MNRAS, 325, 1411

Kellermann, K. I., Lister, M. L., Homan, D. C., et al. 2004, ApJ, 609, 539

Kellermann, K. I. & Pauliny-Toth, I. I. K. 1969, ApJ, 155, L71

Kikuchi, S., Mikami, Y., Inoue, M., Tabara, H., & Kato, T. 1988, A&A, 190, L8

Kochenov, P. Y. & Gabuzda, D. C. 1999, in ASP Conf. Ser. 159: BL Lac Phenomenon, ed. L. O. Takalo & A. Sillanpää, 460

Koenigl, A. & Choudhuri, A. R. 1985, ApJ, 289, 173

Kollgaard, R. I., Wardle, J. F. C., Roberts, D. H., & Gabuzda, D. C. 1992, AJ, 104, 1687

Kovalev, Y. Y., Kellermann, K. I., Lister, D. C., et al. 2005, AJ, in press (astro-ph/0505536)

Kraus, A. 1997, Ph.D. Thesis, Rheinischen Friedrich-Wilhelms-Universität Bonn

Kraus, A., Krichbaum, T. P., Wegner, R., et al. 2003, A&A, 401, 161

Kraus, A., Witzel, A., Krichbaum, T. P., et al. 1999, A&A, 352, L107

Krichbaum, T. P., Alef, W., & Witzel, A. 1996, in IAU Symp. 175: Extragalactic Radio Sources, ed. R. D. Ekers, C. Fanti, & L. Padrielli, 11

Krichbaum, T. P., Alef, W., Witzel, A., et al. 1998, A&A, 329, 873

Krichbaum, T. P., Graham, D. A., Alef, W., et al. 2004, in European VLBI Network on New Developments in VLBI Science and Technology, ed. R. Bachiller, F. Colomer, J.-F. Desmurs, & P. de Vicente, 15–18

Krichbaum, T. P., Kraus, A., Fuhrmann, L., Cimò, G., & Witzel, A. 2002, Publications of the Astronomical Society of Australia, 19, 14

Lähteenmäki, A., Valtaoja, E., & Wiik, K. 1999, ApJ, 511, 112

Lähteenmäki, A. & Valtaoja, E. 1999, ApJ, 521, 493

Laing, R. A. 1980, MNRAS, 193, 439

Lallement, R., Welsh, B. Y., Vergely, J. L., Crifo, F., & Sfeir, D. 2003, A&A, 411, 447

Landecker, T. L., Roger, R. S., & Higgs, L. A. 1980, A&AS, 39, 133

Lazio, T. J. W. 2004, ApJ, 613, 1023

Lazio, T. J. W. & Cordes, J. M. 1998, ApJ, 505, 715

Lazio, T. J. W., Cordes, J. M., de Bruyn, A. G., & Macquart, J.-P. 2004, New Astronomy Review, 48, 1439

Lazio, T. J. W., Waltman, E. B., Ghigo, F. D., et al. 2001, ApJS, 136, 265

Leppänen, K. J., Zensus, J. A., & Diamond, P. J. 1995, AJ, 110, 2479

Lesch, H. & Pohl, M. 1992, A&A, 254, 29

Lister, M. L. & Homan, D. C. 2005, AJ, 130, 1389

Lo, K. Y., Shen, Z.-Q., Zhao, J.-H., & Ho, P. T. P. 1998, ApJ, 508, L61

Lobanov, A. P. & Roland, J. 2005, A&A, 431, 831

Lobanov, A. P. & Zensus, J. A. 2001, Science, 294, 128

Lockman, F. J., Jahoda, K., & McCammon, D. 1986, ApJ, 302, 432

Lovell, J. E. J., Jauncey, D. L., Bignall, H. E., et al. 2003, AJ, 126, 1699

Macquart, J.-P. & de Bruyn, G. 2005, ArXiv Astrophysics e-prints, astro-ph/051049

Maitia, V., Lestrade, J.-F., & Cognard, I. 2003, ApJ, 582, 972

Marcaide, J. M., Alberdi, A., Gomez, J. L., et al. 1994, in Compact Extragalactic Radio Sources, 141

Marscher, A. P. 1983, ApJ, 264, 296

Marscher, A. P. 2005, Memorie della Societa Astronomica Italiana, 76, 13

Marscher, A. P. & Gear, W. K. 1985, ApJ, 298, 114

Marscher, A. P., Gear, W. K., & Travis, J. P. 1992, in Variability of Blazars, 85

Marscher, A. P., Marshall, F. E., Mushotzky, R. F., et al. 1979, ApJ, 233, 498

Matthews, T. A. & Sandage, A. R. 1963, ApJ, 138, 30

Mayall, N. U. 1934, PASP, 46, 134

Molnar, L. A., Mutel, R. L., Reid, M. J., & Johnston, K. J. 1995, ApJ, 438, 708

Momjian, E., Ghosh, T., Salter, C., & Venkataraman, A. 2004, American Astronomical Society Meeting Abstracts, 205

Murphy, D. W., Browne, I. W. A., & Perley, R. A. 1993, MNRAS, 264, 298

Mutel, R. L., Su, B., Bucciferro, R. R., & Phillips, R. B. 1990, ApJ, 352, 81

Myers, S. T., Jackson, N. J., Browne, I. W. A., et al. 2003, MNRAS, 341, 1

Narayan, R. 1992, Royal Society of London Philosophical Transactions Series A, 341, 151

Nordgren, T. E., Cordes, J. M., & Terzian, Y. 1992, AJ, 104, 1465

Ojha, R., Fey, A. L., Jauncey, D. L., Lovell, J. E. J., & Johnston, K. J. 2004, ApJ, 614, 607

Ott, M., Witzel, A., Quirrenbach, A., et al. 1994, A&A, 284, 331

Patnaik, A. R., Browne, I. W. A., Wilkinson, P. N., & Wrobel, J. M. 1992, MNRAS, 254, 655

Pelletier, G. & Sol, H. 1992, MNRAS, 254, 635

Peng, B., Kraus, A., Krichbaum, T. P., et al. 2000, A&A, 353, 937

Peterson, B. M., Ferrarese, L., Gilbert, K. M., et al. 2004, ApJ, 613, 682

Pohl, M., Reich, W., Krichbaum, T. P., et al. 1995, A&A, 303, 383

Qian, S.-J., Britzen, S., Witzel, A., et al. 1998, Chinese Astronomy and Astrophysics, Volume 22, Issue 3, p. 280-287., 22, 280

Qian, S.-J., Kraus, A., Zhang, X.-Z., et al. 2002, Chinese Journal of Astronony and Astrophysics, 2, 325

Qian, S.-J., Li, X.-C., Wegner, R., Witzel, A., & Krichbaum, T. P. 1996a, Chinese Astronomy and Astrophysics, Volume 20, Issue 1, p. 15-25., 20, 15

Qian, S. J., Quirrenbach, A., Witzel, A., et al. 1991, A&A, 241, 15

Qian, S. J., Witzel, A., Kraus, A., Krichbaum, T. P., & Britzen, S. 1996b, in ASP Conf. Ser. 100: Energy Transport in Radio Galaxies and Quasars, ed. P. E. Hardee, A. H. Bridle, & J. A. Zensus, 55

Qian, S. J., Witzel, A., Kraus, A., Krichbaum, T. P., & Zensus, J. A. 2001, A&A, 367, 770

Qian, S.-J. & Zhang, X.-Z. 2001, Chinese Journal of Astronony and Astrophysics, 1, 133

Quirrenbach, A., Kraus, A., Witzel, A., et al. 2000, A&AS, 141, 221

Quirrenbach, A., Witzel, A., Kirchbaum, T. P., et al. 1992, A&A, 258, 279

Quirrenbach, A., Witzel, A., Qian, S. J., et al. 1989, A&A, 226, L1

Quirrenbach, A., Witzel, A., Wagner, S., et al. 1991, ApJ, 372, L71

Readhead, A. C. S. 1994, ApJ, 426, 51

Rees, M. J. 1966, Nature, 211, 468

Rees, M. J. 1978, Phys. Scr, 17, 193

Reynolds, S. P. 1982, ApJ, 256, 13

Rickett, B. 2001, Ap&SS, 278, 129

Rickett, B., Lazio, T. J. W., & Ghigo, F. D. 2005, ArXiv Astrophysics e-prints, astro-ph/0509030

Rickett, B. J. 1986, ApJ, 307, 564

Rickett, B. J. 1990, ARA&A, 28, 561

Rickett, B. J., Coles, W. A., & Bourgois, G. 1984, A&A, 134, 390

Rickett, B. J., Kedziora-Chudczer, L., & Jauncey, D. L. 2002, ApJ, 581, 103

Rickett, B. J., Quirrenbach, A., Wegner, R., Krichbaum, T. P., & Witzel, A. 1995, A&A, 293, 479

Rickett, B. J., Witzel, A., Kraus, A., Krichbaum, T. P., & Qian, S. J. 2001, ApJ, 550, L11

Romani, R. W., Narayan, R., & Blandford, R. 1986, MNRAS, 220, 19

Ros, E., Zensus, J. A., & Lobanov, A. P. 2000, A&A, 354, 55

Rose, W. K., Guillory, J., Beall, J. H., & Kainer, S. 1987, ApJ, 314, 95

Rybicki, G. B. & Lightman, A. P. 1979, Radiative processes in astrophysics (New York, Wiley-Interscience, 1979. 393 p.)

Salvati, M., Spada, M., & Pacini, F. 1998, ApJ, 495, L19+

Savolainen, T., Wiik, K., Valtaoja, E., Jorstad, S. G., & Marscher, A. P. 2002, A&A, 394, 851

Scheuer, P. A. G. & Readhead, A. C. S. 1979, Nature, 277, 182

Schmidt, M. 1963, Nature, 197, 1040

Seyfert, C. K. 1943, ApJ, 97, 28

Shapirovskaya, N. Y. 1978, Soviet Astronomy, 22, 544

Shapirovskaya, N. Y. & Larchenkova, T. I. 1995, Astronomical and Astrophysical Transactions, 7, 29

Shepherd, M. C. 1997, in ASP Conf. Ser. 125: Astronomical Data Analysis Software and Systems VI, ed. G. Hunt & H. Payne, 77

Sillanpaa, A., Haarala, S., Valtonen, M. J., Sundelius, B., & Byrd, G. G. 1988, ApJ, 325, 628

Simonetti, J. H. & Cordes, J. M. 1990, ApJ, 349, 97

Simonetti, J. H., Cordes, J. M., & Heeschen, D. S. 1985, ApJ, 296, 46

Spada, M., Salvati, M., & Pacini, F. 1999, ApJ, 511, 136

Spangler, S. R. & Cordes, J. M. 1998, ApJ, 505, 766

Spangler, S. R., Eastman, W. A., Gregorini, L., Mantovani, F., & Padrielli, L. 1993, A&A, 267, 213

Spangler, S. R. & Reynolds, R. J. 1990, ApJ, 361, 116

Spergel, D. N., Verde, L., Peiris, H. V., et al. 2003, ApJS, 148, 175

Stickel, M., Fried, J. W., & Kuehr, H. 1989, A&AS, 80, 103

Taylor, G. B., Vermeulen, R. C., Pearson, T. J., et al. 1994, ApJS, 95, 345

Taylor, J. H. & Cordes, J. M. 1993, ApJ, 411, 674

Trotter, A. S., Moran, J. M., & Rodriguez, L. F. 1998, ApJ, 493, 666

Türler, M., Courvoisier, T. J.-L., & Paltani, S. 1999, A&A, 349, 45

Turlo, Z., Forkert, T., Sieber, W., & Wilson, W. 1985, A&A, 142, 181

U. S. Naval Observatory & Royal Greenwich Observatory. 1998, The Astronomical Almanac for the year 1999 (The Astronomical Almanac for the year 1999, Publisher: Washington: United States Government Printing Office, (USGPO) and London: Her Majesty's Stationery Office (HMSO), 1998)

Ulrich, M.-H., Maraschi, L., & Urry, C. M. 1997, ARA&A, 35, 445

Urry, C. 2004, in ASP Conf. Ser. 311: AGN Physics with the Sloan Digital Sky Survey, ed. G. T. Richards & P. B. Hall, 49

Urry, C. M. & Padovani, P. 1995, PASP, 107, 803

Urry, C. M., Sambruna, R. M., Worrall, D. M., et al. 1996, ApJ, 463, 424

Valtaoja, E., Lähteenmäki, A., Teräsranta, H., & Lainela, M. 1999, ApJS, 120, 95

Valtaoja, E., Teräsranta, H., Tornikoski, M., et al. 2000, ApJ, 531, 744

Wagner, S. J. & Witzel, A. 1995, ARA&A, 33, 163

Wagner, S. J., Witzel, A., Heidt, J., et al. 1996, AJ, 111, 2187

Wagner, S. J., Witzel, A., Krichbaum, T. P., et al. 1993, A&A, 271, 344

Walker, M. A. 1998, MNRAS, 294, 307

Walker, M. A. 2001, MNRAS, 321, 176

Walker, R. C. 1999, in ASP Conf. Ser. 180: Synthesis Imaging in Radio Astronomy II, ed. G. B. Taylor, C. L. Carilli, & R. A. Perley, 433

Wehrle, A. E., Piner, B. G., Unwin, S. C., et al. 2001, ApJS, 133, 297

Welsh, B. Y., Sallmen, S., & Lallement, R. 2004, A&A, 414, 261

White, R. L. & Becker, R. H. 1992, ApJS, 79, 331

Whitney, A. 2005, in ASP Conf. Ser. 340: Future Directions in High Resolution Astronomy, 588

Whitney, A. R., Shapiro, I. I., Rogers, A. E. E., et al. 1971, Science, 173, 225

Wilkinson, P. N., Browne, I. W. A., Patnaik, A. R., Wrobel, J. M., & Sorathia, B. 1998, MNRAS, 300, 790

Wilkinson, P. N., Narayan, R., & Spencer, R. E. 1994, MNRAS, 269, 67

Williams, R. J., Pogge, R. W., & Mathur, S. 2002, AJ, 124, 3042

Witzel, A., Heeschen, D. S., Schalinski, C., & Krichbaum, T. 1986, Mitteilungen der Astronomischen Gesellschaft Hamburg, 65, 239

Worrall, D. M. & Wilkes, B. J. 1990, ApJ, 360, 396

Xu, W., Readhead, A. C. S., Pearson, T. J., Polatidis, A. G., & Wilkinson, P. N. 1995, ApJS, 99, 297

Zavala, R. T. & Taylor, G. B. 2003, ApJ, 589, 126

Acknowledgements

In the last lines of this thesis, I want to express my gratitude to all those people who helped and supported me in this work.

First of all I would like to express my gratitude to Prof. Dr. Uli Klein, Priv. Doz. Dr. Walter Huchtmeier, Prof. Dr. Karsten Buse and Prof. Dr. Clemens Simmer that they were willing to participate as members of my PhD examination board.

I want to thank to Prof. Dr. Anton Zensus for providing me the opportunity to prepare my PhD thesis in the VLBI group. I want to thank to the International Max Planck International Research School (IMPRS) for Radio and Infrared Astronomy for supporting my PhD project.

I would like to thank my advisors Priv. Doz. Dr. Silke Britzen, Dr. Thomas Krichbaum and Dr. Arno Witzel for their numerous suggestions and advice. I sincerely appreciate the amount of time and effort they spent in helping me to complete my thesis work.

I am especially grateful to Prof. Dr. Hugh Aller, Dr Margo Aller and Dr. Matt Lister for kindly providing data prior to publication.

I would like to thank Dr. Alex Kraus for his prompt answers with any questions related to Effelsberg observations and data reduction and for providing useful data reduction tools.

I would also like to thank all members of the VLBI group. First of all, those two (former) members, Dr. Uwe Bach and Dr. Lars Fuhrmann who were close collaborators in this thesis project. I am very grateful to Uwe for his tireless support in any AIPS and DIFMAP related questions; and to Lars for his helps in all the aspects of the IDV phenomenon. I want to thank Dr. Richard Porcas, his perfect questions always revealed, which parts I understood the least. I am grateful to Dr. Alan Roy for his careful review of this thesis. I want to thank Dr. Eduardo Ros for all his suggestions and support, Dr. Walter Alef for his help on any hardware or software problems.

I want to thank Dr. Thomas Beckert for the many useful discussions.

I am also grateful to the Effelsberg staff for their help and their patience during my observations.

I am indebted to all students and post-docs (also those who have already left the institute already) of the VLBI group for all they contributed to making my stay in the institute a pleasant one. Especially, I want to thank to my roommates Rupal, Anne and Anupreeta for their help in my scientific work and advice on every aspects of life, for their humour, and of course for the marvellous chocolate (and other) cakes. I want to thank to Iván, Manuel, Matthias and Nicola for the many important discussion. I also want to thank to Violetta, Simone, Manolis and Sang-Sung not just for their help in my observations but for the many absolutely non-scientific discussions we had.

I want to thank Gabi Breuer and Elisabeth Lahr-Nilles, for their help in dealing with the German authorities and thus making my everyday life in Germany easier.

This acknowledgement would not be complete unless I mention my teachers, parents and my friends in Hungary. Without their professional or personal support, I would have never been able to work in this field. My high school physics teacher Norbert Horváth, whose tireless support in numerous fields of physics are greatly appreciated. I am extremely grateful to my diploma supervisor, Dr. Sándor Frey, and to Dr. István Fejes who first introduced radio astronomy to me.

My parents' and grandparents' support was essential to complete my thesis work. I want to thank to all my friends: Eszter, Anikó, and Timi. They did not forget me and greeted me with the same love every time I went home to Hungary. Big thanks to Rita, for her help in everything from learning Japanese to cooking (actually she was cooking and I was eating). Lots of thanks to Kistom for everything.

Last but not least, I am very thankful to the HARDWIRED^{TM}. Especially I want to thank to Barny and Birdy. Their encouragement and support are highly appreciated.